The interplay between large scales of motion and the wall shear stress in wall-bounded turbulence

Zur Erlangung des akademischen Grades eines

Doktors der Ingenieurwissenschaften (Dr.-Ing.)

von der KIT-Fakultät für Maschinenbau des
Karlsruher Instituts für Technologie (KIT)
angenommene

Dissertation

von

M.Sc. Andrea Andreolli

Tag der mündlichen Prüfung: 17. Dezember 2024

Hauptreferentin: Prof. Dr.-Ing. Bettina Frohnapfel
Korreferent: Prof. Dr. Nicholas Hutchins

Abstract

Wall-bounded flows are flows of engineering interest in which a fluid flows in the proximity of a solid wall. Examples of wall-bounded flows are the flow of air (or water) around a moving (streamlined) vehicle, or the fluid flow inside a pipe. The fluid and the solid exchange a frictional force (or a stress, to be more precise) which takes the name of wall shear stress. The wall shear stress typically represents an expense for the flow, as for instance it slows down the moving vehicle or it slows down the fluid running inside the pipe. Wall-bounded flows are typically turbulent, meaning that a set of vortices of various sizes is found inside the flow; these vortices advect and distort each other in a chaotic manner. The vortices can be cathegorised into large and small scales of motion depending on how their size changes under changing circumstances (e.g. by increasing the flow velocity).

This manuscript deals with the effects produced by large turbulent vortices on the wall shear stress, and vice-versa with how large scales are influenced by the wall shear stress. This mutual interaction takes many forms. First off, the wall shear stress represents the main cost of driving a flow, and the share of costs caused by the presence of large scales is investigated. Moreover, it is verified how much of these costs can be spared if the large scales are removed from the flow, e.g. by some flow control device. This can help understand whether controlling large scales is a viable cost-reducing strategy: so far, research on flow control has mainly focused on small scales, and the only commercially available flow control device (riblet films, to the author's knowledge) works by targeting small scales indeed.

Additionally, the interaction between large scales and the wall shear stress is explored in terms of two mechanims concerning the dynamics of large scales. Shedding light on the dynamics of large scales could help both to improve turbulence models for large-eddy simulations and to design phyisically-informed large-scale flow control devices. Large scales typically reside further away from the wall than small ones; nevertheless, their footprint can be found in the near-wall region in the form of a large-scaled pattern of the wall shear stress (consisting in regions of higher- and lower-than-average wall shear stress). This pattern is commonly understood to locally distort the small scales in a process named amplitude modulation. To verify whether these distorsions are caused by the pattern of wall shear stress, a numerical experiment is designed, in which large scales are prevented from creating a footprint at the wall. Although the idea behind aplitude modulation is that large scales exert an influence on the near-wall region, a second mechanism is explored in this manuscript, according to which large scales might originate from near-wall flow features instead. As postulated by Townsend (*The structure of turbulent shear flow*, 2 nd ed., 1976), large-scaled patterns of wall shear stress might be able to trigger the formation of self-sustaining large-scaled motions. These motions are then able to become the dominant flow feature thanks to their extended life time. The plausibility of Townsend's hypothesis is assessed by artificially triggering the formation of structures of a controlled size and then measuring their life time.

Kurzfassung

Wandgebundene Strömungen sind Strömungen von technischem Interesse, bei denen ein Fluid in der Nähe einer festen Wand fließt. Beispiele für wandbegrenzte Strömungen sind die Strömung von Luft (oder Wasser) um ein sich bewegendes (stromlinienförmiges) Fahrzeug oder die Flüssigkeitsströmung in einem Rohr. Das Fluid und der Festkörper tauschen eine Reibungskraft (oder genauer gesagt eine Spannung) aus, die als Wandschubspannung bezeichnet wird. Die Wandschubspannung stellt in der Regel einen Energieaufwand für die Strömung dar, da sie beispielsweise das sich bewegende Fahrzeug oder das im Rohr fließende Fluid bremst. Wandbegrenzte Strömungen sind in der Regel turbulent, d. h. es gibt in der Strömung eine Reihe von Wirbeln unterschiedlicher Größe. Diese Wirbel bewegen sich und verzerren sich gegenseitig auf chaotische Weise. Die Wirbel können in große und kleine Bewegungsskalen eingeteilt werden, je nachdem, wie sich ihre Größe unter verschiedenen Bedingungen (z. B. durch Erhöhung der Strömungsgeschwindigkeit) ändert.

Diese Dissertation befasst sich mit den Auswirkungen großer turbulenter Wirbel auf die Wandschubspannung und umgekehrt mit der Beeinflussung großer Skalen durch die Wandschubspannung. Diese gegenseitige Wechselwirkung nimmt viele Formen an. Zunächst einmal stellt die Wandschubspannung den Hauptenergieaufwand für die Strömung dar. Es wird untersucht, welcher Anteil des Aufwands durch das Vorhandensein großer Wirbel verursacht wird. Darüber hinaus wird geprüft, inwieweit der Aufwand reduziert werden kann, wenn die großen Wirbel aus der Strömung entfernt werden (z.B. durch eine Strömungskontrollvorrichtung). Dies kann dazu beitragen, zu verstehen, ob die Kontrolle großer Wirbel eine praktikable Strategie zur Kostenreduzierung ist: Bislang hat sich die Forschung hauptsächlich auf kleine Wirbel konzentriert. Die einzige kommerziell erhältliche Vorrichtung zur Strömungskontrolle (Riblet-Folien, soweit dem Autor bekannt) funktioniert tatsächlich, indem sie auf kleine Wirbel abzielt.

Darüber hinaus wird die Wechselwirkung zwischen großen Wirbeln und der Wandschubspannung anhand von zwei Hypothesen untersucht, die die Dynamik großer Wirbel betreffen. Die Erforschung der Dynamik großer Wirbel könnte sowohl zur Verbesserung von Turbulenzmodellen als auch zur Entwicklung physikalisch fundierter Strömungskontrollvorrichtungen beitragen. Große Skalen befinden sich in der Regel weiter von der Wand entfernt als kleine Skalen; dennoch kann ihr Fußabdruck in der wandnahen Region in Form einer großskaligen Verteilung der Wandschubspannung gefunden werden (bestehend aus Regionen mit höherer und niedrigerer Wandschubspannung als der durchschnittlichen). Es wird allgemein davon ausgegangen, dass diese Verteilung die kleinen Skalen in einem Prozess, der als Amplitudenmodulation bezeichnet wird, lokal verzerrt. Um zu überprüfen, ob diese Verzerrungen durch die Verteilung der Wandschubspannung verursacht werden, wird ein numerisches Experiment entworfen, bei dem große Skalen daran gehindert werden, einen Fußabdruck an der Wand zu erzeugen. Obwohl die Idee hinter der Aplitudenmodulation darin besteht, dass große Skalen einen Einfluss auf die wandnahe Region ausüben, wird in dieser Dissertation ein zweiter Mechanismus untersucht, demzufolge große Skalen stattdessen von wandnahen Strömungsmerkmalen herrühren könnten. Wie von Townsend (*The structure of turbulent shear flow*, 2. Aufl., 1976) postuliert, könnten großskalige Verteilungen der Wandschubspannung in der Lage sein, die Bildung von sich selbst erhaltenden großskaligen Strukturen auszulösen. Diese Strukturen können dann dank ihrer langen Lebensdauer zum dominierenden Strömungsmerkmal werden. Die Plausibilität der Townsend-Hypothese wird geprüft, indem die Bildung von Strukturen kontrollierter Größe künstlich ausgelöst und dann ihre Lebensdauer gemessen wird.

Symbols and abbreviations

Mathematical symbols and operators

SYMBOL	SI UNIT	DESCRIPTION
$(...)$		placeholder
$\langle ... \rangle$		expected value
$\langle ... \rangle_z$		spanwise average of the expected value; coincides with the expected value in the case of spanwise homogeneous quantities
$\frac{\mathrm{d}(...)}{\mathrm{d}(...)}$		ordinary derivative
$\frac{\partial(...)}{\partial(...)}$		partial derivative
∇	m^{-1}	gradient vector (typically in 3D-space)
$(\vec{...})$		vectorial quantity
$\underline{(...)}$		unit vector
$\underline{\underline{(...)}}$		second order tensor
$(...) \cdot (...)$		scalar (dot) product
$(...) \times (...)$		vector (cross) product
$\widehat{(...)}$		Fourier-transformed quantity (in the sense of the Fourier series; transform in one direction only)
$\widehat{\widehat{(...)}}$		Fourier-transformed quantity (in the sense of the Fourier series; transform in two directions)
$(...)^H$		complex conjugate

Latin letters

SYMBOL	SI UNIT	DESCRIPTION
a		share of the total power input Π_t of a Couette-Poiseuille flow that is provided by the pumping power Π_p ($a = \Pi_p/\Pi_t$)
A_1, A_3		non-dimensional constants of the attached eddy log-law
B_1, B_2, B_3		non-dimensional constants of the attached eddy log-law
C_1, C_2		non-dimensional constants of the velocity log-law
C^*_{AM}		amplitude modulation coefficient (two-point inner-scaled scale-decomposed velocity skewness)
C_f		skin friction coefficient
$\vec{f}$	$\mathrm{kg}\,\mathrm{m}^{-2}\,\mathrm{s}^{-2}$	generic force (per unit volume) acting on a fluid element

$f_{ae,i}$		non-dimensional shape function of the i-th velocity component induced by an attached eddy
$\vec{f}_c$	$\mathrm{kg\,m^{-2}\,s^{-2}}$	Coriolis force per unit volume
f_w		non-dimensional wall velocity function
Fo		Fourier number
$\mathcal{F}\left\{...\right\}$	m or s	operator indicating the (continuous) Fourier transform
$\mathcal{FS}\left\{...\right\}$		operator indicating the calculation of the coefficients of the Fourier series
g_d		non-dimensional velocity defect function
G	$\mathrm{kg\,m^{-2}\,s^{-2}}$	streamwise pressure gradient (absolute value)
G_u		non-dimensional coefficient measuring the transient growth of I_u ($G_u > 0$ indicates the presence of transient growth)
h	m	outer length scale – that is, in most cases throughout the present manuscript, the channel half-height
h_a^+, h_s^+		friction Reynolds numbers based on the antisymmetric and symmetric parts of the total shear stress at the wall
h_y	m	distance of a vortex center from the nearest wall
H_{ae}	m	height of an attached eddy
i		imaginary unit
i_u	$\mathrm{m^2\,s^{-2}}$	plane-averaged kinetic energy per unit mass of the streamwise dispersive velocity
$I_{i,j}$		non-dimensional contribution to the Reynolds stresses by a single attached eddy
I_u, I_{vw}	$\mathrm{m^2\,s^{-2}}$	volume-averaged kinetic energy per unit mass of the streamwise and circulatory components of the dispersive velocity field
k		von Kármán constant
Kn		Knudsen number
ℓ	m	slip length
L	m	some generic length scale
L_d	m	streamwise extent of the coherent momentum pathways
L_x, L_z	m	streamwise and spanwise (respectively) extent of the simulation domain
$\underline{n}$		normal unit vector (to a given surface)
$\mathcal{P}$, $\mathcal{P}^L$, $\mathcal{P}^\Delta$	$\mathrm{kg\,s^{-3}}$	turbulence production per unit wetted area: total, laminar and deviation respectively
r_x, r_z	m	separation between two points in the stremwise and spanwise directions respectively
$\underline{\underline{R}}$	$\mathrm{kg\,m^{-1}\,s^{-2}}$	Reynolds stress tensor
$\mathcal{R}e$		real part of a complex number

Re		Reynolds number (generic)
Re_τ		friction Reynolds number
Re_b, Re_w, Re_q		Reynolds number built with h and either the bulk velocity (Re_b) or the velocity at the wall (Re_w); Re_q generally indicates any of Re_b or Re_w
Re_α		Reynolds number based on h, U_α
Re_π		Reynolds number based on h, U_π
Ro		Rotation number
s	m	strip width for strip-type roughness
t	s	time
T_{ae}	s	life time of an attached eddy
T_f	s	duration of a transient simulation; see §6
T_u, T_{vw}	s	life time of the coherent momentum pathways and circulatory motions respectively
T_w	s	life time of a Fourier mode that composes the dispersive wall shear stress pattern
$\vec{u} = (u, v, w)$	$\mathrm{m\,s^{-1}}$	velocity of the fluid (vector) with its streamwise, wall-normal and spanwise components
$\vec{u}_d = (\tilde{u}, \tilde{v}, \tilde{w})$	$\mathrm{m\,s^{-1}}$	dispersive velocity field (vector) with its streamwise, wall-normal and spanwise components
$u_{ae,i}$	$\mathrm{m\,s^{-1}}$	i-th component of the velocity field induced by a single attached eddy
u_p	$\mathrm{m\,s^{-1}}$	alternative definition of the viscous velocity that uses hG instead of τ_w; used when τ_w is not a constant (see §6)
u_τ	$\mathrm{m\,s^{-1}}$	viscous (a.k.a. friction, inner) velocity
$u_{\tau,m}$	$\mathrm{m\,s^{-1}}$	worst-case (that is, maximum in time and space) viscous velocity; applies to cases where u_τ is not constant (see §6)
$\mathcal{U}$	$\mathrm{m\,s^{-1}}$	some generic velocity scale
U	$\mathrm{m\,s^{-1}}$	mean velocity (depends only on the wall-normal coordinate, possibly on time)
U_b, U_w, U_q	$\mathrm{m\,s^{-1}}$	bulk velocity or velocity at the wall; U_q generally indicates any of U_b or U_w
U_c	$\mathrm{m\,s^{-1}}$	centerline velocity
U^L, U^Δ	$\mathrm{m\,s^{-1}}$	laminar and deviation components of the mean velocity according to the extended Reynolds decomposition
U_α	$\mathrm{m\,s^{-1}}$	velocity based on the integral α of the Reynolds shear stress
U_π	$\mathrm{m\,s^{-1}}$	power velocity (velocity scale based on the total power input Π_t)
x, y, z	m	streamwise, wall-normal and spanwise cartesian coordinates
$\mathbb{Z}$		the set of integer numbers

Greek letters

SYMBOL	SI UNIT	DESCRIPTION
α, α_c, α_p	$\mathrm{m^2\,s^{-2}}$	weighted wall-normal averages of the $\langle u'v'\rangle$ correlation: total, Couette part, Poiseuille part
β	$\mathrm{m^4\,s^{-4}}$	wall-normal average of the square of the $\langle u'v'\rangle$ correlation
γ	m	mean free path between molecules
δ_p	m	alternative definition of the viscous length scale that uses hG instead of τ_w; used when τ_w is not a constant (see §6)
δ_v	m	viscous (a.k.a. friction, inner) length scale
$\delta_{v,m}$	m	worst-case (that is, maximum in time and space) viscous length scale; applies to cases where δ_v is not constant (see §6)
Δt	s	time resolution (time step) of a simulation
Δt_{out}	s	sampling time for the simulations (a snapshot is stored every Δt_{out} of simulation time)
Δx, Δz	m	spatial resolution (of a simulation) in the streamwise and spanwise directions.
Δy_w, Δy_c	m	spatial resolution (of a simulation) in the wall-normal direction: resolution at the wall and at the center of the channel respectively.
$\Delta\kappa_x$, $\Delta\kappa_z$	$\mathrm{rad\,m^{-1}}$	Fourier resolution in the streamwise and spanwise directions
ϵ	$\mathrm{kg\,s^{-3}}$	turbulent dissipation per unit wetted area
ε	any	some small quantity ($\varepsilon \to 0$)
ζ	m	conditioned spanwise variable
κ_x, κ_z	$\mathrm{rad\,m^{-1}}$	wavenumbers in the streamwise and spanwise directions
$\varkappa$		non-dimensional function that selects the Fourier modes and wall-normal positions that are targeted by modal damping
λ_x, λ_z	m	wavelengths in the streamwise and spanwise directions
Λ_s	m	spanwise period (twice the strip width) of strip-type roughness
μ	$\mathrm{kg\,m^{-1}\,s^{-1}}$	dynamic viscosity of a fluid
ν	$\mathrm{m^2\,s^{-1}}$	kinematic viscosity of a fluid
Ξ	$\mathrm{kg\,s^{-3}}$	mean dissipation per unit wetted area
Ξ^L, Ξ^Δ	$\mathrm{kg\,s^{-3}}$	laminar and deviation components of the mean dissipation per unit wetted area (as per the extended Reynolds decomposition)
Π_p	$\mathrm{kg\,s^{-3}}$	pumping power per unit wetted area
Π_t	$\mathrm{kg\,s^{-3}}$	total power per unit wetted area provided to a turbulent flow
Π_w	$\mathrm{kg\,s^{-3}}$	power fed at the wall per unit wetted area
ρ	$\mathrm{kg\,m^{-3}}$	density of a fluid
$\underline{\underline{\sigma}}$	$\mathrm{kg\,m^{-1}\,s^{-2}}$	viscous stress tensor

τ	$\mathrm{kg\,m^{-1}\,s^{-2}}$	total shear stress (sum of Reynolds shear stress and mean shear stress)
τ_a, τ_s	$\mathrm{kg\,m^{-1}\,s^{-2}}$	antisymmetric and symmetric parts of the total shear stress profile, evaluated at the wall
τ_B, τ_T	$\mathrm{kg\,m^{-1}\,s^{-2}}$	wall shear stress at the bottom, top walls
τ_w	$\mathrm{kg\,m^{-1}\,s^{-2}}$	wall shear stress
Υ	s	time scale that determines the intensity of modal damping
ϕ	$\mathrm{m^4 s^{-2}}$	two-dimensional (two Fourier transforms in space) velocity spectrum
Φ	$\mathrm{m^3\,s^{-2}}$	one-dimensional (one Fourier transform in space) velocity spectrum
$\vec{\omega} = (\omega_x, \omega_y, \omega_z)$	$\mathrm{s^{-1}}$	vorticity of the fluid with its streamwise, wall-normal and spanwise components
Ω	$\mathrm{rad\,s^{-1}}$	angular velocity

Superscripts

SYMBOL	DESCRIPTION
$(...)^+$	quantity scaled in inner (viscous) units
$(...)^\pi$	quantity scaled in power units
$(...)^o$	quantity scaled in outer units
$(...)'$	fluctuation with respect to the expected value

Subscripts

SYMBOL	DESCRIPTION
$(...)_\ell$	large-scale (low-pass filtered, typically in the spanwise direction) part of a signal
$(...)_s$	small-scale (high-pass filtered, typically in the spanwise direction) part of a signal

Abbreviations

SYMBOL	DESCRIPTION
CFL	Courant-Friedrichs-Lewy (number or condition)
CFR	constant flow rate
CPG	constant pressure gradient
CPI	constant power input
DNS	direct numerical simulation

ESM	extreme-scale motion (refers to the naturally occurring roll modes of turbulent Couette flows)
FIK	Fukagata-Iwamoto-Kasagi identity (see Fukagata et al., 2002)
LES	large-eddy simulation
LSM	large-scale motion. **Important:** this acronym does not indicate a generic large-scaled feature, but rather a specific subclass of large scales whose streamwise extent is smaller than $3h$
MKE	mean kinetic energy (energy of the mean veolocity field)
RANS	Reynolds-averaged Navier Stokes equations
RD	Renard-Deck identity (see Renard and Deck, 2016)
SGS	sub-grid stresses
TKE	turbulent kinetic energy (energy of the fluctuation field)
VLSM	very-large-scale motion (large-scaled feature whose streamwise extent exceeds $3h$)

Contents

1 Introduction

This thesis deals with turbulent wall-bounded flows, with particular emphasis on turbulent motions of large size and their interaction with the near-wall region. In this first chapter it is argued why turbulence is worth investigating (§1.1); this initial discussion is intentionally targeted at a broad audience and is largely inspired by the book of Davidson (2015). A literature review is also provided (§1.2.1 to §1.2.6). The scientific objectives are then derived from the review and the structure of the thesis is explained (§1.3).

1.1 Why study turbulence?

Turbulent flows are ubiquitous, and the reader most likely comes across them in day to day life. The twisted shape of a plume rising from a chimney is an example of a turbulent jet flow; rivers usually flow in a turbulent fashion. Atmospheric phenomena are, generally speaking, turbulent. Many naturally occurring flows are so sensitive to perturbations that even a slight disturbance is sufficient for them to leave their laminar, orderly state and transition to a chaotic, long-lasting turbulent behaviour. Wall-bounded flows are no exception in this respect: these flows of engineering interest are characterised by fluid flow in proximity of a solid object, such as the flow around a vehicle or the flow inside a pipe. Given the complexity of the topic and our scarce understanding of turbulence, this thesis (just like many other works in literature) deals only with channel flows – an idealised case of a wall-bounded flow in which a fluid flows between two parallel, flat and infinitely large plates. Using this setup, turbulence can be observed even if the plates are perfectly smooth; in this way, one can focus on studying turbulent phenomena without the added complexity of having curved walls or corner effects.

Albeit commonly occurring, turbulence is still little understood. For instance, a proper definition of turbulence itself is missing (Davidson, 2015, chapters 1.4 and 2.4); proving the existence of a smooth solution to the three-dimensional time-evolving Navier-Stokes equations (i.e., the equations governing turbulence) is one of the unsolved Millennium Prize problems[1]. One of the first observations put forward about the nature of turbulence is that it includes a set of eddies (or vortices) of many sizes (Richardson and Lynch, 2007; Marusic and Monty, 2019). Eddies of different sizes are sometimes referred to as different *scales of motion*. The largest scales of motion typically hold the most energy and also receive a substantial amount of energy from the mean flow (the meaning of this will be clarified in §2.2.6). At a steady state, these eddies keep a constant level of energy, meaning that they must get rid of the energy they receive from the mean flow. Typically, energy is transferred to the smallest scales of motion, which then dissipate it. According to the original idea of Richardson, this energy transfer happens across a set of eddies of intermediate size. While the details of this interscale energy transmission do not necessarily hold for fluid flow in proximity of a wall (see §1.2.4, or Piomelli et al., 1991; Kawata and Alfredsson, 2018; Chiarini et al., 2022), the co-existence of eddies of a wide range of scales is unquestioned. In particular, turbulent eddies can be classified into small and large ones depending on their size (or, to be exact, on how their size changes under different circumstances; see §1.2.2).

---

[1] `https://www.claymath.org/millennium/navier-stokes-equation/`, accessed on Nov 29^{th}, 2023.

As for wall-bounded flows, advances have recently been made in understanding the physics of the small eddies located in proximity of the wall at a qualitative level (see §1.2.2). This is a relevant milestone, as the near-wall region where these eddies reside is understood to be the one where turbulence originates (Davidson, 2015, chapter 1.3). We are able, for instance, to predict the position and intensity of these eddies; moreover, the vortices are understood to decay and self-regenerate through a qualititative mechanism called the *streak cycle* (see §1.2.2, or Jiménez and Pinelli, 1999). However, a comprehensive quantitative (analyitical) model describing their dynamics is not available (one of the perhaps few attempts to derive a model was carried out by Moehlis et al., 2004), and the dynamics of larger eddies is the object of ongoing research.

This lack of analytical models hinders our ability to accurately analyse and predict the behaviour of turbulent flows. While indeed the Navier-Stokes equations do describe turbulence and its evolution in a deterministic way, their numerical solution (which takes the name of direct numerical simulation, or DNS) in the case of a turbulent flow is typically prohibitively expensive and possibly yields an unnecessary level of detail (Davidson, 2015, chapter 7.1.2). It is indeed arguable whether one needs to know every detail of the smallest, microscopic scales of turbulence when one is calculating the flow around a moving car; it would be sufficient, at least for engineering purposes, to know what the flow field looks like on average. By time (or ensemble) averaging a turbulent flow field, all the fine-grained details of turbulence are smoothed out, so that one is left with a flow that looks like a laminar one. A simplified set of equations (Reynolds-averaged Navier-Stokes equations, or RANS) describing only the mean flow can be derived (Pope, 2000, chapter 4.1). A similar - yet different - strategy consists in writing a set of equations for the low-pass filtered velocity field (Davidson, 2015, chapter 7.1.2). Conceptually, such an equation describes the evolution of the largest turbulent eddies, whereas the expensive computation of the dynamics of the small ones is bypassed; hence the name, *large eddy simulation*, or LES. While the numerical solution of both RANS and LES equations is cheaper than DNS, both system of equations are incomplete and require the addition of one equation (or more): the so-called turbulence model. As previously stated, no definitive turbulence model has been discovered to date; nevertheless, several models are available, each of which has a very limited validity range. Outside of the validity range, the model is not reliable.

To better clarify the issue, let us consider a problem of practical interest such as computing the air flow around a car to optimise its shape. The author estimates that performing a single DNS in this case would require 2 months of uninterrupted computation using the entirety of the Hawk cluster at HLRS Stuttgart; appendix A shows how this crude estimate was obtained. The computational expenses would be dramatic; for the current example, they would amount to roughly 23 million euros. Simulations are typically performed as a faster and cheaper alternative to experiments; clearly, DNS can hardly be regarded as a fast and cheap tool. One could then resort to RANS simulations, which are much cheaper (the calculation can, in some cases, be carried out on a laptop) but require the usage of one of the many available turbulence models. To the author's knowledge, none of the models can be trusted out-of-the-box, so that it is first necessary to calibrate them against experimental data. This might require a preliminary experimental campaign, which is – again – expensive.

The availability of reliable turbulence models would not only make the design process cheaper, avoiding excessive computational or experimental expenses, but also yield improved final designs that can be tailored to reduce expenses or greenhouse gas emissions. To improve the current turbulence models, sound understanding of turbulent phenomena is needed; this represents the main reason to investigate turbulence. In particular, understanding the interaction between small and large scales is of crucial importance for LES equations; the turbulence model required for LES indeed describes a momentum exchange between vortices of different sizes (Pope, 2000, chapter 13.5.2).

While it would surely help, a reliable turbulence model is not strictly necessary to achieve energy savings or a reduction of greenhouse gas emissions. For this purpose, improving our qualitative understanding of turbulence has already proven successful. An entire branch of research named *flow control* is indeed dedicated to reducing the cost (in terms of energy) of performing a given task by actively or passively adjusting and modifying the flow. Typically (Frohnapfel et al., 2012), the cost is represented by the skin friction (the viscous force that opposes a moving airplane, for instance, or that opposes the fluid running inside a pipe); the task would indeed be to have the airplane cruise at a given speed, or to keep a given flow rate inside a pipe. Unlike other fields of engineering, where control laws are designed using rigorous mathematical tools and reduced-order models of the systems to be controlled, flow control is pursued by physically informed trial and error. That being said, a promising reduced-order model of turbulence is currently being developed and tested (McKeon and Sharma, 2010; Toedtli et al., 2019). While most flow control technologies have a low readiness level and are therefore only being researched in an academic context, riblets (a particular passive flow control device) have recently made their appearence in the free market. Lufthansa, a public limited company, is currently deploying a riblet film coating on its fleet of long-haul aircraft; the company claims[2] that this can achieve roughly 1% drag reduction adjusting for flight conditions and mission profile. Applying this to the entire fleet of 10 aircraft will save the CO2-equivalent of 48 freight flights from Frankfurt to Shanghai every year.

The best-performing known drag-reduction devices all work by manipulating the small, near-wall turbulent eddies. This is unsurprising, as our knowledge of other scales of motion is relatively limited. For instance, two of these drag reduction strategies (Quadrio et al., 2009; Luchini et al., 1991) function by distorting the autonomous cycle through which the small eddies self-regenerate and by pushing the small eddies further away from the wall respectively. However, controlling small vortices has its own shortcomings. Mainly, small scales have microscopic size under circumstances of practical interest, meaning that the devices used to control them need to be miniaturised (Kasagi et al., 2009). This usually involves expensive manufacturing processes; while such an expense can be compensated and overcome by the energy (hence, money) savings yielded by the control, larger savings may potentially be achieved by targeting large turbulent eddies instead. Once again, a deeper understanding of the dynamics of large scales - and especially of the mechanism through which they originate and self-sustain - would help designing suited flow control devices.

1.2 Literature review: wall-bounded turbulent flows

In this section, an overview of the relevant literature needed for the definition of the scientific objectives of this dissertation is presented. Notice that the first part of the section (sec. 1.2.1) contains the definition of the all-important viscous units of wall-bounded turbulence. Since this definition is widely accepted and found on any textbook, it would be better suited for the *fundamentals* chapter (ch. 2); it is nevertheless shown here as it is needed for a better understanding of the literature.

1.2.1 Inner and outer units, Reynolds numbers

It is common practice in fluid mechanics to express velocities, pressure values and other values of interest in terms of some reference physical quantity (which takes the name of a *scale* or a *unit*), and not in

---

[2] `https://www.lufthansa-technik.com/en/aeroshark`, accessed on Nov 27th, 2023; the author has no affiliation with Lufthansa.

terms of standard units; this process takes the name of non-dimensionalisation. Consider for instance the flow around a wing profile; the distance between two points in the flow domain is usually expressed as a multiple of the chord of the profile, and not in meters. The chord then acts as a length scale; notice that any other quantity can be used as a length scale, and that the choice of scale is arbitrary (and yet customary). Typically, only a length scale and a velocity one are needed to make all the relevant physical quantities of an incompressible flow non-dimensional.

As for wall bounded turbulence, two different sets of units are usually defined: *inner* and *outer units*. Each set comprises a velocity and a length scale. The *outer length scale* (here indicated by h) is defined as some dominant geometric feature of the flow: for example, the boundary layer thickness in a boundary layer flow, or the channel half-height in a channel flow (notice that this thesis only deals with the latter type of flows). The outer length scale is complemented by an *outer velocity*, which can be some volume-averaged flow velocity (the bulk velocity U_b in a channel flow) or the spatial maximum of the time-averaged velocity (the centerline velocity U_c in a channel flow). Heuristically, the largest turbulent vortices scale in outer units and can be found away from the wall, in the so-called outer layer; however, there exists a thin layer in proximity of the wall where the motion of small eddies is not influenced by the large, outer geometry but rather by the wall itself – owing to its proximity (Davidson, 2015, chapter 4.2). This region is referred to as the *near-wall region* and its behaviour is governed by the *inner units*, which are defined using the wall shear stress τ_w. The latter represents the skin friction per unit wetted area and is indeed the mean shear stress exchanged between the fluid and the wall in the streamwise direction (that is, in the direction of the flow):

$$\tau_w = \left| \underline{x} \cdot \left(\left\langle \underline{\underline{\sigma}} \right\rangle_w \underline{n}_w \right) \right| \tag{1.1}$$

where $\underline{x}$ is the unit vector indicating the streamwise direction, $\underline{\underline{\sigma}}$ is the viscous stress tensor, $\langle \cdot \rangle$ indicates an expected value (eg., it could represent an average in time and along all statistically homogeneous directions), $\underline{n}$ indicates a normal unit vector and subscript $(\cdot)_w$ indicates that quantities are evaluated at the wall. Consequently, the inner velocity scale u_τ - also known as *wall velocity* or *friction velocity* - and the inner length scale δ_v are defined as:

$$u_\tau = \sqrt{\tau_w / \rho} \tag{1.2}$$

$$\delta_v = \nu / u_\tau \tag{1.3}$$

where ρ and ν are the fluid density and kinematic viscosity respectively. Quantities made non-dimensional with inner units are indicated by a plus superscript $(\cdot)^+$.

The dynamics of many incompressible flows whose geometry is fixed (except for a scaling factor) are determined by a single non-dimensional similarity parameter: the *Reynolds number* (*Re*). Even when more than one similarity parameters need to be defined (e.g. when additional phenomena such as buoyancy-driven convection occur), it should be possible to choose a set of parameters that includes a Reynolds number. The Reynolds number is defined as follows:

$$Re = \frac{\text{length scale} \ \cdot \ \text{velocity scale}}{\nu} \tag{1.4}$$

The choice of length and velocity scale is arbitrary and one can define as many Reynolds numbers as desired; the physical interpretation of the Reynolds numer changes therefore depending on the context, even though it is commonly interpreted to be the ratio between inertial and viscous forces. For instance, using outer units, one could define a bulk Reynolds number Re_b or a centerline Reynolds number Re_c.

When building a Reynolds number using the inner length and velocity scales, one always obtains a unitary Reynolds number owing to the definition of such scales.

An additional, frequently used Reynolds number is defined by combining the outer length scale h with the inner velocity scale u_τ:

$$Re_\tau = \frac{hu_\tau}{\nu} = \frac{h}{\delta_v} = h^+ \tag{1.5}$$

This takes the name of *friction Reynolds number* or *Kármán number*; it can be interpreted as the ratio between the outer and the inner length scales or as a measure of the friction at the wall (if the geometry and the viscosity are fixed, a larger Re_τ indicates larger values of the wall shear stress).

1.2.2 Small and large scales of motion

Turbulent motions are classified into small and large scales depending on whether their size scales in inner or outer units under changing circumstances. For instance, an eddy is classified as small if, by changing the Reynolds number, its size remains (roughly) constant in inner units. Otherwise, if its size remains (roughly) constant in outer units, it is classified as large. In the following, the main features of small and large scales of motion will be discussed.

An often-observed signature of both small and large scales is the presence in the flow of streamwise-elongated streaks of alternating high and low streamwise velocity (Kline et al., 1967; Kim et al., 1987; van Dyke, 2012; Tomkins and Adrian, 2003; Hutchins and Marusic, 2007a; Tsukahara et al., 2010; Lee and Moser, 2018); notice, however, that the term *streak* is most commonly associated to small scales. These small and large streaks are almost periodic in the spanwise direction, so that their period – usually called *streak spacing* – can be measured. The streak spacing can be estimated by visual inspection (Kline et al., 1967); alternatively, it can be calculated by analysing the position of the minima of the autocorrelation function of the streamwise velocity in the spanwise direction (Kim et al., 1987). The presence of these streaks can also be easily revealed by scrutinising the spanwise spectra of the streamwise velocity fluctuations (see §2.2.1 for the definition of fluctuations and §2.3.2 for the definition of the spectrum); in this case, the streak spacing can be estimated by checking the spanwise wavelength of the maxima of the spectrum (Kline et al., 1967; Lee and Moser, 2018). There is typically good agreement between estimates of the streak spacing yielded by these three different methods.

The main feature of the small scales is their conjectured, but also well-verified, universality. They reside in the near-wall region and their dynamics is only influenced by inner parameters (u_τ, δ_v, ν); notice that these parameters only depend on the local value of the wall shear stress τ_w and on the viscosity, but not on the outer geometry. This means that small scales should, theoretically, have the same features across flows with different geometries (boundary layers, channel flows, pipe flows) provided that inner scaling is used. This universality hypothesis is well backed by empirical evidence. Small scales can be found in the so-called buffer layer ($y^+ \approx 10$) of several wall-bounded flows and have a typical spanwise spacing of roughly $100\delta_v$ (Kline et al., 1967; Kim et al., 1987; Brereton and Hwang, 1994; Jeong et al., 1997). Their inner-scaled kinetic energy is also roughly constant across different flows and proportional to u_τ^2 (Hoyas and Jiménez, 2006; Marusic et al., 2010a).

An additional feature of the small scales is their ability to self-sustain through an autonomous near-wall cycle. The idea that small scales would be responsible for the production of turbulence through their formation and breakup dates back to the very same study that highlighted the existence of small-scaled streaks (Kline et al., 1967). This idea later evolved into several different mechanisms through which near-wall turbulence might be regenerating itself. These mechanisms have been reviewed by Panton (2001), who distinguished two main categories. The first includes mechanisms in which small eddies interact with the wall to generate offspring eddies. Mechanisms of the second category instead postulate that the typical buffer-layer velocity streaks are unstable; their breakdown triggers the formation of pairs of streamwise-elongated, counter-rotating vortices. These pairs then pull high-speed fluid from the core of the flow and eject low-speed fluid from the wall region. As a consequence, the pattern of streamwise streaks is recreated. Strong evidence in favour of this second category was found by Jiménez and Pinelli (1999). The authors were able to simulate the dynamics of a single or few more low-speed streaks by suitably restricting the simulation domain (Jiménez and Moin, 1991); this setup correctly reproduces the wall-layer in absence of outer-layer large-scale turbulence. Through a series of numerical experiments, they were able to show that indeed the streamwise vortices advect the mean velocity to form the high- and low-speed streaks, and that the streak breakdown does lead to the formation of streamwise vortices. The mechanism is named *streak cycle*.

As for large scales, they have been observed in pipe, boundary-layer, plane Poiseuille and plane Couette flows to name a few (Kim and Adrian, 1999; Hutchins and Marusic, 2007a; Balakumar and Adrian, 2007; Lee and Moser, 2018). Their energy increases with the Reynolds number (Hutchins and Marusic, 2007a; Schlatter et al., 2009) and their features are flow-dependent. For instance, significant differences can be found between the large scales of plane Poiseuille and Couette flows, although these flows share the same geometry and only differ in the way they are driven (by a pressure gradient or by relative motion of the walls respectively). The large-scaled spectral peak of a Poiseuille flow is limited to the outer layer and suggests a spanwise spacing of $1h$ (Lee and Moser, 2015); the same peak of a Couette flow spans instead the whole channel height and indicates a spanwise spacing of $4-5h$ (Kitoh and Umeki, 2008; Pirozzoli et al., 2014; Lee and Moser, 2018). Moreover, this large spectral peak can be seen in Couette flows at an almost transitional ($Re_\tau \approx 50$) Reynolds number (Komminaho et al., 1996), whereas it appears at a higher value of $Re_\tau \approx 5000$ in Poiseuille flows (Lee and Moser, 2015).

While a qualitative mechanism for the self-sustainment of small scales has been proposed and is generally accepted, the same cannot be said about large scales. Many alternative theories try to explain their origin, but no one is widely accepted (e.g. Iwamoto et al., 2004; Toh and Itano, 2005; Del Álamo and Jiménez, 2006; Hwang and Cossu, 2010a; de Giovanetti et al., 2017; Lee and Moser, 2019; Illingworth, 2020; Zhou et al., 2022). However, just like in the self-supporting cycle of the small scales, the large-scale high- and low-speed streaks have been shown to be related to streamwise vortices (Hutchins and Marusic, 2007b; Chung and McKeon, 2010; Baltzer et al., 2013; Hwang et al., 2016). A set of counter-rotating vortices (sometimes seen as a pair depending on the visualisation technique) flanks each streak, so that low-speed streaks correspond to regions of upwelling motion (large-scale ejection) whereas high-speed streaks are associated to regions of downwash (large-scale sweep).

Although the present cathegorisation of turbulent eddies in small and large scales is sufficient for the purpose of this thesis, more detailed taxonomies have been proposed in the literature (e.g. Smits et al., 2011; Marusic and Monty, 2019). For instance, a distinciton has been made between *large-scale motions* (LSMs) and *very-large scale motions* (VLSMs) in pipe, channel and boundary layer flows (Kim and Adrian, 1999; Balakumar and Adrian, 2007; Monty et al., 2009; Bailey and Smits, 2010). LSMs and VLSMs differ in that LSMs have a streamwise extent of roughly $3h$, whereas VLSMs are longer ($> 3h$). It has also been proposed that LSMs consist of packaged hairpin vortices, whereas VLSMs are formed by the merging of LSMs. The streamwise extent of turbulent structures (which defines LSMs and VLSMs) is best studied in experimental setups, whereas numerical studies such as those presented in this thesis are best suited to investigate the spanwise spacing of the structures. For this reason, the distinction between LSMs and

VLSMs will not be much emphasised in this thesis; the term *large scale* will be used to generically refer to any outer-scaled eddy (either a LSM or a VLSM) unless the acronyms are explicitly used.

Finally, it is well known that wall-bounded turbulence features a set of self-similar eddies which extend from the wall towards the bulk of the flow (Marusic and Perry, 1995; Hwang, 2015; Marusic and Monty, 2019; Puccioni et al., 2023). These are called *attached eddies* as they are, indeed, attached to the wall. They are self-similar in the sense that they have a roughly constant axpect ratio; in other words, their (spanwise and streamwise) size is proportional to their wall-normal height. Owing to this property, one can observe attached eddies of any size in proximity of the wall; moving further away from it, one can only observe wall-coherent motions that are larger than a given threshold, and this threshold grows linearly with wall-normal distance (Baars et al., 2017b). While attached eddies will not be discussed in detail in this thesis, they are responsible for the well-established logarithmic scaling of velocity covariances; moreover, it has been shown that some large scales might also be classified as attached eddies (Deshpande et al., 2023). The attached eddy model of turbulence and its main results are presented in §2.2.4; some results that are reminiscent of the attached eddy hypothesis will be presented in §6.

1.2.3 Flow control; the impact of large scales on the wall shear stress

As explained in §1.1, one of the main reasons why wall-bounded turbulence is being researched is to provide physical insights for the design of flow-controlling devices – whose aim is, generally, to reduce the wall shear stress. In this respect, research has so far mainly focused on controlling small scales; although this thesis deals with large ones, some results are worth mentioning. The best performance has been achieved by travelling waves of spanwise motion of the wall (Quadrio et al., 2009; Auteri et al., 2010); this strategy yields a net power saving, meaning that the power saved by the control strategy is less than the power required for it to operate. Travelling waves are understood to function in a similar way to spanwise wall oscillations of the wall (Quadrio et al., 2009; Karniadakis and Choi, 2003), that is by interfering with the self-sustaining cycle of the small scales. Among the other strategies used to control small scales, opposition control (Choi et al., 1994) is of interest for this thesis. Opposition control is based on the idea that turbulent fluctuations are generated by wall-normal velocity fluctuations transporting the mean velocity field (Jiménez and Pinelli, 1999; Del Álamo and Jiménez, 2006); this mechanism is part of the *streak cycle* described in §1.2.2 and represents the physical interpretation of the production term in the turbulent kinetic energy budget, discussed in §2.2.6. Opposition control works – as the name suggests – by opposing these wall-normal fluctuations, so as to stop the production mechanism. In experimental (as opposed to numerical) applications (Rebbeck and Choi, 2006), wall-normal fluctuations are first indirectly detected by sensing streamwise ones (the two are notoriously anti-correlated); then, they are contrasted by a wall-normal jet positioned downstream of the actuator. The delay between sensing and actuation needs to be tuned.

Controlling small scales to achieve drag reduction has two major issues. First off, many authors report that small-scale control strategies loose performance with increasing Reynolds number (Chang et al., 2002; Hurst et al., 2014, for instance). However, theoretical and numerical investigations indicate that this performance loss should not be excessive, so that significant drag reduction should still be possible at high *Re* (Iwamoto et al., 2005; Gatti and Quadrio, 2016). The second issue is, in the author's opinion, more compelling: small scales become increasingly small as the Reynolds number increases (see the definition of the inner length scale in §1.2.1, and recall that the size of small scales is constant in inner units, §1.2.2). Hence the actuators needed for the practical realisation of small-scale control need to be miniaturised (Kasagi et al., 2009); while this might be possible, as microelectricmechanical systems are becoming increasingly available, controlling large scales might be a more straightforward option.

Hence, large-scale control has become of interest. The first – albeit flawed – large-scale control strategy was proposed by Schoppa and Hussain (1998). This consisted in numerically superposing pairs of counter-rotating large vortices to the flow; a series of following studies pointed out and fixed issues with this strategy (Canton et al., 2016a,b; Yao et al., 2017). More recently, large-scale opposition control has been experimentally investigated (Abbassi et al., 2017; Ibrahim et al., 2020). Moreover, significant drag reduction has been observed in experiments deploying spanwise travelling waves to target large scales (Marusic et al., 2021). Although all these studies do indeed rely on large-scale actuation, a significant reduction of the spectral energy associated to large scales is not observed in any of them – at least to the author's knowledge.

Alongside experiments, simulations have been used to determine how much drag large scales are responsible for – and hence determine how much can be theoretically saved by controlling them. This has been done in two ways: first, simulations of flows which exhibit large scales have been analysed to determine the contribution of large scales to the skin friction. Additionally, large scales have been artificially removed from the flow to then assess the effects of their absence on the flow. Both techniques have their issues, which will be discussed below.

The contribution of large scales to skin friction can be calculated by using identities such as the *Fukagata-Iwamoto-Kasagi* (FIK, Fukagata et al., 2002) or the *Renard-Deck* (RD, Renard and Deck, 2016) ones; these express a relation between the wall shear stress and the Reynolds shear stress. By low-pass filtering the velocity field, the Reynolds stress can be decomposed into a small- and large-scale part; by plugging the scale-decomposed Reynolds shear stress into either the FIK or RD identity, one can calculate how much of the skin friction is caused by large scales (Deck et al., 2014; de Giovanetti et al., 2016; Agostini and Leschziner, 2018). This procedure has two different issues; first, the two identities yield disagreeing results, although the FIK one should be more credible based on heuristic arguments (Agostini and Leschziner, 2019a). Most importantly, the contribution of large scales to skin friction does not correspond to the amount of skin friction that would be spared if large scales are removed from the flow (eg. by an ideal, perfectly functioning control law), as is discussed in the next paragraph.

Owing to the non-linearity of turbulent phenomena, the contribution of small scales (or of some other turbulent motions) to the skin friction might increase after the removal of large scales. This has indeed been observed in the literature. Large scales can be numerically removed from a flow by suppressing them with modal damping (de Giovanetti et al., 2016; Fukagata et al., 2010) or by restricting the spanwise simulation domain in order to make them unrepresentable (as they would be larger than the domain, or smaller in terms of wavelength than the Fourier resolution, see de Giovanetti et al., 2016). In both cases, the observed amount of drag reduction is less than what is predicted by the FIK identity due to an increase in the skin-friction contribution of smaller scales. These increased costs associated to smaller scales have been linked to pressure fluctuations (Fukagata et al., 2010) or to alterations in the non-linear scale interactions (de Giovanetti et al., 2016). It is necessary to mention that using modal damping or restricting the spanwise domain is quite intrusive on the flow. Modal damping removes energy from all vortices that are comparable in size to large scales (which might be an issue in low-Re flows, as different scales of motion are not well separated); moreover, it yields discontinuous velocity spectra. Restricting the spanwise domain, instead, causes motions that are wider than the domain to be aliased on a spanwise-invariant mode; this requires an additional correction to the simulation (Hwang, 2013).

In this thesis, both a different way of measuring the impact of the large-scales on the skin friction and a different way of removing large scales will be tested. They will be briefly discussed in the scientific objectives (§1.3) and more thoroughly in §3 and §4 respectively.

1.2.4 Scale interactions, the energy cascade and large eddy simulations (LES)

Turbulence is governed by the Navier-Stokes equations, which are non-linear. A consequence of their non-linearity is that the dynamics of motions of different sizes is coupled; in other words, energy can be transferred between eddies of different scales. Motions of different sizes interact in pairs; the interaction results in the transfer of energy (or, momentum) to eddies of a third size. This process takes the name of *triadic interaction* and will be thoroughly discussed in §2.3.4. Although triadic interactions can provide a rigorous and complete description of scale interactions in turbulent flows, their investigation possibly yields an unnecessary level of detail. For this reason, scale interactions are often discussed in terms of less granular mechanisms, such as the *energy cascade* (covered in this section) and *amplitude modulation* (see the next section, §1.2.5).

The idea of a turbulent energy cascade was introduced by the classical studies of Richardson and Lynch (2007) and Kolmogorov (1991): it refers to the (not always correct) observation that turbulent energy is produced at the largest scales of motion to be then transferred to increasingly smaller ones. The smallest scales put an end to the cascade: instead of passing energy to even smaller eddies, they dissipate it through viscous processes. The concept of LES stems from this very idea: if indeed the role of small scales is to dissipate the energy they receive from large scales, one might as well not simulate their dynamics (saving significant computational resources in doing so) and replace them with dissipation (Davidson, 2015). More precisely, the terms of the LES equations that require modelling are collectively called *sub-grid scale* (SGS) *stresses*; they represent an energy (or momentum) transfer between the large, resolved scales and small, subgrid (that is, unresolved) ones (Pope, 2000).

Although Richardson's idea appears to correctly capture a commonly observed trend, interscale energy transfer processes are more sophisticated than a simple energy cascade from large to small eddies. For instance, the SGS stresses have been exactly calculated for DNS data of isotropic and wall-bounded turbulence by Piomelli et al. (1990, 1991): the authors found that, before averaging, an inverse energy cascade from small to large scales can be observed. The classic, large-to-small energy cascade is only observed on average. Similar results have been found by time tracking the evolution of individual eddies (Lozano-Durán and Jiménez, 2014).

Particularly in the case of wall-bounded flows, it is not reasonable to assume that a simple, direct energy cascade from large to small scales takes place. A significant amount of turbulent energy is produced in the near-wall region by small scales involved in the streak cycle (see §1.2.2, or e.g. Lee and Moser, 2019). This is clearly at odds with the canonic idea that small scales only receive energy from larger ones. Cimarelli et al. (2016) performed simulations of turbulent channel flows and analysed the budget of the second-order structure function, a quantity that approximates the integral amount of energy contained in all eddies smaller than a given size (Davidson, 2015). The authors identify two turbulent kinetic sources – one of which is located near the wall and is related to the streak cycle, whereas the other one is found in the outer layer. These two energy sources trigger an inverse (small to large) and a direct (large to small) cascade respectively. Further evidence of an inverse cascade started by near-wall small scales has been found Kawata and Alfredsson (2018); Chiarini et al. (2022). Individual triadic interactions have also been studied yielding similar results, altough this was done using LES data (Cho et al., 2018).

1.2.5 Amplitude modulation; the wall shear stress as a mediator

As briefly discussed in the previous section, scale interactions can also be discussed in terms of amplitude modulation. Amplitude modulation was discovered (Hutchins and Marusic, 2007b) by low-pass filtering the streamwise velocity fluctuation signal of a wall-bounded flow in the buffer layer. Thanks to filtering, the signal is split into a small- and a large-scale part; it has been observed that the envelope (amplitude) of the small-scale signal correlates well with the large-scale signal. In other words, the energy[3] associated to small scales is larger in near-wall regions where large scales induce positive velocity fluctuations, and smaller in regions where the latter induce negative fluctuations instead. Hence the name *amplitude modulation*: it appears that the small-scale velocity signal acts as a high-frequency (high-wavenumber) carrier wave whose amplitude is modulated by a large-scale envelope, similarly to a radio signal. Before delving into details, it will be argued why amplitude modulation is of practical and scientific interest.

On the practical side, the above mentioned correlation has some implications for LES simulations. In particular, it is crucial to establish whether the position of small-scale, high-energy events dictates the position of the large scales, or whether vice-versa the presence of large scales dictates the modulation of smaller ones. If the phase (that is, the position) of the large scales were dictated by the amplitude of the small scales, then the large scales would be influenced by some highly erratic small-scale quantity. This effect cannot be captured by most LES models (Davidson, 2015, chapter 7.1.2). Fortunately, though, the commonly accepted view is the opposite: most studies suggest that the amplitude of the small scales is influenced by the large ones, and not vice-versa (see the following discussion). In any case, the results of this thesis will show that this mainstream view is flawed to some degree, and that small scales do indeed have some influence on large ones.

As for the theoretical interest, amplitude modulation is commonly understood to be a manifestation of a fundamental feature of wall-bounded turbulence: that the energy of small vortices scales with the friction velocity u_τ (see §1.2.2). Although large scales usually reside in the outer layer, their footprints can also be observed in the near-wall region (Abe et al., 2004; Hoyas and Jiménez, 2006), where they co-exists with the streak cycle. This phenomenon takes the name of *superposition* (or *footprinting*) *of the large scales*. Superposition can be observed in velocity signals and - most importantly - in the wall shear stress (Schlatter et al., 2009). The superposed large scales generate large-scaled regions of high and low wall shear stress; hence the local friction velocity will be respectively higher and lower than average in these regions. Owing to its scaling, the energy of small scales can also be expected to be higher and lower than average, which is indeed what is described by the term amplitude modulation.

The idea that the wall shear stress (or more generally the superposed large-scale velocity) locally modulates the small scales has been developed by Ganapathisubramani et al. (2012), Mathis et al. (2013) and Hutchins (2014), whereas the first studies on amplitude modulation viewed the phenomenon as an interaction between the inner and the outer layer (Hutchins and Marusic, 2007b; Mathis et al., 2009; Marusic et al., 2010b; Mathis et al., 2011a). It has also been verified that regions of higher-than-average wall shear stress correspond to regions of enhanced small-scale energy (Jiménez, 2012). These observations were formalised in the quasy-steady quasi-homogeneous theory of Zhang and Chernyshenko (2016), which postulates that small scales react to changes of the wall shear stress without delay. Agostini and Leschziner (2019a) further elaborated on the underlying physical mechanism, suggesting that small scales instantaneously react to local changes of turbulence production in the buffer layer. These changes in turbulence production are driven by an increase (or decrease) of the local large scale velocity gradient, which is in turn associated to an increase (or decrease) of the wall shear stress.

Having argued why amplitude modulation is of interest and how it is usually interpreted, it is now discussed how amplitude modulation is measured. Typically, the streamwise velocity signal is acquired

---

[3] the amplitude of a wave is heuristically a proxy for its energy. Moreover, it can be rigorously shown that, if a turbulent fluctuation signal is modulated by a sinusoid of wavenumber $\bar{\kappa}$ to yield a modulated signal u, the kinetic energy u^2 has energy content on the $\bar{\kappa}$ wavenumber. Proof is left to the reader; see the spectral representation of modulation in §5.1.2.

at one or more wall-normal positions. As previously stated, the velocity is then low-pass filtered to yield a large- and a small-scale part. Finally, some statistic that quantifies modulation is computed. This process is arbitrary in many ways. Starting with filtering, this can be done in time (which, under Taylor's hypothesis, is equivalent to filtering in the streamwise direction, see Mathis et al., 2009; Baars et al., 2017a) or in the spanwise direction (Bernardini and Pirozzoli, 2011). Moreover, filtering can be done through a Fourier (Pirozzoli et al., 2011) or a wavelet (Baars et al., 2017a) transform, or by using the empirical mode decomposition (Agostini and Leschziner, 2019a). A low-pass filter also requires the definition of a cutoff wavelength (or equivalent); this choice is the least critical, as the typical size of small and large scales is well known (see §1.2.2). Finally, several different statistics have been defined to measure modulation. For instance, Mathis et al. (2009) used a Hilbert transform to calculate the envelope of the small-scale signal; by then computing the correlation between the envelope and the large-scale signal, one can detect the occurrence of modulation. Alternatively (Eitel-Amor et al., 2014), the amplitude of small scales can be approximated by the square of the small-scale signal.

All these alternative procedures have been reviewed by Dogan et al. (2019), who found that all of them robustly return the same qualitative picture of amplitude modulation. The large-scaled velocity signal and the amplitude of the small scales are correlated near the wall, and anticorrelated in the log-layer; this change of sign of the correlation is referred to as *phase reversal*. It is also worth mentioning that both one- and two-point statistics have been used as a way to measure modulation. The usage of one-point statistics has raised some controversy as the amplitude modulation coefficient defined by Mathis et al. (2009) is closely related to the skewness of the velocity fluctuations (Schlatter and Örlü, 2010; Mathis et al., 2011b; Duvvuri and McKeon, 2015). This issue can be circumvented by using a two-point statistic as shown by Bernardini and Pirozzoli (2011): by doing so, it is found that the near-wall small-scale envelope correlates well not only with the local large-scale velocity, but also with the outer-layer one. This correlation is not affected by the skewness of the distribution of the velocity fluctuations. Moreover, owing to the wall-normal coherence of large scales, it can be stated that the amplitude of near-wall small scales correlates well with large scales from any wall-normal position (Agostini et al., 2016).

For the sake of completeness, it has to be acknowledged that not only the amplitude of small scales appears to be modulated, but also their frequency (Ganapathisubramani et al., 2012; Vinuesa et al., 2015; Baars et al., 2017a; Iacobello et al., 2021). That is, near-wall regions of positive (negative) large scales correspond to regions where the time scale between small-scale events is decreased (increased). Bear in mind that the frequency is the inverse of this time scale, so that the frequency is increased (decreased). This is once again coherent with the inner-unit scaling of small scales: an inner time scale $\delta_v/u_\tau = \nu/(u_\tau)^2$ can be defined using the length and velocity ones presented in §1.2.1, and this time scale decreases if u_τ locally increases. In any case, frequency modulation has not been investigated as extensively as amplitude modulation in the literature: this thesis will be no exception and focus on amplitude modulation.

1.2.6 On the recurrence of h-scaled features

As discussed in §1.2.2, the properties of large scales are flow dependent, the common denominator being that their size scales in outer units. In other words, large scales have (by definition) a size in the order of h; often, they constitute the dominant feature of a turbulent flow.

However, large turbulent vortices (and VLSMs in particular) are not the only occurrence of a dominant h-scaled flow feature. Indeed, similar phenomena have been observed in presence of multi-scale roughness at the wall; these phenomena will be referred to as *momentum pathways*. Moreover, it is known that the *secondary motions* that are artificially induced by a spanwise roughness pattern applied to the wall resemble the naturally occurring large scales. In the following, the literature concerning momentum pathways and spanwise heterogeneous roughness will be briefly reviewed; the similarities with the VLSMs will be highlighted. Finally, an explanation of why such h-scaled features dominate the flow in different contexts is proposed.

Turbulent flows over rough walls are typically studied in the presence of homogeneous roghness, meaning that the statistical features of the roughness are spatially constant (see Frohnapfel et al., 2024, for a better discussion of roughness homogeneity and heterogeneity). Nevertheless, naturally occurring rough surfaces, originating for instance from the accumulation of dirt, ice or organic matter over the surface of a vehicle, can seldom be regarded as homogenous. Whereas homogeneous roughness typically causes a vertical shift of the velocity profile (Chung et al., 2021), the effect of heterogeneous roughness on the mean flow is more complex. "For example, Mejia-Alvarez et al. (2013) have inspected the roughness generated on a turbine blade by deposition of foreign materials, finding that it contained randomly distributed elements of different scales. The flow over such a multi-scale roughness has been experimentally investigated in a boundary layer wind tunnel (Mejia-Alvarez and Christensen, 2013; Barros and Christensen, 2014). It was found that the ensemble-averaged velocity field is highly heterogeneous as it contains coherent regions of low and high momentum (low and high momentum pathways); these occur in absence of obvious geometric features (e.g., ridges). The pathways have an h-scaled extent in the streamwise and wall-normal direction, where h is the outer length scale (the boundary layer thickness for the studies mentioned here). Nikora et al. (2019) observed similar coherent motions over multi-scale roughness in open channel flows, finding that the pathways provide a contribution to skin friction that adds up to the direct effect of roughness. Comparable low- and high-momentum pathways were found both experimentally (Womack et al., 2022) and numerically (Kaminaris et al., 2023) by studying the turbulent flow over a random distribution of truncated conical roughness elements resembling the barnacles that accumulate on ship hulls. These pathways extend for at least $18h$ (Womack et al., 2022) in the streamwise direction; the position at which they occur is reproducible across different repetitions of the same experiment. Also, high- and low- momentum pathways of a h-scaled spanwise period were observed by Reynolds et al. (2007) in a boundary layer evolving over an array of staggered cubic roughness elements. In this last case, however, the spanwise period of the momentum pattern increased with streamwise fetch in an almost quantized manner.

There is no consensus over what triggers the formation of these momentum pathways. Kaminaris et al. (2023) found that the spanwise topology of the pathways correlates well with the one of the leading edge of the roughness (that is, the first row of roughness elements stretching over the spanwise direction). They went on to show that the pathways are effectively triggered by the leading edge, and persist for a long distance downstream of it regardless of whether they evolve over a smooth or a rough surface. Conversely, Barros and Christensen (2014) found a local correlation between the roughness topology and the pathways, suggesting that the pathways originate from heterogeneity in the roughness properties in a similar way to secondary motions over spanwise heterogeneous roughness. It is unclear which of these two mechanisms is dominant; it cannot be excluded that both contribute to the formation of the pathways. Nevertheless, there is a close resemblance between the pathways and secondary motions observed over spanwise heterogeneous roughness (as will be discussed below), to the point that the pathways themselves are also referred to as secondary motions. Both the pathways and the secondary motions, in turn, have often been linked" [MY24b] to VLSMs as mentioned at the beginning of this section.

"Spanwise heterogeneous roughness is usually studied in terms of spanwise-alternating streamwise-elongated strips with different roughness properties (Hinze, 1967; Nugroho et al., 2013; Türk et al., 2014; Willingham et al., 2014; Anderson et al., 2015; Stroh et al., 2016a; Vanderwel et al., 2019; Stroh et al., 2020; Frohnapfel et al., 2024). The strip width is typically indicated by s; notice that this is half the period Λ_s of the spanwise roughness pattern. The roughness pattern induces secondary motions; as long as the strips are narrow ($s \leq h$), the secondary motions consist in high- and low- momentum pathways flanked by cross-sectional circulatory motions (for instance, Chung et al., 2018). The same topology has been observed for the pathways occurring over multi-scale roughness (Barros and Christensen, 2014; Nikora et al., 2019). Conditional views of VLSMs (Hutchins and Marusic, 2007b; Hwang et al., 2016) also share the same geometry, the main difference being that VLSMs occur at random spanwise positions whereas the position of secondary motions is based on the roughness topology. It has been proposed that momentum pathways and secondary motions originate as the geometric or roughness features at the wall provide a preferential spawning position for VLSMs (Mejia-Alvarez and Christensen, 2013; Chung et al., 2018; Wangsawijaya and Hutchins, 2022). This view is corroborated by the observation that randomly occurring VLSMs do not coexist with fixed-position secondary motions of comparable size ($s/h \approx 1$, Barros and Christensen, 2019; Zampiron et al., 2020; Schäfer, 2023). Moreover, both VLSMs and secondary motions have been found to meander about their spawning position, although the associated streamwise periods are slightly different (Hutchins and Marusic, 2007a; Kevin et al., 2017, 2019; Vanderwel et al., 2019; Wangsawijaya and Hutchins, 2022). Another difference is given by the fact that VLSMs are typically observed in the log-layer, whereas secondary motions of comparable size extend to the wake region (Wangsawijaya et al., 2020)." [MY24b]

The key common feature of VLSMs, momentum pathways and secondary motions over heterogeneous roughness is – as previously stated – their h-scaled extent. The typical spanwise scale of VLSMs occurring over smooth walls is indeed $1 - 4\,h$ as discussed in §1.2.2. "The momentum pathways found over multi-scale and randomly distributed roughness are also h-spaced in the spanwise direction (as can be seen from the data of Reynolds et al., 2007; Barros and Christensen, 2014; Womack et al., 2022). Secondary motions induced by a spanwise roughness pattern are most energetic when the strip spacing s is in the order of h (Vanderwel and Ganapathisubramani, 2015; Medjnoun et al., 2018; Wangsawijaya et al., 2020); as the strip spacing is increased to larger values ($s \gg h$), the secondary motions stop growing in size and rather remain confined to a h-wide region around roughness transitions.

There are at least two possible explanations for the frequent observation of dominant h-scaled features in turbulent flows; they are not necessarily mutually exclusive. The study of the linearised Navier-Stokes equations in wall-bounded flows has revealed that the perturbations they amplify the most are either inner- or h-scaled in the spanwise direction (Del Álamo and Jiménez, 2006; Cossu et al., 2009; Alizard et al., 2015). Large-scaled perturbations evolve into structures reminiscent of the conditional views of VLSMs, of secondary motions and of the momentum pathways flanked by rolling motions, although linear analysis tends to overestimate the spanwise wavelength of these features (Alizard et al., 2015). Similar results have been found by searching the volume forcing mode that is most amplified by the linearised Navier-Stokes equations (Hwang and Cossu, 2010b; Illingworth, 2020). In light of these linear amplification mechanisms, then, the phenomenology described above can be explained as follows. A broadband disturbance (as a velocity perturbation or a volume force) is provided either by non-linear interactions between small scales or by the roughness topology; the flow then acts to selectively amplify disturbances of a particular, h-scaled set of wavelengths to yield the observed VLSMs or momentum pathways. The plausibility of this hypothesis is corroborated by evidence that channel flows are particularly sensitive to spanwise disturbances at the wall (Jovanović and Bamieh, 2005). An alternative, yet similar explanation is provided by Townsend (1976, chapter 7.19) in an attempt to explain the persistence of some h-scaled perturbations often seen in wind tunnels. Using suited approximations, Townsend estimated that spanwise variations of the wall-shear stress whose characteristic wavelength falls in a limited ($\leq 4h$), h-scaled range should be able to self-sustain" [MY24b] through an induced secondary motion and eventually dominate the remaining flow features. "It is then conceivable (as pointed out by Wangsawijaya et al., 2020) that a broadband perturbation could trigger a set of motions of different scales, of which some h-scaled ones would outlive the others to yield VLSMs or the h-scaled momentum pathways." [MY24b] In this sense, VLSMs could be thought of as transient secondary motions triggered by randomly-occurring large-scale patterns of the wall shear stress. In any case, empirical support for Townsend's idea is lacking; finding evidence in its favour is one of the aims of this thesis.

1.3 Research questions and approach

This dissertation explores the mutual interactions between the wall shear stress and the large-scaled vortices of wall-bounded turbulence. This interplay takes many forms. First off, the wall shear stress quantifies the force (per unit wet area) that needs to be overcome or balanced to drive a turbulent flow; it can be trivially shown that it is intimately linked to the energy expense necessary to drive a flow. As explained in §1.2.3, how much large scales contribute to the wall shear stress and how much can be saved by controlling them is the object of ongoing research. This information can help determine whether large-scale control is a viable strategy. Other than quantifying the expenses of the flow, the wall shear stress can interact with the dynamics of the large scales; for instance, the scale interaction known as amplitude modulation is typically understood to be mediated by the wall shear stress (see §1.2.5). Studying scale interactions can help improve turbulence models used in LES simulations (see §1.2.4). Finally, in light of Townsend's hypothesis (see §1.2.6), large scales could be interpreted as transient secondary motions originating from large-scaled perturbations of the wall shear stress. These aspects are investigated in terms of the following research questions:

1. **How do the costs (in terms of power input or wall shear stress) associated to small and large scales differ?**
   While identities such as the FIK one (see §1.2.3, or Fukagata et al., 2002) clearly indicate that both small and large scales have a negative impact on the skin friction, the comparison of the costs associated to each of them is not trivial. To investigate the matter, two flows are compared, of which one (plane Couette flow) is characterised by much stronger large scales with respect to the second (plane Poiseuille flow; see §1.2.2, or e.g. Lee and Moser, 2015, 2018). This strategy implicitly raises the question of how to compare flows that are different in nature, which is also addressed. A proper discussion of the matter is enabled by extending the framework introduced by Gatti et al. (2018) to describe global energy fluxes, so as to allow the discussion of the fluxes in Couette flows (the original framework was developed for Poiseuille ones) and to discriminate small- and large-scale energy fluxes. This analysis tool is then applied to a database of both new and published direct numerical simulations to investigate the costs associated to small and large scales.
2. **How much of the cost (power input or skin friction) caused by large scales can be saved by removing them?**
   Previous investigations (e.g. Fukagata et al., 2010; de Giovanetti et al., 2016) have highlighted that, by removing large scales from a flow, the costs associated to smaller ones unexpectedly increase. In other words, only a fraction of the cost associated to large scales can be saved by controlling them. However, as discussed in §1.2.3, the strategies used in these studies to suppress large scales

are quite intrusive. In this thesis, the matter is investigated numerically by using a different, less intrusive strategy: large scales are suppressed by applying a weak Coriolis force to the flow as pioneered by Komminaho et al. (1996). The validity of the approach is discussed by scrutinising the effects of the Coriolis force on the energy spectra; the intensity of the Coriolis force needed for a satisfactory suppression of large scales is discussed. Once again, the analysis of costs is performed using the framework developed by Gatti et al. (2018) and extended to address the previous scientific question.

3. **Is the wall-shear stress the mediator in the scale-interaction mechanism known as amplitude modulation?**
   Or, more precisely, is the amplitude of near-wall small scales modulated by large-scaled fluctuations of the wall shear stress, which are in turn imprinted on the wall by outer-layer large scales? This mechanism is indeed commonly understood to be responsible for the correlation between the amplitude of near-wall small scales and the outer-layer large-scale velocity signal (see §1.2.5). Causal relationships in this mechanism are investigated by performing numerical experiments in a channel flow at a moderately high Reynolds number. First, the near-wall imprint of the large scales (including their imprint on the wall shear stress) is removed. If the mechanism described above is correct, meaning that the presence of large scales at the wall causes the modulation of small ones, this should prevent small scales from being modulated. The dual numerical experiment is also performed: to verify whether possibly the causal relation is inverse, meaning that modulated small scales trigger the formation of a large-scaled wall shear stress pattern, small scales are artifically prevented from having a large-scaled envelope; the effects on the near-wall large scales are then investigated.
4. **Is Townsend's hypothesis (as formulated in §1.2.6) plausible? Or, in other words: can secondary motions induced by a lateral wall shear stress pattern of a specific, large size self-sustain, so as to outlive motions of any other size?**
   If the hypothesis is proven correct, naturally occurring large scales could be interpreted as transient secondary motions originating from perturbances of the wall shear stress; the fact that only motions of a specific, large-scale size are able to self-sustain would also explain the recurrence of h-scaled features in turbulent flows. The plausibility of the hypothesis is verified through the following numerical setup. Turbulent channel flows are simulated, in which the walls are covered by spanwise-alternating streamwise-elongated strips of rough and smooth wall (strip-type roughness). This spanwise roughness pattern produces both a spanwise variation of the wall shear stress and secondary motions; the size of the motions is governed by the width of the roughness strips. By suddenly replacing the roughness pattern with a homogeneous, smooth wall, the secondary motions decay towards a spanwise-homogeneous configuration. The time needed by secondary motions of different sizes to decay is then measured; it is expected that motions of a specific, h-scaled size would persist longer than any other motion.

This dissertation is based on the research documented in several articles published by the present author and is structured as follows. Fundamental results on wall-bounded flows as well as the numerical algorithms used for their simulation are presented in chapter 2. Results addressing each of the above research questions are presented in chapters 3, 4, 5 and 6 respectively. A concluding remark is provided in chapter 7; additionally, the results of individual chapters are combined in this chapter to provide useful insights on flow control and on the dynamics of large scales.

Chapters 3, 4, 5 and 6 contain direct quotations from the author's own work (see [MY21], [MY24a], [MY23] and [MY24b] respectively). Sections 1.2.6 and 2.2.1 also contain direct quotations. Notice that the author's own publications are cited with a different style, so as to better distinguish them from other publications. Quotations of the author's own work are highlighted by quotation marks, e.g.:

> "This is a fictitious direct quotation." [MY21]

Major changes to the original version are clearly marked, whereas the nomenclature is adjusted without further comments. Parts of an article (see [MY21], or chapter 3) were adapted from the author's own Master's thesis; these parts are included in the present thesis for the sake of clarity.

2 Fundamentals

2.1 The incompressible Navier-Stokes equations

The aim of this manuscript is to investigate turbulent flows. Several physical phenomena can be taken into account when modelling fluid flow; for instance, one could model heat exchange, buoyancy effects, and the compressibility of the flow. However, none of these effects are necessary to observe turbulence; turbulence, indeed, is mainly an inertial phenomenon (Davidson, 2015, e.g. ch. 3.1.3) which requires very few assumptions to be captured. Most importantly, viscosity plays a crucial role in the generation and destruction of turbulence. As explained by Sherman (1990), and quoted by Davidson (2015, ch. 7.1.2),

> *viscosity is both the midwife and executioner in the life story of turbulence. As a midwife, it delivers the vorticity from its birthplace at the wall. Thus, the flow receives something without which it cannot be unstable, and hence possibly turbulent. As executioner, it applies torques that rub out the local concentrations of vorticity.*

Hence, both inertial advection and viscosity need to be captured to satisfactorily describe turbulence. This requirement is satisfied by the incompressible Navier-Stokes equations, which describe the evolution in time (t) of a velocity field $\vec{u}$ with cartesian components u, v, w defined at a continuous set of points in space (x, y, z). Each point in space is also associated to a continuous distribution of mass per unit volume – that is, the density ρ. Although a fluid is effectively made of separate molecules, fluid motion is well described by such continuous fields if the mean free path (γ) between molecules is much smaller than some typical length scale (L) of the flow; this takes the name of *continuum hypothesis*. For instance, such a typical length scale could be the streamwise extent of some object the fluid molecules move around. Formally, the continuum hypothesis it is only valid if the Knudsen number Kn is sufficiently large,

$$Kn = \frac{\gamma}{L}. \tag{2.1}$$

Other than the continuum hypothesis, few other ones are needed to exactly derive the Navier-Stokes equations. These simply follow from Newtonian mechanics by assuming that each portion of the fluid is subject to a normal stress (the pressure P) and a viscous one. Viscous stresses are further assumed to be Newtonian, meaning that the stress tensor is directly proportional to the strain rate tensor through a proportionality constant (the dynamic viscosity μ). In writing the Navier-Stokes equations, the kinematic viscosity $\nu = \mu/\rho$ is typically used.

One final hypothesis is given by the incompressibility constraint: it is assumed that the volume of a given portion of fluid remains constant in time, for each portion of fluid that can possibly be considered. To satisfy this condition, it is sufficient (and necessary) that the velocity field be solenoidal (see equation 2.3 below). As a consequence of this hypothesis, the density ρ is a passive scalar that gets transported by the velocity field; as a further simplification, the density is assumed to be constant. Finally, the Navier-Stokes equations read:

$$\frac{\partial \vec{u}}{\partial t} + (\vec{u} \cdot \nabla)\,\vec{u} + \frac{1}{\rho}\nabla P = \nu\,\nabla^2 \vec{u} \tag{2.2}$$

$$\nabla \cdot \vec{u} = 0 \tag{2.3}$$

where the first row expresses the conservation of momentum, the second the incompressibility constraint. These satisfactorily capture turbulent phenomena and will be used throughout the manuscript.

2.2 Wall-bounded turbulence

This section deals with the fundamental theoretical results concerning wall-bounded turbulence. These will be discussed in the context of a plane channel flow (described in §2.2.1) for two reasons. First, the investigations presented in this manuscript (§3 to §6) are based on data extracted from such channel flows; moreover, the simple geometry makes the discussion straightforward. Notice that results and theories such as the Reynolds-averaged Navier-Stokes equations presented in equation 2.6, the law of the wall (§2.2.3), the attached-eddy theory (§2.2.4) and the physical mechanism underlying turbulent production (§2.2.6) are of general validity.

2.2.1 Geometry and definitions: Couette-Poiseuille flows

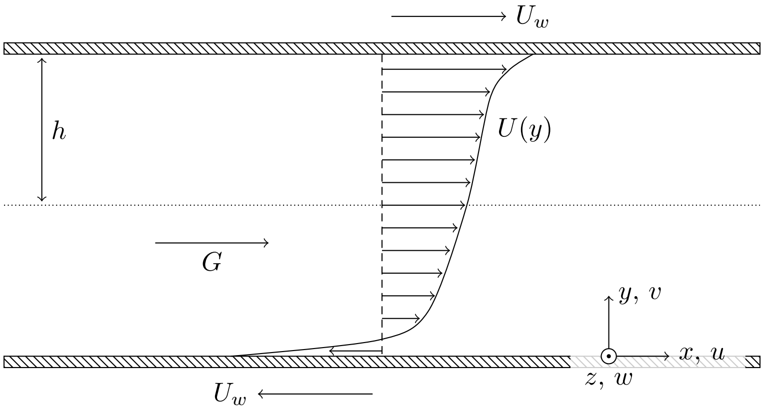

Figure 2.1: Sketch of the flow and reference system. Adapted from [MY21].

Throughout this manuscript, either plane Couette or Poiseuille flows will be considered as examples of wall-bounded flows. Their geometry will be discussed in this section by considering the combined Couette-Poiseuille flow family.

Consider the flow between two indefinite, parallel plates (walls); h indicates the half-distance between them. The space between the two walls is referred to as the *channel*. Let x, y and z be the cartesian streamwise, wall-normal and spanwise axes; u, v and w are the associated velocity components. Axes are centered at the bottom wall, and the wall-normal one points upwards towards the fluid. Two external agents drive the flow. The first is a constant, streamwise pressure gradient $\partial \langle P \rangle / \partial x = -G$. The second is given by the motion of the two walls in the streamwise direction with the same speed U_w, but in opposite directions. In case of a null pressure gradient, the flow is referred to as a Couette one; if the velocity U_w of the walls is zero instead, the flow is a Poiseuille one.

We only consider cases in which the flow inside the channel is turbulent. Under these circumstances, an average flow can be defined by leveraging the expected value operator, indicated by $\langle ... \rangle$. The expected value is typically computed as an average over statistically homogeneous spatial directions, and possibly as a time average if the flow is at a statistically steady state. If both the streamwise and spanwise directions are statistically homogeneous (notice that this will not be the case in §6), the usual Reynolds decomposition can be used to separate a mean field $U(y)$ from the fluctuation field $\vec{u}'$:

$$\vec{u} = U\underline{x} + \vec{u}' \tag{2.4}$$

where $U\underline{x} = \langle \vec{u} \rangle$ is the mean field and $\underline{x}$ the unit vector in the x direction. The fluctuation field is consequently defined.

The volume flow rate is measured by the bulk velocity U_b, that is – the volume-average of the mean field U:

$$U_b = \frac{1}{2h} \int_0^{2h} U \, \mathrm{d}y \tag{2.5}$$

The flow rate per unit span is then trivially $2h\,U_b$. Notice that the bulk velocity is only non-zero when a pressure gradient is present ($G \neq 0$). In a pure Couette flow, the bulk velocity is necessarily zero owing to the definition above (as the velocity profile is antisymmetric with respect to the channel mid-plane). However, "the wall velocity U_w can be regarded as the bulk velocity once the flow is observed in a reference frame where one of the two walls is at rest[1]. Hence, the flow rates realized by simple Poiseuille and Couette flows are U_b and U_w respectively" [MY21]; the symbol U_q will be generally used to indicate either of the two.

2.2.2 Reynolds-averaged Navier-Stokes equations; Reynolds stresses

As explained in the previous section, the velocity field of a turbulent flow can be decomposed in its average $\langle \vec{u} \rangle$ and fluctuation $\vec{u}'$ parts; this process takes the name of Reynolds decomposition. An evolution equation for the average velocity is trivially found from the Navier-Stokes equation (2.2) by applying the Reynolds decomposition and taking the expected value of the left- and right-hand sides:

$$\frac{\partial \langle \vec{u} \rangle}{\partial t} + \left(\langle \vec{u} \rangle \cdot \nabla \right) \langle \vec{u} \rangle + \frac{1}{\rho} \nabla \langle P \rangle = \nu \nabla^2 \langle \vec{u} \rangle + \frac{1}{\rho} \nabla \cdot \underline{\underline{R}} \tag{2.6}$$

$$\nabla \cdot \langle \vec{u} \rangle = 0 \tag{2.7}$$

These are the Reynolds-averaged Navier-Stokes (RANS) equations; as compared to the regular ones, an additional forcing term appears to the right-hand side of equation 2.6 – the divergence of the Reynolds stress tensor $\underline{\underline{R}}$. The Reynolds stress tensor is defined as follows:

$$\underline{\underline{R}} = -\rho \begin{pmatrix} \langle u'u' \rangle & \langle u'v' \rangle & \langle u'w' \rangle \\ \langle u'v' \rangle & \langle v'v' \rangle & \langle v'w' \rangle \\ \langle u'w' \rangle & \langle v'w' \rangle & \langle w'w' \rangle \end{pmatrix} \tag{2.8}$$

---

[1] the change of reference system implies an uniform additive shift $+U_w$ of the mean velocity U. Hence, the flow rate is increased by $2hU_w$ with respect to its original zero value.

Notice that the tensor is symmetric. Mathematically, it contains the second-order central velocity moments (variances); physically, it represents the stress perceived by the average field arising from the self-advection of turbulent fluctuations. The value of $\underline{\underline{R}}$ is generally not known a priori, and cannot be explicitly cast as a function of the unknown $\langle \vec{u} \rangle$ of the considered equations. Hence, equation 2.6 cannot be solved as it is; an additional equation for each component of $\underline{\underline{R}}$ is needed. As will be shown in §2.2.5, such an equation is readily available, but it contains the third-order velocity moments among its terms. Hence an equation for the third-order moments would be needed, which in turn would require an equation for the fourth-order moments, and so on. Practically, one cannot obtain a closed set of equations; this is the well-known closure problem of turbulence.

In light of the above, if one wants to directly solve the RANS equations to find the mean velocity field (as is typical in industrial applications), a model is needed to express $\underline{\underline{R}}$ in terms of the unknowns of the problem. Several models are available, none of which is exact. Some of them assume the Reynolds stress tensor to be proportional to the rate-of-strain tensor in analogy to the viscous stress tensor. Some others, instead, define additional quantities (such as an isotropic turbulent kinetic energy or vorticity) which evolve according to their own separate equation; the tensor $\underline{\underline{R}}$ is then expressed in terms of these quantities. Finally, some models directly approximate the evolution equation for each term in the Reynolds stress tensor.

For the present manuscript, no turbulence model will be needed. Indeed, the RANS equations will never be solved to calculate the velocity field; instead, direct numerical simulations (DNS) will be performed to calculate the fully-resolved, time-evolving turbulent field. The Reynolds stress tensor can be then exactly calculated by averaging the DNS data; this can be done, for instance, to shed light on some turbulent phenomena. That is, the Reynolds stress tensor can also be used as an analysis tool.

As for the channel flow described in §2.2.1, its symmetries can be used to much simplify the RANS equations. After suited approximations and assuming that the flow is at a statistically steady state, these read (Davidson, 2015, ch. 4.2):

$$\nu \frac{\mathrm{d}^2 U}{\mathrm{d}y^2} - \frac{\mathrm{d}\langle u'v' \rangle}{\mathrm{d}y} = -\frac{G}{\rho} \tag{2.9}$$

The interpretation of the above equation is straightforward. In a channel flow, the mean velocity U results from the equilibrium between the viscous stress (first term on the left-hand side), the Reynolds shear stress $\langle u'v' \rangle$ and the pressure gradient (right-hand side). Typically, a total shear stress function $\tau(y)$ is defined as the sum of the viscous and Reynolds shear stress:

$$\tau = \mu \frac{\mathrm{d}U}{\mathrm{d}y} - \rho \langle u'v' \rangle \tag{2.10}$$

By plugging this definition into equation 2.9, one finds that the total shear balances the pressure gradient. By letting τ_B and τ_T indicate the value of τ at the top and bottom walls respectively, one finds, upon integration:

$$\tau_T - \tau_B = -2Gh \tag{2.11}$$

so that in a pure Poiseuille flow ($\tau_T = -\tau_B = -\tau_w$ owing to symmetries):

$$\tau_w = Gh \qquad \text{(pure Poiseuille)} \tag{2.12}$$

The total shear stress is a linear function of the wall-normal coordinate in pure Poiseuille flows and a constant function in pure Couette flows:

$$\tau(y) = \left(1 - \frac{y}{h}\right)\tau_w \qquad \text{(pure Poiseuille)} \tag{2.13}$$

$$\tau(y) = \tau_w \qquad \text{(pure Couette)} \tag{2.14}$$

In a combined Couette-Poiseuile problem, the distribution of the total stress is given by the linear superposition of the two elementary solutions shown in equations 2.13 and 2.14.

2.2.3 The law of the wall

Similarly to the discussion of §1.2.1, a turbulent wall-bounded flow can be split into two wall-normal regions: the inner and the outer layer. These are typically defined in terms of the inner- and of the outer-scaled wall-normal coordinate, namely y^+ and y/h.

In the inner, near-wall region ($y/h \ll 1$) the flow is not significantly influenced by the outer geometry, but rather from the presence of the wall itself. In particular, the flow is governed by the distance y from the wall and by the so-called inner (or, viscous) units u_τ, δ_v defined by the wall shear stress and the kinematic viscosity (see §1.2.1). Here, the inner-scaled mean velocity U^+ is assumed to be a function (generically indicated by f_w) of the inner-scaled distance from the wall y^+ in the near-wall region (Pope, 2000; Davidson, 2015):

$$U^+ = f_w(y^+) \qquad \text{for } y/h \ll 1 \tag{2.15}$$

Notice that the dependence on the inner units is manifested through the non-dimensional quantitities $U^+ = U/u_\tau$ and $y^+ = y/\delta_v$. The function f_w is supposed to be universal across different flows and Reynolds numbers; this conjecture is robustly backed by empirical data (e.g. Pope, 2000, ch. 7.3, fig. 7.27). Typically, the near-wall region is considered to extend up to $y/h = 0.1$ (as indicatively suggested by Pope, 2000); it is further split into a viscous sublayer, a buffer layer and an overlap region. In the viscous sublayer (indicatively, $y^+ \leq 5$), viscous stresses dominate the contributions to the total shear stress τ, whereas Reynolds stresses are negligible. In other words, the flow is substantially laminar there. The velocity profile is well approximated by a linear function:

$$U^+ = y^+ \qquad \text{for } y^+ \leq 5 \tag{2.16}$$

The buffer layer ($y^+ \approx 10$) is instead the region where turbulence is the most intense; moreover, most of the turbulent kinetic energy is produced in this region through the mechanism described in §2.2.6. Finally, the overlap region will be discussed in a couple of paragraphs.

The viscous phenomena that dominate the flow dynamics in proximity of the wall become less intense further away from it. In the outer layer ($y^+ \gg 1$), the dependence on viscous units is thus partially lost: it is assumed that the velocity profile does not depend on the viscous length scale δ_v, but rather on the outer length scale h. Dependency on the friction velocity u_τ is instead retained: indeed, u_τ quantifies the wall shear stress by definition (see equation 1.2), and thus the total shear stress in light of equations 2.13 and 2.14. The total shear stress, in turn, has an influence on the dynamics of the whole channel.

Typically (Davidson, 2015; Luchini, 2018), the velocity distribution in the outer-layer is written in terms of the velocity defect law:

$$U_c^+ - U^+ = g_d\left(\frac{y}{h}\right) \qquad \text{for } y^+ \gg 1 \tag{2.17}$$

where g_d is a function that depends on the considered flow (so that, for instance, the velocity defect of a channel flow is different from the one of a boundary layer) and U_c is the centerline velocity (or, e.g. in a boundary layer flow, the velocity at the edge of the boundary layer itself).

Under appropriate circumstances ($Re_\tau \gg 1$), there exists an overlap region where both $y/h \ll 1$ and $y^+ \gg 1$ are verified. The friction Reynolds number Re_τ needs to be particularly high to verify both these two conditions at the same physical point in space; the former can be indeed rewritten (following equation 1.5) as:

$$Re_\tau = \frac{y^+}{y/h} \qquad \forall\, y \tag{2.18}$$

so that large values of the numerator and small values of the denominator at the same physical y imply that Re_τ must have a large value. In the overlap region, both 2.15 and 2.17 are valid. Both can be used to find an expression for $y\frac{\mathrm{d}U}{\mathrm{d}y}$:

$$y\frac{\mathrm{d}U}{\mathrm{d}y} = \underbrace{u_\tau\, y^+ f_w'\left(y^+\right)}_{\text{(A)}} = \underbrace{-\, u_\tau \frac{y}{h}\, g_d'\left(\frac{y}{h}\right)}_{\text{(B)}} \qquad \text{in the overlap region} \tag{2.19}$$

Notice that term (A) is only a function of y^+, and term (B) is only a function of y/h. It follows:

$$y^+ f_w'\left(y^+\right) = \text{const.} = \frac{1}{k} \qquad \text{in the overlap region} \tag{2.20}$$

$$\frac{y}{h}\, g_d'\left(\frac{y}{h}\right) = \text{const.} = -\frac{1}{k} \qquad \text{in the overlap region} \tag{2.21}$$

where k is the von Kármán constant; different sources report different values for it[2], typically in the range $0.38 - 0.43$. The log-law is found upon integration:

$$U^+ = \frac{1}{k}\ln\left(y^+\right) + C_1 \qquad \text{in the overlap region} \tag{2.22}$$

$$U_c^+ - U^+ = -\frac{1}{k}\ln\left(y/h\right) + C_2 \qquad \text{in the overlap region} \tag{2.23}$$

where C_1 and C_2 are constants. As a rule of thumb, the overlap region is said to be found for $y^+ > 50$ and $y/h < 0.1$ (Pope, 2000). Its existence is also well backed by empirical data (Luchini, 2018) – although the log-law, unlike the law of the wall, is somewhat controversial.

Indeed, the above derivation of the log-law (which follows Davidson, 2015) has no mathematical validity whatsoever. Finding an expression for $y\frac{\mathrm{d}U}{\mathrm{d}y}$ as done in equation 2.19 is a mere trick that yields a logarithmic functional form. By finding an expression for some other quantity (for instance, the velocity gradient $\frac{\mathrm{d}U}{\mathrm{d}y}$ alone), one obtains different expressions. Other ways of deriving a log-law (e.g. Pope, 2000; Luchini, 2018) may appear more rigourous, but require similarly arbitrary assumptions. It is no surprise, then, that power laws have been proposed as an alternative for the overlap layer (Buschmann

---

[2] widespread rumors suggest that a group of famed (and not so) turbulence researchers gathered and celebrated in front of a large, white screen reporting $k = 0.384$ on July 25th, 2023 in occasion of the 10th iTi Conference on Turbulence. It is left to the reader to decide whether such anedoctical evidence should be treated as scientifically relevant.

and Gad-El-Hak, 2003, for instance). Nevertheless, the log-law formulation is more frequently used and will be preferred in the present manuscript.

2.2.4 The attached-eddy hypothesis

In the previous paragraph, a functional form for the velocity in the overlap layer was provided. It will be now shown that, under appropriate assumptions, a similar logarithmic functional form can be found for the normal Reynolds stresses. This result is achieved through the attached eddy hypothesis of Townsend (1976).

Townsend's fundamental assumption is that the *main eddies* of a turbulent flow extend to the wall – hence the name *attached eddy*, as in attached to the wall. The *main eddies* mentioned in Townsend's original wording can be regarded as the eddies that dominate the overlap region when Re_τ is sufficiently high; indeed, his theory only considers inertial motions that are not affected by viscosity, hence it cannot model small-scale energy-dissipating eddies (Marusic and Monty, 2019). Assuming that eddies are attached to the wall has an important implication: at a given wall-normal distance y, one can only observe eddies whose height H_{ae} is larger than y. Similarly, the Reynolds stresses only receive contributions from eddies that are taller than y. Notice that an upper bound for the height H_{ae} of a generic eddy is given by the outer length scale h (typically the boundary layer thickness; here, the channel half-height).

In addition to the hypothesis of eddies being attached, two more are required by Townsend's theory:

- Attached eddies are geometrically self-similar: their aspect ratio (that is, their width and length relative to their height H_{ae}) is constant for changing values of H_{ae}.
- Attached eddies have a constant characteristic velocity scale. Without loss of generality, this length scale will be here directly assumed to be u_τ; notice that this assumption is usually performed at a later point in the discussion (Marusic and Monty, 2019).

In light of the above assumptions, the i-th velocity component $u_{ae,i}$ induced by a generic attached eddy of height H_{ae} can be written as:

$$u_{ae,i}(x, y, z; H_{ae}) = u_\tau \, f_{ae,i}\left(\frac{x}{H_{ae}}, \frac{y}{H_{ae}}, \frac{z}{H_{ae}}\right) \tag{2.24}$$

where $f_{ae,i}$ is some non-dimensional function. Here, the self-similarity hypothesis is encoded in the fact that the velocity induced by each attached eddy depends on the self-similar variables x/H_{ae}, y/H_{ae}, z/H_{ae}.

The fluctuation field is assumed to results from the linear superposition of eddies of height H_{ae}; the probability of observing an eddy of height H_{ae} is then indicated as $P(H_{ae})$. Notice that, to the author's understanding, $P(H_{ae})$ is not a probability density function – so that effectively the model can account for the possibility that multiple attached eddies overlap[3]. A value for the Reynolds stresses can be found using the following expression (Marusic and Monty, 2019):

$$\left\langle u_i' u_j' \right\rangle (y) = u_\tau^2 \int_{H_0}^{h} P(H_{ae}) \, I_{ij}\left(\frac{y}{H_{ae}}\right) \mathrm{d}H_{ae} \tag{2.25}$$

---

[3] Still to the author's understanding, it is also necessary to assume that non-linear interactions between overlapping eddies are negligible: indeed, no cross contribution between eddies of different heights appears in the term I_{ij}.

Notice that, as previously explained, the only permissible values of the height H_{ae} at a given wall-normal distance y fall in the range $[H_0, h]$, with $H_0 \geq y$; hence the extremes of the integral. The term I_{ij} represents the contribution to the Reynolds stresses by each individual eddy:

$$I_{ij}\left(\frac{y}{H_{ae}}\right) = \frac{1}{c_a H_{ae}^2} \int_{-\infty}^{\infty} \int_{-\infty}^{\infty} f_{ae,i}\, f_{ae,j}\, \mathrm{d}x\, \mathrm{d}y \tag{2.26}$$

where the dimensionless constant c_a is used to normalise the integral, so that the integral recovers a meaningful average value in case, for instance, the integrand has a compact support[4] (bear in mind that the aspect ratio of each attached eddy is fixed).

By assuming suited functional forms for the integrands of equation 2.25, Townsend (1976) found that, in the log-layer:

$$\langle u'u' \rangle^+ = B_1 - A_1 \ln\left(\frac{y}{h}\right) \tag{2.27}$$

$$\langle v'v' \rangle^+ = B_2 \tag{2.28}$$

$$\langle w'w' \rangle^+ = B_3 - A_3 \ln\left(\frac{y}{h}\right) \tag{2.29}$$

The above expressions are well supported by empirical data, as reported in the review by Marusic and Monty (2019). Nevertheless, the logarithmic functional form stems from the plausible, and yet arbitrary, hypotheses made by Townsend on the functional form of $P(H_{ae})$ and I_{ij}; there likely exists another set of assumptions that yields a different, equally valid result. That is, the above expressions are only one of the many possible ways of approximating the Reynolds stresses in the log-layer.

Perhaps, though, the importance of the attached eddy hypothesis lies in the fact that its assumptions are well descriptive of turbulent phenomena at a qualitative level. For instance, as will be seen in §6, most of the energy of a turbulent wall-bounded flow is found on Fourier modes of constant x-z-aspect ratio, consistently with the self-similarity hypothesis. Moreover, it has been found that only turbulent motions whose size is larger than a given threshold are coherent with the near-wall region (Baars et al., 2017b); the threshold gets larger as one moves away from the wall, in agreement with the idea that eddies are wall-attached, so that only progressively taller (hence, larger) eddies can be seen as one moves away from the wall.

2.2.5 Budget equations: Reynolds stress tensor, mean and turbulent kinetic energy

In this section, the budget equations for the Reynolds stress tensor and for the kinetic energy of the flow (decomposed in its mean and fluctuating parts) will be discussed. It will be shown how these equations simplify when the channel geometry described in §2.2.1 is considered. The integral energy budgets will also be presented, as they will later be needed for the discussion of §3. Finally, the equations shown in this section will help explain how turbulent energy is produced and redistributed across velocity components in wall-bounded flows (see §2.2.6). Notice that turbulent kinetic energy can also be redistributed across different scales of motion (see §2.3.4).

---

[4] Notice that different definitions of I_{ij} are available (Townsend, 1976; Marusic and Perry, 1995; Marusic and Monty, 2019).

Most of the equations shown in this section can be trivially derived from the budget equation for the Reynolds shear stress tensor, which is provided by Pope (2000). Using Einstein's notation for vectors and tensors:

$$\begin{aligned}\frac{\partial \langle u_i' u_j' \rangle}{\partial t} + \langle u_k \rangle \frac{\partial \langle u_i' u_j' \rangle}{\partial x_k} = & \underbrace{-\frac{\partial}{\partial x_k} \langle u_i' u_j' u_k' \rangle}_{\text{turb. transport}} + \underbrace{\nu \nabla^2 \langle u_i' u_j' \rangle}_{\text{visc. diffusion}} \\ & \underbrace{- \langle u_i' u_k' \rangle \frac{\partial \langle u_j \rangle}{\partial x_k} - \langle u_j' u_k' \rangle \frac{\partial \langle u_i \rangle}{\partial x_k}}_{\text{production}} \\ & \underbrace{-\frac{1}{\rho} \left(\frac{\partial}{\partial x_j} \langle u_i' P' \rangle + \frac{\partial}{\partial x_i} \langle u_j' P' \rangle \right)}_{\text{pressure transport}} \\ & \underbrace{+\frac{1}{\rho} \left\langle P' \left(\frac{\partial u_i'}{\partial x_j} + \frac{\partial u_j'}{\partial x_i} \right) \right\rangle}_{\text{pressure-strain correlation}} \\ & \underbrace{-2\nu \left\langle \frac{\partial u_i'}{\partial x_k} \frac{\partial u_j'}{\partial x_k} \right\rangle}_{\text{viscous dissipation}}\end{aligned} \tag{2.30}$$

Notice that this equation is of general validity, i.e. it applies to flows of any geometry. The sum of the terms on the left-hand side represents how the Reynolds stress perceived by a fluid particle that moves with the mean flow changes in time. Viscosity yields the usual diffusion term as well as the dissipation one. The latter is non-positive for $i = j$ (that is, for normal Reynolds stresses, which can be seen as contributions to the turbulent kinetic as will be explained in the next paragraph), so that it is interpreted to dissipate turbulent kinetic energy. As for the remaining terms, two transport ones appear on the right-hand side of equation 2.30. The turbulent transport accounts for the fluctuating field advecting each component of the Reynolds stress tensor; this term is a key player in non-linear scale interactions, as will be discussed in §2.3.4. The pressure transport term, instead, only truly represent a transport term if the trace of the Reynolds stress tensor is considered. Finally, the production and pressure-strain correlation terms respectively produce turbulent kinetic energy and redistribute it between velocity components. This will be better discussed in §2.2.6.

The Reynolds decomposition introduced in §2.2.1 also decomposes the expected value of the kinetic energy (per unit volume) of the flow in two separate contributions:

$$\left\langle \frac{1}{2} \rho \vec{u} \cdot \vec{u} \right\rangle = \underbrace{\frac{1}{2} \rho U^2}_{\text{MKE}} + \underbrace{\frac{1}{2} \rho \langle u_i' u_i' \rangle}_{\text{TKE}} \tag{2.31}$$

Here, MKE stands for *mean kinetic energy*; the wording might be misleading, as the expected (mean) kinetic energy of the flow would be the term on the left-hand side of equation 2.31, whereas the MKE indicates the energy held by the mean flow. Such a wording will nevertheless be adopted for consistency with the literature. The turbulent kinetic energy (TKE) represents the energy of the fluctuations; it is exactly identical to half the trace of the Reynolds stress tensor. The mean and fluctuation components of the velocity field are orthogonal through the expected value operator, so that no cross terms arise.

The budget equation of the TKE for the geometry described in §2.2.1 can be readily obtained from equation 2.30 by applying suited simplifications due to symmetries and homogeneity:

$$\begin{aligned}\left(\frac{\partial}{\partial t}+U\frac{\partial}{\partial x}\right)\frac{1}{2}\rho\left\langle u_i'u_i'\right\rangle \; &= \underbrace{-\frac{1}{2}\rho\frac{d}{dy}\left\langle v'u_i'u_i'\right\rangle}_{\text{turb. transport}} + \underbrace{\nu\frac{d^2}{dy^2}\frac{\rho\left\langle u_i'u_i'\right\rangle}{2}}_{\text{viscous diffusion}} + \underbrace{-\rho\left\langle u'v'\right\rangle\frac{dU}{dy}}_{\text{production}} \\ &\quad + \underbrace{-\frac{d}{dy}\left\langle P'v'\right\rangle}_{\text{pressure transport}} - \underbrace{\mu\left\langle\frac{\partial u_i'}{\partial x_k}\frac{\partial u_i'}{\partial x_k}\right\rangle}_{\text{viscous dissipation}}\end{aligned} \tag{2.32}$$

Again, the term to the left represents the rate of change of the kinetic energy of a fluid particle that moves with the mean flow U. As for the terms to the right, the viscous diffusion, the turbulent and the pressure transport only redistribute energy across the channel, so that globally they do not produce or waste any kinetic energy (their volume-average is indeed zero[5]). The only two terms that effectively act as a source and as a sink of kinetic energy are the turbulent production and dissipation respectively. Notice that the latter is written in its pseudo-dissipation formulation (as is common practice) rather than in its thermodynamically correct version (Bradshaw and Perot, 1993). The effective rate of energy (per unit volume) lost to viscous dissipation would indeed be given by the work done by the viscous stress tensor against the rate of strain (Davidson, 2015, ch. 2.1.4):

$$\frac{\mu}{2}\left(\frac{\partial u_i'}{\partial x_j}+\frac{\partial u_j'}{\partial x_i}\right)^2$$

The quantitative differences between this formulation and the one of equation 2.32 are however negligible; notice moreover that equation 2.32 remains exact (simply, its formulation does not highlight the thermodynamically exact dissipation rate).

A budget equation for the MKE in the channel flow described in §2.2.1 can also be found by multiplying the mean momentum equation (whose expression for a statistically steady flow is given in equation 2.9) times the mean velocity U:

$$\left(\frac{\partial}{\partial t}+U\frac{\partial}{\partial x}\right)\rho\frac{U^2}{2} \; = \underbrace{GU}_{\text{pumping power}} + \underbrace{-\rho U\frac{d\left\langle u'v'\right\rangle}{dy}}_{\text{pow. of Re. stresses}} + \underbrace{\nu\frac{d^2}{dy^2}\left(\frac{1}{2}\rho U^2\right)}_{\text{viscous diffusion}} - \underbrace{\mu\left(\frac{dU}{dy}\right)^2}_{\text{dissipation}} \tag{2.33}$$

Here, the pumping power is generally a source term; viscosity yields – again – the typical diffusion and dissipation terms. An additional term indicates the power provided to a fluid element by the resultant of the Reynolds stresses, which is closely related to the production of TKE (see eq. 2.32). Although the two terms do not balance locally, they do so in an integral sense. By integrating across the channel height:

$$\int_0^{2h}\underbrace{-\rho U\frac{d\left\langle u'v'\right\rangle}{dy}}_{\text{MKE power of R.S.}}\,\mathrm{d}y+\int_0^{2h}\underbrace{-\rho\left\langle u'v'\right\rangle\frac{dU}{dy}}_{\text{TKE prod.}}\,\mathrm{d}y \;=\; -\rho\left[U\left\langle u'v'\right\rangle\right]_0^{2h} \;=\; 0 \tag{2.34}$$

---

[5] proof is trivial. All of these terms can be written in the form dF/dy, so that their integral across the channel is equal to $F_{top}-F_{bot}$, where F_{top} and F_{bot} are the values of F at the top and bottom walls. These two values are generally zero; hence the integral is zero. This is true also for the viscous diffusion as dk/dy is zero at the wall. Hint for the proof: consider $0.5d\left\langle u'u'\right\rangle/dy$. This is exactly equal to $\left\langle u'\,du'/dy\right\rangle$. Since u' is exactly zero at the wall, the whole term is also null.

The TKE term is typically positive, so that it is interpreted to provide energy to turbulent fluctuations. Half its integral in the wall-normal direction – that is, the total turbulent production per unit wetted area – will be indicated as $\mathcal{P}$:

$$\mathcal{P} = \frac{1}{2}\int_0^{2h} -\rho \left\langle u'v' \right\rangle \frac{dU}{dy}\,\mathrm{d}y \qquad > 0 \quad \text{(typically)} \tag{2.35}$$

In light of equation 2.34, the energy provided to the TKE is subtracted from the MKE by the Reynolds stresses. This process is not local, in the sense that the energy that is subtracted from the MKE at a given point in space could be received by the TKE at some other spatial position (Davidson, 2015, ch. 4.1.3): once again, the balance only holds in an integral sense.

A better understanding of the global energy balance in a channel flow can be achieved by integrating equations 2.32 and 2.33 across the channel height and by halving the result so as to obtain the integral power balance per unit wetted area:

$$\text{MKE:} \qquad \Pi_p + \Pi_w - \Xi - \mathcal{P} = 0 \tag{2.36}$$

$$\text{TKE:} \qquad \mathcal{P} - \epsilon = 0 \tag{2.37}$$

Equation 2.36 describes the integral energy balance of the mean flow. The mean flow receives energy from two external agents: the pressure gradient and the external force that keeps the walls of the channel in (relative) motion. The former yields the pumping power Π_p (the integral of the pumping power term in equation 2.33, indeed). The latter provides momentum (and, consequently, energy) to the flow with a non-zero flux at the walls; this is represented by the power Π_w in equation 2.36, which arises from the integration of the viscous diffusion term in equation 2.33. A relation between Π_p, Π_w and the total shear stress τ at the top and bottom walls (τ_T and τ_B respectively) is recovered by integration:

$$\Pi_p = \frac{1}{2}\left(\tau_B - \tau_T\right) U_b \tag{2.38}$$

$$\Pi_w = \frac{1}{2}\left(\tau_T + \tau_B\right) U_w \tag{2.39}$$

Both the expressions above simplify to the product between the wall shear stress τ_w and a characteristic velocity in case of a pure Couette or Poiseuille flow (owing to their respective symmetries). The sum of Π_p and Π_w is the total power input Π_t provided to the flow by the external agents:

$$\Pi_t = \Pi_p + \Pi_w \tag{2.40}$$

As highlighted by equation 2.36, part of the total power input is directly dissipated by the mean dissipation Ξ,

$$\Xi = \frac{1}{2}\int_0^{2h} \mu \left(\frac{dU}{dy}\right)^2 \mathrm{d}y \tag{2.41}$$

whereas the remaining part is fed to the TKE through the production term $\mathcal{P}$ as previously explained. Finally, as highlighted by equation 2.37, all of the energy supplied by $\mathcal{P}$ to the turbulence is dissipated as turbulent dissipation ϵ:

$$\epsilon = \frac{1}{2}\int_0^{2h} \mu \left\langle \frac{\partial u_i'}{\partial x_k}\frac{\partial u_i'}{\partial x_k} \right\rangle \mathrm{d}y \tag{2.42}$$

To sum up, energy is fed from some external agent to the mean flow; the mean flow directly dissipates it as mean dissipation or passes it to turbulence through the turbulent production. All of the energy passed to the turbulence is finally wasted as turbulent dissipation.

2.2.6 The production and redistribution of turbulent kinetic energy

In the previous section (2.2.5), it was shown that the kinetic energy held by a turbulent flow can be decomposed into the mean (MKE) and turbulent (TKE) kinetic energy. Local and integral budgets for these two quantities have been provided; it was finally shown that the only source of energy for the fluctuation field is the turbulence production term, which passes energy from the MKE to the TKE. In this section, the production of turbulent kinetic energy in a wall-bounded flow will be further discussed; its redistribution between velocity components will also be explored.

As explained in §2.2.5, the TKE is equivalent to half the trace of the Reynolds stress tensor. The normal Reynolds stresses $\langle u'u' \rangle$, $\langle v'v' \rangle$, $\langle w'w' \rangle$ can be thus be interpreted to be contributions to the turbulent kinetic energy. To better highlight how the TKE is produced and redistributed across velocity components in the channel flow described in §2.2.1, the budget equation for each of these normal Reynolds stresses is shown here:

$$\begin{aligned}
\left(\frac{\partial}{\partial t} + U\frac{\partial}{\partial x}\right)\frac{1}{2}\rho\left\langle u'u'\right\rangle &= \underbrace{-\rho\left\langle u'v'\right\rangle\frac{dU}{dy}}_{\text{production}} + \underbrace{\left\langle P'\frac{\partial u'}{\partial x}\right\rangle}_{\text{press.-strain}} + \ldots \\
\left(\frac{\partial}{\partial t} + U\frac{\partial}{\partial x}\right)\frac{1}{2}\rho\left\langle v'v'\right\rangle &= + \underbrace{\left\langle P'\frac{\partial v'}{\partial y}\right\rangle}_{\text{press.-strain}} + \ldots \\
\left(\frac{\partial}{\partial t} + U\frac{\partial}{\partial x}\right)\frac{1}{2}\rho\left\langle w'w'\right\rangle &= + \underbrace{\left\langle P'\frac{\partial w'}{\partial z}\right\rangle}_{\text{press.-strain}} + \ldots
\end{aligned}$$

Such an equation is trivially obtained by applying suited simplifications to equation 2.30. Only the production and pressure-correlation terms are shown: the remaining terms mostly redistribute energy in space or dissipate it and are not of interest for the present discussion. The production term is zero for all components except the streamwise one: that is, only streamwise fluctuations receive energy from the mean flow. Clearly, though, this energy must be redistributed to the remaining components, which would otherwise be damped by dissipation until they hold no energy. This inter-component redistribution happens thorugh the pressure-strain correlation. The pressure-strain correlation only appears in the budget equation of each individual normal Reynolds stress; when these three are summed together to yield the budget of TKE (equation 2.32), the term disappears owing to continuity:

$$\left\langle P'\frac{\partial u'_k}{\partial x_k}\right\rangle = 0$$

That is, the pressure-strain correlation cannot increase nor decrease the total amount of TKE; it can only alter the share of TKE held by each component of the velocity. In other words, it resdistributes energy between velocity components. To summarise, turbulent kinetic energy is produced on the streamwise component and then redistributed to the wall-normal and spanwise ones. This holds true not only for the channel geometry considered here, but also for homogeneous shear flows (Davidson, 2015, chapter 4.4.1).

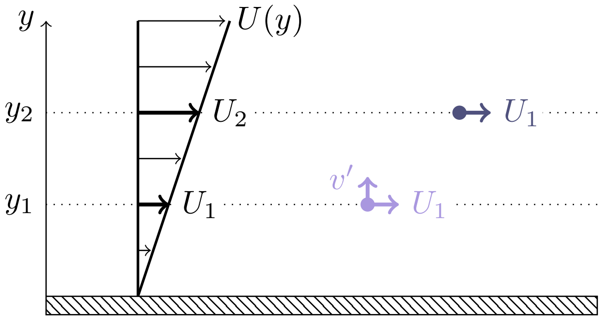

Figure 2.2: A simplified description of the mechanism that produces turbulence in a wall-bounded flow; $U(y)$ represents the mean velocity profile in proximity of a wall (hatched area). A generic fluid particle is marked in purple in the sketch, both before (lighter shade) and after (darker shade) being displaced in the wall-normal direction by a v' fluctuation. The displaced particle is perceived by the mean flow as a fluctuation.

Next, the physical mechanism underlying the production of turbulent kinetic energy in a wall-bounded flow is discussed. Once again, the production term reads:

$$-\rho \langle u'v' \rangle \frac{dU}{dy}$$

This term only appears in the equation of the streamwise normal Reynolds stress $\langle u'u' \rangle$. It can thus be interpreted as the product of a body force (acting on the streamwise fluctuation field) and the velocity u' the body force works for. Before averaging, such a body force reads:

$$-v' \frac{\mathrm{d}\,(\rho U)}{\mathrm{d}y} \tag{2.43}$$

The physical interpretation of the above body force is straightforward: it represents the momentum flux ensuing from v' fluctuations transporting the mean streamwise momentum ρU in the wall-normal direction. This mechanism underlies the production of turbulence in the considered channel flow; notice that the existence of a mean shear is necessary for the formation of turbulence (this being generally true for any turbulent flow, see Davidson, 2015, ch. 4.1.3). Turbulence cannot originate without the strong mean shear produced by viscosity; as mentioned at the beginning of the chapter, *viscosity is [...] the midwife [...] in the life story of turbulence* (Sherman, 1990).

The physical mechanism underlying the term of equation 2.43 has an even simpler phyisical interpretation, which is explained with the help of figure 2.2. Consider the flow over a flat wall as in the sketch; typically, a positive mean velocity gradient dU/dy is observed. A fluid particle is originally located at a wall-normal position y_1; its velocity U_1 matches the expected velocity at that position, $U_1 = U(y_1)$. The particle is displaced in the wall-normal direction by a fluctuation $v' > 0$, so that it reaches a second wall-normal position y_2. Assuming that the particle maintains its original velocity, it will be now be surrounded by fluid that, on average, moves at a faster velocity $U_2 = U(y_2)$. That is, the displaced particle is perceived by the surrounding flow as a velocity fluctuation $u' = U_1 - U_2 < 0$: hence, the mechanism proposed here can explain how streamwise turbulent fluctuations are produced. Additionally, it can help explain how the Reynolds shear stress is generated: in spite of its simplicity, the mechanism described here correctly predicts that u' and v' fluctuations tend to have opposite sign – as a positive wall-normal perturbation produces a negative streamwise one. Indeed, $\langle u'v' \rangle < 0$ is typically verified if $dU/dy > 0$.

2.3 Turbulence in the spectral domain; scale interactions

As mentioned in §1.1, the scientific community still hasn't come up with a proper definition of turbulence. It appears, though, that one of its intrinsic features is the existence of eddies of a wide range of sizes (also referred to as *scales of motion*) that interact with each other. Richardson and Lynch (2007) captured this idea in a short poem:

> *Big whirls have little whirls*
> *which feed on their velocity,*
> *and little whirls have lesser whirls,*
> *and so on to viscosity.*

There is however a crucial issue that arises when one tries to investigates the distribution (and, redistribution) of energy across vortices of different scales. No universally accepted definition of a turbulent eddy is available, let alone a mathematically well-behaved one. In other words, it is not possible to isolate (physically or mathematically) a single turbulent eddy of a given size. Some other strategy to define the scales of motion is then needed. This is usually done by decomposing the velocity signal extracted from a turbulent flow into a set of modes; each mode then corresponds to a specific scale.

Many different modal decomposition techniques could be (and have been) used for this task. For instance, one could resort to a data-driven modal decomposition such as the one used by Agostini and Leschziner (2019a). Alternatively, one can decompose the velocity field of a turbulent flow into a set of sinusoidal functions through the Fourier series (or, transform); the sum of all these sinusoids returns the original velocity field, and the wavelength of each of them identifies a scale of motion. The Fourier series is much better mathematically understood than its empirical counterparts; for this reason, it will be the modal decomposition of choice for this manuscript.

In the next sections, the definition of the Fourier series (transform) will be reported. It will be shown how the Fourier series can be used to quantify the amount of energy held by a specific scale of motion (velocity spectra, §2.3.2). It will be finally shown how the Fourier series enables a rigorous discussion of scale interactions (§2.3.4).

A caveat has to be made on the use of the Fourier series. Although the discussion that follows from the adoption of the Fourier series is mathematically rigorous, it is based on the assumption that scales of motion are well described by sine waves. Yet, a sine wave is not necessarily suited to describe the shape of a turbulent eddy; there could exist another decomposition that yields a more phyisically sound picture of turbulence. To the author's knowledge, such a decomposition has not been discovered yet.

A final comment on the notation. In the following sections, the Fourier series will be defined for one velocity component only (the streamwise one, u) and in one spatial direction only (again, the streamwise one, x). The dependence of u on the remaining spatial directions and on time will often be neglegted to simplify the notation. The generalisation of the definitions presented here to other velocity components and spatial directions is trivial and left to the reader.

2.3.1 The Fourier transform and series

A note of caution. Several definitions of the Fourier transform, of the series and of the discrete transform are available, which only differ by a constant factor. In this manuscript, the definitions reported by Pope (2000) will be used; all the formulae presented here will be consistent with this choice. Notice, however, that parts of this and of the following sections are inspired by the book of Brigham (1988), which uses a different definition of the discrete and regular Fourier transforms.

The Fourier transform $\mathcal{F}\{g\}$ of a generic function $g(x)$ is a complex function of a real variable κ_x that yields an alternative (and equivalent) representation of $g(x)$. It is defined as (Pope, 2000, appendix D):

$$\mathcal{F}\{g\}(k_x) = \frac{1}{2\pi} \int_{-\infty}^{\infty} g(x) e^{-i\kappa_x x} \, \mathrm{d}x \tag{2.44}$$

where i is the imaginary unit. Instead of representing $g(x)$ in real space, the Fourier transform provides its representation in the spectral space – that is, in a space described by complex sinusoidal waves. Each of these waves (also referred to as Fourier modes) can be written as:

$$e^{i\kappa_x x} \tag{2.45}$$

where κ_x is the wavenumber and it is inversely proportional to the wavelength λ_x of each sine wave:

$$\kappa_x = \frac{2\pi}{\lambda_x} \tag{2.46}$$

The value of the Fourier transform at a given value of κ_x represents the projection of the function g on the Fourier mode $e^{i\kappa_x x}$ of matching wavenumber; that is, the value of the Fourier transform represents the amplitude (and phase, as it is a complex number) of the mode $e^{i\kappa_x x}$. The original function $g(x)$ can be recovered by cumulating the contributions given by each Fourier mode:

$$g(x) = \int_{-\infty}^{\infty} \mathcal{F}\{g\}(\kappa_x) \, e^{i\kappa_x x} \, \mathrm{d}\kappa_x \tag{2.47}$$

The above formula is also known as the antitransform.

There are two issues with using the Fourier transform in the context of turbulence research. First off, equation 2.44 contains an integral over an infinite domain, which is of course not practically computable (both numerical and experimental datasets are defined, of course, over a finite domain). Besides, the Fourier transform of the velocity signal $u(x)$ extracted from the channel flow of §2.2.1 is not necessarily defined. Indeed, $u(x)$ is a random function that does not decay to zero for $|x| \to \infty$ (hence, it is not Lebesgue-integrable); proving the existence of its transform becomes then tricky[6] (see Brigham, 1988, ch. 2.3).

In practice, these issues are avoided by using the Fourier series. The series is a specific formulation of the transform for periodic functions (for a discussion of how the series stems from the transform, see Brigham, 1988, ch. 4.2). It is thus well suited to analyse simulation data, as simulations of turbulence are typically carried out in periodic domains. Let L_x be the streamwise period of the simulation box; the coefficients $\widehat{u}$ of the Fourier series of the velocity signal $u(x)$ are then then defined as:

$$\widehat{u}(\kappa_x) = \frac{1}{L_x} \int_{0}^{L_x} u(x) \, e^{-i\kappa_x x} \, \mathrm{d}x \tag{2.48}$$

Notice that a double hat ($\widehat{\widehat{u}}$) will be used in this manuscript to indicate a quantity that is transformed (in the sense of the Fourier series) in two spatial directions, e.g. x and z. Although the notation $\widehat{u}(\kappa_x)$ used here to indicate the coefficients of the series is standard (see for instance Pope, 2000, ch. 6.4),

---

[6] Some variants of the Fourier transform have been proposed to avoid this issue: see Pope (2000, appendix E.3).

it is misleading. Indeed, $\widehat{u}(\kappa_x)$ is not a continuous function of κ_x as the notation suggests. The only admissible values of κ_x are:

$$\kappa_x = n\Delta\kappa_x \qquad \text{with } n \in \mathbb{Z},\ \Delta\kappa_x = \frac{2\pi}{L_x} \tag{2.49}$$

where $\mathbb{Z}$ indicates the set of integer numbers and $\Delta\kappa_x$ will be referred to as the Fourier resolution.

This notational abuse will be tolerated both because it is customary and because it simplifies the discussion of the next sections. The coefficients $\widehat{u}(\kappa_x)$ will be used to approximate the well-defined transforms of some velocity moments, which are continuous function of κ_x. This operation is well justified on mathematical grounds: once again, the series is a particular case of the transform, and the two definitions of equations 2.44 and 2.48 are indeed very similar. The differences are, fundamentally, two: as already stated, the coefficient of the series are only defined for discrete values of κ_x, whereas the transform is a continuous function of κ_x. Last but not least, the coefficients $\widehat{u}$ have the same dimensions of the velocity u by definition; instead, the transform of u would have the dimensions of a velocity times a length (if it existed).

So far, only the coefficients of the series (which are analogous to the transform) have been defined. The series itself is, properly, the discrete version of the anti-transform:

$$u(x) = \sum_{\kappa_x \to -\infty}^{\infty} \widehat{u}(\kappa_x)\, e^{i\kappa_x x} \tag{2.50}$$

The interpretation of the Fourier transform is then perhaps clearer from the above formula: it allows to rewrite a velocity signal as the sum of many modes. Each mode is a sinusoid of wavelength $\lambda_x = 2\pi/\kappa_x$; heuristically, then, each mode represents a turbulent motion of scale λ_x.

2.3.2 Velocity spectra

The amount of energy held by each scale of motion (that is, by each Fourier mode) is quantified by the velocity spectrum. In this section, only the one-dimensional streamwise spectrum $\Phi_{uu}(\kappa_x)$ of the streamwise velocity will be discussed; the definition presented here can be easily generalised to the one-dimensional spanwise spectrum $\Phi_{uu}(\kappa_z)$ and to the spectra of other Reynolds stresses (e.g., Φ_{vv}, Φ_{uu}). Moreover, spectra can also be two-dimensional (corresponding to a double Fourier transform in the x and z direction); two-dimensional spectra will be indicated with a lowercase ϕ, and their definition is also easily obtainable from the one presented here.

The velocity spectrum Φ_{uu} is defined as the Fourier transform of the two-point velocity correlation $\langle u'(x)\, u'(x+r_x)\rangle$. Notice that $\langle u'(x)\, u'(x+r_x)\rangle$ is only a function of r_x, and it quantifies the correlation between the velocity fluctuations at any two points that are separated in the streamwise direction by r_x (assuming that the x direction is statistically homogeneous). The quantity $\langle u'(x)\, u'(x+r_x)\rangle$ typically decays to zero for $|r_x| \to \infty$, so that its Fourier transform is well defined. It follows:

$$\Phi_{uu}(\kappa_x) = \frac{1}{2\pi}\int_{-\infty}^{\infty} \langle u'(x)\, u'(x+r_x)\rangle\ e^{-i\kappa_x r_x}\, \mathrm{d}r_x \tag{2.51}$$

An important consequence of this definition is that the spectrum has the units of a velocity squared per unit wavenumber.

Notice that, for $r_x = 0$, the correlation $\langle u'(x)\, u'(x+r_x)\rangle$ reduces to the Reynolds stress $\langle u'u'\rangle$. By leveraging this information and the definition of the Fourier antitransform (eq. 2.47), one obtains:

$$\begin{aligned}\langle u'u'\rangle &= \langle u'(x)\, u'(x+r_x)\rangle\,(r_x = 0) = \int_{-\infty}^{\infty} \Phi_{uu}\, e^{i\kappa_x 0}\,\mathrm{d}\kappa_x\\ \langle u'u'\rangle &= \int_{-\infty}^{\infty} \Phi_{uu}(\kappa_x)\,\mathrm{d}\kappa_x \end{aligned} \tag{2.52}$$

Equation 2.52 provides a phyisical interpretation of what the spectrum represents. The spectrum Φ_{uu} indicates the spectral density of turbulent kinetic energy (per unit mass), consistently with its dimensions; in other words, the value of the spectrum at a given κ_x represents the amount of kinetic energy (per unit mass and wavenumber) held by the corresponding Fourier mode. The total kinetic energy can be found by cumulating (integrating) the contributions of all Fourier modes.

2.3.3 The practical computation of a velocity spectrum

The definition of the spectrum provided in equation 2.51 is not of practical use. Numerical and experimental data is never defined on an infinite domain, and it is typically sampled. This introduces two requirements:

- data needs to be observed (measured or simulated) on a long enough domain in order to be able to estimate the spectrum that would be observed in an infinite domain;
- the spacing between samples needs to be sufficiently small to make aliasing effects small, as explained below.

Moreover, the calculation of the correlation $\langle u'(x)\, u'(x+r_x)\rangle$ is not particularly efficient: there exists a faster way of calculating the spectrum that can be used in case of a periodic velocity signal.

The need for a long enough simulation domain. Let's begin by analysing the definition of the spectrum once again. As stated in §2.3.2, the spectrum is the Fourier transform of the velocity correlation $\langle u'(x)\, u'(x+r_x)\rangle$; such function typically decays to zero for large absolute values of r_x. It will be now assumed that there exists a value $L_x/2$ such that the velocity correlation is identically zero for $|r_x| \geq L_x/2$ (in practice, having a small enough value of the velocity correlation – as is typically the case – is also sufficient). Under such an assumption, the definition of the spectrum (eq. 2.51) can be rewritten as:

$$\Phi_{uu}(\kappa_x) = \frac{1}{2\pi}\int_{-L_x/2}^{L_x/2} \langle u'(x)\, u'(x+r_x)\rangle\; e^{-i\kappa_x r_x}\,\mathrm{d}r_x \tag{2.53}$$

The assumption made above is typically well verified, and it implies that all the information provided by the velocity correlation function is contained on a L_x-long subset of its domain. In other words, an infinite domain is not needed to describe it; rather, a restricted domain is sufficient provided that it is sufficiently long. An L_x-long domain is suited, for instance.

A faster way of calculating the spectrum. Typically, simulations of turbulence are carried out in a periodic box; owing to the periodicity, the Fourier transform has to be replaced by a Fourier series. We will assume that the box has size (period) L_x; that is, the box is large enough to observe the decay to zero of the velocity correlation as previously discussed. The velocity correlation will also be periodic with period L_x. It is assumed that the velocity correlation $\langle u'(x)\, u'(x+r_x)\rangle$ computed in the box for

$r_x \in [-L_x/2, L_x/2)$ matches the one that would be observed in an infinitely long domain for the same values of r_x. The Fourier coefficients $\widehat{a}(\kappa_x)$ of the periodic velocity correlation are given by:

$$\widehat{a}(\kappa_x) = \frac{1}{L_x} \int_0^{L_x} \langle u'(x)\, u'(x + r_x) \rangle \; e^{-i\kappa_x r_x} \, \mathrm{d}r_x \tag{2.54}$$

$$= \frac{1}{L_x} \int_{-L_x/2}^{L_x/2} \langle u'(x)\, u'(x + r_x) \rangle \; e^{-i\kappa_x r_x} \, \mathrm{d}r_x \tag{2.55}$$

$$\text{with } \kappa_x = n \Delta\kappa_x, \qquad n \in \mathbb{Z}$$

Notice that the extremes of integration can be arbitrarily shifted owing to the periodicity. By comparing equations 2.53 and 2.55, one easily obtains:

$$\Phi_{uu}(\kappa_x) = \frac{L_x\, \widehat{a}(\kappa_x)}{2\pi} = \frac{\widehat{a}(\kappa_x)}{\Delta\kappa_x} \tag{2.56}$$

That is, when using a Fourier series instead of the transform to define the spectrum, one needs to adjust the results by a factor $1/\Delta\kappa_x$, where $\Delta\kappa_x$ is the Fourier resolution. Please be aware that this factor effectively depends on the choice of normalisation used for both the Fourier transform and series.

There exists a computationally efficient way of computing the Fourier coefficients $\widehat{a}$ of the velocity correlation that does not require the calculation of the velocity correlation itself. Indeed, only the Fourier coefficients $\widehat{u}(\kappa_x)$ of the velocity $u(x)$ are needed; owing to the correlation theorem (see e.g. Brigham, 1988, for its version for the Fourier transform; generalisation to the series is trivial),

$$\widehat{a}(\kappa_x) = \left\langle \widehat{u}^H(\kappa_x)\, \widehat{u}(\kappa_x) \right\rangle \tag{2.57}$$

where $(...)^H$ indicates the conjugate of a complex number. This, combined with equation 2.56, yields:

$$\Phi_{uu}(\kappa_x) = \frac{\left\langle \widehat{u}^H(\kappa_x)\, \widehat{u}(\kappa_x) \right\rangle}{\Delta\kappa_x} \tag{2.58}$$

Equation 2.58 is practically used to calculate a spectrum. Importantly, it highlights that the spectrum Φ_{uu} is a real number; this generally holds for all spectra of the normal Reynolds stresses (but not for the remaining ones, e.g. the shear one).

Aliasing. Numerical data is typically sampled on an uniformly spaced grid. Hence, the integral 2.48 and consequently the spectrum Φ_{uu} as defined in equation 2.58 cannot be exactly calculated. Instead, one can approximate the coefficients of the Fourier series of u with a discrete Fourier transform. Let u^m be the sampled value of the velocity at the position $x^m = m\,\Delta x$, where Δx is the grid spacing and $m = 0, ..., N-1$ for a total of N points. For simplicity, it is assumed that N is even. The coefficients $\overset{\triangle}{u}$ of the discrete Fourier transform are defined as (Pope, 2000, appendix F):

$$\overset{\triangle}{u}(\kappa_x) = \frac{1}{N} \sum_{m=0}^{N-1} u^m e^{-i\kappa_x x^m} \tag{2.59}$$

which can be interpreted as an approximation of the integral defining the coefficients of the Fourier series (eq. 2.48). The admissible values of κ_x are the same as the ones for the Fourier series, with an exception. Sampling the signal $u(x)$ makes its transform periodic in the κ_x domain (Brigham, 1988, ch.

6); the period is given by $2\pi/\Delta x$, so that the discrete transform is fully determined by the coefficients found for values of κ_x satisfying:

$$\kappa_x \in (-\pi/\Delta x, \pi/\Delta x] \tag{2.60}$$

The remaining coefficients can be determined leveraging the periodicity. Formally, the coefficients of the discrete transform are computed for:

$$\kappa_x = n\Delta\kappa_x \qquad \text{with } 1 - \frac{N}{2} \leq n \leq \frac{N}{2}, \quad n \in \mathbb{Z} \tag{2.61}$$

for a total of N coefficients[7] Bear in mind that $L_x/N = \Delta x$ owing to periodicity[8]. The definition of the antitransform is the same as the one of the Fourier series (2.50), except that the number of Fourier modes is limited and not infinite:

$$u^m \;=\; u(x^m) \;=\; \sum_{\kappa_x \,=\, \Delta\kappa_x - \pi/\Delta x}^{\pi/\Delta x} \overset{\triangle}{u}(\kappa_x)\, e^{i\kappa_x x^m} \tag{2.62}$$

Suppose now that the exact coefficients $\widehat{u}$ of the series of a signal $u(x)$ are known. The signal is also sampled and the coefficients $\overset{\triangle}{u}$ of the discrete transform are calculated. It is trivially shown that both the Fourier series (eq. 2.50) and the discrete antitransform (eq. 2.62) exactly return the original values of the velocity; by evaluating the velocity at some point x^m, one can write (Pope, 2000, appendix F):

$$u^m \;=\; u(x^m) \;=\; \sum_{\kappa_x \,=\, -\infty}^{+\infty} \widehat{u}(\kappa_x)\, e^{i\kappa_x x^m} \;=\; \sum_{\kappa_x \,=\, \Delta\kappa_x - \pi/\Delta x}^{\pi/\Delta x} \overset{\triangle}{u}(\kappa_x)\, e^{i\kappa_x x^m} \tag{2.63}$$

Notice that the above expression is exact. The summation of the discrete antitransform returns the same value as the summation of the series; the two summations are almost identical, except that the discrete antitransform uses a finite number of Fourier modes satisfying $|\kappa_x| \leq \pi/\Delta x$. This is only possible (with $\overset{\triangle}{u} \approx \widehat{u}$) if the energy contained on the modes of the Fourier series with $|\kappa_x| > \pi/\Delta x$ (that is, the modes that are not considered by the discrete transform) is negligible. If, instead, these high-wavenumber modes do hold a significant amount of energy in the series, this energy will be distributed to the low-wavenumber modes of the discrete transform, so that $\overset{\triangle}{u} \neq \widehat{u}$ – as the equivalence of equation 2.63 must be exactly verified. This is known as aliasing and prevents the discrete Fourier transform from correctly approximating the value of the series.

In practice, the error caused by aliasing can be minimised by sampling the signal $u(x)$ with a small enough Δx such that the spectral band of $u(x)$ falls in the range $(-\pi/\Delta x, \pi/\Delta x]$. The threshold value $\pi/\Delta x$ is the spatial equivalent of the Nyquist frequency used in the discussion of discrete transforms in time.

---

[7] Notice that further simplification are possible. If the function being transformed is real, its transform is Hermitian (Brigham, 1988, chapter 3.9). The function $u(x)$, for instance, satisfies this requirement, so that $\widehat{u}(-\kappa_x) = \widehat{u}^H(\kappa_x)$. Owing to this property, the transform $\widehat{u}$ is fully defined by its values for $\kappa_x \geq 0$.

[8] On a non-periodic domain, one would typically have $\Delta x = L_x/(N+1)$.

2.3.4 Triadic interactions

It was shown in §2.3.2 how the Fourier transform can be leveraged to discuss the amount of energy held by each scale of motion. In this section, it will be shown how the Fourier series can be used to discuss scale interactions.

To do so, consider the incompressible Navier-Stokes equations shown in equation 2.2. These comprise both linear and non-linear operators. By grouping them together under a single operator $\mathcal{L}\{\vec{u}\}$ for the linear ones and $\mathcal{N}\{\vec{u}\}$ for the non-linear ones, the equations read:

$$\frac{\partial \vec{u}}{\partial t} = \mathcal{L}\{\vec{u}\} + \mathcal{N}\{\vec{u}\} \tag{2.64}$$

Let the non-linear terms be neglected, for the time being; the Fourier transform (in the sense of the Fourier series, if one is in a periodic domain) of both sides of the equation is taken, and it is indicated by the operator $\mathcal{FS}\{...\}$:

$$\mathcal{FS}\left\{\frac{\partial \vec{u}}{\partial t}\right\} = \mathcal{FS}\{\mathcal{L}\{\vec{u}\}\} \tag{2.65}$$

Now, $\mathcal{FS}$ is a linear operator and it commutes with the time derivative on the left-hand side. Similarly, it can be easily shown that the transform of $\mathcal{L}\{\vec{u}\}$ can be written as a linear operator $\widehat{\mathcal{L}}$ acting on the transform $\mathcal{FS}\{\vec{u}\}$ of the velocity[9]:

$$\frac{\partial \mathcal{FS}\{\vec{u}\}}{\partial t} = \widehat{\mathcal{L}}\{\mathcal{FS}\{\vec{u}\}\} \tag{2.66}$$

By evaluating the above equation for some value of κ_x of choice, one observes that the time evolution of a Fourier mode is only influenced by the Fourier mode itself, without interactions with the remaining modes. Bear in mind that non-linear terms are being neglected.

The above discussion shows that linear terms are not responsible for the occurrence of scale interactions. Scale interactions are then necessarily caused by the non-linear terms, which can be written as:

$$\mathcal{N}\{\vec{u}\} = (\vec{u} \cdot \nabla)\,\vec{u} - \frac{1}{\rho}\nabla P \tag{2.67}$$

The contribution of the pressure is here considered as a non-linear term as the laplacian of the pressure has to balance the divergence of the other term on the right-hand side of equation 2.67. It can be shown, however, that the pressure can be eliminated from the incompressible Navier-Stokes equations (see, for instance, Pope, 2000, chapter 6.4.2; alternatively, a Helmholtz-Leray decomposition can be used), so that the divergence-less part of $(\vec{u} \cdot \nabla)\,\vec{u}$ remains as the only non-linear term. We will thus refer to $(\vec{u} \cdot \nabla)\,\vec{u}$ as *the* non-linear term; the present discussion will focus on it. Using Einstein's notation and owing to the incompressibility constraint, the non-linear term can be rewritten as:

$$u_k \frac{\partial u_i}{\partial x_k} = \frac{\partial u_i u_k}{\partial x_k} \tag{2.68}$$

---

[9] This follows from the fact that Fourier modes are eigenfunctions of the Laplace operator. The pressure gradient is here classified as a non-linear term for reasons that are clarified later; hence, the Laplace operator is the only linear term. One can also decide to include the pressure gradient among the linear operators; in this case, the pressure gradient can be eliminated by taking the curl of the momentum equation, so that an equation for the vorticity is found. The present discussion then still holds, but for the vorticity and not for the velocity field.

To simplify the discussion, only the streamwise momentum balance equation is now considered. Moreover, without loss of generality, only the term $\partial uu/\partial x$ will be discussed; the transform will be only performed in the streamwise direction:

$$\frac{\partial \widehat{u}(\kappa_x)}{\partial t} = \ldots + \mathcal{FS}\left\{\frac{\partial uu}{\partial x}\right\} \tag{2.69}$$

$$= \ldots + i\kappa_x\, \mathcal{FS}\left\{uu\right\} \tag{2.70}$$

By exploiting the convolution theorem (Brigham, 1988), it follows:

$$\frac{\partial \widehat{u}(\kappa_x)}{\partial t} = \ldots + i\kappa_x \sum_{\bar{\kappa}=-\infty}^{\infty} \widehat{u}(\bar{\kappa})\, \widehat{u}(\bar{\kappa} - \kappa_x) \tag{2.71}$$

Equation 2.71 shows that the evolution ($\partial\widehat{u}/\partial t$) of a Fourier mode κ_x is influenced by an infinite number of contributions (the ones appearing after the summation sign). Each of these contributions results from the interaction between two Fourier modes ($\bar{\kappa}$ and $\bar{\kappa}-\kappa_x$) that are distanced by κ_x in the spectral domain.

In other words, Fourier modes interact in pairs to yield a momentum- (or, energy-) transfer to a third mode of a different scale. These interactions take the name of *triadic*, as indeed they involve three different Fourier modes. In the context of the TKE budget of equation 2.32, triadic interactions are captured by the turbulent transport term, which stems from the non-linear term of the momentum equation. In this sense, the turbulent transport term is responsible for the redistribution of energy across different scales of motion.

2.4 Numerical methods

The present scientific work is based on the numerical analysis of wall-bounded turbulent flows. The focus is not much on the geometry of the problem, but rather on turbulent eddies and their interaction with the wall. The simple geometry of the channel flow described in §2.2.1 is thus suited to discuss the present scientific objectives.

Clearly, the geometry described in §2.2.1 cannot be simulated as-is: it would involve infinitely extended walls, which are not representable in a computer simulation. When pursuing a theoretical approach, an infinite domain extent in the streamwise and spanwise directions is needed to make the problem homogeneous in these two directions. The same effect is achieved, in the context of a simulation, by using periodic boundary conditions. Notice that the simulation box size still needs to be large enough to observe the decay of the velocity correlation function (see §2.3.3) – or, heuristically, to accomodate the largest turbulent structures (that are indeed responsible for the correlation seen at large separations). Additionally, the grid spacing needs to be low enough to resolve the smallest structures (that is, to avoid aliasing, see again §2.3.3).

While the requirements on the resolution and on the box size typically need to be satisfied regardless of which equation is being solved, there are two additional issues that need to be considered that specifically apply to the incompressible Navier-Stokes equations.

1. If no precaution is taken, the calculation of the pressure field is typically a numerically unstable procedure; an example of such an instability is given in §2.4.1.
2. The Navier-Stokes equations contain a diffusion and a convective term, each of which can lead to numerical instabilities under certain circumstances.

The second issue can be easily worked around by using a suited pair of time- and spatial-discretisation schemes, and by adjusting the temporal resolution Δt of the simulation (§2.4.3). As for the first issue, two different algorithms will be presented (sections 2.4.2 and 2.4.4) which differ in the way they deal with the instability of the pressure. Both of them will be used for the production of data for the analyses of the following chapters.

2.4.1 Spurious pressure modes

To discuss how the pressure term of the Navier-Stokes equations can lead to numerical instabilities, consider a simplified problem where only the streamwise velocity is considered; the velocity only depends on time and on the streamwise direction (clearly, this violates the incompressibility constraint, but such an issue is not of concern in the present context). In other words, motion is described by the following equation:

$$\frac{\partial u}{\partial t} = \frac{1}{\rho}\frac{\partial P}{\partial x} + \mathrm{RHS}\{u\} \tag{2.72}$$

where RHS indicates some operator acting on u. Let u^m indicate the velocity at some spatial position x^m and Δx be the spacing between grid points; the same notation applies for the pressure, so that the pressure and velocity grids are co-located. The pressure term is discretised with centered finite differences; the operator RHS will be ignored, as it is not relevant for the present discussion. The discretised equations read:

$$\frac{\partial u^m}{\partial t} = \frac{1}{\rho}\frac{P^{m+1} - P^{m-1}}{2\Delta x} + \ldots \tag{2.73}$$

Notice that the time evolution of the velocity field is only influenced by the difference $P^{m+1} - P^{m-1}$ between values of the pressure at different spatial positions; this difference is always calculated between values at positions whose indices $m+1$, $m-1$ are either both odd or both even. Now, suppose that equation 2.73 admits a solution (u^m, P^m) if completed by suited boundary conditions. The pressure field is distorted by adding a constant value at all spatial positions whose index m is even; this results in a perturbed pressure field Q^m. Such a perturbation satisfies

$$P^{m+1} - P^{m-1} = Q^{m+1} - Q^{m-1} \qquad \forall m \tag{2.74}$$

as indeed the difference is never calculated between even and odd points; hence, the pair (u^m, Q^m) is also a solution of the discretised problem. In other words, the solution to the discretised problem of equation 2.73 is not unique, as one can always add some pressure perturbation (also referred to as a spurious mode) such that the perturbed solution is still a solution of the original problem. The existence of spurious pressure modes can lead to numerical instabilities (see e.g. Quarteroni, 2009, chapter 15.3.3).

One straightforward way to avoid this issue is to use a staggered grid, meaning that the pressure and velocity fields are not evaluated at the same spatial positions. Rather, let now u^m be the velocity at some position x^m and P^m be the pressure at the position $x^n + \Delta x/2$. The discretised version of equation 2.72 now reads:

$$\frac{\partial u^m}{\partial t} = \frac{1}{\rho}\frac{P^{m} - P^{m-1}}{\Delta x} + \ldots \tag{2.75}$$

Here, the difference $P^m - P^{m-1}$, which is still centered with respect to x^m, references the values of the pressure at two spatial positions – one of which has an even index and the other an odd one. This prevents the existence of spurious modes such as the one previously described; the discretised problem is thus stabilised.

2.4.2 Method 1: compact finite differences on a partially staggered grid

As explained in §2.4.1, issues linked to the spurious pressure modes can be avoided by using a staggered grid. The first numerical method presented here, which is implemented in the program Xcompact3d (Laizet and Lamballais, 2009; Laizet and Li, 2011; Bartholomew et al., 2020), makes use of this stabilisation strategy. All velocity components are co-located, whereas the pressure grid is shifted by half a cell in each spatial direction.

As for the time- and space-discretisation, a third-order time-marching Runge-Kutta scheme is combined with compact finite differences in the spatial directions. The temporal and spatial discretisations will be separately discussed in the following paragraphs. The discretised equations are solved for the channel flow geometry of §2.2.1; at the walls of the channel, no-slip and no-penetration conditions are imposed. Periodic boundary conditions are used for the streamwise and spanwise directions.

Time-discretisation and pressure correction. To help the discussion of its discretisation in time, the momentum balance of the Navier-Stokes equations (2.2) is rewritten as:

$$\frac{\partial \vec{u}}{\partial t} = \vec{F}(\vec{u}) - \frac{1}{\rho}\nabla P \tag{2.76}$$

where $\vec{F}$ is used to indicate the advection and diffusion terms. Two important things should be noticed here. First off, the above momentum balance is complemented by the incompressibility constraint:

$$\nabla \cdot \vec{u} = 0 \tag{2.77}$$

Secondly, the pressure P appears in the above momentum balance (2.76); however, no evolution equation for the pressure is provided. Then, the momentum balance equation (2.76) is the only equation that describes the time evolution of some quantity – the velocity field, in this case. Hence, this equation will be discretised in time, so that the velocity field $\vec{u}^{\,n+1}$ at the time t^{n+1} can be calculated if the velocity field $\vec{u}^{\,n}$ at the previous instant in time t^n is known. The time step $\Delta t = t^{n+1} - t^n$ is kept constant.

Each time step is performed through three intermediate steps using the third-order low-storage Runge-Kutta scheme described by Williamson (1980). Notice that the original formulation is here simplified for the sake of clarity. The simplifications are exact from an algebraic (theoretical) standpoint; however, the formulation proposed by Williamson (1980) is able to better compensate the roundoff errors that arise when floating point numbers are digitised by a computer. At each intermediate step, an intermediate, uncorrected solution $\vec{u}^{\,k,*}$ is computed by considering the velocity increment $\Delta\vec{u}^{\,k}$ given by the advection and diffusion terms. Since the so-obtained $\vec{u}^{\,k,*}$ field does not necessarily satisfy the incompressibility constraint, a pressure correction is applied to obtain the divergence-less, intermediate solution $\vec{u}^{\,k}$. The procedure is repeated for $k = 1, 2, 3$, where k indicates the current intermediate step of the Runge-Kutta method; for $k = 3$, the new solution $\vec{u}^{\,n+1}$ is produced (the old solution $\vec{u}^{\,n}$ is instead represented by $\vec{u}^{\,k}$ with $k = 0$). The complete procedure is described by the following equations (see Williamson, 1980):

$$\Delta\vec{u}^{\,k} = a^k\,\Delta\vec{u}^{\,k-1} + \Delta t\,\vec{F}^{\,k-1} \tag{2.78}$$

$$\vec{u}^{\,k,*} = \vec{u}^{\,k-1} + b^k\,\Delta\vec{u}^{\,k} \tag{2.79}$$

$$\vec{u}^{\,k} = \vec{u}^{\,k,*} - \frac{b^k\Delta t}{\rho}\,\nabla P^k \tag{2.80}$$

where a^k, b^k are constants such that $a^1 = 0$; the remaining values are given by Williamson (1980). The pressure field P^k used for the pressure correction (equation 2.80) is found by solving the following Poisson equation (Laizet and Lamballais, 2009):

$$\nabla^2 P^k = \frac{\rho}{b^k\Delta t}\,\nabla\cdot\vec{u}^{\,k,*} \tag{2.81}$$

so that, effectively, the pressure correction (eq. 2.80) ensures that the field $\vec{u}^{\,k}$ is divergenceless by removing the non-solenoidal part of $\vec{u}^{\,k,*}$.

Spatial discretisation. So far, it has been shown how the values of velocity field at the time t^n can be updated to yield the velocity field at the next discrete instant in time $t^{n+1} = t^n + \Delta t$. There is however one more issue to address: the velocity field $\vec{u}$, which would theoretically be a continuous field, must be stored as a collection of discrete values when performing a simulation. Then, spatial derivatives (which are needed for the calculation of $\vec{F}(\vec{u})$, see above) must be approximated using these available discrete values.

To simplify the discussion, only the streamwise component of the velocity will be considered; it will be further assumed that u only depends on the streamwise coordinate x. Once again, u^m will indicate the value of u at the position x^m; the grid spacing $\Delta x = x^m - x^{m-1}$ is constant. Let $\overset{'}{u}$ indicate the first derivative of u in x; the sixth-order accurate finite compact difference approximation of $\overset{'}{u}$ on the discrete grid x^m is given by (Lele, 1992; Laizet and Lamballais, 2009):

$$c_1\overset{'}{u}^{m-1} + \overset{'}{u}^{m} + c_1\overset{'}{u}^{m+1} = c_2\frac{u^{m+1} - u^{m-1}}{2\Delta x} + c_3\frac{u^{m+2} - u^{m-2}}{4\Delta x} \tag{2.82}$$

The values of the coefficients c_1, c_2 and c_3, as well as an expression for second derivatives can be found on Laizet and Lamballais (2009); alternatively, they can be found by considering the Taylor series expansions of the function u and its derivative $\overset{'}{u}$ at selected grid points around x^m. Notice that it was here assumed that the grid spacing is uniform; while this is certainly true for the streamwise and spanwise directions, it does not hold for the wall-normal one. A different formulation of the compact differences will be needed in this case.

Compact differences are able to achieve a higher order of accuracy on a smaller stencil than regular finite differences. However, they require the solution of a non-linear system: equation 2.82 cannot be used to directly calculate the value of $\overset{'}{u}$ at some position x^m. Instead, by writing equation 2.82 for all admissibile values of m (taking care that the simulation domain has finite boundaries), one obtains an implicit linear system.

By using compact finite differences and the time-marching scheme described here, the time evolution of the discretised velocity field can be computed – as long as an initial condition is provided.

2.4.3 Numerical stability: convection and diffusion

In the previous section (2.4.2), it was shown how an explicit time-marching method can be used to solve convective-diffusive problems such as the one given by the incompressible Navier-Stokes equations. The numerical procedure might however get unstable under given circumstances owing to either the convective or the diffusion term. In the following, two typical numerical stability critera will be reported; these criteria can be used to determine the largest value of the time step Δt for which a numerical scheme remains stable. Rigorously speaking, these two criteria are not of general validity: to the author's knowledge, stability criteria are always implementation-dependent (meaning that they depend on the equation being discretised as well as on the discretisation scheme). Nevertheless, the derivation of stability criteria for equations containing convective and diffusive terms usually results in the below criteria.

The first criterion takes the name of Courant-Friedrichs-Lewy (CFL) condition (see Quarteroni, 2009, ch. 12.4.2 for its formulation in case of a purely convective problem discretised with finite differences) and typically represents a necessary (but not always sufficient) condition for the numerical stability of schemes that discretise an equation containing an advection term:

$$\frac{\mathcal{U}\Delta t}{L} \leq \mathrm{CFL}_{max} \tag{2.83}$$

The term to the left takes the name of CFL number and is built with some velocity scale $\mathcal{U}$ and some lenght scale L. The term to the right (CFL_{max}) is some threshold value that depends on the equation being discretised as well as on the choice of spatio-temporal discretisation. Similarly, the definition of the velocity and length scales also depends on the context; typically, L represents the spatial resolution (for instance, Δx), whereas $\mathcal{U}$ could be the maximum value of the two- or infinity-norm of the velocity vector among all points of the domain.

Similarly, if the equations being discretised contain a diffusion term, the following condition is typically necessary for the stability of the numerical scheme (see Quarteroni, 2009, chapter 5.4, for an analogous criterion):

$$\frac{\nu\Delta t}{L^2} \leq Fo_{max} \tag{2.84}$$

where the term to the left is referred to as Fourier number (Fo) and Fo_{max} is its maximum value for which the numerical scheme is not unstable.

Both the conditions above typically need to be verified for schemes that discretise the Navier-Stokes equations. Once again, the critical values CFL_{max} and Fo_{max} depend on the choice of time- and space-discretisation schemes; for instance, their values for the scheme described in §2.4.2 can be found on the documentation of the TLab solver[10]. Generally speaking, implicit time-marching schemes are less sensitive to numerical instabilities than explicit ones, so that they tolerate larger values of the Fourier and CFL numbers. Some implicit schemes may be unconditionally stable, whereas some other combinations of time- and space-discretisation schemes may be unconditionally unstable.

2.4.4 Method 2: a spectral, pressure-less formulation of the Navier-Stokes equations

A second numerical method for the discretisation of the Navier-Stokes equations will be used in this manuscript: its complete description can be found on Luchini and Quadrio (2006). Instead of relying on

---

[10] `https://github.com/turbulencia/tlab/blob/master/doc/manual.pdf`

a staggered grid to avoid spurious pressure modes (see sections 2.4.1 and 2.4.2), this method is based on a formulation of the Navier-Stokes equations that does not include any contribution from the pressure. Indeed, the pressure is not truly an unknown of the incompressible Navier-Stokes equations (for instance, as shown in §2.4.2, no evolution equation for it is provided); rather, it is a Lagrangian multiplier that ensures the fulfilment of the incompressibility constraint (Taha et al., 2023). If such a constraint is satisfied a-priori by ensuring that the velocity field $\vec{u}$ belongs to a set of divergence-less fields, the pressure disappears from the equations.

The automatic fulfilment of the incompressibility constraint is achieved by reformulating the Navier-Stokes equations so that the unknowns of the problem are given by the wall-normal velocity v and the wall-normal vorticity ω_y (Kim et al., 1987; Luchini and Quadrio, 2006). The complete velocity field (u, v, w) can be then recovered by considering the definition of the vorticity (first row of equation 2.85) and the incompressibility constraint (rewritten in the second row of equation 2.85):

$$\begin{cases} \dfrac{\partial u}{\partial z} - \dfrac{\partial w}{\partial x} = \omega_y \\[2em] \dfrac{\partial u}{\partial x} + \dfrac{\partial w}{\partial z} = -\dfrac{\partial v}{\partial y} \end{cases} \tag{2.85}$$

The above set of equations, completed by suited boundary conditions, can be solved for u and w to express these two velocity components as a function of the unknowns of the problem (v, ω_y). In doing so, the incompressibility constraint ($\nabla \cdot \vec{u}$) is automatically satisfied – as it appears in the second row of equation 2.85. As shown in Kim et al. (1987), a closed set of two evolution equations for the variables v, ω_y can be derived from the momentum balance of the Navier-Stokes equations. The equations can be solved without computing the pressure field, thus avoiding issues with spurious modes and the need for a pressure correction[11].

Other than eliminating the pressure from the equations of motion, the approach described in Luchini and Quadrio (2006) has an additional advantage given by the way it handles spatial discretisation. Instead of sampling the unknowns on a discrete spatial grid, the unknowns are approximated by a truncated Fourier series (effectively, a discrete Fourier transform; see §2.3.3) in the streamwise and spanwise directions. Effectively, then, $\widehat{\widehat{v}}$ and $\widehat{\widehat{\omega_y}}$ become the unknowns of the problem; the number of retained Fourier modes can be linked to the spatial resolution thanks to equation 2.60. Such a spectral approach has several advantages: derivatives in the streamwise and spanwise directions can be exactly calculated through an algebraic (hence, cheap) operation. Moreover, the system of partial differential equations shown in equation 2.85 becomes algebraic:

$$\begin{cases} i\kappa_z \widehat{\widehat{u}} - i\kappa_x \widehat{\widehat{w}} = \widehat{\widehat{\omega_y}} \\[2em] i\kappa_x \widehat{\widehat{u}} + i\kappa_z \widehat{\widehat{w}} = -\dfrac{\partial \widehat{\widehat{u}}}{\partial y} \end{cases} \tag{2.86}$$

A complication linked to the use of Fourier modes arises, however, when computing non-linear terms. In physical space, non-linear terms can be rewritten so that they involve the calculation of a product between velocity components – for instance, uu for the streamwise component (see equation 2.68). This product corresponds to a convolution in spectral domain (see equation 2.71). In practice, the direct com-

---

[11] The solution of the Poisson problem associated to the pressure correction accounts for a large share of the computational cost of a time step.

putation of the convolution is an expensive operation, so that it is preferred to anti-transform $\widehat{\widehat{u}}$ to yield u, to then calculate the product uu in physical space and to finally transform it back to the Fourier domain. The issue, here, is that the spectral band of the product uu is twice as large as the one of u: aliasing issues might occur. De-aliasing is thus performed: before performing the anti-transform that yields u, the set of Fourier coefficients $\widehat{\widehat{u}}$ is expanded with some additional, high-wavenumber modes whose coefficients are set to zero (this operation is commonly referred to as zero-padding). Typically, zero-padding is performed so that the final, total number of Fourier modes is larger than $3/2$ of its original value (Luchini and Quadrio, 2006). The zero-padded set of modes is anti-transformed to real space and the product uu is computed; upon transforming back to the Fourier domain, the additional modes added though zero-padding are discarded, so that only the original set of Fourier modes is retained. It can be shown that, by doing so, the retained modes are free of aliasing errors; these can ensue only for the discarded modes.

Although the use a Fourier series makes the computation of streamwise and spanwise derivatives trivial, wall-normal derivatives still need to be approximated with a canonical method. The code of Luchini and Quadrio (2006) uses compact finite differences to do so (similarly to scheme described in §2.4.2). As for the advancement in time of the numerical solution, convective terms are discretised with an explicit, third-order Runge-Kutta scheme (again, similarly to scheme described in §2.4.2). However, diffusion terms are discretised with an implicit, second-order Crank-Nicholson scheme. This semi-implicit strategy is common practice (Kim et al., 1987; Quarteroni, 2009); it combines the accuracy of a higher-order scheme and the stability of an implicit method. The latter relieves the stability constranint on the time step Δt given by condition 2.84.

3 Global energy fluxes in Couette and Poiseuille flows

The results shown in this chapter have been published in Andreolli et al. [MY21].

In this chapter, turbulent plane Couette and Poiseuille flows (as described in §2.2.1) will be compared in an attempt to investigate the different costs (in terms of skin friction, or power needed to drive the flow) associated to small and large scales of turbulence. Indeed, Couette flows are characterised by strong large-scale structures which can be found in Poiseuille flows only at much higher Reynolds numbers (see §1.2.2, or Lee and Moser, 2015, 2018; Pirozzoli et al., 2014), so that the comparison of the two flows can highlight the role of large scales in the generation of skin friction. The present chapter will thus address the following research question:

1. **How do the costs (in terms of power input or wall shear stress) associated to small and large scales differ?**

Additionally, previous studies suggest that turbulence develops faster with the Reynolds number in Couette flows. For instance, the shear and wall-normal Reynolds stresses saturate for lower values of the Reynolds number in Couette flows; transition to turbulence also happens at lower values of Re (Orlandi et al., 2015). These aspects will also be addressed.

The flows will be analysed using the framework first introduced by Gatti et al. (2018), which will be discussed and generalised to the combined Couette-Poiseuille problem considered here (see §3.1); specialisation to the isolated Couette and Poiseuille flows trivially follows. The framework will be then used to compare the two flows in §3.2.

Comparing flows that are different in nature is no trivial operation. It is indeed necessary to define how the comparison is carried out: for instance, the two flows can be compared at constant Re_τ as is usually done in the literature (Monty et al., 2009; Sillero et al., 2013). This approach, which will be pursued in §3.2.1, is not necessarily the best suited one, and two alternatives will be tested. In §3.2.2, the two flows will be compared in such a way that they receive the same input power from some external agent. A novel comparison strategy stemming from the analytical results of §3.1 is also proposed in §3.2.3.

Finally, a concluding remark for this chapter is provided in §3.3. More general conclusions will be drawn in §7.

3.1 The CPI framework for the Couette-Poiseuille flow family

In this section, a framework for the analysis of integral (global) energy budgets in Couette-Poiseuille flows (as described in §2.2.1) will be presented – the so called CPI framework, originally derived by Gatti et al. (2018) to evaluate the performance of flow control strategies in Poiseuille flows. The framework presented here is readily applicable to isolated Couette and Poiseuille flows. Apart from the flow case, the present formulation differs from the one of Gatti et al. (2018) in that a novel velocity scale is used for non-dimensionalisation; this choice of velocity scale allows to recover analyitical results that are generally valid for both Couette and Poiseuille flows (see §3.1.3). Moreover, the framework will be further extended to discriminate small- and large-scale fluctuations in §3.2.4.

In §2.2.5, it was shown that a Couette-Poiseuille flow receives power from two external agents: the pressure gradient and the external forces keeping the walls in motion. The sum of these two energy fluxes – the pumping power Π_p and power Π_w provided by the walls – represents the total power Π_t per unit wetted area that is provided to the flow:

$$\Pi_t = \Pi_p + \Pi_w \tag{3.1}$$

The pumping and the wall power Π_p and Π_w ensue from the antisymmetric and symmetric wall shear stresses τ_a and τ_s (defined in the equations below) working for the bulk and wall velocities respectively (see, once again, equations 2.38 and 2.39 in §2.2.5):

$$\Pi_p = \underbrace{\frac{1}{2}\left(\tau_B - \tau_T\right)}_{\tau_a} U_b = \tau_a U_b \tag{3.2}$$

$$\Pi_w = \underbrace{\frac{1}{2}\left(\tau_T + \tau_B\right)}_{\tau_s} U_w = \tau_s U_w \tag{3.3}$$

The derivation of the CPI framework requires the definition of a suited set of units that allows for a meaningful non-dimensionalisation. The choice of length scale naturally falls on the channel half-height h; as for the velocity scale, the present discussion will rely on the so-defined "power velocity U_π:

$$U_\pi = \left(\frac{\Pi_t}{\rho}\right)^{1/3} \tag{3.4}$$

which in its definition resembles the friction velocity, except that the total power input per unit wetted area Π_t is used instead of the wall shear. This naturally leads to the definition of a power-based Reynolds number $Re_\pi = hU_\pi/\nu$. The definition (3.4) of the power velocity is more general than the one $U_{\pi,Pois}$ given in previous works (Hasegawa et al., 2014; Gatti et al., 2018) and valid for Poiseuille flows only; the following relation holds:

$$U_\pi = \left(3\frac{\nu}{h}\right)^{1/3} \left(U_{\pi,Pois}\right)^{2/3} . \tag{3.5}$$

Under the general definition (3.4), any two Couette–Poiseuille flows with the same values of Re_π are driven by the same power input. The definition is also independent from the reference frame, and immediately applies to unusual flow configurations such as Poiseuille flows with no flow rate (Tuckerman et al., 2014) or experimental results for Couette and Couette–Poiseuille flows (Kawata and Alfredsson, 2019; Klotz et al., 2021).

Thanks to the definitions (3.2), (3.3) and (3.4), the equation defining the total power (3.1) can be recast in terms of Reynolds numbers:

$$Re_\pi^3 = (h_s^+)^2 Re_w + (h_a^+)^2 Re_b \,, \tag{3.6}$$

where h_s^+ and h_a^+ are the friction Reynolds numbers defined with the friction velocities descending from the values of the symmetric and anti-symmetric wall shear stresses:

$$h_s^+ = \frac{h}{\nu}\sqrt{\frac{\tau_s}{\rho}}; \qquad h_a^+ = \frac{h}{\nu}\sqrt{\frac{\tau_a}{\rho}} \tag{3.7}$$

Instead, $Re_b = hU_b/\nu$ and $Re_w = hU_w/\nu$ are Reynolds numbers where the velocity scale is given by the flow rates" [MY21]; the expression Re_q will be generically used to indicate either of Re_b or Re_w. Bear in mind that, as explained in §2.2.1, the wall velocity U_w of a Couette flow is analogous to the bulk velocity (which in turn is closely linked to the flow rate) of a Poiseuille flow.

In addition to the power Reynolds number, a second parameter is needed to fully characterise the Couette–Poiseuille flow decribed in §2.2.1. "The two usually employed parameters (Telbany and Reynolds, 1980, 1981; Nakabayashi et al., 2004) are the friction Reynolds number h_B^+ of the bottom wall and the flow parameter θ:

$$h_B^+ = \frac{h\sqrt{\tau_B/\rho}}{\nu}, \qquad \theta = \frac{h}{\tau_B}\frac{d\tau}{dy} \tag{3.8}$$

where τ is the total shear stress. In the present, power-focused approach, we use instead Re_π and the pumping power share $a = \Pi_p/\Pi_t$. Hence, a pair (Re_π, a) or equivalently (h_b^+, θ) fully describes the state of a Couette–Poiseuille flow. Thanks to equations (3.1), (3.2), (3.3) and (3.6), the two parameter sets can be related as:

$$\begin{cases} Re_\pi = \left((1+\theta)(h_b^+)^2 Re_w - \theta (h_b^+)^2 Re_b \right)^{1/3} \\ a = \left(1 - \frac{1+\theta}{\theta}\frac{Re_w}{Re_b} \right)^{-1} \end{cases} \tag{3.9}$$

where Re_w and Re_b implicitly depend on h_b^+ and θ (an explicit relation cannot be obtained due to the closure problem of turbulence)." [MY21]

3.1.1 The extended Reynolds decomposition; integral energy budgets

"The next step of the analysis consists in extending the classic Reynolds decomposition, as in Gatti et al. (2018). After splitting the velocity field into a mean component $U(y)$ and a fluctuating part, the former is further decomposed as the sum of a Stokes (laminar) and a deviation part:

$$U(y) = U^L(y) + U^\Delta(y) \tag{3.10}$$

where U^L is the Stokes solution of the problem under consideration that achieves the same flow rate as the turbulent one." [MY21]. An expression for U^L is given by the solution of the laminar Couette-Poiseuille problem (notice that in this case the Stokes solution and the laminar one are coincident):

$$U^L(y) = U_w \left(\frac{y}{h} - 1 \right) + \frac{3}{2} U_b \left(\frac{2y}{h} - \frac{y^2}{h^2} \right). \tag{3.11}$$

It can be trivially shown that the above expression satisfies:

$$\int_0^{2h} U^L \,\mathrm{d}y = \int_0^{2h} U \,\mathrm{d}y = 2hU_b \tag{3.12}$$

It follows that "the deviation profile U^Δ is zero at the wall and has zero integral; in other words, it does not contribute to either U_b or U_w. For a generic parallel flow with constant cross-section, U^L is the solution that minimizes the power required to generate a given flow rate (Bewley, 2009; Fukagata et al., 2009)." [MY21]

It will be now shown that, using the extended Reynolds decomposition, the terms of the volume-averaged budgets of mean and turbulent kinetic energy (MKE and TKE) are also split in a laminar and deviation part. The two budgets were presented in §2.2.5 and read:

$$\text{MKE:} \qquad \Pi_t - \Xi - \mathcal{P} = 0 \tag{3.13}$$

$$\text{TKE:} \qquad \mathcal{P} - \epsilon = 0 \tag{3.14}$$

They can be interpreted as follows. Of the total power Π_t provided to the mean flow, one part is directly dissipated as mean dissipation Ξ, whereas the remaining part is passed to turbulence by the turbulence production term $\mathcal{P}$. The entirety of the power that is fed to turbulence is then lost to the turbulent dissipation ϵ.

From now on, energy fluxes will be expressed in power units. Quantities made non-dimensional with power units (h, U_π) will be indicated by a π superscript, $(...)^\pi$. Notice that expressing any energy flux in power units is equivalent to expressing it as a fraction of the total power input Π_t: as an example,

$$\Xi^\pi = \frac{\Xi}{\rho U_\pi^3} = \frac{\Xi}{\Pi_t}. \tag{3.15}$$

Using this non-dimensionalisation and by substituting equation 3.10 into the definitions of Ξ and $\mathcal{P}$ (see equations 2.41 and 2.35, §2.2.5), the two energy fluxes can be decomposed into the sum of a laminar (Ξ^L, $\mathcal{P}^L$) and a deviation part (Ξ^Δ, $\mathcal{P}^\Delta$):

$$\Xi^\pi = \frac{1}{2}\int_0^2 \frac{1}{Re_\pi}\left(\frac{dU^\pi}{dy^\pi}\right)^2 \mathrm{d}y^\pi = \underbrace{\frac{1}{2}\int_0^2 \frac{1}{Re_\pi}\left(\frac{dU^{L,\pi}}{dy^\pi}\right)^2 \mathrm{d}y^\pi}_{\Xi^{L,\pi}} + \underbrace{\frac{1}{2}\int_0^2 \frac{1}{Re_\pi}\left(\frac{dU^{\Delta,\pi}}{dy^\pi}\right)^2 \mathrm{d}y^\pi}_{\Xi^{\Delta,\pi}} \tag{3.16}$$

$$\mathcal{P}^\pi = \frac{1}{2}\int_0^2 -\langle u'v'\rangle^\pi \frac{dU^\pi}{dy^\pi}\mathrm{d}y^\pi = \underbrace{\frac{1}{2}\int_0^2 -\langle u'v'\rangle^\pi \frac{dU^{L,\pi}}{dy^\pi}\mathrm{d}y^\pi}_{\mathcal{P}^{L,\pi}} + \underbrace{\frac{1}{2}\int_0^2 -\langle u'v'\rangle^\pi \frac{dU^{\Delta,\pi}}{dy^\pi}\mathrm{d}y^\pi}_{\mathcal{P}^{\Delta,\pi}} \tag{3.17}$$

Notice that, in principle, a cross-term should appear in equation 3.16; such cross term can be easily shown to be zero by substituting the expression 3.11 for the laminar velocity U^L and by then integrating by parts. "Moreover, it can be proven that[1]:

$$\mathcal{P}^\Delta = -\Xi^\Delta < 0 \tag{3.18}$$

Hence the positive production term $\mathcal{P}^L$ transfers energy from the mean to the fluctuation field, whereas the deviation production $\mathcal{P}^\Delta$ acts in the opposite direction to be a sink for TKE. Eventually, thanks to the extended decomposition, equations (3.13) and (3.14) can be rewritten as:

$$\text{MKE:} \qquad 1 - \Xi^{L,\pi} - \mathcal{P}^{L,\pi} = 0 \tag{3.19}$$

$$\text{TKE:} \qquad \mathcal{P}^{L,\pi} - \Xi^{\Delta,\pi} - \epsilon^\pi = 0 \tag{3.20}$$

where the total power input term Π_t becomes unity as a result of the power-based scaling." [MY21] The budgets can now be interpreted as follows. The mean flow receives a power input Π_t, which either gets dissipated as laminar dissipation Ξ^L or passed to turbulence by the laminar production $\mathcal{P}^L$. Owing to its definition (eq. 3.16), the laminar dissipation Ξ^L is the dissipation that would be felt by the laminar

---

[1] Proof is non-trivial; it can be found in the appendix of the Master's thesis of the author, `https://hdl.handle.net/10589/153027`

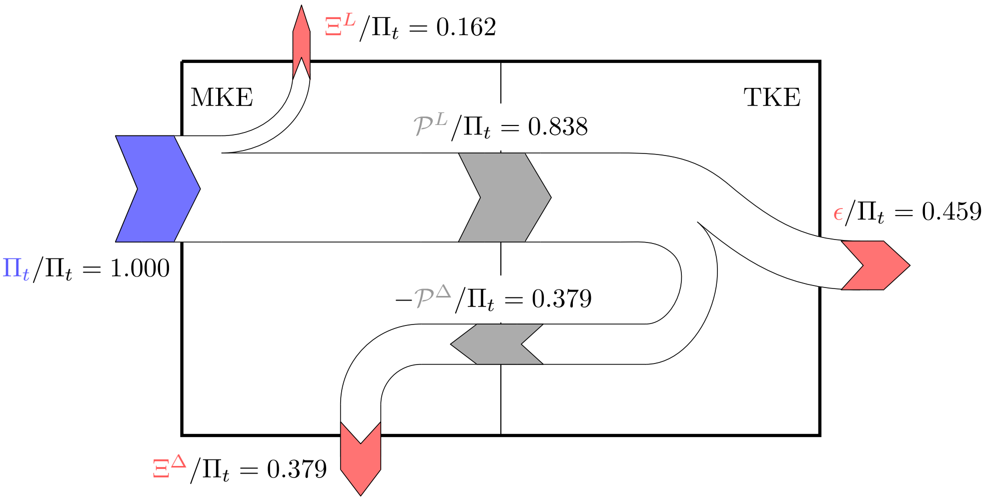

Figure 3.1: Extended energy box for a Couette flow at $Re_\tau = 102$, with numerical values of the integral terms expressed as a fraction of the total power input Π_t (equivalent to power units). Adapted from [MY21].

solution U^L; bear in mind that U^L is the flow solution that requires the least power to produce the observed flow rate (Bewley, 2009; Fukagata et al., 2009). Then, "the dissipated fraction $\Xi^{L,\pi} = \Xi^L/\Pi_t$ is the smallest amount of power required to achieve the given flow rate for the flow under consideration (Gatti et al., 2018). The remaining dissipation is caused by the presence of turbulence, and exits the system either as turbulent (ϵ) or deviational (Ξ^Δ) dissipation; the two contributions sum up to $\mathcal{P}^L$. The whole process is conveniently represented by the energy box (Quadrio, 2011; Ricco et al., 2012), drawn in figure 3.1 for a Couette flow at $Re_\tau = 102$ (one of the cases discussed below). The various components of the balance are a function of the flow type and Reynolds number." [MY21]

3.1.2 Analytical expressions for the energy fluxes

"Most of the quantities defined above can be expressed analytically in terms of the Reynolds number Re_π, the pumping power share $a = \Pi_p/\Pi_t$, and the following two weighted integrals of the Reynolds shear stress $-\langle u'v' \rangle$:

$$\alpha_p^\pi = \frac{1}{2}\int_0^2 -\langle u'v' \rangle^\pi \,(1-y^\pi)\,dy^\pi, \qquad \alpha_c^\pi = \frac{1}{2}\int_0^2 -\langle u'v' \rangle^\pi \; dy^\pi. \tag{3.21}$$

Due to the anti-symmetric weight, α_p is only determined by the anti-symmetric part of the Reynolds stress, and is therefore zero for Couette flows; conversely, α_c depends on the symmetric part alone, and is zero for Poiseuille ones. The weight functions are the wall-normal derivatives of the laminar profile $U^L(y)$, normalized by their wall value." [MY21]

Each of these integrals, then, either relates to the Couette- or to the Poiseuille-part of the flow; they indeed have separate effects on various quantities of interest. For instance, an expression for the flow rates can be found, "with U_w and U_b associating to α_c and α_p respectively:

$$U_w^\pi = \frac{Re_\pi \alpha_c^\pi}{2}\left(\sqrt{1+\frac{4(1-a)}{Re_\pi(\alpha_c^\pi)^2}}-1\right), \qquad U_b^\pi = \frac{Re_\pi \alpha_p^\pi}{2}\left(\sqrt{1+\frac{4a}{3Re_\pi(\alpha_p^\pi)^2}}-1\right). \tag{3.22}$$

These expressions are the CPI equivalent of the FIK identity originally derived by Fukagata et al. (2002).” [MY21] Proofs for the above formulae can be found in the appendix of the author’s Master’s thesis[2]. Additionally, “an expression for $\mathcal{P}^L$ can be found:

$$\mathcal{P}^{L,\pi} = \frac{Re_\pi(\alpha_c^\pi)^2}{2}\left(\sqrt{1+\frac{4(1-a)}{Re_\pi(\alpha_c^\pi)^2}}-1\right)+\frac{3Re_\pi(\alpha_p^\pi)^2}{2}\left(\sqrt{1+\frac{4a}{3Re_\pi(\alpha_p^\pi)^2}}-1\right) \tag{3.23}$$

and, since from equation (3.19) $\Xi^{L,\pi} = 1-\mathcal{P}^{L,\pi}$, Ξ^L becomes analytically known too. Lastly, an expression for Ξ^Δ is needed; first, the following integral is defined:

$$\beta^\pi = \frac{1}{2}\int_0^2 \left(\langle u'v'\rangle^\pi\right)^2 dy^\pi . \tag{3.24}$$

Then, Ξ^Δ can be written as:

$$\Xi^{\Delta,\pi} = Re_\pi\left(\beta^\pi-(\alpha_c^\pi)^2-3(\alpha_p^\pi)^2\right). \tag{3.25}$$

The Cauchy–Schwarz inequality proves that this quantity is always non-negative.” [MY21]

3.1.3 Simple Couette and Poiseuille flows

“Expressions for simple Couette and Poiseuille flows are obtained by setting $a=0$ or $a=1$ respectively. Simple Couette flows have an antisymmetric mean velocity profile, hence shear and Reynolds stresses are symmetric; additionally, $\alpha_p=0$ and $U_b=0$. Conversely, simple Poiseuille flows have a symmetric mean velocity profile, hence shear and Reynold stresses are antisymmetric with $\alpha_c=0$ and $U_w=0$. For both, equation (3.6) can be simplified to:

$$Re_\pi^3 = Re_\tau^2 Re_q \tag{3.26}$$

where Re_q is the flow-rate-based Reynolds number, i.e. $Re_q = Re_w$ for Couette flows and $Re_q = Re_b$ for Poiseuille ones.

Equation (3.23) can be further simplified into an expression for $\mathcal{P}^L$ (or Ξ^L) that is valid for both simple Couette and Poiseuille flows. To this purpose, a new Reynolds number is introduced, based on a new velocity scale U_α. The latter is given by the ratio between the weighted integral α of the Reynolds shear stress and the flow rate U_q:

$$U_\alpha = \frac{\alpha}{U_\mathrm{q}}, \qquad \alpha = \frac{1}{2h}\int_0^{2h} -\langle u'v'\rangle\,\psi(y)\,dy, \tag{3.27}$$

where $\psi(y) = \left(\mathrm{d}U^L/\mathrm{d}y\right)/\left(\mathrm{d}U^L/\mathrm{d}y\right)_{y=0}$ is the same non-dimensional weight of equation (3.21), such that $\alpha=\alpha_c$ for Couette flows, or $\alpha=\alpha_p$ for Poiseuille ones. The new Reynolds number $Re_\alpha = hU_\alpha/\nu$ is consequently defined; Re_α already appears in the FIK identity for Couette flows (Kawata and Alfredsson, 2019), which can be cast as

$$Re_\alpha = \frac{Re_\tau^2}{Re_w} - 1, \tag{3.28}$$

---

[2] `https://hdl.handle.net/10589/153027`

and the one for U_b^+ of Poiseuille flows (Marusic et al., 2007),

$$Re_\alpha = \frac{Re_\tau^2}{3Re_b} - 1. \tag{3.29}$$

Eventually, the aforementioned fluxes $\mathcal{P}^L$ and Ξ^L can be written as functions of Re_α:

$$\mathcal{P}^{L,\pi} = \frac{1}{1 + 1/Re_\alpha}, \qquad \Xi^{L,\pi} = \frac{1}{1 + Re_\alpha}. \tag{3.30}$$

As discussed in §3.1.1, the non-dimensional laminar production $\mathcal{P}^{L,\pi}$ expresses the fraction of external power wasted because of turbulence, and is of particular interest as it quantifies the overhead in producing flow rate from a given power. Moreover, due to the used non-dimensionalisation, the dissipation $\Xi^{L,\pi}$ of the laminar component is the ratio between the power Π_L required by the Stokes solution and the total power input Π_t,

$$\Xi^{L,\pi} = \frac{\Pi_L}{\Pi_t}, \tag{3.31}$$

with Π_L being the theoretical minimum power needed to achieve a given flow rate. Therefore, $\Xi^{L,\pi}$ represents an efficiency: the closer $\Xi^{L,\pi}$ to one, the closer the flow to the ideal situation where the whole power is spent to produce flow rate. Summing up, the whole MKE box is determined by the value of Re_α; it remains to be determined when a given Re_α is obtained, and what happens to the TKE box. This requires additional information from DNS datasets because of the unknown distribution $-\langle u'v' \rangle$, and will be addressed below." [MY21]

3.2 Numerical results

"The discussion that follows is based on a set of DNS simulations of turbulent Poiseuille and Couette flows. The dataset includes simulations carried out for the present work as well as published data from Lee and Moser (2015); Orlandi et al. (2015); Gatti and Quadrio (2016); Gatti et al. (2018); Lee and Moser (2018)." [MY21] New simulations are produced using the algorithm described in §2.4.4 applied to the channel geometry of §2.2.1. Practically, simulations are "carried out with the code described in Luchini and Quadrio (2006), includes two Couette flows with $Re_\tau \simeq 100$ and 500, as well as Poiseuille flows at $Re_\tau = 100$, 150, 316 and 500, selected to provide additional data points when needed; details of the various cases and their spatial discretization are reported in table 3.1. As for the Couette simulations, a streamwise domain length long enough to accommodate large-scale motions in the core of the channel has been used; following Orlandi et al. (2015), a value of $12\pi h$ is chosen here for the low Reynolds number simulation, while $16\pi h$ is used for the higher Reynolds number. These domain lengths have limited effects on one-point statistics (Lee and Moser, 2018), mainly affecting two-point statistics and the spatial orientation of structures (Komminaho et al., 1996), neither of which is of primary interest in this study." [MY21]

3.2.1 Comparison at constant Re_τ

"First, the relationship among the various Reynolds numbers is discussed, and figure 3.2 plots their variation with Re_τ. Panel (a) shows that Re_q varies with Re_τ quite similarly in the two flows; the similarity is even more striking when the variation of Re_π is considered, as shown in panel (b). In both cases, available data shows the expected nearly linear increase. For example, Abe and Antonia (2016)

	Dataset	Flow	$L_x/(\pi h)$	$L_z/(\pi h)$	Δx^+	Δz^+	Δy_w^+	Δy_c^+	Re_τ	Re_π	Re_q	Re_α
▲	Orlandi et al. (2015)	C	18	8	7.6	4.8	0.03	N.A.	171	445	3000	8.556
▲	Orlandi et al. (2015)	C	18	8	7.2	5.1	0.04	N.A.	260	688	4800	12.728
▲	Orlandi et al. (2015)	C	18	8	7.0	5.0	0.06	N.A.	508	1373	10134	24.296
▲	Orlandi et al. (2015)	C	18	8	6.8	4.8	0.08	N.A.	986	2744	21334	44.281
⬟	Lee and Moser (2018)	C	100	5	9.5	5.1	0.03	2.4	93	235	1500	4.623
⬟	Lee and Moser (2018)	C	100	5	11.2	4.5	0.03	3.7	219	578	3995	10.864
⬟	Lee and Moser (2018)	C	100	5	10.3	5.1	0.04	6.3	501	1360	9995	23.817
|	Gatti et al. (2018)	P	4	2	9.8	4.9	0.47	2.6	200	502	3177	3.190
●	Gatti and Quadrio (2016)	P	4	2	12.3	6.1	0.97	7.1	1001	2715	19993	15.573
◆	Lee and Moser (2015)	P	8	3	4.5	3.1	0.07	3.4	182	456	2829	2.872
◆	Lee and Moser (2015)	P	8	3	8.9	5.0	0.02	4.5	544	1435	9952	8.823
◆	Lee and Moser (2015)	P	8	3	10.9	4.6	0.02	6.2	1000	2715	19930	15.681
◆	Lee and Moser (2015)	P	8	3	12.2	6.1	N.A.	N.A.	1995	5572	43378	29.543
◆	Lee and Moser (2015)	P	8	3	12.7	6.4	0.50	10.3	5186	14980	124863	70.357

	Flow	$L_x/(\pi)$	$L_z/(\pi)$	Δx^+	Δz^+	Δy_w^+	Δy_c^+	$\Delta t_{out}\, u_\tau/h$	N_s	Re_τ	Re_π	Re_q	Re_α
∗	C	12	4	10.0	5.0	0.49	2.6	0.305	408	102	258	1667	5.215
∗	C	16	8	12.5	6.2	0.99	7.2	0.5	223	507	1376	10133	24.40
⅄	P	4	2	9.8	4.9	0.48	2.6	1.00	600	100	245	1467	1.270
⅄	P	4	2	7.4	3.7	0.72	3.9	1.81	71	150	373	2296	2.259
⅄	P	4	2	10.4	5.3	0.50	2.7	0.76	152	316	812	5370	5.191
⅄	P	4	2	12.3	6.1	0.97	7.1	1.00	186	500	1314	9085	8.177

Table 3.1: DNS datasets for Poiseuille (P) and Couette (C) flows, including published (top) as well as new (bottom) simulations. L_x and L_z are the domain lengths in the streamwise and spanwise directions, with the corresponding Δx^+ and Δz^+ resolutions in wall units. Δy_w^+ is the wall-normal resolution at the wall in viscous units, and Δy_c^+ represents the same quantity at the centerline. Finally, Δt_{out} and N_s are the sampling time and the number of samples used for averaging. Additionally, the table introduces the color scheme and symbols used later. Adapted from [MY21].

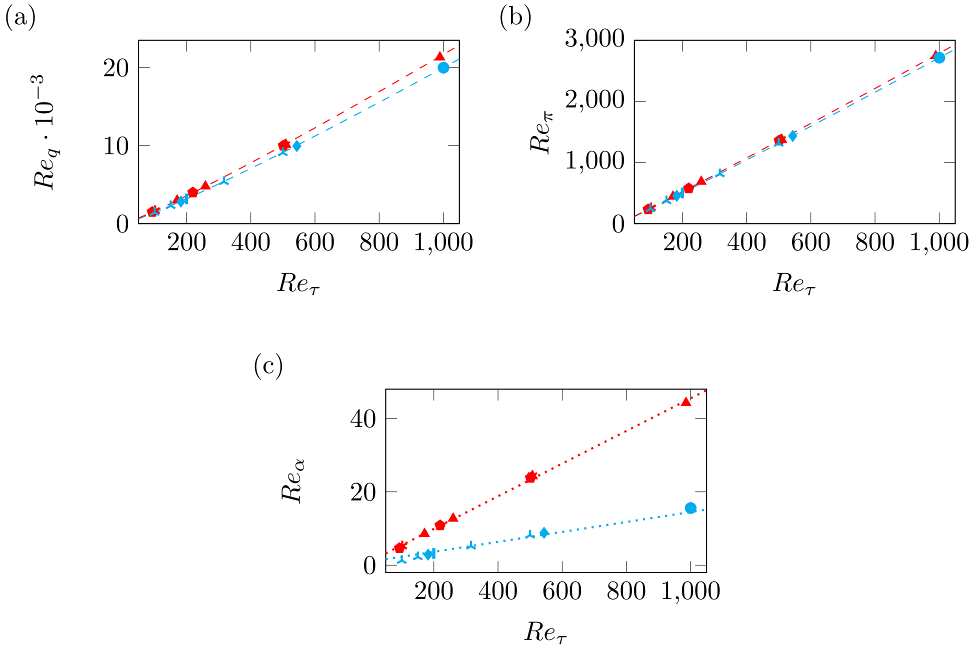

Figure 3.2: Dependence of the Reynolds numbers (a) Re_q, (b) Re_π and (c) Re_α on the friction Reynolds number Re_τ, for Couette (red) and Poiseuille (blue) flows. The dashed lines in the panels above indicate analytical fits, whereas the dotted lines in (c) are an empirical linear fit. For colors and symbols, refer to table 3.1. Adapted from [MY21].

linked Re_τ and Re_b for Poiseuille flows by assuming that deviations from the logarithmic law in the mean velocity profile near the mid-plane of the channel are negligible; the same approximation was found to be valid for Couette flows as well (Orlandi et al., 2015). The underlying functional form fitted to the present data yields:

$$\frac{Re_b}{Re_\tau} = 2.85 + 2.48\ln(Re_\tau) \tag{3.32}$$

$$\frac{Re_w}{Re_\tau} = 5.17 + 2.39\ln(Re_\tau) \tag{3.33}$$

and the use of (3.26) leads to analogous expressions for Re_π vs Re_τ. In both cases, the approximations are satisfactory. The most interesting result, however, is contained in panel (c) of figure 3.2, where the change of Re_α with Re_τ is shown. Considerable quantitative differences are seen between Couette and Poiseuille flows: the slope of a linear fit to Couette data is approximately three times larger than the same slope for Poiseuille flows.

Comparing Couette and Poiseuille flows at the same Re_τ is the most natural choice, as discussed at the beginning of this chapter. This comparison yields quite a similar flow rate, and does not immediately reveal why a Couette flow possesses an increased level of turbulent activity with respect to a Poiseuille one at the same Re_τ. However, under such condition, Re_α differs considerably between the two flows, suggesting a new and potentially informative comparison.” [MY21]

3.2.2 Comparison at constant Re_π

“Before addressing the comparison at the same Re_α, which will provide a better indication of turbulent activity, we compare Couette and Poiseuille flows at constant power input. The relationship between Re_π and Re_τ has been already shown in figure 3.2(b) to be nearly linear for the available data, and

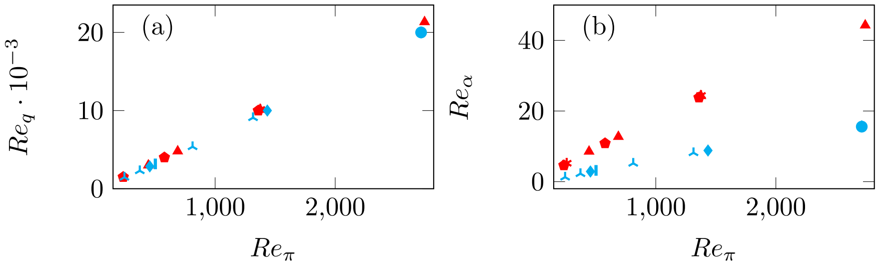

Figure 3.3: Reynolds numbers (a) Re_q and (b) Re_α against Re_π. For colors and symbols, refer to table 3.1. Adapted from [MY21].

to not depend on the flow type. Re_q and Re_α are plotted against Re_π in figure 3.3(a,b), respectively. The former panel allows to asses the effectiveness $Re_q(Re_\pi)$ of the flow, i.e. the amount of flow rate Re_q produced out of a given power input Re_π. Data for Poiseuille and Couette flows almost collapse, meaning that they are similarly effective. The marginal difference between the two flows indicates that Couette flows are slightly more effective than Poiseuille ones on the whole range of available data. This was already pointed out by Orlandi et al. (2015), and seems to be at odds with many evidences in literature of a higher turbulent activity in Couette flows, e.g. from the same authors. Such higher turbulent activity is here confirmed in panel (b): when the two flows are compared under the same power input, Couette flows achieve a much higher Re_α than Poiseuille ones. In view of the discussion in §3.1.3, this implies that Couette flows exhibit a larger turbulent overhead $\mathcal{P}^L$, hence a lower efficiency Ξ^L. Figure 3.4 better shows how efficiency Ξ^L and its complement overhead (or inefficiency) $\mathcal{P}^L$ change with Re_π; it is clearly seen that the turbulent overhead is larger in Couette flows than in Poiseuille ones for a given power input.

Provided that a Couette flow is more turbulent than a Poiseuille one at CPI and that turbulence has an adverse effect, the reason for the better effectiveness (meaning, the ability to produce a larger flow rate out of a given power input) of the Couette case has to be sought in its Stokes solution. The lower efficiency Ξ^L means that the Stokes component U^L of a generic Couette flow is fed with a smaller fraction of the total power input; still, this U^L requires less power than its Poiseuille counterpart to achieve a given flow rate, hence compensating for the lower power supply. In other words, the concept of efficiency – after equation (3.31) – addresses performance with respect to the ideal case of the flow under consideration, while effectiveness $Re_q(Re_\pi)$ does that in absolute terms.

Another significant difference between the two flows is the presence of energetic, large-scale structures in Couette flows (Lee and Moser, 2018; Pirozzoli et al., 2014; Kitoh and Umeki, 2008). These essentially realize an inertial mechanism (Papavassiliou and Hanratty, 1997) that transfers momentum from one wall to the other – or, in other words, produce flow rate. While they surely do not provide a better performance with respect to the optimal case of a Stokes solution, their comparison with smaller-scale turbulence is not trivial. Large-scale rolls in Couette flows can either be suppressed or energised by a Coriolis force; in the first case, drag reduction is observed at constant flow rate (Komminaho et al., 1996), in the latter a drag increase is obtained instead (Kawata and Alfredsson, 2016b; Bech and Andersson, 1996), suggesting that large-scale structures have a negative impact on effectiveness. Additionally, de Giovanetti et al. (2016) reported a degrading effect of large-scale structures on flow performance – albeit in Poiseuille flows." [MY21] The above considerations suggest that the presence of strong large scales in Couette flows does not help explain why they are more effective than Poiseuille ones.

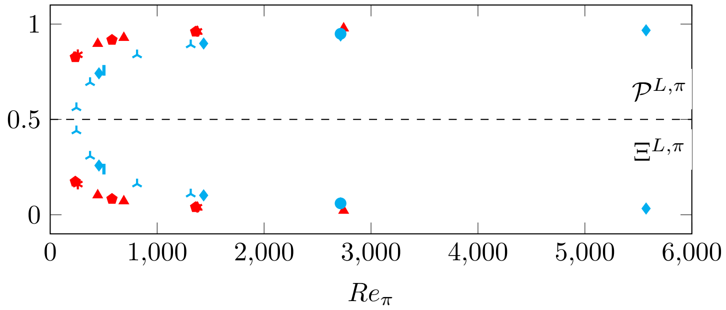

Figure 3.4: Plot of $\mathcal{P}^L$ and $\Xi^L = 1 - \mathcal{P}^L$ against Re_π. For colors and symbols, refer to table 3.1. Adapted from [MY21].

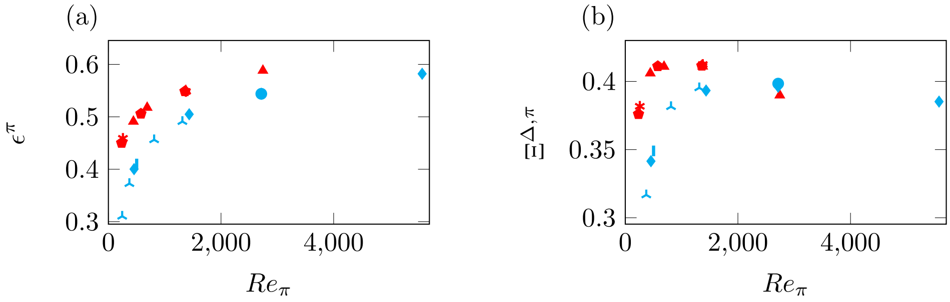

Figure 3.5: Turbulent dissipation ϵ (a) and deviation dissipation Ξ^Δ (b) versus Re_π. For colors and symbols, refer to table 3.1. Adapted from [MY21].

"The remaining flux terms of the TKE energy box are plotted in figure 3.5. Here the data points follow qualitatively similar curves for the two flows, but with significant quantitative differences. The TKE dissipation ϵ is found to monotonically increase in both flows, in agreement for example with Abe and Antonia (2016), even though Couette flows yield significantly larger values than Poiseuille ones. As for the deviation dissipation Ξ^Δ, Gatti et al. (2018) observed an increasing trend for Poiseuille flows until a maximum at intermediate Re_π is reached; then, the curve decreases monotonically to asymptotically approach zero. The same trend is here confirmed for Couette flows, except that the maximum is reached much earlier than in Poiseuille ones, supporting once more the notion that the former develop faster with Re. Moreover, the available Couette data points are consistently above those for Poiseuille flows, except the one at the highest Re; a trend reversal is thus possible at high Reynolds number, even though additional high-Re Couette data would be needed to establish it properly." [MY21]

3.2.3 Comparison at constant Re_α

"Additional considerations can be made when the two flows are compared at the same value of Re_α. It has already been shown how this is equivalent to enforcing an identical MKE box (see §3.1.3), and that Re_α significantly differs for the two flows at the same Re_τ or Re_π.

Figure 3.6 plots the turbulent dissipation ϵ against Re_α. A single point on this plot, i.e. a pair of (Re_α, ϵ) values, is sufficient to determine the whole energy box. Indeed, the value of Re_α sets both $\mathcal{P}^L$ and Ξ^L, while the value of ϵ provides the missing information to recover deviation dissipation from equation (3.20) as well as deviation production, since $\Xi^\Delta = -\mathcal{P}^\Delta$.

The two curves for Poiseuille and Couette flows in figure 3.6 are very similar, not only qualitatively but also quantitatively. This is quite remarkable, since in principle nothing prescribes such different flows with different mechanisms of power input and at different Re_τ and Re_π to redistribute the same power

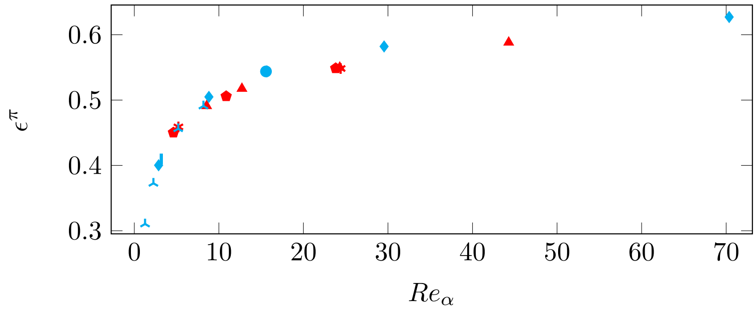

Figure 3.6: Turbulent dissipation ϵ against Re_α. For colors and symbols, refer to table 3.1. Adapted from [MY21].

fraction $\mathcal{P}^L$ identically between ϵ and Ξ^Δ. A striking difference with respect to figure 3.5(a) is that, here, Couette flows show a lower turbulent dissipation than Poiseuille ones, albeit marginally. Moreover, the present data indicates a tendency for this difference to increase with Re. In other words, when the same fraction of power $\mathcal{P}^L$ is transferred to the field of turbulent fluctuations, a Couette flow dissipates less of it as turbulent dissipation (and consequently more of it as Ξ^Δ), in a manner that becomes more evident for increasing Re. This trend occurs despite both flows achieve $\epsilon \to 1$ (thus $\Xi^\Delta \to 0$) in the limit $Re_\alpha \to \infty$, which is then approached at a faster rate in Poiseuille flows. This can be readily shown through equation (3.25) under the asymptotic-Re assumption that $-\langle u'v' \rangle$ equals the total shear stress $\tau_w \psi(y)$." [MY21]

3.2.4 Discriminating large- and small-scale dissipation

"The above observation can be explained by the role of the large-scale structures in the two flows; as already stated, such structures are more intense in Couette than in Poiseuille flows, at least for the relatively wide range of Reynolds numbers observed in literature. The lower turbulent dissipation in Couette flows might thus be attributed to the reduced ability of these large-scale motions to transform $\mathcal{P}^L$ into ϵ. Moreover, the implied larger Ξ^Δ is a sign of the large-scale motions being more efficient at producing Reynolds shear stresses, consistently with observations by Lee and Moser (2018). Since the shear stress is directly related to the mean flow by the mean momentum equation, large scales affect the mean flow more than small ones.

To confirm this hypothesis, a decomposition of the fluctuating velocity field into large- and small-scale components is carried out. The procedure closely follows the one devised by Kawata and Alfredsson (2018). A large-scale field $\vec{u}_\ell$ is defined via a sharp Fourier filter in the homogeneous directions, and the small-scale field is consequently defined as $\vec{u}_s = \vec{u}' - \vec{u}_\ell$. Budget equations were derived by Kawata and Alfredsson (2018) for the kinetic energy of these two fields. These equations resemble the one for the kinetic energy of the whole fluctuation field, and feature equivalent terms, plus a key additional transport term that describes the energy transfer between the large and small scales. The cross-scale transport term is conventionally defined to be positive when the large-scale field is receiving power. The equation for the large-scale kinetic energy becomes:

$$\left(\frac{\partial}{\partial t} + U\frac{\partial}{\partial x}\right)\frac{\langle u_{\ell,i}\, u_{\ell,i}\rangle}{2} = \underbrace{-\langle u_\ell v_\ell\rangle \frac{dU}{dy}}_{\text{production}} + \underbrace{-\frac{1}{2}\frac{d}{dy}\langle v' u_{\ell,i}\, u_{\ell,i}\rangle}_{\text{turb. transport}} + \underbrace{-\left\langle u_{\ell,i} u'_k \frac{\partial u_{s,i}}{\partial x_k}\right\rangle}_{\text{cross-scale transport}} + \underbrace{-\frac{1}{\rho}\frac{d}{dy}\langle P' v_\ell\rangle}_{\text{press. transport}} \\ + \underbrace{\nu \frac{d^2}{dy^2}\frac{\langle u_{\ell,i}\, u_{\ell,i}\rangle}{2}}_{\text{viscous diffusion}} \underbrace{- \nu \left\langle \frac{\partial u_{\ell,i}}{\partial x_k}\frac{\partial u_{\ell,i}}{\partial x_k}\right\rangle}_{\text{turb. dissipation}} \qquad (3.34)$$

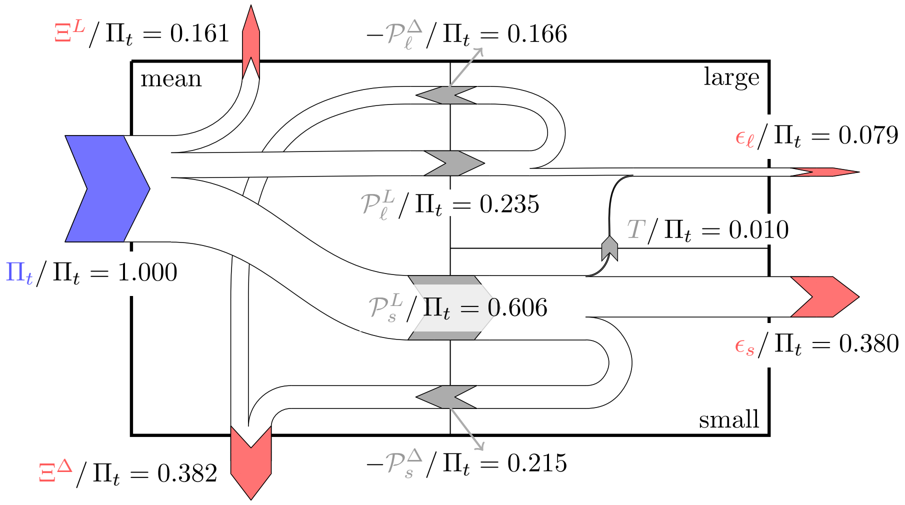

Figure 3.7: Extended energy box for a Couette flow at $Re_\tau = 102$, with the TKE box split into large- and small-scale contributions. Adapted from [MY21].

and substituting $\vec{u}_\ell$ with $\vec{u}_s$ provides the analogous equation for the small-scale field. The crucial cross-scale term describes the energy exchange between small and large scales, and represents a non-local process in the physical space, so that the exchange only balances after integration on the whole domain" [MY21] similarly to the turbulent production term of equation (2.34):

$$\int_0^{2h} \underbrace{-\left\langle u_{\ell,i} u'_k \frac{\partial u_{s,i}}{\partial x_k} \right\rangle}_{\text{cross-scale, large}} + \underbrace{-\left\langle u_{s,i} u'_k \frac{\partial u_{\ell,i}}{\partial x_k} \right\rangle}_{\text{cross-scale, small}} dy = 0 \tag{3.35}$$

"Volume-integration of the budget equation (3.34) and its small-scale equivalent yields the energy fluxes $\mathcal{P}^L$, $\mathcal{P}^\Delta$ and ϵ separated into their small- and large-scale components, which will be indicated by subscripts $\cdot_s$ and $\cdot_\ell$ respectively, plus the interscale transfer T.

We compute the decomposed energy budget for two Couette flows at $Re_\tau \simeq 100$ and 500. As in Kawata and Alfredsson (2018), no filtering is carried out in the streamwise direction, owing to the very elongated nature of the large-scale structures. For spanwise filtering, the selection of the wavelength λ_z to discriminate the large-scale motion is guided by the rather flat peak of the energy spectrum observed in Lee and Moser (2018) in the range $3 < \lambda_z < 6.5$. Detailed scrutiny of the same spectrum for the present datasets has determined the range of interest to be $\lambda_z \geq \pi$, which is used as a criterion to discriminate the large scales from the small ones.

The decomposed energy budget is given in figure 3.7 for the Couette flow at $Re_\tau \simeq 100$, where the TKE box is separated into two sub-boxes pertaining to the small and large scales. It is confirmed that the large scales are less efficient than the small ones at producing ϵ, with $\epsilon^\pi_\ell = 0.079$ versus $\epsilon^\pi_s = 0.380$. Not only do small scales produce more turbulent dissipation, but they also convert a larger fraction of the received energy into it, as $\epsilon_\ell / \mathcal{P}^L_\ell = 0.336$ while $\epsilon_s / \mathcal{P}^L_s = 0.627$. Obviously, their impact on the deviational dissipation is opposite, with $|\mathcal{P}^\Delta_\ell| / \mathcal{P}^L_\ell = 0.706$ and $|\mathcal{P}^\Delta_s| / \mathcal{P}^L_s = 0.355$. The same picture is observed in figure 3.8 for a Couette flow at $Re_\tau \simeq 500$, with even more pronounced features because of the higher Re and the increased separation between large and small scales. The large-scale contribution to turbulent dissipation becomes much smaller than the small-scale one ($\epsilon^\pi_\ell = 0.034$ against $\epsilon^\pi_s = 0.515$); moreover, the large scales account for the most of the deviation dissipation with $|\mathcal{P}^\Delta_\ell| / \Xi^\Delta = 0.8398$.

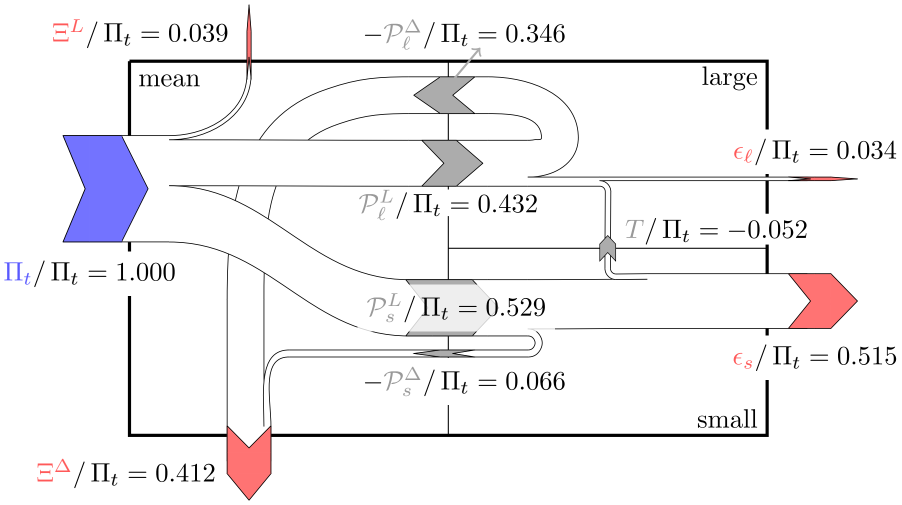

Figure 3.8: Extended energy box for a Couette flow at $Re_\tau = 507$, with the TKE box split into large- and small-scale contributions. Adapted from [MY21].

In other words, turbulent dissipation is clearly dominated by small-scale effects, whereas deviation dissipation is mainly caused by large-scale ones." [MY21]

"In both cases, the interscale net energy flux is rather small: $T^\pi = 0.01$ for $Re_\tau \simeq 100$ and $T^\pi = -0.052$ for $Re_\tau \simeq 500$. However small, the net integral effect at the lower Reynolds number is to transfer energy from the small to the large scales. The same result was obtained by Papavassiliou and Hanratty (1997) by treating large-scale structures as secondary motions; this differs however from the more recent observation put forward by Kawata and Alfredsson (2018), where an inverse interscale transport was only found for the Reynolds shear stress $-\langle u'v' \rangle$. At higher Reynolds number the direction of the transfer is reversed, and power goes from large to small scales. This inversion can be explained by figure 3.9, that plots the y-profile of the cross-scale transport term of the large scales, i.e.

$$-\left\langle u_{\ell,i} u'_k \frac{\partial u_{s,i}}{\partial x_k} \right\rangle .$$

A positive peak is present in the near-wall region, where the large scales are receiving power;" [MY21] further away from the wall, the term turns negative, indicating that large scales are losing power to small scales. Judging on the present data, the position of the zero-crossing of the above term appears to scale in inner units. The present observations are in good agreement with the findings of Cho et al. (2018) and Kawata and Tsukahara (2021), who detected an inverse energy cascade from large energy-containing motions to even larger ones in the proximity of the wall. The positive, buffer-layer peak "covers a large portion of the domain at low Reynolds number – meaning that the integral flux T is dominated by near-wall effects, and ends up being positive at $Re_\tau \simeq 100$. Conversely, at higher Re_τ the integral is dominated by the core region of the flow, where the large scales lose energy, thus explaining the negative value of T at $Re_\tau \simeq 500$." [MY21] Notice that the data shown in figure 3.9 is pre-multiplied, so that the area seen under the plotted curves is representative of the integral amount of power being exchanged in spite of the logarithmic axis.

3.3 Summary and conclusions

"Turbulent plane Poiseuille and Couette flows have been compared in terms of their integral energy fluxes, thanks to the analysis of a database of direct numerical simulations. The work is based on the

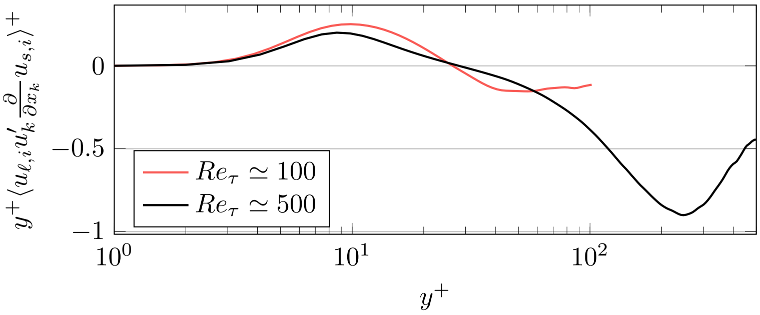

Figure 3.9: Profiles of the premultiplied cross-scale transport term for the large-scale fluctuation field $\vec{u}_\ell$ in Couette flows, plotted in viscous units. Red: $Re_\tau = 102$; black: $Re_\tau = 507$. Adapted from [MY21].

framework introduced by Gatti et al. (2018) to compare two Poiseuille flows with and without flow control under the same power input (i.e. at Constant Power Input, or CPI). The CPI approach is extended here to the case of a generic plane parallel flow driven by both shear and a pressure gradient. A power-based velocity scale U_π and a corresponding Reynolds number Re_π are defined and used for non-dimensionalisation, so that two flows with the same power input possess the same U_π and the same Re_π. After a standard Reynolds decomposition, the mean flow is further split into a laminar (Stokes) and a mean deviation contribution. This procedure also decouples all the volume-integrated energy fluxes into a laminar and a deviational part. The extended decomposition, together with normalization by the total power input, enables expressing all the energy fluxes as functions of the sole variables Re_π and two wall-normal integrals of the Reynolds shear stress.

Comparing Couette and Poiseuille flows at the same Re_π ascertains that Couette ones produce a slightly larger flow rate, i.e. Couette flows are more effective at converting a given input power into flow rate. However, the efficiency of the process is a completely different concept. Among the volume-integrated fluxes, the flux $\mathcal{P}^{L,\pi}$ (laminar production of turbulent kinetic energy, expressed in power units) indicates the total fraction of power that is wasted as an overhead expense owing to the presence of turbulence, or the flow (in)efficiency. The flux $\Xi^{L,\pi} = 1 - \mathcal{P}^{L,\pi}$ is the laminar dissipation, i.e. the dissipation of the laminar flow, and similarly expresses the efficiency of the flow, being the ratio between the theoretical minimum power necessary to realize a given flow rate and the actual power used to drive the turbulent flow. For a comparison under the CPI condition, Couette flows produce a larger $\mathcal{P}^{L,\pi}$ (see figure 3.4) and a lower efficiency $\Xi^{L,\pi} = 1 - \mathcal{P}^{L,\pi}$. The two observations that Couette flows are at the same time more effective (i.e. produce a larger flow rate for a given power) and less efficient (i.e. waste a larger power share to turbulence) are only apparently contradictory: the laminar Couette solution requires less power than its Poiseuille counterpart to produce the same flow rate, hence compensating for the higher turbulent activity of the former. The Stokes solution is therefore quite relevant in determining the absolute performance of a turbulent flow at producing flow rate. Also, the efficiency $\Xi^{L,\pi}$ should not be used to compare effectiveness at producing flow rate across different flows, but only to indicate how the flow compares to the ideal situation.

In the case of simple Couette and Poiseuille flows, both fluxes $\Xi^{L,\pi}$ and $\mathcal{P}^{L,\pi}$ have been written as functions of a sole variable: the Reynolds number Re_α, which is embedded in the FIK identity. Its velocity scale is the ratio between a weighted integral of the shear stress and the flow rate. Surprisingly, these two functions of Re_α turn out to be identical for Couette and Poiseuille flows. However, the same value of Re_α is achieved by Couette flows at a lower value of Re_τ, explaining and – more importantly – quantifying how turbulence in Couette flows develops faster with the Reynolds number.

Couette and Poiseuille flows can also be compared at the same value of Re_α, which corresponds to a situation where the fluctuating field is fed with the same fraction $\mathcal{P}^{L,\pi}$ of the total power. In this case, Couette flows are found to achieve a smaller turbulent dissipation ϵ^π, even though for both flows ϵ^π tends to unity at infinite Reynolds number. Indeed, Couette flows feature stronger large-scale structures, which are efficient at modifying the mean flow, but carry a lower contribution to turbulent dissipation compared to smaller scales. To verify this, an inter-scale analysis of the energy fluxes has been performed on two Couette flows at $Re_\tau \simeq 100$ and 500. The TKE integral budget is further divided in small- and large-scale contributions, with an additional transport term that quantifies the cross-talk between scales, as shown in figure 3.7 and 3.8. By setting the scale separation threshold in such a way that the large rolls are included into the large-scale part, it is found that the large scales produce only a minor fraction of the total ϵ (approximately $10-20\%$ of it); moreover, they convert to turbulent dissipation only a small fraction (approximately $10-30\%$) of the power $\mathcal{P}_\ell^L$ they are fed with. This behaviour is opposite to the one of the small-scales, and becomes more pronounced as the Reynolds number increases. At low Reynolds numbers, the interscale transport term is found to move energy from the small to the large scales; the opposite happens at higher Reynolds number. Such an inverse interscale transport was indeed already observed by Kawata and Alfredsson (2018) but limited to the shear stress, whereas other studies (Kawata and Tsukahara, 2021; Cho et al., 2018) have already reported a reversed energy cascade in proximity of the wall. Our data suggest that this near-wall, inverse-cascade region scales in viscous units; hence it contributes more to the cross-talk at lower Reynolds numbers, and becomes less important as Reynolds increases.

The framework proposed here for the analysis of global energy budgets in turbulent flows, by also accounting for the presence of large-scale structures, has been demonstrated for the Couette–Poiseuille family of flows, but its usability is larger. It can be applied to unconventional cases such as Poiseuille flows with zero flow rate (Tuckerman et al., 2014) or Couette flows in a rotating reference frame (Kawata and Alfredsson, 2019; Bech and Andersson, 1996). Every term of the energy box except ϵ (and T in the scale-decomposed version) can be obtained from the profile of the Reynolds shear stress, hence the framework suits experimental studies as well. Flow control schemes can also be assessed, as done in Gatti et al. (2018), providing useful insights on the role played by large-scale motions in the context of drag reduction. Roccon et al. (2021) have recently and successfully applied it to two-phases flows with complex physics. Flows featuring large or secondary motions, such as open channel flows (Zampiron et al., 2021), are of interest as well; the same applies to to straight duct flows with arbitrary geometry. Finally, as pointed out by Frohnapfel et al. (2012), generalisation to external flows such as spatially developing boundary layers is also possible.” [MY21]

4 Suppressing large scales in turbulent Couette flows

The results shown in this chapter have been published in Andreolli et al. [MY24a].
Data for this chapter is available at `https://dx.doi.org/10.35097/EhgiloDgsqkMSqTn`.

4.1 Introduction

In this chapter, the intense large scales that are typical of Couette flows will be removed from the flow with the help of a weak Coriolis force. The aim is to verify whether the costs linked to the large scales (which have been identified in chapter 3) can be saved by removing them, or if, as an example, the removal of large scales leads to additional expenses owing to non-linear changes in the flow as highlighted by other authors using different techniques (Fukagata et al., 2010; de Giovanetti et al., 2016). The following scientific question will be addressed:

> **2. How much of the cost (power input or skin friction) caused by large scales can be saved by removing them?**

The next section (§4.1.1) contains a notice on the nomenclature used in this chapter. As previously mentioned, a weak Coriolis force is used here to suppress large scales in Couette flows; although such a usage has not been widely investigated in the literature, the effects of rotation (hence, of the Coriolis force) on turbulent flows have long been the object of research owing to their relevance in atmospheric flows. A brief review of the literature on such a topic is presented in §4.1.2; the structure of this chapter is then presented in §4.1.3.

4.1.1 A note on the nomenclature: LSMs, VLSMs, and ESMs

Although in the rest of this manuscript the wording *large scale* is generally used to indicate any turbulent eddy that scales in outer units, a more precise nomenclature is needed in this chapter. Indeed, as will be discussed in the next sections, the Coriolis force used here only suppresses a particular type of large scale: the extreme-scale rolling motion observed, for instance, by Lee and Moser (2018). In the following, this structure will be referred to as an *extreme scale motion* (ESM).

Such a choice of nomenclature was first introduced by Lee and Moser (2018) and is particularly fitting. Large scales are typically cathegorised in VLSMs and LSMs depending on their streamwise extent (see §1.2.2). If their streamwise extent does not exceed $3h$, they are classified as LSMs; otherwise, as VLSMs. According to this definition, ESMs could be labelled as VLSMs; however, the streamwise extent of an ESM (which can exceed $100h$, see Lee and Moser, 2018; Gandía-Barberá et al., 2018) is at least one order of magnitude larger than the one of a VLSM ($6 - 20\,h$, see Monty et al., 2009). Moreover, as will be seen in §4.3.1, structures that are reminiscent of VLSMs arise when ESMs are suppressed. Thus, a distinction between ESMs and VLSMs will be made.

4.1.2 Turbulent flows under the effects of rotation

"Wall-bounded turbulent flows are known to be sensitive to a weak spanwise rotation of the reference frame, which can either stabilise or destabilise the flow - meaning that the fluctuation intensities and turbulent production are either decreased or increased, as well as the wall-layer streak bursting rate (Johnston et al., 1972). The effect of the rotation is determined by the ratio $S(y) = -2\Omega/(\mathrm{d}U/\mathrm{d}y)$ between the angular velocity Ω of the reference frame and the spanwise flow vorticity $\langle \omega_z \rangle = -\mathrm{d}U/\mathrm{d}y$, where U is the mean streamwise velocity and y the wall-normal coordinate (Johnston et al., 1972). A cyclonic rotation of the reference frame - that is, one where Ω and $\langle \omega_z \rangle$ have the same sign, hence $S > 0$ - always locally stabilises the flow. An anticyclonic rotation (when Ω and $\langle \omega_z \rangle$ have opposite sign, $S < 0$) is instead locally destabilising as long as $|S| < 1$.

The (de-)stabilising action is mainly provided by the Coriolis force in a similar way to how a temperature (or density) gradient can stabilise or destabilise a buoyancy-driven flow (Lezius and Johnston, 1976; Tritton, 1992; Komminaho et al., 1996). The effects of the Coriolis force are most easily observed in a plane Couette flow, where the vorticity $\langle \omega_z \rangle$ has the same sign across the channel height, meaning that the Coriolis force has a stabilising or destabilising effect across the entire channel. By contrast, a plane Poiseuille (or, simply, channel) flow has different signs of the vorticity at the two walls, meaning that one side of the channel is stabilised by rotation, whereas the other is destabilised (Kristoffersen and Andersson, 1993). Rotating plane Couette flows have been studied (Bech and Andersson, 1996; Tillmark and Alfredsson, 1996; Kawata and Alfredsson, 2016a, 2019) in both stabilising and destabilising configurations; a comprehensive description of the flow regimes obtained with varying Reynolds number and angular velocity is provided by Tsukahara et al. (2010). The destabilised configuration has been more thoroughly investigated owing to the counter-rotating roll cells that can be observed in such conditions. Such roll cells closely resemble, but differ from (Tsukahara et al., 2010) the naturally occurring ESM that can be observed in Couette flows without rotation (Pirozzoli et al., 2014; Lee and Moser, 2018).

The less investigated stabilising regime of the Coriolis force is of interest for this manuscript: it has been shown both experimentally (Tsukahara et al., 2010) and numerically (Komminaho et al., 1996) that a weak stabilising Coriolis force can remove the ESM from the flow. The latter authors went on to compare a natural Couette flow with one where the ESM is suppressed; since the small-scales are minimally affected, they were able to estimate the contribution of the ESM to the turbulent kinetic energy. Yet, this was done at an almost transitional Reynolds number, and a parametric study on the intensity of the Coriolis force needed to yield a satisfactory suppression of the the ESM with minimal intrusiveness is missing." [MY24a]

4.1.3 Structure of the chapter

The numerical setup used for the present study is described in §4.2. As already stated, it involves the suppression of the ESM through the use of a weak stabilising Coriolis force. The suitability of the Coriolis force for such a usage has not been thoroughly investigated in the literature (see §4.1.2): for this reason, the intensity of the Coriolis force needed to yield a satisfactory suppression is discussed in §4.3.1, and the effects of the force on the remaining scales of motion (small scales, in particular) are investigated using velocity spectra.

The effects of the ESM-suppression on the skin friction are then discussed using the CPI framework, which was presented in chapter 3. First, it is shown that the energy fluxes calculated through the CPI framework are exactly equivalent to skin friction contributions if properly rescaled; moreover, it is argued that the CPI framework yields a better estimate of the share of skin friction associated to small and

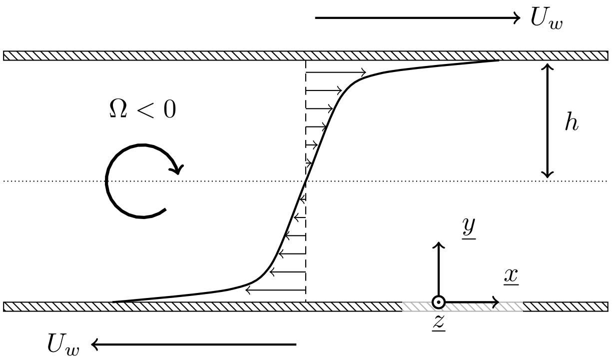

Figure 4.1: A schematic representation of a Couette flow subject to a spanwise, cyclonic rotation of the reference axis. Adapted from [MY24a].

large scales as compared to the FIK identity (§4.3.2). Then, the CPI framework is used to discuss how the costs associated to small and large scales change when the large ones are removed from the flow (§4.3.3).

Although it deviates from the main scientific objective, an additional aspect is investigated in this chapter: how the Coriolis force is able to suppress the ESM. A mostly analyitical discussion of the matter is presented in §4.4. Finally, §4.5 contains a concluding remark.

4.2 Numerical setup

Numerical simulations of turbulent plane Couette flows (see §2.2.1) are performed using the method described in §2.4.4. The flow geometry is reported in figure 4.1; notice that the unit vectors associated to the x, y and z axes will be indicated as $\underline{x}$, $\underline{y}$ and $\underline{z}$ respectively.

"The flow is subject to the Coriolis body force $\vec{f}_c$ that would be given by a rotation of the reference system about the spanwise axis:

$$\vec{f}_c = -2\rho\,\Omega\underline{z} \times \vec{u}, \tag{4.1}$$

where ρ is the uniform density of the fluid. The direction of rotation is cyclonic, meaning that the angular velocity Ω has the same sign of the mean vorticity $\langle\omega_z\rangle$ of the flow ($\Omega < 0$ as $\langle\omega_z\rangle < 0$). Notice that the Coriolis force is orthogonal to the velocity field $\vec{u}$ by definition; hence it cannot provide nor subtract energy to the flow." [MY24a]

Having taken the Coriolis force into account, the Navier-Stokes equations (see §2.1) are made non-dimensional with the channel half height h and the speed U_w of the walls, so that the corresponding Reynolds number is Re_w. Quantities made non-dimensional in this way are indicated by a $(\cdot)^o$ superscript. This results in:

$$\nabla^o \cdot \vec{u}^{\,o} = 0 \tag{4.2}$$

$$\frac{\partial \vec{u}^{\,o}}{\partial t^o} + \left(\vec{u}^{\,o} \cdot \nabla^o\right)\vec{u}^{\,o} + \nabla^o P^o = \frac{1}{Re_w}\left(\nabla^o\right)^2 \vec{u}^{\,o} - \underbrace{2\frac{\Omega h}{U_w}}_{Ro}\,\hat{z} \times \vec{u}^{\,o} \tag{4.3}$$

"In addition to the Reynolds number, a second dimensionless group appears in the equations, that is, the rotation number $Ro = 2\Omega h/U_w$ (Lezius and Johnston, 1976) governing the relative intensity of the Coriolis force." [MY24a]

Re_w	Ro	Re_τ	N_f	L_x/h	L_z/h	Δx^+	Δz^+	Δy_w^+	Δy_c^+
1667	0	101.7	408	$12\,\pi$	$4\,\pi$	10.0	5.0	0.5	2.6
1667	$-2\cdot 10^{-3}$	100.8	250	$12\,\pi$	$4\,\pi$	9.9	4.9	0.5	2.6
1667	$-5\cdot 10^{-3}$	99.5	250	$12\,\pi$	$4\,\pi$	9.8	4.9	0.5	2.6
1667	$-1\cdot 10^{-2}$	97.3	250	$12\,\pi$	$4\,\pi$	9.6	4.8	0.5	2.5
1667	$-2\cdot 10^{-2}$	92.5	250	$12\,\pi$	$4\,\pi$	9.1	4.5	0.4	2.4
1667	$-3\cdot 10^{-2}$	86.5	250	$12\,\pi$	$4\,\pi$	8.5	4.2	0.4	2.2
10133	0	507.1	223	$16\,\pi$	$8\,\pi$	12.5	6.2	1.0	7.2
10133	$-5\cdot 10^{-3}$	473.4	150	$16\,\pi$	$8\,\pi$	11.6	5.8	0.9	6.8
10133	$-1\cdot 10^{-2}$	457.8	150	$16\,\pi$	$8\,\pi$	11.2	5.6	0.9	6.5
10133	$-2\cdot 10^{-2}$	435.1	150	$16\,\pi$	$8\,\pi$	10.7	5.3	0.8	6.2

Table 4.1: Numerical details for the present numerical dataset. Here, N_f represents the number of snapshots acquired at a statistically steady state for the calculation of statistics; the spacing between snapshots is of roughly $1\,h/u_\tau$ (except for the simulations at $Ro = 0$, which are taken from chapter 3). Adapted from [MY24a].

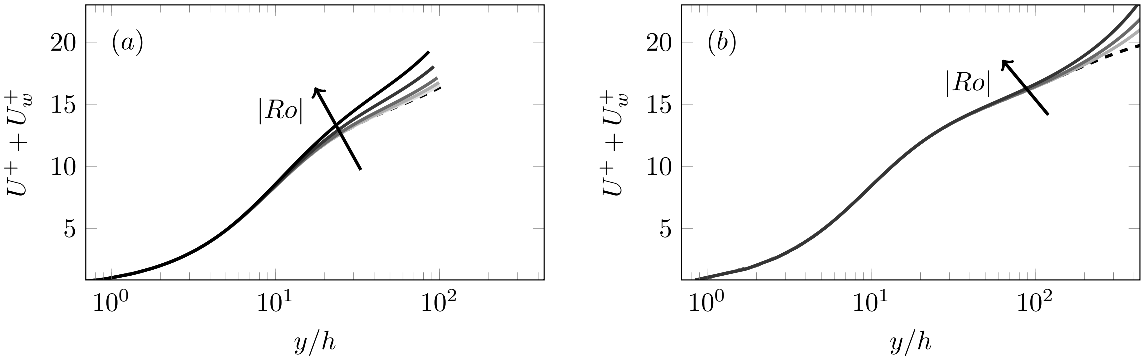

Figure 4.2: Inner-scaled mean velocity profile $U^+(y^+) + U_w^+$ for all available simulations (see table 4.1), adjusting for the velocity of the bottom wall. The dashed lines indicate $Ro = 0$; otherwise, darker shades of gray indicate a larger absolute value of Ro. (a) $Re_\tau \approx 100$; (b) $Re_\tau \approx 500$. Adapted from [MY24a].

The present dataset is produced by progressively increasing "the control intensity Ro as the Reynolds number Re_w is kept constant; this is equivalent to performing a parametric analysis at constant flow rate (CFR), since Re_w represents an analogue of the bulk Reynolds number in a Couette flow (see §2.2.1). This is done at a low and at a moderate Reynolds number, corresponding to a friction Reynolds number $Re_\tau = hu_\tau/\nu$ of roughly 100 and 500 respectively when no control is applied. Data for uncontrolled Couette flows are taken from the simulations of chapter 3. The same mesh is used for the controlled cases; this choice is suited as the suppression of the ESM and the consequent drag reduction relieve the constraints on both the box size and the resolution. A summary of the numerical details is provided in table 4.1." [MY24a]

4.3 Results

4.3.1 Mean velocity, spectra and ESM suppression

In this section, the ability of the Coriolis force to suppress the ESM is discussed. This is done by inspecting basic flow statistics and how they change with increasing rotation number. Effects on small scales are also highlighted.

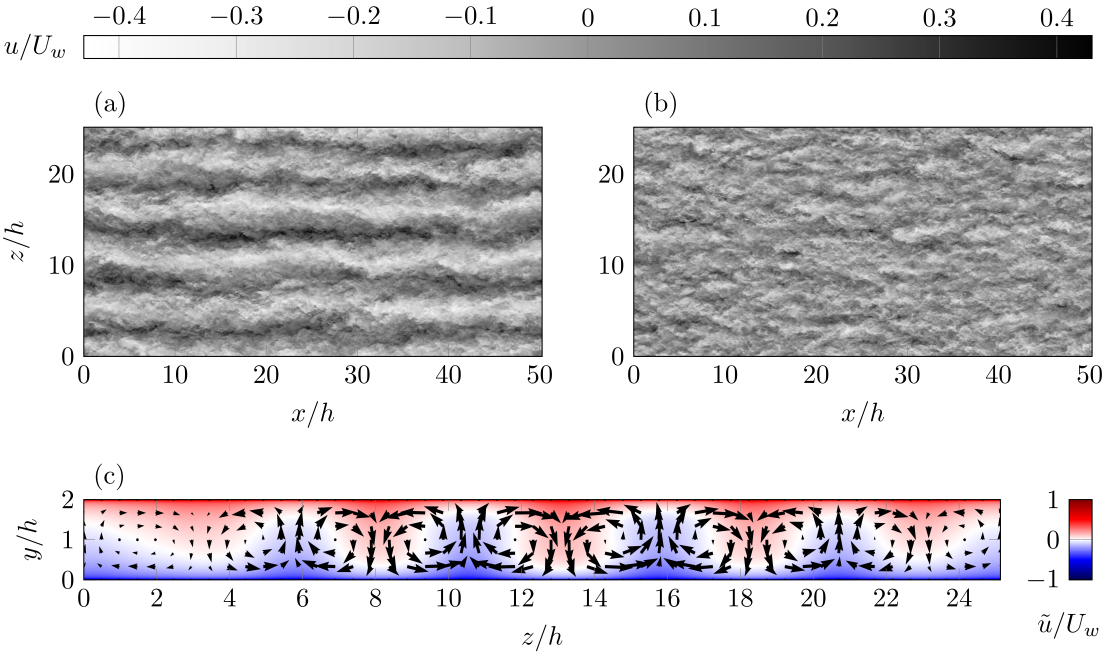

Figure 4.3: Instantaneous visualisations of the streamwise velocity u at the centerline ($y/h = 1$); $Re_\tau \approx 500$, $Ro = 0$ (a) and $Ro = -10^{-2}$ (b). Cross-sectional view of the streamwise- and time-averaged velocity field (c); $Re_\tau \approx 500$, $Ro = 0$. The color indicates the streamwise component $\tilde{u}$; the two remaining components are represented as vectors. Adapted from [MY24a].

To begin with, the way the Coriolis force affects the mean velocity profile is shown in figure 4.2 for all available simulations. "Notice that figure 4.2 compensates for the fact that both walls have a non-zero velocity in our numerical setup;" [MY24a] moreover, u_τ decreases for increasing value of Ro, and the value of u_τ is estimated by computing the derivative the U-profile at the wall. "The usual collapse of the inner-scaled velocity profile is seen in the near-wall region, indicating that the control force does not substantially alter the near-wall dynamics. Deviations of the mean velocity profiles from the uncontrolled case are seen only towards the centerline: there, larger absolute values of the rotation number Ro are associated to larger values of the inner-scaled centerline velocity. This could be a symptom of drag reduction; a thorough discussion of the matter will be given in §4.3.3.

The presence of the ESM in Couette flows is usually revealed by analyzing velocity spectra or visually inspecting flow snapshots (Lee and Moser, 2018). The ESM is indeed easily observable without further postprocessing of the acquired data, although a short-time average or a long-exposure picture may help (see, for instance, Tsukahara et al., 2010). We begin by comparing two flow snapshots at $Re_\tau \approx 500$: one from an uncontrolled simulation and one subject to the Coriolis force with a given value of the rotation number ($Ro = -10^{-2}$). This is done to show both the appearence of the ESM and the effects of the Coriolis force in physical space; a more thorough discussion of the ESM-suppression is presented later. Figure 4.3(a-b) shows the instantaneous distribution of streamwise velocity at the midplane for the two selected flow cases. In the uncontrolled one, streamwise-coherent regions of low and high momentum can be clearly distinguished; they repeat themselves quasi-periodically in the spanwise direction with a period of roughly $5h$. These high- and low-momentum streaks are the most easily indentifiable feature of the ESM (Pirozzoli et al., 2014; Lee and Moser, 2018); they disappear when the Coriolis force is applied, suggesting that the ESM is being suppresed. Following Lee and Moser (2018), an averaged visualisation of the ESM can be produced by exploiting its extended streamwise and time coherence. We average the velocity field of the uncontrolled simulation in the streamwise direction as well as in time (using

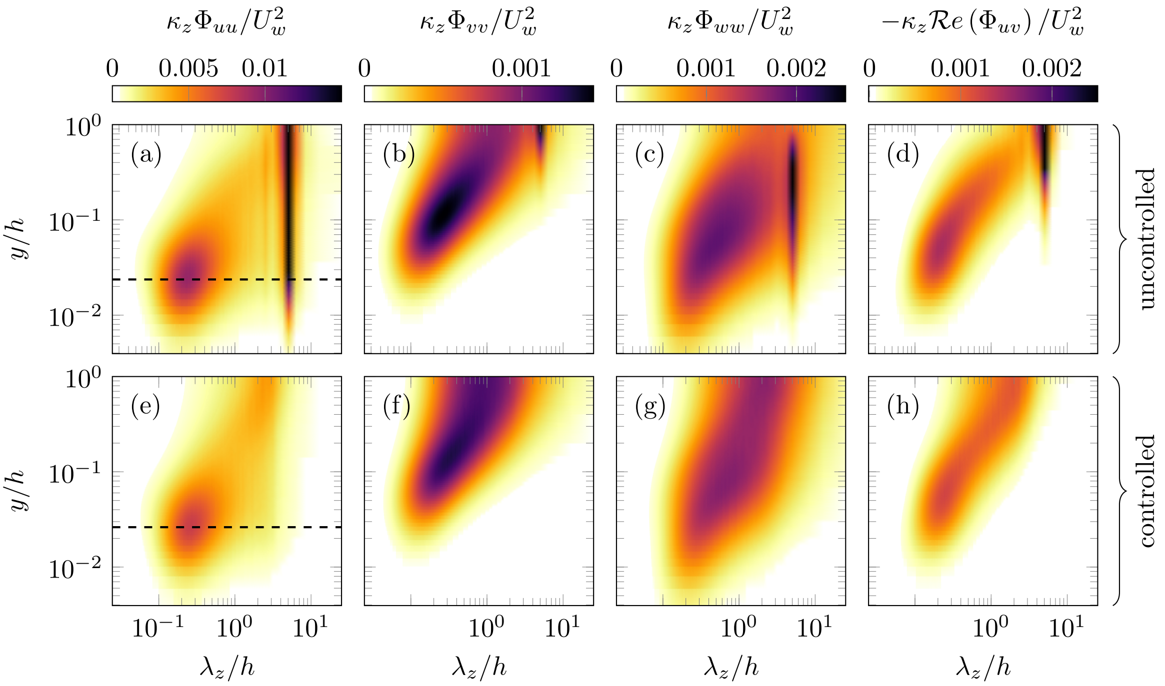

Figure 4.4: Premultiplied one-dimensional spanwise (co-)spectra $\kappa_z\Phi_{uu}$, $\kappa_z\Phi_{vv}$, $\kappa_z\Phi_{ww}$, $-\kappa_z\mathcal{R}e\left(\Phi_{uv}\right)$ ($\mathcal{R}e$ indicating the real part of a complex number) of the non-zero Reynolds stress tensor components; streamwise, wall-normal and spanwise normal stresses and shear stress respectively. (a-d) $Re_\tau \approx 500$, $Ro = 0$; (e-h) $Re_\tau \approx 500$, $Ro = -10^{-2}$. The dashed lines in panels (a), (e) indicate the inner-layer wall-normal position ($y^+ = 12$) at which the spectrum is re-analyzed in figure 4.7. Adapted from [MY24a].

all saved snapshots, which span a time window of $2220\,h/U_w$). The result is shown in figure 4.3(c), revealing the presence of quasi-periodically repeating pairs of counter-rotating vortices extending from one wall to the other. Neighbouring vortices induce regions of upwelling and downwelling motion where low- and high-momentum fluid is pulled away from the bottom and top walls respectively, so that the streaks seen in figure 4.3(a) are formed.

To better investigate the ESM-suppression, we analyse the spectra of both controlled and uncontrolled flows. Figure 4.4 shows the spanwise (co-)spectra for each of the nonzero Reynolds stresses for the uncontrolled and a selected controlled Couette flow at $Re_\tau \approx 500$. The remaining cases are not shown for conciseness and return the same qualitative picture described here. The uncontrolled case features a spectral peak around a spanwise wavelength of $\lambda_z/h = 5$ for each component of the Reynolds stress tensor. This is the spectral representation of the streaky structure seen in figure 4.3(a); it has also been observed, for instance, by Lee and Moser (2018). The main effect of the applied forcing is the disappearance of this spectral peak for all components of the Reynolds stress tensor; otherwise, all (co-)spectra maintain the qualitative structure of the uncontrolled case. The only other noticeable difference is a moderate increase in the fluctuation energy at the centerline; this is particularly relevant for the Reynolds shear stress, which receives at $y/h \approx 1$ an increased contribution from motions that are outer-scaled ($\lambda_z/h \approx 2$), yet smaller than the ESM.

This shows that the main effect of the application of a weak Coriolis force to a Couette flow is the suppression of the ESM, accompanied by a modest increase in the energy of large, non-ESM eddies; further effects on the remaining scales of motion will be discussed at the end of this section. One advantage of the Coriolis force approach with respect to modal damping or spanwise domain restriction (used, for instance, by de Giovanetti et al., 2016) is that the former does not suppress the large-scaled motions (possibly attached eddies) coexisting with the ESM at the same spanwise wavelengths. Indeed,

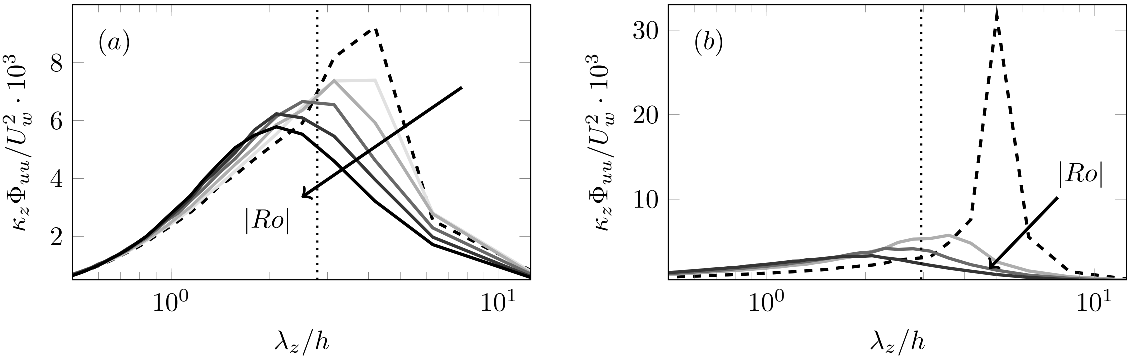

Figure 4.5: Premultiplied one-dimensional spanwise spectrum $\kappa_z \Phi_{uu}$ of the streamwise fluctuations for changing value of the control intensity $|Ro|$ at the midplane ($y/h = 1$); (a) $Re_\tau \approx 100$ and (b) $Re_\tau \approx 500$. The dashed lines indicate $Ro = 0$; as for the solid lines, darker shades indicate an increasing magnitude of Ro. Values of Ro as of table 4.1. The dotted lines indicate the critical value of the spanwise wavelength used to determine whether the ESM is fully suppressed. Adapted from [MY24a].

spectral energy content is still observable in the (co)-spectra at $\lambda_z/h = 5$ after the suppression of the ESM, ensuring smoothness of the spectra. This would not be the case if modal damping were used, as all energy at large wavelengths would be removed yielding a discontinuous spectrum; similarly, if one were to restrict the spanwise simulation domain, large wavelengths would be unrepresentable (see de Giovanetti et al., 2016).

The spectrum Φ_{uu} of streamwise fluctuations of figures 4.4(a,e) is re-analyzed in the outer layer (at $y/h = 1$, more precisely) for all available simulations in figure 4.5. The peak associated to the ESM is sharp, indicating that the ESM is rather monochrome - meaning that its spectral representation mainly involves one or two Fourier modes only. By comparing the spectra of uncontrolled simulations (dashed lines) at low and high Reynolds number (panels a and b respectively), the Reynolds number dependence of the patterns of high- and low-speed streaks composing the ESM can be appreciated. Even when scaling it in outer units, the energy associated to the pattern significantly increases with Reynolds number; moreover, its characteristic spanwise wavelength shifts from $\lambda_z/h \approx 3 - 4$ to a larger value of $\lambda_z/h \approx 5$, meaning that the pattern becomes larger in physical terms. This behavior is expected and can also be observed in the data of Lee and Moser (2018).

As for the dependence on the rotation number at constant flow rate, the sharp spectral peak associated to the ESM disappears already at the lowest value of Ro tested here - as far as the high-Re dataset is concerned (figure 4.5b). We interpret this as the ESM being suppressed. The ESM-peak is replaced by a weaker, smooth one, which shrinks in size and intensity as Ro further increases. At the lower Reynolds number (figure 4.5a), instead, the sharp energy peak progressively shrinks in size and intensity until it becomes smooth; determining the critical value of Ro for which the ESM is fully suppressed is thus an arbitrary process, as no clear saturation effect is seen. This arbitrarity constitutes the main drawback of using the Coriolis force instead of other ESM-suppressing strategies.

The critical value of Ro could be defined, for instance, as the one of minimum absolute value for which no sharp spectral peak is observed; the underlying argument would be that the ESM is associated to a sharp spectral peak, as discussed before, whereas the spectral contributions of non-ESM large scales are instead broadband. Alternatively, one can analyze the λ_z-position of the large-scaled outer-layer spectral peak seen in figure 4.5(a-b). The critical value of the rotation number could be defined as the one of minimum absolute value for which the outer-layer maximum of the power spectral density of u-fluctuations falls at a wavelength that is smaller than a given threshold. In §3.2.4, $\lambda_z/h \geq \pi$ was chosen as a suited criterion to discriminate the ESM from the remaining scales of motions; owing to the discrete

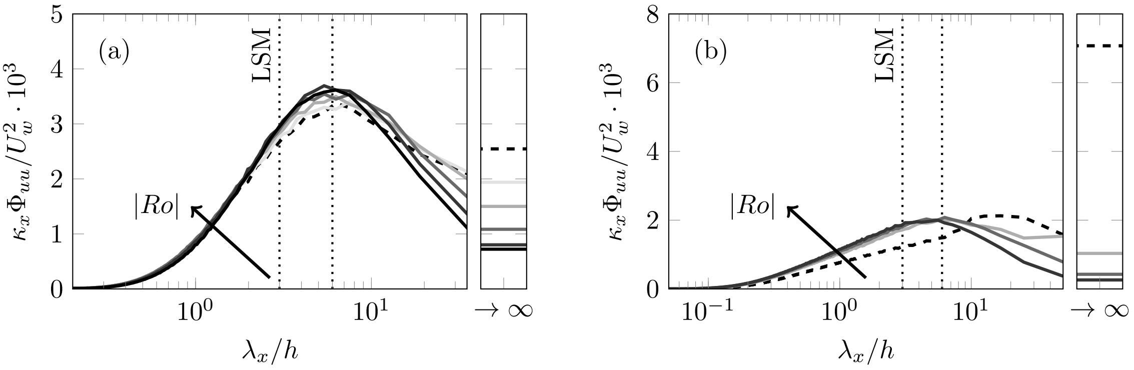

Figure 4.6: Premultiplied one-dimensional streamwise spectrum $\kappa_x \Phi_{uu}$ of the streamwise fluctuations for changing value of the control intensity $|Ro|$ at the midplane ($y/h = 1$). Line styles as of figure 4.5; (a) $Re_\tau \approx 100$, (b) $Re_\tau \approx 500$. To the right of each panel, the value of the spectrum at $\lambda_x \to \infty$ is shown; such a value is premultiplied with the Fourier resolution $\Delta\kappa_x$ of the simulations. Two vertical dotted lines indicate the expected streamwise periodicity of LSMs ($\lambda_x/h = 3$) and the approximate wavelength ($\lambda_x/h \approx 6$) at which a maximum of the spectrum is seen for most of the present simulations. Adapted from [MY24a].

mesh used, this can be rewritten as $\lambda_z/h > 0.889\pi$ and $\lambda_z/h > 0.941\pi$ for the simulations at the low and high Reynolds numbers respectively. These values are used in this manuscript as the threshold defining the ESM, and are shown in figure 4.5(a-b) as dotted lines.

These two methods both return the same value $Ro = -0.01$ for the low-Re dataset. As previously discussed, at high Reynolds number we consider the ESM to be suppressed already at the lowest tested value of the rotation number ($Ro = -0.005$), although analyzing the wavelength of maximum outer-layer spectral energy suggests a critical value of $Ro = -0.01$. The previous estimate based on visual inspection is deemed more credible, as the spectrum is substantially changed by increasing the magnitude of the rotation number from $Ro = 0$ to $Ro = -0.005$, whereas a further increase to $Ro = -0.01$ only leads to marginal changes. In other words, it seems that most of the ESM-suppression has already taken place at $Ro = -0.005$ at high Reynolds number.

It appears, then, that the critical value of Ro at which the ESM is fully suppressed decreases with Reynolds number. This is unsurprising. The rotation number is equal to (twice) the angular velocity Ω scaled in outer units, and it multiplies the flow velocity to yield the Coriolis acceleration. The magnitude of large-scale velocity fluctuations increases with Re even if scaling in outer units (see figures 4.5 a,b; notice the different scale for the y-axis). Hence, the magnitude of the Coriolis force acting on large scales will increase with Re even if one keeps the angular velocity constant in outer units (that is, $Ro = const.$). In other words, it is reasonable to expect the same value of Ro to produce larger effects at a larger Reynolds number, as is here observed. Nonetheless, the data produced for this study is rather limited for a discussion of Reynolds number effects; further investigation is needed.

So far, we have only scrutinised spanwise velocity spectra. While these clearly identify the ESM, they do not contain information about the streamwise extent of the turbulent structures. To recover this kind of information, figure 4.6 shows the premultiplied streamwise spectra of streamwise fluctuations for all available simulations. Data is shown at the centerline, where the Coriolis force has its strongest effects. Next to each panel, the value of the spectrum for $\lambda_x \to \infty$ (where λ_x is the streamwise wavelength) is shown; notice that the Fourier resolution $\Delta\kappa_x$ of the simulations is used for premultiplication in this case, as using the wavenumber $\kappa_x = 2\pi/\lambda_x = 0$ would hide the energy content of the spectrum. Such a value of the spectrum represents the energy contained in all streamwise-invariant Fourier modes or, in other words, the energy held by streamwise-invariant vortices. Although it is usually not shown, the energy of streamwise-invariant vortices is surprisingly high in the uncontrolled simulations of the

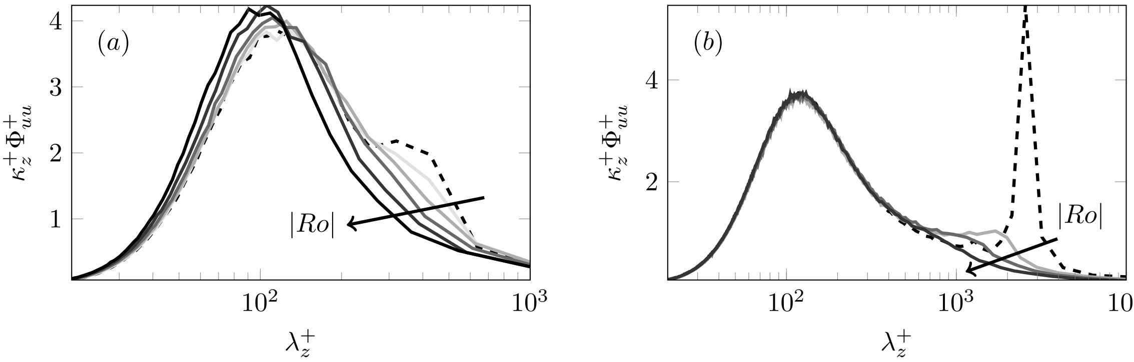

Figure 4.7: Inner-scaled premultiplied one-dimensional spanwise spectrum $\kappa_z \Phi_{uu}$ of the streamwise fluctuations for changing value of the control intensity $|Ro|$ at $y^+ = 12$; (a) $Re_\tau \approx 100$ and (b) $Re_\tau \approx 500$. Line styles as of figure 4.5. Adapted from [MY24a].

present dataset, both at the lower (a) and especially at the higher (b) Reynolds number. We interpret this observation as follows. Despite being sufficiently wide in the spanwise direction, the simulation box used for the present study is too short in the streamwise one to correctly capture the extent of the ESM: the latter is thus misrepresented as a streamwise-invariant vortex. In other words, most of the energy of the ESM is contained on streamwise-invariant Fourier modes. Unlike in spanwise spectra (figure 4.5), no particularly pronounced sharp spectral peak is observed for finite values of the streamwise wavelength λ_x in figure 4.6, which reinforces our interpretation. Similar conclusions were drawn by Lee and Moser (2018) upon inspecting streamwise spectra in a much longer domain at $Re_\tau \approx 500$; the authors also note that the streamwise coherence length of the ESM at $Re_\tau \approx 500$ exceeds $310h$. Correctly capturing the streamwise extent of such a long structure in a direct numerical simulation is prohibitively expensive.

What is also surprising about the streamwise spectra of figure 4.6 is the lack of an expected feature. Typically, a spectral peak associated to LSMs is observed at $\lambda_x/h = 3$; it is observed in channel, pipe and boundary layer flows (Monty et al., 2009). We do not observe it here in any of our simulations, including the uncontrolled ones. At the lower Reynolds number (figure 4.6a), a spectral peak is seen at around $\lambda_x/h \approx 6$ in the uncontrolled simulation; at the higher one (b), the peak is seen around $\lambda_x/h \approx 20$." [MY24a] The wavelengths of both the low- and high-Re peaks are comparable to the typical wavelengths of VLSMs in channel and pipe flows (Monty et al., 2009). The present data might then suggest that LSMs are either absent or too weak to be detected in Couette flows, whereas VLSMs can be observed. Nevertheless, care should be exerted in comparing the large-scale features of different shear flows (as pointed out by Monty et al., 2009, themselves): the taxonomy of large scales needs not be the same for different flows.

"As for the effects of the Coriolis force on streamwise spectra, larger absolute values of the rotation number $|Ro|$ are associated to a reduction of the energy of streamwise-invariant vortices. This reinforces the idea that most of the energy of the ESM is contained on streamwise-invariant Fourier modes, and that the ESM is getting suppressed. A reduction of spectral content is also seen for the largest wavelengths represented in our simulations ($\lambda_x \approx 50$). Instead, motions of wavelenght $\lambda_x/h \approx 6$ are energised by applying the Coriolis force both at the lower and higher Reynolds numbers. By combining this information with the one provided by spanwise spectra (see figures 4.4 and 4.5), we conclude that the control force considered here energises outer-scaled motions that are shorter and narrower than the suppressed ESM." [MY24a] Possibly, these energised large scales could be classified as VLSMs owing to their streamwise extent.

“While we observe that the main effect of a weak Coriolis force is to suppress the ESM and energise some other outer-scaled eddies, effects on small scales cannot be excluded a-priori. Indeed, it is known that a strong enough rotation can also suppress small-scale turbulence (Tsukahara et al., 2010). Kline et al. (1967) suggested that the rotation might prevent small-scale low-speed streaks from being lifted up from the wall, halting turbulence-producing events. Therefore, we discuss the effects of the Coriolis force on small scales by analyzing the spectrum Φ_{uu} of streamwise fluctuations in the near-wall region at $y^+ = 12$. This is done in figure 4.7, once again for all available simulations. The wall-normal position is chosen to match the one at which the maximum of the near-wall fluctuation energy is seen. The near-wall footprint of the ESM is clearly observable both at low (a) and high (b) Reynolds number in the uncontrolled setting (dashed line). As the control intensity increases, the footprint gradually vanishes as expected. As for the small-scale peak at $\lambda_z^+ \approx 100$, its inner-scaled intensity and the wavelength at which it occurs are unaltered by the Coriolis force at high Reynolds number, as seen in panel (b). This observation matches the expected universal scaling in viscous units of the small-scale peak (Marusic et al., 2010a), suggesting that the effect of a weak Coriolis force on the small scales is negligible. On the contrary, at the lower Reynolds number, the spectra of the controlled cases do not collapse on the one of the uncontrolled simulation, not even for small values of λ_z^+. A separate analysis, not shown for brevity, indicates that the streak spacing (as measured by the λ_z-position of the small-scale spectral maximum; this is conceptually similar to, but differs slightly from, using the minimum of the velocity autocorrelation for this estimate, as done in Kim et al., 1987) decreases, whereas the peak intensity is increased. At the critical value of Ro previously determined ($Ro = -0.01$), the maximum small-scale value of the Φ_{uu} spectrum is 8% larger than in the reference case, and the streak spacing is reduced by 3.5%.

Owing to the nonlinearity of turbulent phenomena, the observed increase in small-scale energy at low Re could be linked to distortions in nonlinear large-small interactions that arise as large scales are suppressed (de Giovanetti et al., 2016). High-Re data indicates instead that small-scales are only minimally affected by the Coriolis force for the weak rotations here investigated. We conjecture that this difference is due to scale separation: at the lower Reynolds number (figure 4.7 a), the small- and large-scale spectral peaks are much closer together than they are at high-Re (b).” [MY24a]

4.3.2 Contributions to the skin friction: CPI framework versus FIK identity

A framework for the analysis of integral energy budgets in turbulent Couette and Poiseuille flows (the CPI framework) was presented in chapter 3. The same framework will be used in this chapter to discuss how energy fluxes associated to small and large scales change as the ESM is being suppressed. As will be proven in the following lines, these energy fluxes are exactly equivalent to skin friciton contributions if properly rescaled. Hence the CPI framework can be used to directly calculate the skin-friction contributions of small and large scales, similarly to the FIK identity (Fukagata et al., 2002; de Giovanetti et al., 2016). The differences between such two methods are also discussed.

“According to the CPI framework, the input power (per unit wet area) Π_t provided to a turbulent plane Couette or Poiseuille of a given flow rate flow is either spent as laminar dissipation Ξ^L (corresponding to the theoretic minimum power per unit wet area needed to achieve such a flow rate) or as an overhead expense $\mathcal{P}^L$ caused by the presence of turbulence:

$$\Pi_t = \Xi^L + \mathcal{P}^L. \tag{4.4}$$

Keep in mind that the power input Π_t is the product of the wall shear stress and some characteristic velocity, that is $\Pi_t = \tau_w U_w$ in a Couette flow and $\Pi_t = \tau_w U_b$ in a Poiseuille one (see §2.2.5). The energy fluxes Ξ^L and $\mathcal{P}^L$ are defined as (see §3.1.1):

$$\Xi^L = \int_0^h \mu \left(\frac{\mathrm{d}U^L}{\mathrm{d}y} \right)^2 \mathrm{d}y, \tag{4.5}$$

$$\mathcal{P}^L = \int_0^h -\rho \left\langle u'v' \right\rangle \frac{\mathrm{d}U^L}{\mathrm{d}y} \mathrm{d}y, \tag{4.6}$$

If a Poiseuille flow is considered and equation 4.4 is made non-dimensional with $\frac{1}{2}\rho U_b^3$, the FIK identity (Fukagata et al., 2002) is obtained:

$$\begin{aligned} \frac{\tau_w U_b}{\rho U_b^3/2} = \frac{1}{\rho U_b^3/2} \int_0^h \mu \left(\frac{\mathrm{d}U^L}{\mathrm{d}y} \right)^2 \mathrm{d}y \, + \\ + \frac{1}{\rho U_b^3/2} \int_0^h -\rho \left\langle u'v' \right\rangle \frac{\mathrm{d}U^L}{\mathrm{d}y} \mathrm{d}y \end{aligned} \tag{4.7}$$

$$C_f = \frac{6}{\rho h U_b/\mu} + 6 \int_0^1 -\frac{\left\langle u'v' \right\rangle}{U_b^2} \left(1 - \frac{y}{h} \right) \mathrm{d} \left(\frac{y}{h} \right) \tag{4.8}$$

where $C_f = 2\tau_w/(\rho U_b^2)$. That is, equation 4.4 is exactly the same as the FIK identity, except for a factor; indeed, it represents an expression for the non-dimensional input power, whereas the FIK identity is an expression for the non-dimensional wall-shear stress. In particular, $\mathcal{P}^L$ is the direct analogous of the integral of the Reynolds shear stress appearing in the FIK identity (equation 4.8). The CPI framework differs from the FIK identity in that the turbulent overhead $\mathcal{P}^L$ is further decomposed into an expense ϵ (turbulent dissipation) directly caused by turbulent fluctuations and an expense Ξ^Δ (deviation dissipation) which is indirectly caused by turbulence by inducing distortions of the mean velocity profile (see §3.1.1),

$$\mathcal{P}^L = \Xi^\Delta + \epsilon. \tag{4.9}$$

As discussed in §1.2.3, the FIK identity has been used to estimate the share of skin friction for which the large scales are responsible. Usually (de Giovanetti et al., 2016; Agostini and Leschziner, 2018), the Reynolds shear stress $\left\langle u'v' \right\rangle$ is split into its small-scale and large-scale contributions, $\left\langle u'v' \right\rangle = \left\langle u'v' \right\rangle_s + \left\langle u'v' \right\rangle_\ell$. This enables then to calculate the contribution of small and large scales to C_f through the integral term in equation 4.8. Owing to the previous discussion, this procedure is exactly equivalent to calculating a small- and large-scale contribution to the turbulent overhead $\mathcal{P}^L$ ($\mathcal{P}_s^L$ and $\mathcal{P}_\ell^L$ respectively) as done in chapter 3.2.4. However, $\mathcal{P}_s^L$ and $\mathcal{P}_\ell^L$ do not exactly correspond to the energy losses caused by small and large fluctuations. In the following, this statement will be motivated with the help of the energy box introduced by Quadrio (2011) and later reworwked by Gatti et al. (2018) and in chapter 3 to distinguish small and large fluctuations.

The energy box graphically represents how the input power Π_t is redistributed among the mean flow, small-scale fluctuations and large-scale ones. As an example, figure 4.8 shows the energy box for two flows considered in this chapter, with and without Coriolis force. Notice that the Coriolis force does not exchange work with the flow (see §4.2), so that no power input associated to the control force needs to be added to the energy box. Although it is already clear from figure 4.8 that the Coriolis force disproportionately affects energy fluxes to and from large scales, a thorough discussion of its effect is given later in §4.3.3. The power input Π_t is supplied to the mean flow by some external agent; part of it is directly dissipated by the mean flow as Ξ^L, whereas the remaining part is passed to the small- and large-scale

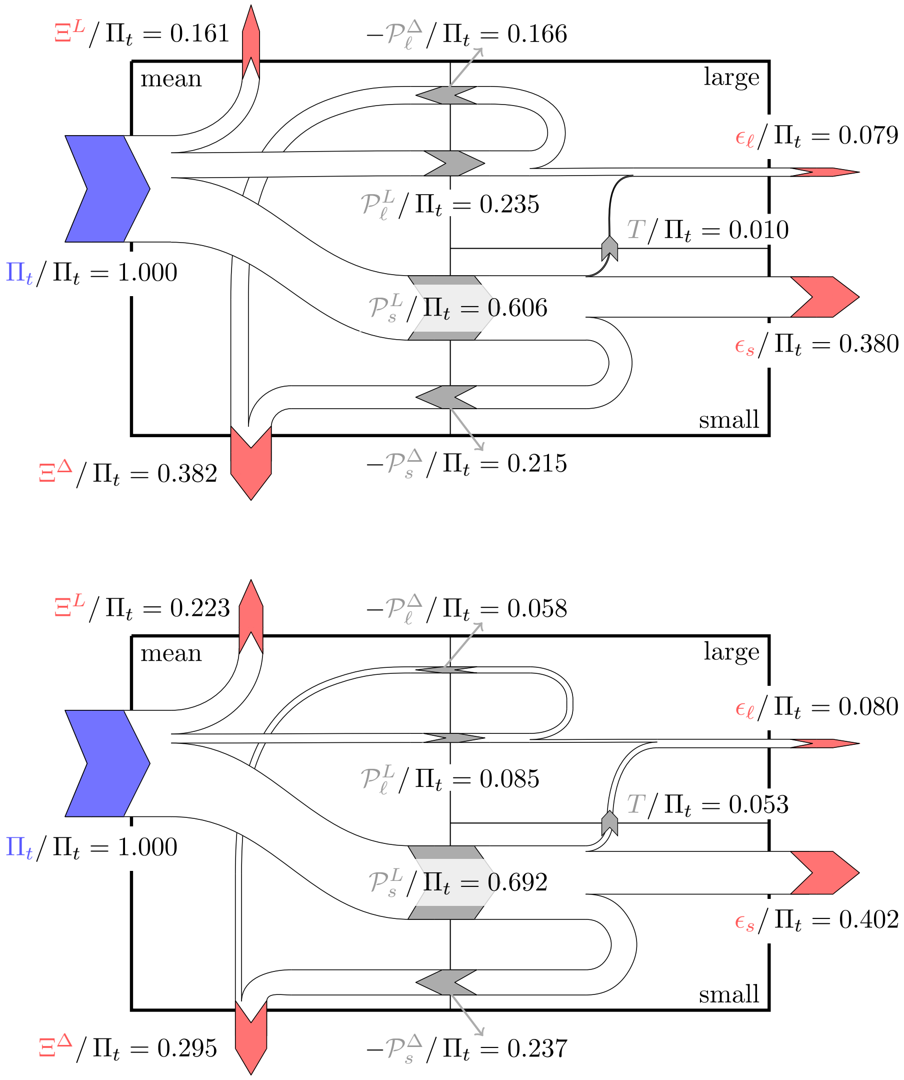

Figure 4.8: Scale-decomposed energy box for two Couette flows at $Re_\tau \approx 100$: no control (top), $Ro = -0.03$ (bottom). Adapted from [MY24a].

fluctuations through $\mathcal{P}_s^L$ and $\mathcal{P}_\ell^L$ respectively. Small- and large-scale fluctuations then exchange power through the cross-talk term T. Alternatively, they dissipate the received power either directly as turbulent dissipation ($\epsilon = \epsilon_s + \epsilon_\ell$) or indirectly by feeding it back to the mean flow through the deviation production ($\mathcal{P}^\Delta = \mathcal{P}_s^\Delta + \mathcal{P}_\ell^\Delta$; notice that $\mathcal{P}^\Delta < 0$). The entirety of deviation production is then lost as deviation dissipation, $\Xi^\Delta = -\mathcal{P}^\Delta$. Hence, small- and large-scale contributions to $\mathcal{P}^\Delta$ can be regarded as small- and large-scale contributions to the deviation dissipation Ξ^Δ, which are defined as follows:

$$\Xi_s^\Delta = -\mathcal{P}_s^\Delta, \qquad \Xi_\ell^\Delta = -\mathcal{P}_\ell^\Delta. \tag{4.10}$$

Using this notation, the integral turbulent kinetic energy balance for small- and large-scale fluctuations depicted in figure 4.8 can be written as:

$$\mathcal{P}_s^L = \Xi_s^\Delta + \epsilon_s + T, \tag{4.11}$$

$$\mathcal{P}_\ell^L = \Xi_\ell^\Delta + \epsilon_\ell - T. \tag{4.12}$$

	using $\Xi_\ell^\Delta + \epsilon_\ell$	using $\mathcal{P}_\ell^L$
	(exact)	(equivalent to FIK)
$Re_\tau \approx 100$	24.5%	23.5%
$Re_\tau \approx 500$	38%	43.2%

Table 4.2: Share of the total power input Π_t that is dissipated by large scales in absence of control ($Ro = 0$), quantified either using $\Xi_\ell^\Delta + \epsilon_\ell$ (exact method) or $\mathcal{P}_\ell^L$. The second method is equivalent to calculating the effect of the large scales on the skin friction using the large-scale contribution to the integral term of the FIK identity (see eq. 4.8). Data from chapter 3. Adapted from [MY24a].

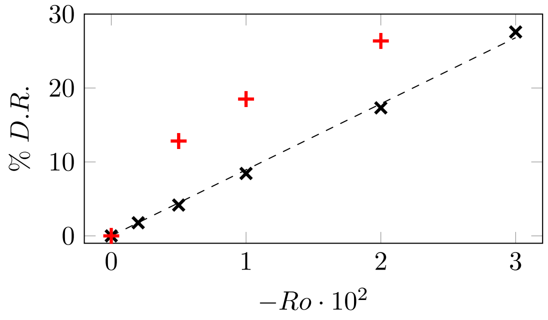

Figure 4.9: Percentage drag reduction ($\%\ D.R.$) obtained by applying the Coriolis force associated to a rotation number Ro at CFR; $Re_\tau \approx 100$ (black, ×) and $Re_\tau \approx 500$ (red, +). The black, dashed line indicates a linear fit for the low-Re data. Adapted from [MY24a].

It is clear from the above equation that $\mathcal{P}_\ell^L$ does not exactly represent the total dissipation $\Xi_\ell^\Delta + \epsilon_\ell$ caused by large scales, as it needs to be corrected by considering the inter-scale power transfer T. Similarly, the large-scale contribution to the integral term of equation 4.8 (which directly corresponds to $\mathcal{P}_\ell^L$) does not exactly quantify the large-scale contribution to the wall shear stress. The magnitude of the cross-talk term T is usually one order of magnitude smaller than the one of $\mathcal{P}_\ell^L$ and has a positive sign at low Reynolds number, meaning that a net power transfer from small to large scales is globally seen. By using $\mathcal{P}_\ell^L$ instead of $\Xi_\ell^\Delta + \epsilon_\ell$, then, the share of power wasted by large scales (or, equivalently, the large-scale contribution to τ_w if using the FIK method) is underestimated. As the Reynolds number increases, T changes in sign (meaning that an usual energy cascade from large to small scales is seen) and increases in magnitude, so that using $\mathcal{P}_\ell^L$ might result in a modest overestimation of the effect of large scales.

As an example, the data from chapter 3 is used to compare these two different ways of accounting for the power dissipated by large scales; results are shown in table 4.2. Owing to the analogy with the FIK identity, these values also represent the contribution of large scales to the skin friction; they can also be interpreted as an upper bound for the drag-reduction achievable by the suppression of large scales.” [MY24a]

4.3.3 Drag reduction

"The drag reduction obtained by applying a Coriolis force with a given rotation number Ro at constant flow rate (CFR, $Re_w = const.$) is calculated using the friction Reynolds number $Re_\tau\left(Ro; Re_w\right)$ observed at that rotation number:

$$D.R.\left(Ro; Re_w\right) = 1 - \frac{Re_\tau^2\left(Ro; Re_w\right)}{Re_\tau^2\left(0; Re_w\right)}. \tag{4.13}$$

Results are shown in figure 4.9 for both the lower and higher Reynolds number datasets. For the low-Re dataset, the obtained drag reduction increases linearly with the control intensity ($-Ro$); the same cannot be said at high Reynolds number. While no saturation effect is seen at low-Re, high-Re data reveals that the gains in performance obtained by an increase of $|Ro|$ decrease with $|Ro|$ itself. We interpret this behaviour as follows: for small absolute values of the rotation number, the ESM is progressively suppressed, so that a slight increase of $|Ro|$ yields a significant increase in performance owing to the suppression. As the rotation number approaches larger magnitudes, most of the ESM-energy has already been removed; any increase in performance mostly stems from the effect of the Coriolis force on the remaining scales of motion, hence the reduced improvements over an increase of $|Ro|$. This is confirmed by the trends of CPI-fluxes shown in figure 4.10, which are discussed below, and matches the observations made on the energy spectra (§4.3.1).

Although the process is imperfect, it was shown in §4.3.1 that the suppression of the ESM is satisfactory for $Ro = -0.01$ and $Ro = -0.005$ at the lower and higher Reynolds numbers respectively. These values of Ro correspond to 8.44% drag reduction at low-Re (starting from a reference friction Reynolds number $Re_\tau \approx 100$) and 12.8% at high-Re ($Re_\tau \approx 500$). We consider these values of drag reduction to be a sensible estimate of the drag reduction achievable by suppressing the ESM: the control force might be too intrusive for larger magnitudes of Ro, whereas for lower ones the ESM is not fully suppressed. Both values lie well below the theoretical maximum drag reduction given in table 4.2. One obvious reason for the mismatch is that the values given in table 4.2 estimate the drag reduction achievable by removing all motions whose spanwise wavelength is larger than a given threshold, including the ESM; the Coriolis force instead only suppresses the ESM. Moreover, a similar mismatch in the predicted and observed drag reduction was reported by both Fukagata et al. (2010) and de Giovanetti et al. (2016). Both authors found the reason for the mismatch in an increased small-scale contribution to skin friction, which in turn they attribute to different causes. The former argued that a decrease in pressure fluctuations causes the energisation of small scales; the latter attributed it to altered scale interactions. While both authors resorted to the FIK identity for their theoretical predictions, which possibly over-estimates the contribution of large scales to the skin friction (see §4.3.2), we expect the error introduced in doing so to be rather small at the Reynolds numbers considered. We further investigate the matter with the help of the CPI framework.

Owing to the discussion in §4.3.2, an expression for the skin friction coefficient is given by:

$$C_f = \frac{2}{\rho U_w^3}\left(\Xi^L + \epsilon + \Xi^\Delta\right). \tag{4.14}$$

As the laminar dissipation Ξ^L is constant at CFR by definition, only a reduction of the turbulent or deviation dissipation (ϵ and Ξ^Δ respectively) can yield a reduction of skin friction. Both these terms, as well as their small- and large-scale contributions (which have been calculated using a spanwise threshold wavelength of $\lambda_{z,c} = \pi$ as in chapter 3), are plotted in figure 4.10 for both the high and low Reynolds

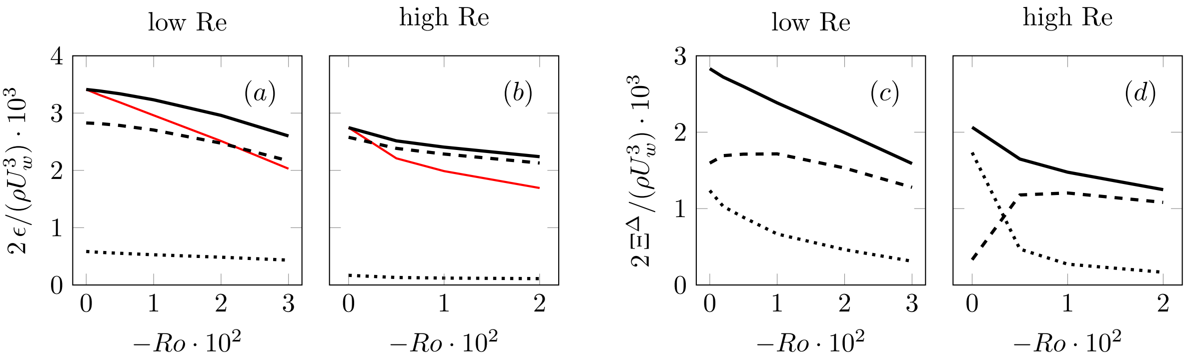

Figure 4.10: Turbulence-induced dissipation terms scaled in outer units for changing control intensity $-Ro$ at CFR; turbulent dissipation ϵ (a,b) and deviation dissipation Ξ^Δ (c,d) split into their small- (dashed) and large-scale components (dotted). (a,c) $Re_\tau \approx 100$; (b,d) $Re_\tau \approx 500$. The red, solid lines indicate the expected $\epsilon \sim \rho u_\tau^3 \log(Re_\tau)$ scaling. Adapted from [MY24a].

number datasets for increasing magnitude of Ro. These energy fluxes are scaled with $\frac{1}{2}\rho U_w^3$, since the velocity U_w of the walls remains constant as the simulations are carried out at CFR. Doing so, a decrease of a non-dimensional flux is associated to a decrease of its dimensional value. Moreover, the so-scaled energy fluxes can be interpreted as contributions to the skin friction as of equation 4.14.

A decrease of both the total turbulent and deviation dissipation is observed. Since the ESM is known to primarily contribute to the deviation dissipation Ξ^Δ (see chapter 3), substantial savings in terms of the large-scaled contribution Ξ_ℓ^Δ are expected. These are indeed seen at both low and high Reynolds number (c,d), as the value of Ξ_ℓ^Δ approaches zero with increasing magnitude of Ro. At the higher Reynolds number, the value of Ξ_ℓ^Δ saturates fast towards a zero-value, coherently with the idea that the ESM is already satisfactorily suppressed at $Ro = -0.005$ (see §4.3.1). This might also explain why the trend of drag reduction deviates from a linear one at high Reynolds number (see figure 4.9), as previously discussed. Savings in Ξ_ℓ^Δ are partially compensated by an increase of the contribution Ξ_s^Δ of smaller scales to deviation dissipation; this holds for all the considered values of Ro at high Reynolds number, and only for low magnitudes of Ro at low Reynolds number.

As for the turbulent dissipation, its large-scale contribution ϵ_ℓ is expectedly marginal in absence of control and is only slightly decreased by the Coriolis force. The latter causes a significant decrease of the small-scale dissipation ϵ_s instead. Such a decrease is expected, and can be interpreted as an indirect effect of the removal of the ESM: its suppression indeed triggers a reduction of the wall shear stress, which is well known to govern the scaling of the small scales. Hence, a decrease of small scale activity is expected, including a decrease of their contribution ϵ_s to dissipation; this further reduces the wall shear stress. Despite their absolute reduction, though, the observed values of ϵ_s are higher than expected. It is indeed known (see Abe and Antonia, 2016) that the turbulent dissipation ϵ scales as $\rho u_\tau^3 \log(Re_\tau)$; the trend that would result if such a scaling were to hold when the Coriolis force is applied is shown in figure 4.10. As can be seen, the observed values of ϵ exceed the expected ones. The excess dissipation can be attributed to ϵ_s, as the magnitude of ϵ_ℓ is negligible.

Both the trends of Ξ_s^Δ and ϵ_s highlight that the drag reduction achieved by suppressing large scales is mitigated by a higher-than-expected contribution to skin friction from smaller scales. Notice that the threshold wavelength $\lambda_{z,c} = \pi$ used to separate large- and small-scale energy fluxes effectively separates the extremely large ESM from the remaining scales of motion; in other words, Ξ_s^Δ and ϵ_s receive contributions not only from inner-scaled eddies, but also from large, outer-scaled ones that are still smaller than the ESM. The latter are, for instance, eddies whose spanwise wavelength falls in the range $1 \leq \lambda_z/h \leq \pi$; likely, they are responsible for the unexpectedly high values of Ξ_s^Δ and ϵ_s. Indeed, the analysis of §4.3.1 has revealed that inner-scaled eddies hold the usual, viscous-scaling amount of energy even after the ESM is suppressed. Instead, some outer-scaled motions located at the centerline (satisfying $1 \leq \lambda_z/h \leq \pi$) are energised by the Coriolis force, and this energisation possibly leads to increased values of the skin friction." [MY24a]

4.4 Discussion: the Coriolis force as a feedback control

"We have so far shown that applying a Coriolis force to the flow achieves drag reduction by suppressing the ESM. In this section, we argue that the Coriolis force functions in a way that resembles the feedback control proposed by Fukagata et al. (2005).

The Coriolis force $\vec{f}_c$ can be Reynolds-decomposed to yield its mean $\left\langle \vec{f}_c \right\rangle$ and fluctuating $\vec{f}'_c$ parts:

$$\vec{f}_c = -2\rho\,\Omega\hat{z}\times\vec{u} = \underbrace{-2\rho\,\Omega\hat{z}\times U\hat{x}}_{=\langle\vec{f}_c\rangle} + \underbrace{-2\rho\,\Omega\hat{z}\times\vec{u}\,'}_{=\vec{f}'_c}. \tag{4.15}$$

As U only depends on the wall normal coordinate y, so does the mean Coriolis force $\left\langle \vec{f}_c \right\rangle$; moreover, the only non-zero component of $\left\langle \vec{f}_c \right\rangle$ is the one in the wall-normal direction. Such a force field can be trivially shown to be conservative; as a consequence, its effect on the flow field is null, as it simply gets balanced by a static pressure gradient in the wall-normal direction. For the same reason, the Coriolis force has no impact on laminar flows (see Hide, 1977, sec. 2, lemma *iv*).

Hence, the ESM-suppressing action must be provided by the fluctuating part $\vec{f}'_c$ of the force, which operates in the wall-normal and streamwise directions with magnitudes:

$$f'_{c,x} = \vec{f}'_c \cdot \underline{x} = -2\rho|\Omega|v' \tag{4.16}$$

$$f'_{c,y} = \vec{f}'_c \cdot \underline{y} = 2\rho|\Omega|u' \tag{4.17}$$

where the angular velocity has been rewritten as $\Omega = -|\Omega|$ for ease of reading; indeed, we only consider cyclonic rotations ($\Omega < 0$). To illustrate the action of the fluctuating part of the Coriolis force, we resort to the displaced-particle analysis shown in Tritton (1992). Consider a fluid particle at some wall-normal distance where the value of the mean velocity is U_1; U_1 is also the expected value of the streamwise velocity of the fluid particle. The particle is then displaced upwards by $\xi \to 0, \xi > 0$ over a time frame $\Delta t \to 0$ as an effect of an upwards velocity fluctuation, $v'_* > 0$, where $v'_* = \xi/\Delta t$. As this happens, the fluid particle is slowed down by the Coriolis force to reach a velocity U_* in its displaced position:

$$U_* \;=\; U_1 + \int_0^{\Delta t} \frac{f'_{c,x}}{\rho}\,\mathrm{d}t \;=\; U_1 + \int_0^{\Delta t} -2|\Omega|v'_*\,\mathrm{d}t \tag{4.18}$$

$$\approx\; U_1 - 2|\Omega|\xi. \tag{4.19}$$

At this new wall-normal position, the expected value of the velocity is $U_2 \approx U_1 + (dU/dy)\,\xi$, with $U_2 > U_1$ owing to the positive velocity gradient. Even in absence of a Coriolis force, the displaced particle would then induce a negative velocity fluctuation $-(dU/dy)\,\xi$; this can explain the negative sign of the Reynolds shear stress $\langle u'v' \rangle$. Additionally, the Coriolis force slows down the displaced particle as illustrated before, so that the observed velocity fluctuation u'_* reads:

$$u'_* = U_* - U_2 \approx - \left(2|\Omega| + \frac{\mathrm{d}U}{\mathrm{d}y} \right) \xi. \tag{4.20}$$

In other words, the streamwise component of the Coriolis force tends to increase the magnitude of the streamwise velocity fluctuations; this is however at odds with the observed stabilisation associated to the suppression of the ESM. The stabilising effect is instead given by the wall-normal component of the Coriolis force fluctuation,

$$f'_{c,y\,*} = 2\rho|\Omega|u'_* \approx -2\rho|\Omega|\xi \left(2|\Omega| + \frac{\mathrm{d}U}{\mathrm{d}y} \right) < 0, \tag{4.21}$$

which is negative, hence it tends to return the displaced particle to its original position. The Coriolis force, then, interferes with the mechanism that produces the anti-correlation of u' and v' fluctuations – that is, it hinders the formation of a negative Reynolds shear stress.” [MY24a] Moreover, the expression of the stabilising force (eq. 4.21) might shed light on why the Coriolis force primarily affects the ESM. Owing to its large scale, the ESM displaces fluid particles by a larger extent than other scales of motion. Thus, ESM-induced fluctuations will be larger (see eq. 4.20); as the stabilising force is proportional to streamwise fluctuations, ESM-fluctuations would also feel a larger stabilising force.

“The displaced particle analysis then indicates that the Coriolis force functions in a similar way to the feedback control of Fukagata et al. (2005), which is designed to directly weaken the Reynolds shear stress. Such a feedback control is exactly equivalent to the present Coriolis force deprived of its streamwise component, so that the control force only acts in the wall-normal direction with an intensity that is proportional to streamwise velocity fluctuations (see equation 4.17; notice that Fukagata et al., 2005, use a cylindrical coordinate system where the wall-normal axis points towards the wall, leading to an opposite sign of the control force with respect to the present manuscript). Streamwise velocity fluctuations are statistically associated to wall-normal fluctuations of opposite sign; the latter are opposed by both the Coriolis force and the feedback control of Fukagata et al. (2005), which deliver a wall-normal acceleration of the same sign as streamwise fluctuations. In this sense, both control strategies are analogous to an opposition control scheme; the obvious difference is that the sensing and the actuation for an opposition control is usually performed at the wall (eg. Abbassi et al., 2017), whereas the Coriolis force and the feedback control act at each point in the fluid domain.

To provide evidence in favour of the proposed analogy, we carry out an additional simulation at low Reynolds number and $Ro = -0.01$, where the streamwise and spanwise average of the Coriolis force as well as its streamwise component are removed. In other words, only the fluctuating part of the wall-normal component of the Coriolis force is retained, so as to effectively mimic the feedback control of Fukagata et al. (2005). Results are shown in figure 4.11, that compares the so-obtained one-dimensional spanwise spectrum of the streamwise fluctuations at $y/h = 1$ with the one of the corresponding simulations with and without Coriolis force. The modified Coriolis force is able to suppress the spectral peak associated to the ESM and to closely replicate the velocity spectrum yielded by the standard Coriolis force, confirming our hypothesis.

Following Fukagata et al. (2005), we now proceed to show how the Coriolis force changes the budget equation of the Reynolds shear stress, as this may better hint at why the force selectively suppresses the ESM. To be precise, we inspect the co-spectrum Φ_{uv} of the Reynolds shear stress. Its real part $\mathcal{R}e\left(\Phi_{uv}\right)$

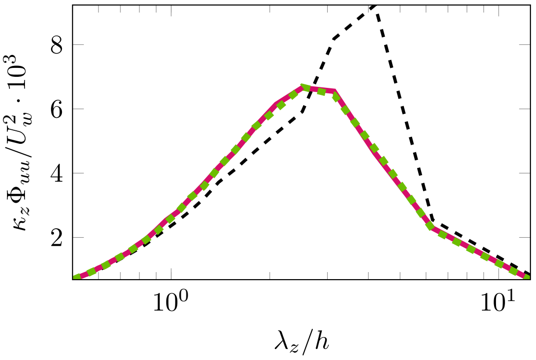

Figure 4.11: Premultiplied one-dimensional spanwise spectrum $\kappa_z\Phi_{uu}$ of the streamwise fluctuations at $y/h = 1$ for the low Reynolds number dataset ($Re_\tau \approx 100$). The black dashed lines indicates the uncontrolled simulation ($Ro = 0$); the solid magenta line represents data with the usual Coriolis force and $Ro = -0.01$. For the green, dashed line, only the wall-normal component of the Coriolis force ($Ro = -0.01$) is retained; moreover, the stream- and span-wise average of the force is removed from it. Adapted from [MY24a].

represents the contribution of each Fourier mode of wavenumber κ_z to $\langle u'v' \rangle$: it can be trivially shown (following e.g. Davidson, 2015, chapter 8) that

$$\langle u'v' \rangle = \int_{-\infty}^{\infty} \mathcal{Re}\left(\Phi_{uv}\right) \mathrm{d}\kappa_z. \tag{4.22}$$

A budget equation for Φ_{uv} is provided by Lee and Moser (2019); by adding the contribution of the Coriolis force and taking the real part of both sides of the equation, it can be written as:

$$\frac{\partial}{\partial t} \underbrace{\mathcal{Re}\left(\Phi_{uv}\right)}_{\text{typically } <0} = \mathcal{Re}\left(\text{RHS}\right) \underbrace{- 2|\Omega|\Phi_{vv}}_{\text{cont. of } f'_{c,x}} + \underbrace{2|\Omega|\Phi_{uu}}_{\text{cont. of } f'_{c,y}} \tag{4.23}$$

where RHS indicates all the terms normally appearing in the budget equation (not shown for brevity). The real part $\mathcal{Re}\left(\Phi_{uv}\right)$ of the co-spectrum is typically negative, as is the Reynolds shear stress. The contributions of the streamwise and wall-normal components $f'_{c,x}$ and $f'_{c,y}$ of the Coriolis force are proportional to the spectra Φ_{vv} and Φ_{uu} of the streamwise and wall-normal normal Reynolds stresses respectively; both Φ_{vv} and Φ_{uu} are real, positive numbers and the latter is typically larger by roughly an order of magnitude (see figure 4.4). Hence the contribution of the Coriolis force to the right hand side of equation 4.23 is dominated by the wall-normal component $f'_{c,y}$ (as expected from the above analysis) and has a positive sign. That is, the Coriolis force results in a sink term for the budget of $\mathcal{Re}\left(\Phi_{uv}\right)$ (as this last quantity is negative). We have once again shown that the Coriolis force acts to directly destroy the Reynolds shear stress like the feedback control of Fukagata et al. (2005) does.

Equation 4.23 has further implications. In an uncontrolled setting, the spectrum Φ_{uu} is maximum at the spanwise scale (i.e. wavenumber, or wavelength) of the ESM, as shown by the spectrum of figure 4.4[1]. Consequently, the application of a Coriolis force would primarily target the Reynolds shear stress at the scale of the ESM. While the destruction of Reynolds shear stress clearly explains the observed drag reduction (as implied by equation 4.8), explaining how energy at the ESM-scale is removed from the normal Reynolds stresses is not as straightforward. Indeed, the direct effect of the Coriolis force on the streamwise and wall-normal spectra Φ_{uu} and Φ_{vv} is to transfer energy from the wall-normal

---

[1] Notice that the spectrum is premultiplied; values of the spectrum seen at large scales are effectively larger with respect to the ones at small scales than it appears from figure 4.4. Moreover, the values of the spectrum at $\kappa_z = 0$ are not shown in figure 4.4 owing to the logarithmic scale. Although such a spanwise-invariant mode may usually contain a significant amount of energy, a separate analysis has shown that the energy held by the ESM is still much larger than the energy found at $\kappa_z = 0$.

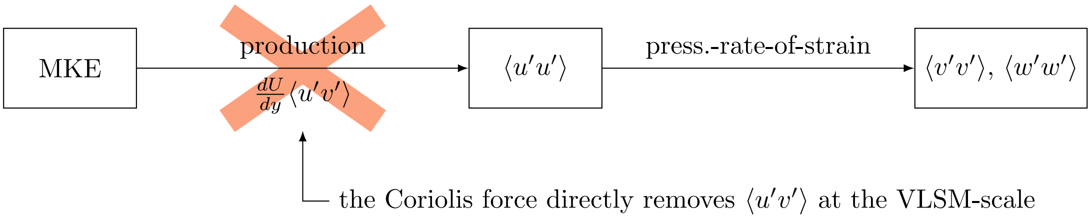

Figure 4.12: Proposed mechanism for the selective suppression of the ESM in Couette flows. The acronym MKE indicates the energy of the mean flow U (Mean Kinetic Energy). The Coriolis force directly suppresses $\langle u'v'\rangle$ at the scale of the ESM. As a consequence, production of $\langle u'u'\rangle$ is stopped at such a scale; eventually, this will affect the formation of $\langle v'v'\rangle$ and $\langle w'w'\rangle$ energy too. Adapted from [MY24a].

to the streamwise one, as can be shown by writing a budget equation analogous to equation 4.23 (not shown for brevity). This is consistent with the fact that the Coriolis force does not exchange work with the flow (see §4.2). Most importantly, this direct effect cannot explain the destruction of energy at the ESM-scale seen in figure 4.4.

Instead, the destruction of ESM-energy must happen through an indirect mechanism. We have already argued that the Coriolis force directly suppresses the Reynolds shear stress at the ESM-scale. The Reynolds shear stress is the intermediary through which $\langle u'u'\rangle$ receives energy from the mean flow (production of turbulent kinetic energy, see §2.2.6); a reduction of the shear stress at the ESM-scale would likely result in a reduction of $\langle u'u'\rangle$-stresses at the same scale. The remaining contributions $\langle v'v'\rangle$ and $\langle w'w'\rangle$ to the kinetic energy do not receive energy from the mean flow in the present geometrical configuration; instead, the energy fed to streamwise fluctuations is redistributed to the remaining components by the pressure-rate-of-strain correlation (see, once again, §2.2.6). It is then conceivable that the lack of $\langle u'u'\rangle$-energy at the ESM-scale would result in lacking energy at the same scale on the other velocity components.

The mechanism described above is summarised in figure 4.12 and might explain how the ESM is selectively suppressed by the Coriolis force. It has however its own limitations. For instance, once the ESM is removed, the small scales would become the dominant feature of the Φ_{uu} spectrum (at least in the near-wall region). Owing to the above discussion, then, the Coriolis force would proceed to destroy Φ_{uv} at these scales - which does not happen for the limited values of Ro considered in this paper. Likely, the degree of suppression is determined by the relative magnitude of the contributions of the Coriolis force with respect to the terms labelled RHS in equation 4.23. Also, an alternative way of discussing the selective suppression of the ESM would be to consider linear transient growth mechanisms. These lead to the amplification of flow structures that are comparable in size and topology to the small and outer-layer scales of wall turbulence (for instance, Del Álamo and Jiménez, 2006); it has been argued (Lozano-Durán et al., 2021) that the existence of these mechanisms is a sufficient condition for the formation of the typically observed structures. Perhaps, adding a Coriolis force to the flow selectively hinders the mechanisms leading to the amplification of outer-scaled motions, without much affecting smaller-scale mechanisms. The verification of this hypothesis is left for future research.” [MY24a]

4.5 Summary and conclusions

The numerical study presented in this chapter shows “that a feedback control that exchanges no power with the flow is able to suppress the streamwise-elongated, outer-scaled rolling motion (the ESM) typical of a turbulent Couette flow at a low to moderate Reynolds number. It is argued that the control force works by directly suppressing the Reynolds shear stress $\langle u'v' \rangle$ at selected scales; in this sense, it resembles the feedback control of Fukagata et al. (2005).

Using the CPI framework, which has been shown to be an extended and rescaled version of the FIK identity, the ESM can be associated to costly distortions of the mean velocity profile (see chapter 3); the share of power wasted in this way is referred to as deviation dissipation Ξ^Δ. While large-scale contributions to Ξ^Δ are greatly reduced by suppressing the ESM (corroborating the previous statement), these gains in performance are hindered by a higher-than-expected contribution to Ξ^Δ and to the turbulent dissipation ϵ by smaller (but not necessarily small) scales. This observation is consistent with previous similar works (Fukagata et al., 2010; de Giovanetti et al., 2016) and we attribute the unexpected skin friction contributions to the energisation of outer-scaled eddies that is observed as the ESM is suppressed.

While the approach used here yields a progressive suppression of the ESM, making it complicated to determine when the suppression is complete, a sensible estimate of the drag reduction achievable by targeting the ESM is in the order of 8% starting from a reference friction Reynolds number $Re_\tau \approx 100$ and 13% for $Re_\tau \approx 500$. The latter value is higher than the drag reduction reported by de Giovanetti et al. (2016), who also performed a numerical experiment that suppressed outer-scaled motions in a channel flow. This discrepancy can be explained by differences in the suppressing strategy; most importantly, the above authors were considering a flow in which outer-scaled motions are weaker than in the Couette one considered here. However, since large scales are known to get more intense with the Reynolds number (Hutchins and Marusic, 2007b), higher values of drag reduction can be expected also in channel and boundary layer flows at a high Reynolds number. This is encouraging, as high Reynolds numbers are usually encountered in applications of industrial interest.” [MY24a]

5 Separating large-scale superposition and modulation in turbulent channel flows

The results shown in this chapter have been published in Andreolli et al. [MY23].
Data for this chapter is available at `https://dx.doi.org/10.35097/EEXRgyvGozfhsyqo`.

This chapter deals with scale interactions, and in particular with amplitude modulation (see §1.2.4 and §1.2.5). As previously explained, amplitude modulation is typically understood to be the result of the following mechanism. Outer-layer large scales are able to leave a footprint in the near-wall region in the form of coherent large-scale velocity fluctuations; this process takes the name of superposition of the large scales. The superposed large-scaled fluctuations cause a local increase (or decrease) of the wall shear stress, which in turn triggers a local increase (decrease) of the energy of near-wall small scales (owing, for instance, to the inner-scaling of small scales; see §1.2.2 or §1.2.5). This or similar mechanisms (see §1.2.5) are understood to produce the observed correlation between the amplitude (envelope) of the small scales and the large-scale velocity signal (amplitude modulation).

The aim of this chapter is to verify whether amplitude modulation is indeed caused by the superimposed large-scale wall shear stress pattern as discussed in section §1.2.5 and summarised in the above paragraph. Additionally, the dual hypothesis is tested – that is, whether the existence of small-scales whose amplitude is modulated by a large-scale envelope triggers the formation of a large-scale wall shear stress pattern. The following scientific question is thus addressed:

> **3. Is the wall-shear stress the mediator in the scale-interaction mechanism known as amplitude modulation?**

The above question is investigated through a couple of numerical experiments. First, the superposition of large scales to the wall is prevented (suppression of superposition) to verify whether amplitude modulation is still observed. Then, small scales are prevented from having a large-scale envelope (suppression of modulation) to verify whether a near-wall large-scale velocity pattern is still observed. The suppression of superposition and of modulation is achieved through purposely defined body forces. The numerical experiments are carried out both in standard, large simulation domains as well as in much shorter minimal streamwise units. Minimal streamwise units are able to reproduce healthy turbulence in the buffer layer as well as the main features of the outer-layer large scales at a much reduced computational cost; by comparing them simulations in long and short domains, the ability of the minimal streamwise unit to correctly capture scale interactions is discussed.

The chapter is structured as follows. A description of the numerical setup is provided in §5.1; the strategy used to selectively suppress superposition and modulation is discussed in §5.1.1 and §5.1.2 respectively. The present modulation suppressing strategy requires an additional smoothing of the velocity spectra (described in §5.1.3) to help their visualisation. After a brief overview of the main results concerning amplitude modulation in natural channels (§5.2), the results concerning suppression of modulation and of superposition are shown in sections §5.2.1 and §5.2.2 respectively. The results of §5.2.1 concerning the suppression of superposition are of particular relevance for the quasi-steady,

Type	Re_τ	L_x/h	L_z/h	L_x^+	L_z^+	$N_x \times N_y \times N_z$	Δx^+	Δz^+	Δy^+_{min}	Tu_τ/h
LSD	1000	4π	2π	12566	6283	$1024 \times 500 \times 1024$	12.3	6.1	0.97	150
MSU	1000	0.4	7	400	7000	$40 \times 500 \times 1148$	10.0	6.1	0.97	300

Table 5.1: Details of the Long Streamwise Domain (LSD) and Minimal Streamwise Unit (MSU) simulations. N_x and N_z are the numbers of Fourier modes in the homogeneous directions (additional modes are used for dealiasing, according to the 3/2 rule), while N_y is the number of collocation points in the wall-normal direction. The resulting spatial resolutions Δx^+ and Δz^+ in the streamwise and spanwise directions respectively, as well as the wall-normal resolution Δy^+_{min} at the wall, are reported. T is the temporal interval over which statistics have been collected after discarding the transient. Adapted from [MY23].

quasi-homogeneous theory of Zhang and Chernyshenko (2016); this will be discussed in §5.3. A summarising remark is given in §5.4.

5.1 Methodology

The analyses presented in this chapter are based “on a newly-produced direct-numerical-simulation (DNS) database of turbulent Poiseuille flows (see §2.2.1) at friction Reynolds number $Re_\tau = 1000$ in stream- and spanwise periodic domains; its peculiarity is the selective suppression of either modulation or superposition phenomena, which is discussed below.” [MY23] The simulations are carried out at constant pressure gradient (CPG) using the method described in §2.4.4. “As for the size of the computational domain, we resort to both moderately long streamwise domains (LSD), in which the streamwise periodicity is $L_x/h = 4\pi$, and minimal streamwise units (MSU), for which $L_x^+ = 400$ (Abe et al., 2018). MSUs are here used by virtue of their simplified flow physics and reduced computational cost; their suitability for the study of amplitude modulation is also assessed. All other discretisation parameters are set to values that are standard in DNS practice; a summary can be found in table 5.1.

To quantify amplitude modulation, the two-point scale-decomposed skewness C^*_{AM} (Schlatter and Örlü, 2010; Bernardini and Pirozzoli, 2011; Mathis et al., 2011b; Eitel-Amor et al., 2014) is used:

$$C^*_{\text{AM}} = \left\langle {u_s^+}^2(y_s^+)\, u_\ell^+(y_\ell^+) \right\rangle \,, \tag{5.1}$$

where u_ℓ and u_s indicate, respectively, the low- and high-pass filtered streamwise velocity fluctuation signals at two different wall-normal positions y_ℓ, y_s. Notice that the asterisk in C^*_{AM} is kept for consistency with literature. Positive values of C^*_{AM} indicate the presence of amplitude modulation, whereas negative values indicate a region of phase-reversal (see §1.2.5). C^*_{AM} has been preferred to many other statistics available in the literature (see, for instance, Dogan et al., 2019) owing to the fact that it is not normalised by $\langle u_\ell^+ u_\ell^+ \rangle^{1/2}$. Indeed, as will be explained below in the context of the suppression of superposition, the large scale signal u_ℓ^+ is damped in specific portions of the channel, thus yielding $\langle u_\ell^+ u_\ell^+ \rangle \to 0$. Filtering is performed in the spanwise direction with a sharp Fourier filter; a conventional threshold wavelength $\lambda^+_{z,c} = h^+/2 = 500$ is used (see, for instance, Bernardini and Pirozzoli, 2011, at a similar value of Re_τ), unless explicitly stated. In the context of suppression of modulation, practical considerations led to a choice of $\lambda^+_{z,c} = h^+ = 1000$.

The suppression of either superposition or modulation is achieved by artificial damping of selected turbulent motions via a volume-force term $\vec{f}$ added to the right-hand side of the momentum balance of the incompressible Navier–Stokes equations, such that:

$$\frac{\partial \vec{u}}{\partial t} + (\vec{u} \cdot \nabla)\, \vec{u} = -\frac{1}{\rho} \nabla p + \nu \nabla^2 \vec{u} + \frac{1}{\rho} \vec{f}\,, \tag{5.2}$$

$$\nabla \cdot \vec{u} = 0\,, \tag{5.3}$$

The artificial damping is most conveniently defined in the spectral Fourier space;" [MY23] using index notation for vectors,

$$\widehat{\widehat{f}}_i = -\frac{\varkappa\,(\kappa_x, \kappa_z, y)}{\Upsilon} \widehat{\widehat{u}}_i \qquad \text{for } i = 1, 2, 3\,, \tag{5.4}$$

"where $\widehat{\widehat{(...)}}$ denotes the Fourier coefficient for a given stream- and spanwise wavenumber pair (κ_x, κ_z) at a specific y-position. The arbitrary parameter Υ determines the strength of the damping; its value of $\Upsilon/(h/u_\tau) = 10^{-3}$ is chosen empirically (see, for instance, Stroh et al., 2016b; Forooghi et al., 2018) to achieve a forcing that is as small as possible, while still ensuring satisfactory damping of the selected modes. The dimensionless function $\varkappa\,(\kappa_x, \kappa_z, y)$ selects which scales and wall-normal locations are damped and is defined in the following, depending on whether superposition (denoted by subscript S, $\varkappa_{\mathrm{S}}$) or modulation ($\varkappa_{\mathrm{AM}}$) are removed.

Notice that the forcing is active on all components of velocity, although the amplitude modulation analysis is only carried out on the streamwise component. Moreover, the equations of motion are solved using the wall-normal velocity and vorticity formulation that automatically fulfils the divergence-free constraint. Although the forcing we use might have non-zero divergence (just like the non-linear term of equation 5.2), only its solenoidal component affects the governing equations – so that the continuity equation 5.3 is verified at all times." [MY23]

5.1.1 Suppression of superposition

"A straightforward way of preventing the superposition of large scales at the wall is damping spanwise Fourier modes contributing to u_ℓ in that region. While this clearly defines the scales at which modal damping is activated ($\lambda_z^+ > h^+/2$, owing to the definition of u_ℓ in §5.1), the wall-normal portion of the domain in which this is done is yet to be specified. To address this issue, we propose a definition of the space-scale region in which superposition takes place as the one where large, near-wall motions are fed energy from other scales and wall-normal positions; this region can be rigorously identified by analysing the spectral turbulent kinetic energy (TKE) budget decomposed in spanwise Fourier modes (Cho et al., 2018)," [MY23]

$$\frac{\partial \left\langle \widehat{e} \right\rangle^+}{\partial t^+} = \widehat{\Sigma}_{\mathcal{P}}^+ + \widehat{\Sigma}_{\epsilon}^+ + \widehat{\mathcal{T}}_t^+ + \widehat{\mathcal{T}}_p^+ + \widehat{\mathcal{T}}_\nu^+ = 0\,. \tag{5.5}$$

As explained in §2.3.1 , $\widehat{(...)}$ indicates the coefficient of the spanwise Fourier series associated to the wavenumber $\kappa_z = 2\pi/\lambda_z$, λ_z being the spanwise wavelength, and $\langle \hat{e} \rangle$ is defined as follows:

$$\left\langle \widehat{e} \right\rangle^+ \left(y^+, \kappa_z^+\right) = \frac{\Phi_{uu}^+ + \Phi_{vv}^+ + \Phi_{ww}^+}{2} = \frac{\left\langle \widehat{u}'^H \widehat{u}' + \widehat{v}'^H \widehat{v}' + \widehat{w}'^H \widehat{w}' \right\rangle^+}{2\,\Delta \kappa_z^+} \tag{5.6}$$

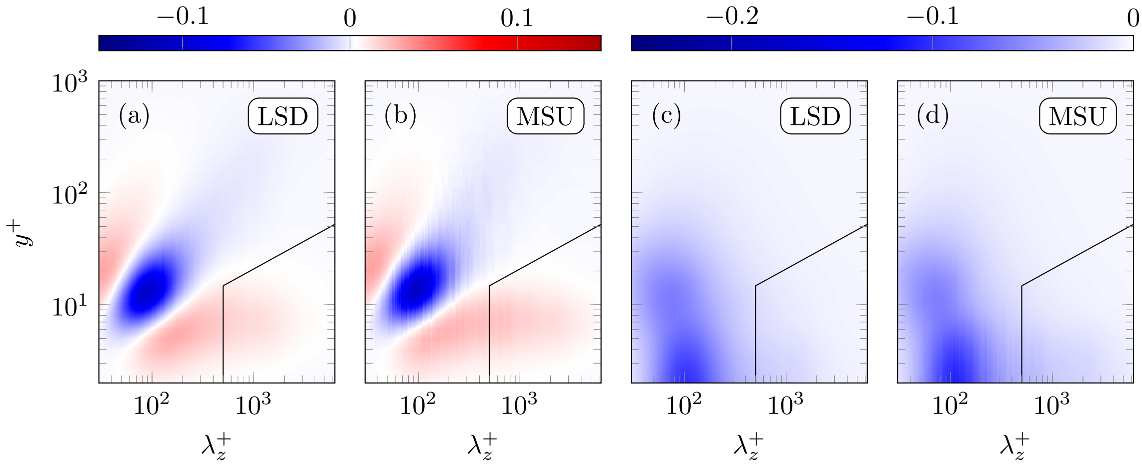

Figure 5.1: Premultiplied spanwise spectra of the turbulent transport ($\kappa_z^+ \mathcal{T}_t^+$, a,b) and dissipation term ($\kappa_z^+ \widehat{\Sigma}_\epsilon^+$; c,d) of the spectral TKE budget. Both the reference (unperturbed) LSD and MSU cases are reported. The solid black lines mark the boundaries of the region in which modal damping is performed. Adapted from [MY23].

Notice that the quantities being averaged in equation 5.6 do not depend on the spanwise coordinate z, as the dependence on z is replaced by the one on κ_z owing to the transform. Hence, averaging is only performed in time and in the streamwise direction. “The terms $\widehat{\Sigma}_{\mathcal{P}}$, $\widehat{\Sigma}_\epsilon$ denote respectively turbulent production and dissipation, while $\widehat{\mathcal{T}}_t$, $\widehat{\mathcal{T}}_p$ and $\widehat{\mathcal{T}}_\nu$ are turbulent, pressure and viscous transport respectively. Particular focus lies on the turbulent transport

$$\widehat{\mathcal{T}}_t^+ = \frac{\mathcal{R}e\left(\left\langle -\left(\widehat{u_i'}^+\right)^H \frac{\partial}{\partial x_j^+} \widehat{u_i' u_j'}^+ \right\rangle\right)}{\Delta \kappa_z^+}, \tag{5.7}$$

and turbulent dissipation

$$\widehat{\Sigma}_\epsilon^+ = -\frac{1}{\Delta \kappa_z^+} \left\langle \left(\frac{\partial \widehat{u_i'}^+}{\partial x_j^+}\right)^H \frac{\partial \widehat{u_i'}^+}{\partial x_j^+} \right\rangle, \tag{5.8}$$

where the superscript $(\cdot)^H$ denotes the complex conjugate and $\mathcal{R}e$ stands for the real part of a complex number. As reported by Cho et al. (2018) and Lee and Moser (2019), these two terms dominate the TKE budget in the vicinity of the wall for large wavelengths λ_z (small κ_z); while by definition turbulent dissipation subtracts energy from given Fourier modes, turbulent transport can actually feed them power (when $\widehat{\mathcal{T}}_t > 0$), thus being suitable for the identification of superposition modes.

From our definition and figure 5.1, which shows $\widehat{\mathcal{T}}_t^+$ and $\widehat{\Sigma}_\epsilon^+$ for the reference MSU and LSD cases, we identify the near-wall region in which superposition is suppressed as $2.3\,(y^+)^2 \leq \lambda_z^+$, as this region corresponds to the near-wall positive peak of $\mathcal{T}_t^+$; in other words, large scales in are here being fed energy. A similar locus was identified by Cho et al. (2018).

This complements the criterion $\lambda_z^+ > h^+/2$ that defines u_ℓ; the complete boundaries of the space-scale region suppressed in this section are shown in figure 5.1. Desirably, the near-wall turbulent dissipation peak (panels c,d), which is commonly associated to small scales, is excluded from the definition of the large, superposed ones. The following expression for $\varkappa_\mathrm{S}\left(\kappa_x^+, \kappa_z^+, y^+\right)$ stems from the present discussion:

$$\varkappa_\mathrm{S}\left(\kappa_x^+, \kappa_z^+, y^+\right) = \begin{cases} 1, & \text{if } \kappa_z^+ \leq \min\left(\frac{2\pi}{500}, \frac{2\pi}{2.3(y^+)^2}\right) \text{ except } \kappa_x^+ = \kappa_z^+ = 0 \\ 0, & \text{otherwise} \end{cases} . \tag{5.9}$$

Note that mode $(\kappa_x^+, \kappa_z^+) = (0, 0)$ is not damped, since this corresponds to the instantaneous stream- and spanwise spatial average; other than that, the value of κ_x plays no role, meaning that all κ_x modes are suppressed if the condition on κ_z is verified. While similar damping strategies have been attempted in literature (see, for instance, de Giovanetti et al., 2016), the peculiarity of the present one is that large scales are removed only in the vicinity of the wall and not throughout the whole domain." [MY23]

5.1.2 Suppression of modulation

"As for amplitude modulation, its suppression is not as trivial, and its spectral representation needs to be discussed first. Let us consider a toy problem, where a large-scale spanwise sinusoid $\cos(\kappa_\ell z)$ modulates a small-scale *carrier* wave, $\cos(\kappa_s z)$, κ_ℓ and κ_s being the respective wavenumbers; the Fourier representation of the large-scale signal has energy content only on the $\kappa_z = \pm\kappa_\ell$ mode (or $\kappa_z = \pm\kappa_s$ for the small-scale one). The modulated signal will be, for example, $[1 + \cos(\kappa_\ell z)]\cos(\kappa_s z)$. It can be easily proven by applying the angle addition formula for trigonometric functions (Abramowitz and Stegun, 1964) that such a modulated signal has energy content exclusively on modes $\kappa_z = \pm\kappa_s$, corresponding to the original carrier wave, and $\kappa_z = \pm(\kappa_s \pm \kappa_\ell)$, such modes being named *sidebands*.

In the context of our spectral DNS, we identify the first six non-zero spanwise discrete Fourier modes $\kappa_z = \pm(\Delta\kappa_z, ..., 6\,\Delta\kappa_z)$ as the large-scale, modulating signal. Bear in mind that the simulation grid is equally spaced in the Fourier-κ_z direction, the spacing being $\Delta\kappa_z = 2\pi/L_z \approx 0.898/h$. Consider now a generic small-scale carrier with wavenumber $\kappa_z = \kappa_s$ being modulated by the large modes; the sideband will comprise the six discrete Fourier modes preceding and following κ_s, namely $\kappa_z = \pm\kappa_s \pm (\Delta\kappa_z, ..., 6\,\Delta\kappa_z)$. As an example, figure 5.2 highlights the sideband of mode $\kappa_s = 14\Delta\kappa_z$; the integer n_z there referenced is defined as:

$$n_z = \kappa_z/\Delta\kappa_z\ . \tag{5.10}$$

By suppressing the sidebands of each possible small-scale carrier in our simulation, we make amplitude modulation non-representable in our domain - in other words, we suppress it. Practically, this is done by suppressing six spanwise modes every seven for the small scales, as shown in figure 5.2; the effective spacing $\Delta\kappa_{z,\mathit{eff}}$ between non-zero (or, more precisely, non-damped) spanwise small-scale modes is thus increased from $\Delta\kappa_{z,\mathit{eff}} = \Delta\kappa_z$ to $\Delta\kappa_{z,\mathit{eff}} = 7\Delta\kappa_z$. This is done only in proximity of the wall ($y^+ \leq 40$), where positive modulation takes place, in order to limit intrusiveness. Hence, $\varkappa_\mathrm{AM}$ is defined as:

$$\varkappa_\mathrm{AM}\left(\kappa_x^+, \kappa_z^+, y^+\right) = \begin{cases} 1, & \text{if } y^+ \leq 40 \ \wedge \ n_z/7 \notin \mathbb{Z} \ \wedge \ n_z > 6 \\ 0, & \text{otherwise} \end{cases} , \tag{5.11}$$

where $\mathbb{Z}$ is the set of integer numbers. Once again, the value of κ_x plays no role in the above definition, so that suppression is active for all κ_x modes in correspondence of values of κ_z that get suppressed.

Notice that the large scales are here effectively defined as having $|n_z| < 7$, which translates to $\lambda_z^+ > h^+ = 1000$ in terms of wavelengths. This value of the large-small threshold wavelength is larger than

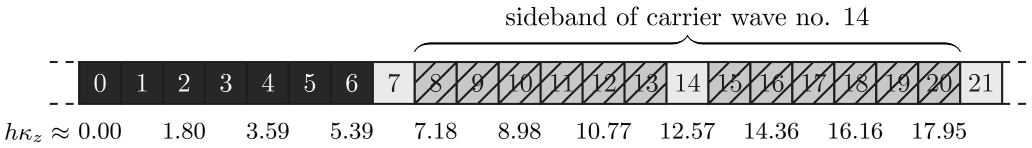

Figure 5.2: Schematic representation of the suppression of modulation for the discretisation used in this paper. Each box represents a spanwise Fourier mode with its value of n_z; wavenumbers are reported under the boxes. Note that only low-wavenumber, positive modes are represented. Large-scale, modulating modes are coloured in black, while small-scale carrier ones are white. The modes being suppressed, namely the sideband of each carrier, are cancelled out. Adapted from [MY23].

the one stated in §5.1 and will be exclusively used in cases where modulation is suppressed, also for the calculation of C^*_{AM}. The different choice is meant to limit intrusiveness of the forcing: by choosing a larger threshold wavelength, not only the bandwidth of the large scales is reduced, but also the width of the sidebands of small carrier modes is reduced. Since these sidebands are here being suppressed, the smaller the sidebands, the smaller the amount of energy being subtracted from the flow.

The effect of this forcing on scale interactions is better understood by considering triadic interactions (see e.g. §2.3.4, or Cho et al., 2018) between spanwise Fourier modes. These interact in pairs through the non-linear term of the Navier-Stokes equations, resulting in a transfer of momentum (and energy) to a third mode. Using the angle addition formula as before, it can be shown that, where the forcing is active, interactions between small-scale modes cannot yield a transfer of energy to (nor from) large scales, with the exception of the large $\kappa_z = 0$ mode. Moreover, interactions between a large-scale (except $\kappa_z = 0$) mode and a smaller-scale (except $\kappa_z = 7\Delta\kappa_z$) one would produce an energy transfer to (or from) suppressed modes; the effects of these interactions are thus nullified.

As for C^*_{AM}, similar considerations show that, where the forcing is active, the signal u_s^2 has no content on large-scale Fourier modes, except for mode $\kappa_z = 0$. Thus the covariance $C^*_{\mathrm{AM}} = \langle u_s^{+2}\, u_\ell^+ \rangle$ has at most contributions from the interaction between u_s^2 and mode $\kappa_z = 0$ of u_ℓ; all other contributions are null. In other words, the only modulation-like effect which could be observed is a correlation in time (and in the streamwise direction) between the spanwise-average of u_ℓ and the spanwise average of u_s^2. This is a very weak effect, as will be shown later; moreover, if it were removed, the value of C^*_{AM} should be zero where the suppression of modulation is performed." [MY23]

5.1.3 Energy-conserving smoothed spectra

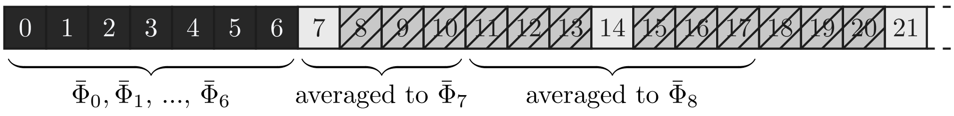

Figure 5.3: Schematic representation of the averaging procedure used to recover smooth (co-)spectra of the Reynolds stresses. Adapted from [MY23].

"The modulation-suppressing procedure described in §5.1.2 produces a banded pattern in the spanwise (co-)spectra of the Reynolds stresses, as can be seen later in figure 5.13, for instance. The banded pattern does not only affect the near-wall region where the forcing is active, but rather propagates to the core of the channel, making the spectra hard to visualise. We therefore define a smoothed version $\bar{\Phi}$ of a generic spanwise (co-)spectrum Φ that improves the visualisation while being energy-conserving, meaning that the correct values of the Reynolds stresses can be recovered by integrating the smoothed spectral contributions given by $\bar{\Phi}$.

In the context of our numerical simulations, the spanwise spectrum Φ (at any wall-normal distance) is evaluated at a discrete set of equally spaced spanwise wavenumbers $\kappa_{z,n} = n_z \Delta\kappa_z$" [MY23] (where for simplicity n_z is assumed, without loss of generality, to be a non-negative integer), yielding a set $\Phi(\kappa_{z,n})$. Notice that the notation used so far conceals the fact that only discrete values of κ_z are admissible (as this generally improves readability, see §2.3.1); however, the present discussion requires explicit handling of the discretisation. "The smoothed spectrum is evaluated at a set of spanwise wavenumbers corresponding to modes that are not suppressed, yielding a set of values $\bar{\Phi}_j$ (j also being a non-negative integer). These are defined so that:

$$\begin{cases} \bar{\Phi}_j = \Phi(\kappa_{z,\,j}) & \text{if } 0 \leq j \leq 6 \\ \bar{\Phi}_j = \frac{1}{4}\sum_{i=0}^{3} \Phi(\kappa_{z,\,j+i}) & \text{if } j = 7 \\ \bar{\Phi}_j = \frac{1}{4}\sum_{i=-3}^{0} \Phi(\kappa_{z,\,n_{max}+i}) & \text{if } j = j_{max} \\ \bar{\Phi}_j = \frac{1}{7}\sum_{i=-3}^{3} \Phi(\kappa_{z,\,7(j-6)+i}) & \text{otherwise} \end{cases} \tag{5.12}$$

where n_{max} and j_{max} are the maximum values of n_z and j respectively. In other words, the spectrum is left untouched for large-scale modes; for the small scale modes, the value of Φ of each non-suppressed mode is averaged with the values of Φ of the six adjacent suppressed modes (three per side) to yield a single value of $\bar{\Phi}$. For the first ($j = 7$) and for the last ($j = j_{max}$) small-scale modes the average is performed only on one side, that is, only with the three preceding or successive suppressed modes. Notice that the number of points in the spanwise direction is chosen so that the mode with the highest wavenumber is not suppressed. The procedure is illustrated in figure 5.3, and yields a sensible spectral representation of the Reynolds stresses when applied at all wall-normal positions - including those at which the forcing is not active. See, for instance, figure 5.13." [MY23]

5.2 Results

"To begin with, statistics of interest are reported for the reference (unperturbed) LSD and MSU cases for reference and validation." [MY23] The main difference between LSD and MSU cases is that "large-scale structures of streamwise velocity fluctuations are significantly enhanced in MSUs due to the impaired nature of the pressure-strain correlation (Abe et al., 2018); they are quasi streamwise-invariant and thus lack the characteristic inclination observed in larger domains. Figure 5.4 shows the mean velocity profile $U^+ = \langle u \rangle^+$ (panel a) and fluctuation intensities (b) for two LSD and MSU unperturbed simulations, used as a reference case for the numerical experiments[1]. Both cases compare well against literature LSD data by Lee and Moser (2019) and MSU data by Abe et al. (2018). The enhanced streamwise fluctuations of the MSU, clearly visible from figure 5.4(b), result in a plateau for $\langle u'u' \rangle^+$ that is otherwise visible at much higher values of Re in longer domains. On the other hand, v' and w' fluctuations have lower intensity in MSUs, and the mean velocity profile exhibits an anomalous wake region starting at about $y^+ \approx 400$ (Flores and Jiménez, 2010). An enhancement of u' fluctuations in the MSU can also be observed from the spanwise one-dimensional spectrum, reported in figure 5.5(a,b) for the LSD and MSU

---

[1] Interestingly, the MSU simulation produces larger values of the mean velocity at the centerline. That is, the same pressure gradient produces a larger flow rate in the MSU: drag reduction is observed. This is surprising. As explained in the main body of the text, MSUs have stronger $u'u'$ structures; it appears counterintuitive that this would be associated to drag reduction. A possible explanation could be the following. Although streamwise fluctuations are stronger in the MSU, wall-normal ones are weakened with respect to the LSD (as can be seen in the present data) owing to the impaired pressure-strain energy redistribution (Abe et al., 2018). Possibly, then, the weakened wall-normal fluctuations result in a weakened anti-correlation between u' and v', which can explain the observed drag reduction. Indeed, the shear stress $\langle u'v' \rangle$ – and not the normal $\langle u'u' \rangle$ one – is the only dynamically relevant (active) Reynolds stress. In any case, even if the impaired nature of the pressure-strain term could not explain the present observations, the large scales of the MSU must be comparatively inefficient at producing Reynolds shear stress.

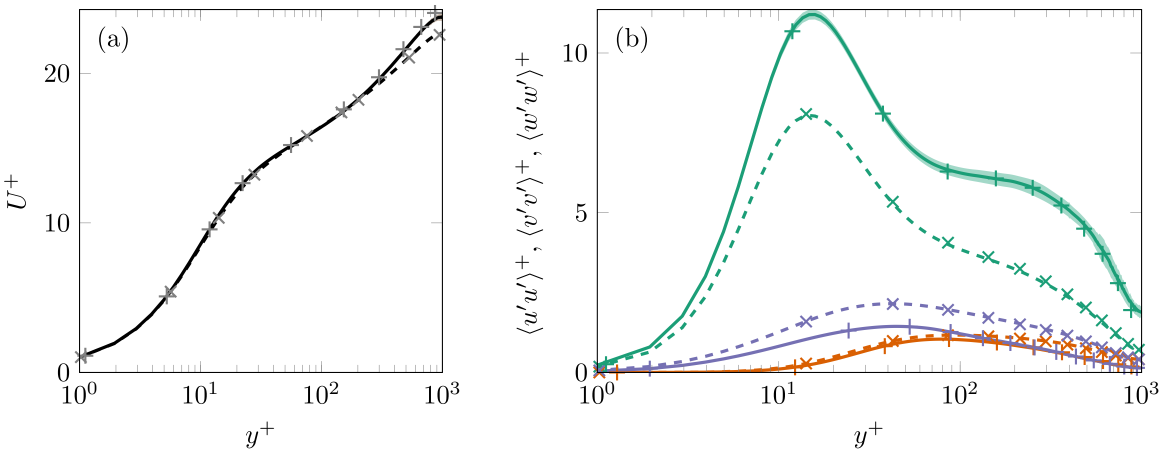

Figure 5.4: Profiles of the mean velocity (a) and fluctuation intensities (b) for the unperturbed MSU (solid) and LSD (dashed) cases. Green: $\langle u'u'\rangle^+$. Red: $\langle v'v'\rangle^+$. Blue: $\langle w'w'\rangle^+$. The uncertainty at a 99.7% confidence level quantified as described in Russo and Luchini (2017) is shown for the MSU case as a shaded area. MSU data by Abe et al. (2018) is marked with $+$, while $\times$ indicates LSD data by Lee and Moser (2015). Adapted from [MY23].

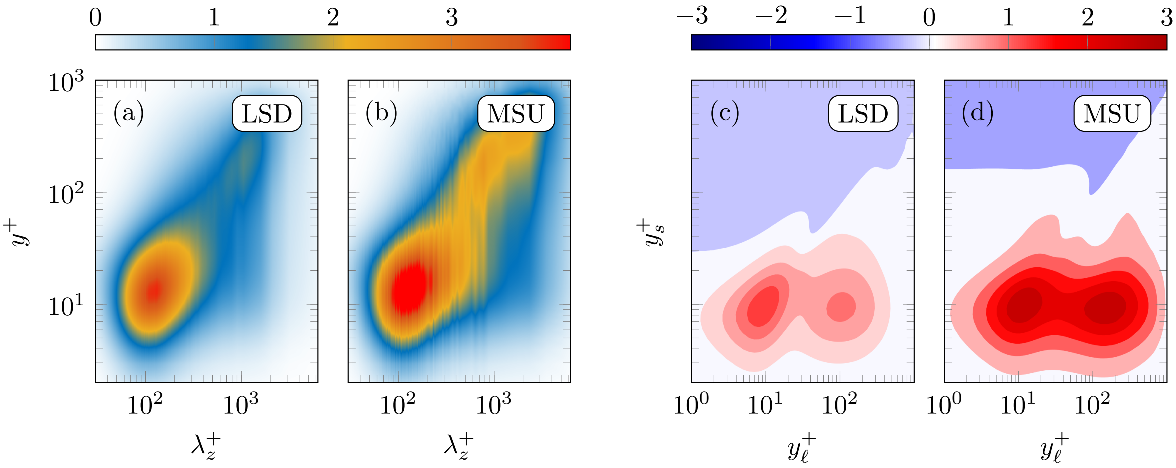

Figure 5.5: All panels refer to reference simulations (without forcing). Premultiplied one-dimensional spanwise spectra $\kappa_z^+ \Phi_{uu}^+$ of the streamwise velocity fluctuations (a,b). Amplitude modulation coefficient C^*_{AM} (c,d); colour levels starting from zero (white) with increments of ± 0.3 for the LSD (panel c) and ± 0.5 for the MSU (panel d). Adapted from [MY23].

cases. Although both spectra share the same qualitative behaviour, with a small-scale, buffer-layer energy peak and a large-scale, outer-layer one (see also Lee and Moser, 2018), both these peaks are more intense for the MSU case.

It is possibly these energised large scales, combined with the absence of their meandering, that make amplitude modulation more intense in the MSU; this can be observed from figure 5.5(c,d), which compares the distribution of the two-point scale-decomposed skewness C^*_{AM} for the LSD and the MSU. Apart from the intensity, the qualitative structure of the C^*_{AM}-map of figure 5.5 in the $y_s^+ < 30$ region is the same for both LSD and MSU, suggesting that the smaller domain can still correctly capture scale-interaction phenomena such as amplitude modulation. In agreement with previous observations (Bernardini and Pirozzoli, 2011; Agostini et al., 2016; Dogan et al., 2019), two positive peaks are present at $y_s^+ \approx 10$, one of which lies on the diagonal of the plot ($y_\ell^+ \approx 10$), whereas the other will be referred to as off-diagonal ($y_\ell^+ \approx 150$). As already discussed, the diagonal peak of C^*_{AM} is affected by the skewness of the velocity signal (Mathis et al., 2011b; Schlatter and Örlü, 2010), whereas the off-diagonal peak is not, hence consti-

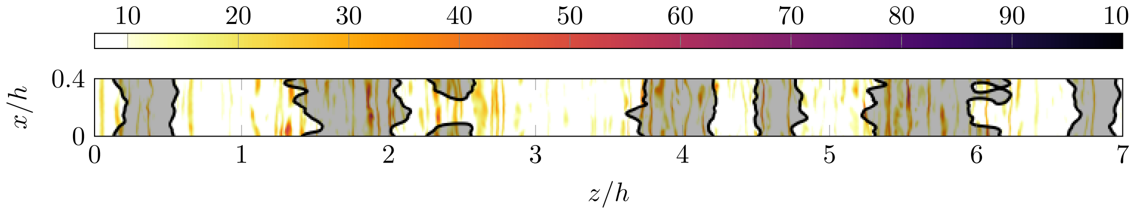

Figure 5.6: Visualisation of an instantaneous streamwise velocity field on wall-parallel planes for the reference (unperturbed) MSU simulation. Colour: small-scale activity u_s^{+2} at $y^+ = 10$. Black lines: contours of zero-large-scale fluctuations ($u_\ell^+ = 0$) at $y^+ = 100$. Regions of positive large scales are shaded. Adapted from [MY23].

tuting a more reliable detector of modulation phenomena (Bernardini and Pirozzoli, 2011). As expected, a negative-C^*_{AM} region is also present, mainly involving small scales in the outer layer; the contour of this region becomes much more regular for the MSU case, and can be approximated by a straight horizontal line $y_s^+ \approx 100$ for $y_\ell^+ < 150$. This regularity is possibly a consequence of the lack of inclination of the large structures, which are quasi-homogeneous along the streamwise direction in the MSU cases.

A graphical representation of what the skewness coefficient C^*_{AM} quantifies is provided in figure 5.6. Here, the near-wall ($y_s^+ \approx 10$) small scale activity u_s^{+2} and the log-layer ($y_\ell^+ \approx 100$) large scale signal u_ℓ^+ from an instantaneous flow realisation of the unperturbed MSU simulation are represented in a streamwise-spanwise plane. Notice that these wall-normal coordinates correspond to the off-diagonal peak of the C^*_{AM}-map (figure 5.5 c,d), and that the covariance of the two represented quantities corresponds to C^*_{AM}. Expectedly, regions of positive large scales exhibit increased values of the small-scale activity with respect to regions of negative large scales, although this correspondence is imperfect as it only holds in a statistical sense. An analogous consideration was done by Hutchins and Marusic (2007b), who first observed amplitude modulation in experimental data, except that modulation was seen in time signals. Due to the minimal streamwise domain size, in MSUs regions of positive (or negative) large scales extend all across the streamwise domain length, whereas changes of sign of the large scales are mainly encountered along the spanwise direction. Hence, in MSUs the correlation between u_ℓ and u_s^2 is mainly to be seen in the spanwise direction." [MY23]

5.2.1 Suppression of superposition

"In §5.1.1 it was shown how the footprint of large scales at the wall (also known as superposition) can be numerically removed through modal damping; essentially, energy is removed from selected near-wall large scales. To validate the data produced with this forcing, some simple statistics are reported in figure 5.7. Figure 5.7(a) shows the mean velocity profile for the forced MSU and LSD cases as compared to the unperturbed simulations; desirably, the suppression strategy has no substantial effect on the mean velocity profile, neither in the inner nor in the wake region. The same holds for the distribution of Reynolds shear stress (b), as well as for the spanwise and wall-normal fluctuation intensities (panels c, d), although the forcing is also active on these two components of the velocity. This suggests that the removed motions only have a marginal relevance for both the inner and the outer dynamics of the flow.

The forcing only has a significant effect on the streamwise fluctuation intensity $\langle u'u' \rangle$ (figure 5.7c-d), which is significantly reduced in the near wall region; this drop in turbulent kinetic energy is expected, as the forcing subtracts power from the flow in proximity of the wall. The drop is larger for the MSU case (panel c) than for the LSD (d) one; indeed, as explained above, the removed large scales are more intense in the former case." [MY23] Moving further away from the wall, reduced values of $\langle u'u' \rangle$ are observed

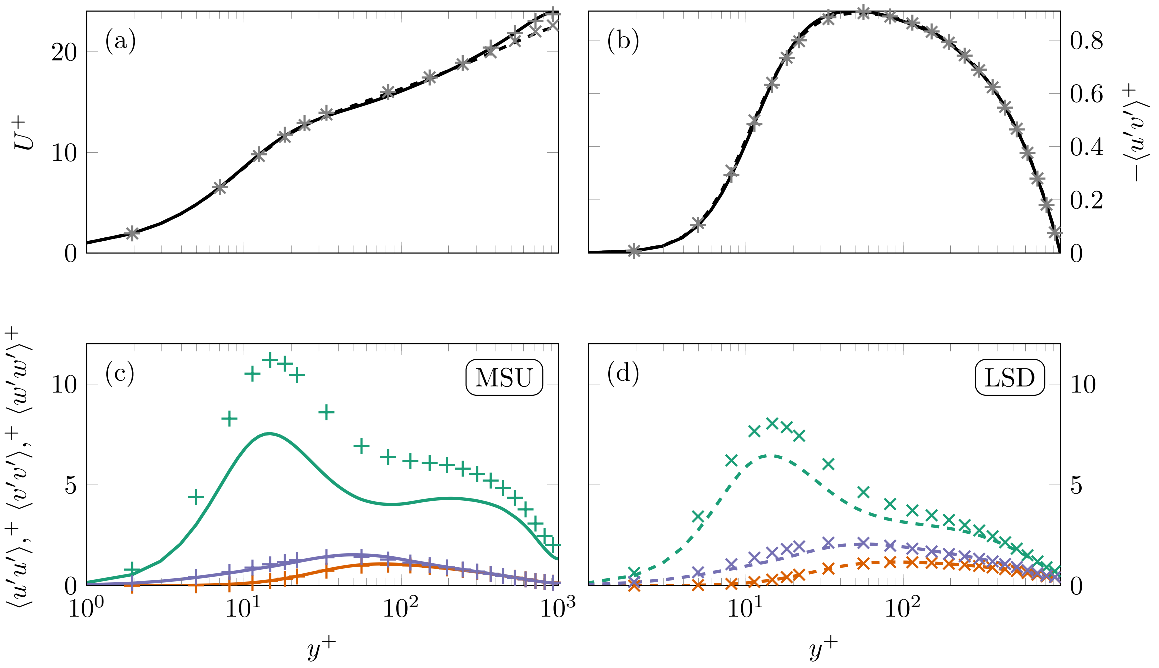

Figure 5.7: One-point statistics for the simulations with suppression of superposition (solid line for MSU; dashed for LSD). For comparison, the same statistics are reported for the reference unperturbed cases (+ for MSU; × for LSD). Mean velocity profile (a), Reynolds shear stress (b), fluctuation intensities (c, d; colours as in figure 5.4). Adapted from [MY23].

for almost the entirety of the channel height, even in regions where the control force is not active. It is only at the centerline that the $\langle u'u' \rangle$ values of the forced and unforced simulations are comparable.

“The effect of superposition removal is further explored by analysing the spanwise energy and turbulent transport spectrum, as well as the C^*_{AM}-map. These are reported in figure 5.8 for the MSU case; results for the longer domain are not shown for brevity, except for the C^*_{AM}-map.” [MY23] For each plot, data from both the reference, unperturbed simulations (left panel) and from simulations where superposition is suppressed (right panel) is shown to facilitate the comparison. “The energy spectrum (a) and the turbulent transport one (b) indicate success of the suppressing action: when the suppression is active, not only no energy content is present for the superposition modes as expected, but also no energy content is being deposited by $\widehat{\mathcal{T}}_t^+$ on these modes. For wavelengths at which modal damping is active (b, right panel), the usual near-wall positive peak of $\widehat{\mathcal{T}}_t^+$ seen in the left panel vanishes, and reappears at the nearest position to the wall where the suppressing action is absent. This also results in the negative, large-scale region of $\widehat{\mathcal{T}}_t^+$ being shifted towards the core of channel.” [MY23] In the outer layer, large scales are still observed even when their near-wall footprint is suppressed (figure 5.8a, right panel). Their persistence might suggest that the outer flow region has some degree of autonomy from the wall, consistently with the results of Flores and Jiménez (2006), Mizuno and Jiménez (2013) and Kwon and Jiménez (2021). However, the amount of energy found on large-scale modes is generally reduced with respect to the unforced simulations (a, left panel). In particular, the suppression of near-wall large scales appears to result in the lack of large-scale energy in the unforced region found at $y^+ \leq 100$. This could be explained as follows. Perhaps, the missing energy in this region is energy that is held by attached eddies; removing the near-wall part of the attached eddies results in their complete removal, so that energy is missing not only in the near-wall region but also at all the wall-normal heights reached by the attached eddies. According to this explanation, the outer-layer large-scale energy peak (possibly linked to VLSMs) which persists in the forced simulations could be interpreted to be contributed by detached

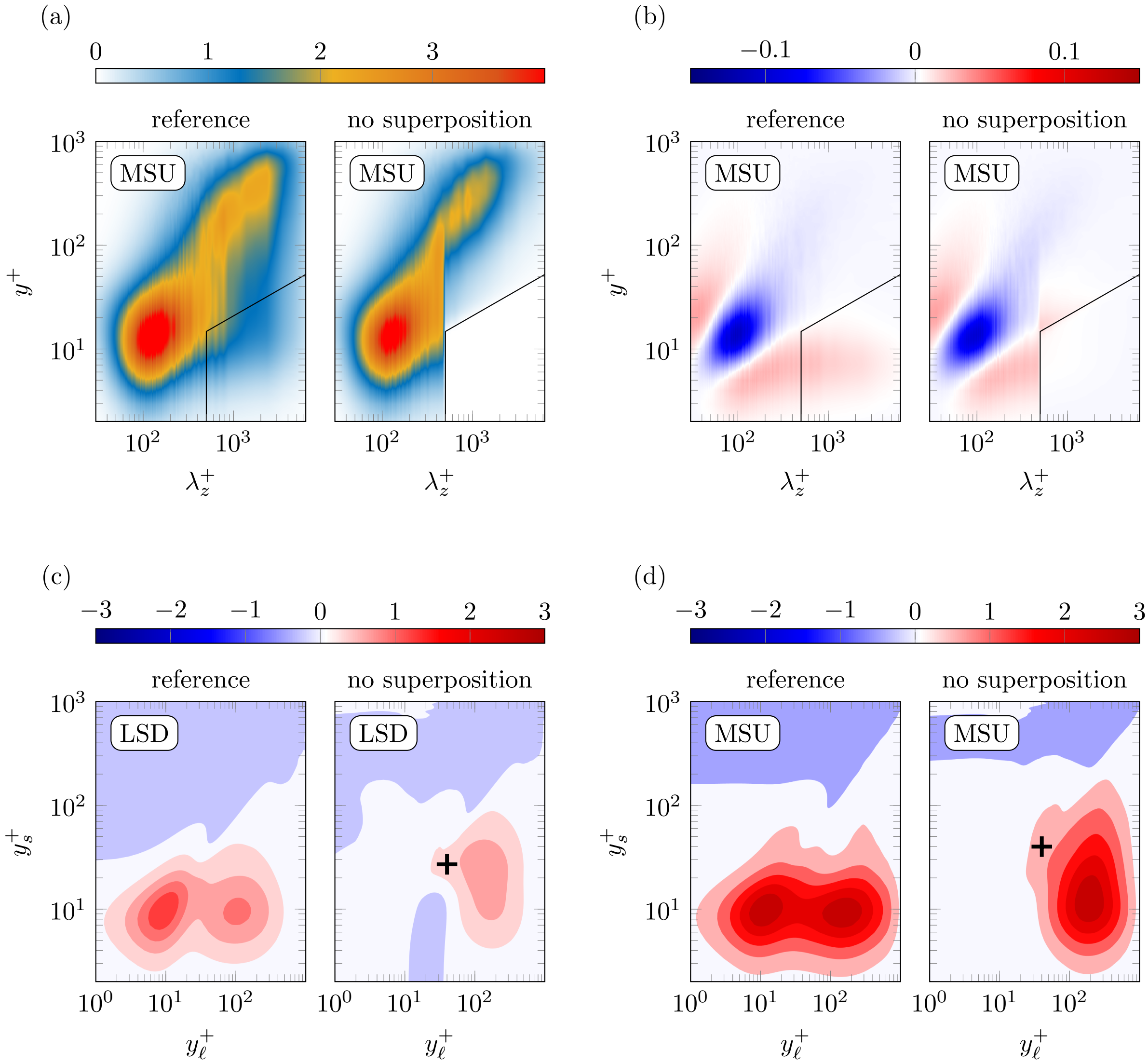

Figure 5.8: Each subplot (a-d) shows reference data from unperturbed simulations (left panel) and data from simulations where superposition is suppressed (right). Premultiplied spanwise spectra of the streamwise fluctuation ($\kappa_z^+ \Phi_{uu}^+$, a) and of the turbulent transport term ($\kappa_z^+ \mathcal{T}_t^+$, b) for the MSU case; a solid black line marks the border of the scale-space region which is targeted by the superposition-suppressing forcing. Amplitude modulation coefficient C^*_{AM} for the LSD (c) and MSU (d) cases; a black cross marks a possible secondary peak appearing in forced simulations. Colour levels as in figure 5.4. Adapted from [MY23].

eddies. Notice that such an explanation is purely speculative, and that the thorough discussion of such a complex topic is out of the scope of this chapter.

"Unexpected results can be observed in the C^*_{AM}-maps of figure 5.8(c) and (d)." [MY23] As previously discussed, two C^*_{AM}-peaks can be seen in reference data (as seen in figure 5.5 and reproduced in the left panels of 5.8c and d). When superposition is suppressed (right panels), "the diagonal peak predictably disappears, whereas the off-diagonal one is not only still present, but also roughly unaltered in intensity. This is a sign of the persistence of modulation phenomena in the buffer layer ($y_s^+ \approx 10$), suggesting that superposition and modulation are not so closely interlinked as previously thought: one phenomenon can be suppressed without significantly affecting the other. It is noteworthy, moreover, that the large scale signal u_ℓ is being entirely suppressed for $y^+ < 14.7$, whereas the small scale signal still exhibits modulation in that region; this clearly rules out the possibility that amplitude modulation

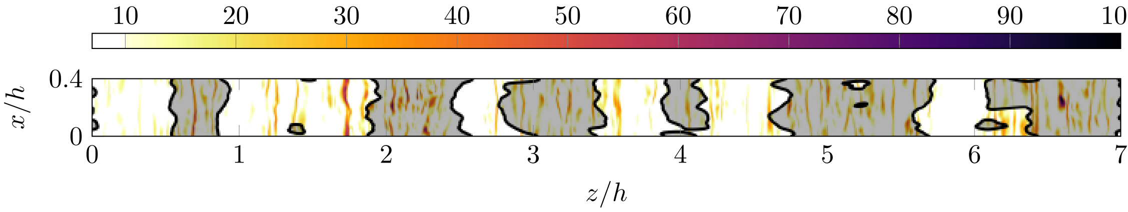

Figure 5.9: Visualisation of an instantaneous streamwise velocity field on wall-parallel planes for the MSU simulation with suppression of superposition. Colour: small-scale activity u_s^{+2} at $y^+ = 10$. Black lines: contours of zero-large-scale fluctuations ($u_\ell^+ = 0$) at $y^+ = 100$. Regions of positive large scales are shaded. Adapted from [MY23].

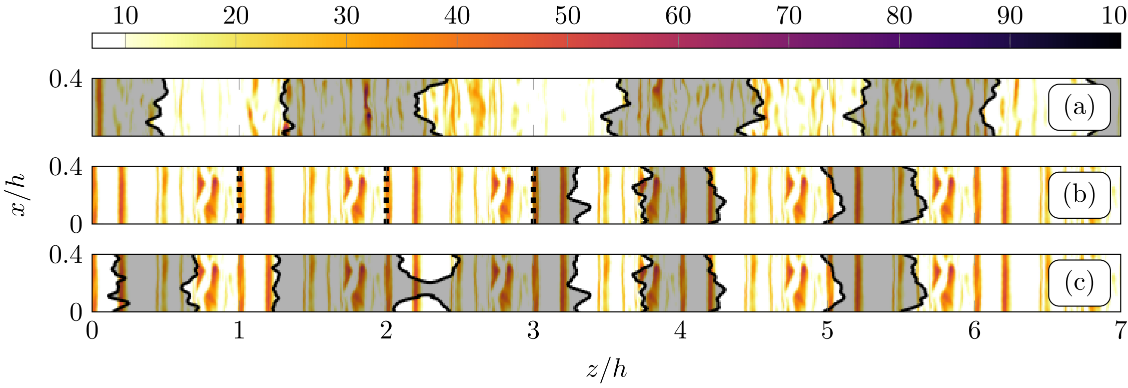

Figure 5.10: Visualisation of an instantaneous streamwise velocity field on wall-parallel planes for the reference MSU simulation with $\lambda_{z,c}^+ = h^+ = 1000$ (a) and the MSU simulation with suppression of modulation (b, c). Colour: small-scale activity u_s^{+2} at $y^+ = 10$. Black lines: contours of zero-large-scale fluctuations ($u_\ell^+ = 0$) at $y^+ = 100$. Regions of positive large scales are shaded. In panel (b), large scales are plotted only for $z/h > 3$; on the left, dashed lines are used to highlight the reduced period of small scales. Panel (c): same as panel (b), but the large scales are plotted at all available spanwise positions. Adapted from [MY23].

is entirely caused by the superimposed, local large scales, or by fluctuations in the wall-shear stress. Since the superposition-suppressing forcing is active on all components of velocity, there cannot be any converging or diverging spanwise large-scale motion at the wall either.

The persistence of modulation phenomena is reinforced by figure 5.9, showing an instantaneous realisation of the near-wall small-scale activity u_s^{+2} and of the log-layer large-scale signal u_ℓ^+. No qualitative difference with respect to figure 5.6 can be observed, suggesting that not only the forcing does not significantly alter the flow structure, but also a correlation between the large scales and the small-scale activity is still present.

In spite of the above evidence, theories implying that modulation of the small scales is caused by near-wall large ones might still be able to capture the behaviour of the diagonal peak of the C^*_{AM}-map. Indeed, if the variation of the amplitude of the small-scale signal is caused by the large-scale shear, as proposed for instance by Agostini and Leschziner (2019a), a positive peak of C^*_{AM} should appear at the nearest wall-normal position where no modal damping is active. A weak diagonal peak (marked by a black cross) seems to appear in figure 5.8(c,d) at $y_s^+ \approx 30 - 40$; however, this peak cannot be clearly distinguished from the non-diagonal positive-modulation region, thus making further investigation necessary." [MY23]

5.2.2 Suppression of modulation

"The modulation-suppression strategy presented and explained in the spectral domain in §5.1.2 also has a clear physical interpretation. The small-scales u_s perceive a computational box whose spanwise periodicity is forcedly reduced to h (from $7h$, that is the spanwise size of the periodic simulation domain); indeed, the modal damping effectively increases the spacing $\Delta\kappa_{z,eff}$ between non-zero small-scale spanwise Fourier modes (see §5.1.2 or figure 5.2), which translates to a decrease of the spanwise period of u_s owing to the definition of the Fourier series (see §2.3.1, equation 2.49). Large-scale modes are not affected. The shortened spanwise period can be observed in figure 5.10(b), where near-wall small-scale activity u_s^{+2} and large-scales u_ℓ^+ from the log-layer are represented for a MSU with suppression of modulation. Patterns of u_s^{+2} have a spanwise period of $1\,h$, whereas the large-scale isocontours are qualitatively similar to figures 5.6 and 5.9, with a spanwise period matching the spanwise domain size ($7\,h$). As a consequence of the different period, large and small scales are now uncorrelated: x, z-regions of positive u_ℓ^+ (shaded in figure) do not correspond to regions of increased small-scale activity anymore, and vice-versa. The observed pattern differs from the one of figure 5.10(a), which shows the same plot for the reference MSU case – hence being a reproduction of figure 5.6, except that the spanwise threshold wavelength of the filter now matches the one used in this context ($\lambda_{z,c}^+ = h^+$, see §5.1.2). In the reference case, small- and large-scales appear to be correlated, as is later confirmed by calculating C^*_{AM}.

In light of the above, the present modulation-suppressing strategy does not differ much from the multi-block large-eddy simulation (LES) strategy of Pascarelli et al. (2000), which captures the near-wall small scales of a boundary layer by using a small periodic simulation domain. This is then reproduced several times in the spanwise direction to match the width of a larger domain, designed to capture large scales in the outer layer. Notice that, unlike ours, this approach (as well as many improvements of it, see Tang and Akhavan, 2016; Sandham et al., 2017) cannot reproduce near-wall large scales. A refined multi-block strategy was proposed by Chen and He (2022), which allows for the presence of near-wall small scales with a restricted spanwise period as well as near-wall large scales, analogously to the present approach. In their case, however, the coupling between blocks of different sizes manages to overcome the different periodicity and to reproduce modulation phenomena, which we instead suppress; also notice that, unlike all LES studies mentioned here, our concern is the investigation of the flow physics, rather than the reduction of computational costs.

Also for this forcing, one-point statistics produced in both MSU and LSD domains are compared to the ones of the unperturbed simulations (figure 5.11). As for the mean velocity (panel a), the usual collapse of the near-wall profile is seen. However, forced simulations differ significantly from the reference cases in the wake region, showing increased values of the flow rate at constant pressure gradient; that is, the forcing has a drag-reducing effect. The different velocity profiles are closely linked to the Reynolds shear stress profiles seen in panel (b). For $y^+ \leq 40$ (where the forcing is active), the profiles of forced simulations are shifted towards the channel core with respect to their references; this is expected in drag-reduced flows where near-wall turbulence is affected (e.g. flows over riblets; see, for instance, Luchini et al., 1991). Otherwise, there is good agreement between forced and reference simulations.

Profiles of the various fluctuation intensities (panels c-d) also show a qualitative agreement between forced and reference simulations, with a close collapse towards the channel centerline. Where the forcing is active ($y^+ \leq 40$), the profile of $\langle u'u' \rangle$ of the forced simulations appears to be slightly shifted towards the core of the channel, just like the Reynolds shear stress. Moreover, $\langle u'u' \rangle$ profiles reach slightly higher peak values in the forced simulations, whereas $\langle v'v' \rangle$ and $\langle w'w' \rangle$ show reduced values in the near-wall region. This suggests that the forcing alters the way energy is redistributed among components. Right

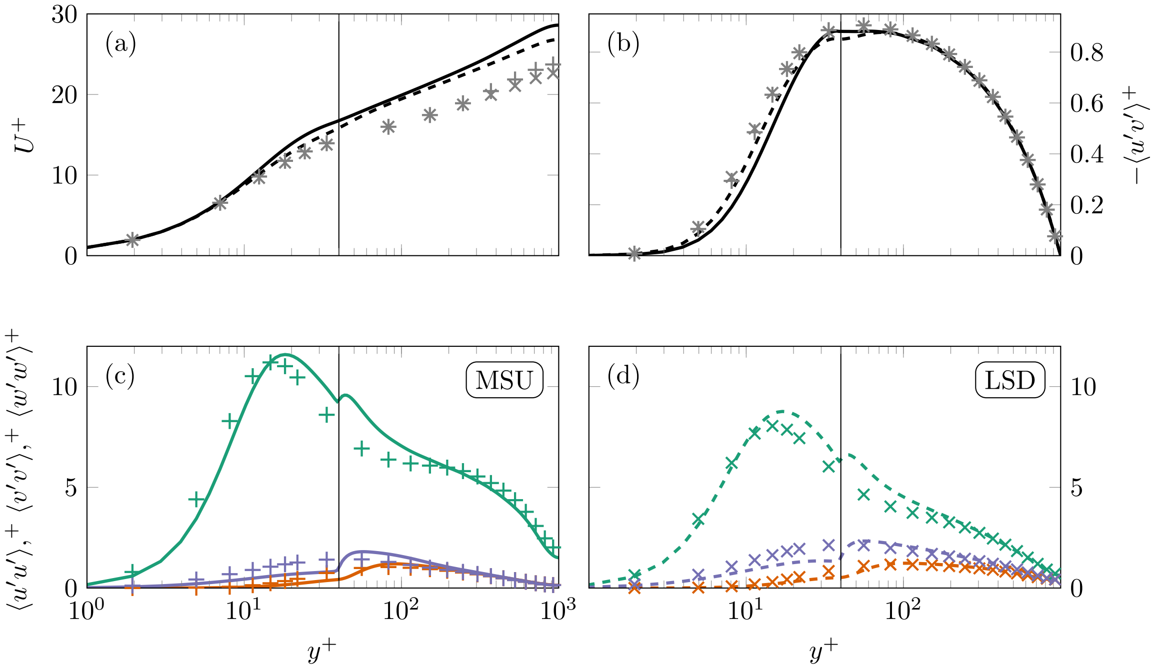

Figure 5.11: One-point statistics for the simulations with suppression of modulation (solid line for MSU; dashed for LSD). For comparison, the same statistics are reported for the reference unperturbed cases (+ for MSU; × for LSD). Mean velocity profile (a), Reynolds shear stress (b), fluctuation intensities (c, d; colours as in figure 5.4). A black vertical line marks the boundary to the left of which modal damping is active. Adapted from [MY23].

above the region where the forcing is active, at $y^+ = 50 - 100$, the values of the fluctuation intensites of all three velocity components rapidly increase in forced simulations, so that $\langle v'v' \rangle$ and $\langle w'w' \rangle$ reach their maxima and $\langle u'u' \rangle$ has a secondary peak. The suppressed modes effectively perceive a wall at $y^+ = 40$ and are therefore only free to develop above such position; it is their development that causes the presence of the observed peak and maxima. Interestingly, no corresponding bulging of the Reynolds shear stress can be observed in this region, suggesting that the energy produced by the developing suppressed modes is not coherent in terms of u' and v'.

The increased flow rate and changes in the buffer-layer fluctuation intensities are not to be attributed to the reduced spanwise period of the near-wall small scales, as confirmed by an additional simulation with a spanwise-restricted domain (not shown for brevity); we therefore attribute them to the modified interaction between small- and large-scales described in §5.1.2.

The C^*_{AM}-maps resulting from the suppression of modulation are reported in figure 5.12(b-d). The map is also shown for the reference MSU simulation (a), with an updated filter threshold wavelength to match the one used for simulations with suppression of modulation ($\lambda^+_{z,c} = h^+$, see §5.1.2). The suppressing action is successful: in the MSU case with suppression of modulation of panel (b), for instance, both positive peaks disappear from the C^*_{AM}-maps (in comparison to the reference case of panel a); the LSD case of panel (d) shows the same topology, but with lower values. Owing to the effect of mode $\kappa_z = 0$ (see §5.1.2), the value of C^*_{AM} is not zero as expected in the region where the forcing is active ($y^+_s \leq 40$): a slight positive peak can be observed at $y^+_\ell \approx y^+_s \approx 10$, as well as some regions where the correlation is negative. By recomputing the values of C^*_{AM} without including contributions from mode $\kappa_z = 0$ (panel c), a well-behaved map is recovered. A further analysis (not shown for brevity) reveals that the positive, diagonal peak of panel (b) is mainly caused by mode $(\kappa_x, \kappa_z) = (0, 0)$ - that is, by time fluctuations of a stream- and spanwise constant mode of u_ℓ. Fluctuations of this mode are expected to

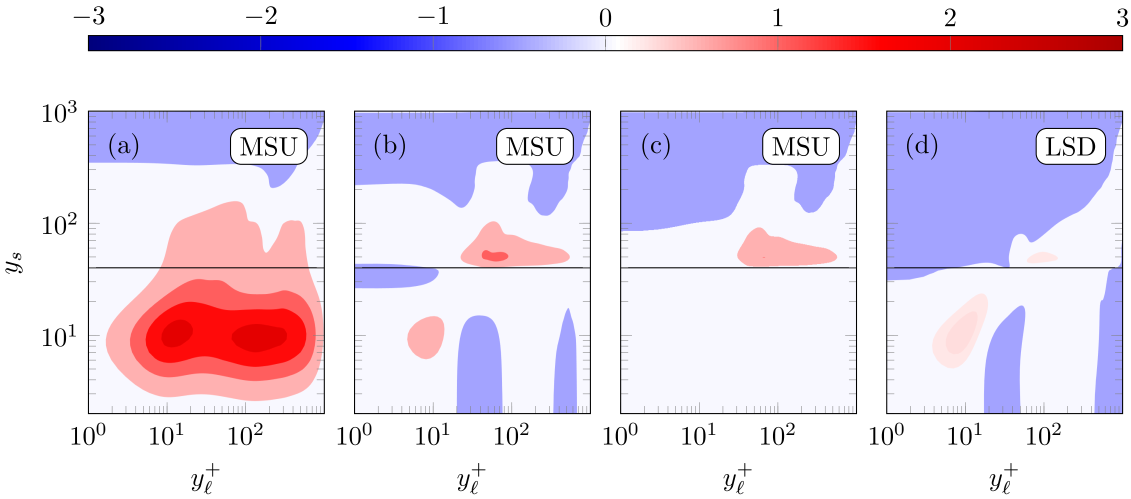

Figure 5.12: $C^*_{\rm AM}$-maps with a modified threshold wavelength $\lambda^+_{z,c} = 1000$. Reference, unperturbed MSU case (a); MSU with suppression of modulation (b-c), where in (c) the modulating effects given by mode $\kappa_z = 0$ have been removed; LSD with suppression of modulation (d). The modulation-suppressing forcing is active on small scales at $y_s^+ \leq 40$; the boundary of this region is marked with a black line. Colour levels as in figure 5.5 except for panel (d), for which colour levels are $(-0.5; 0; 0.18; 0.25)$. Adapted from [MY23].

be lower the larger the domain is, as the larger the domain the better the mode approximates the mean velocity. This explains why this diagonal, positive peak is weaker for the LSD, to the point that it seems to disappear. The remaining regions of negative-$C^*_{\rm AM}$ below $y^+ = 40$ are caused by spanwise-constant modes, whose streamwise wavelength is though small (as a consequence of the small domain size in that direction). Finally, right above the region where suppression of modulation takes place (that is, right above $y^+ = 40$), a positive diagonal $C^*_{\rm AM}$ peak appears; this is possibly linked to the fact that this area serves as a buffer layer for suppressed modes as previously discussed.

Having confirmed that the $C^*_{\rm AM}$-map behaves as expected, the focus is now turned to the main result of interest for this case - that is, energy spectra. These are shown in figure 5.13 for the MSU and LSD cases with suppression of modulation;” [MY23] spectra from reference simulations are also shown to facilitate the comparison. “The boundaries of the region that is targeted by the modulation-suppressing volume force are marked by a solid black line. Expectedly, spectra exhibit a striped pattern in this region when modulation is suppressed, alternating single, extremely excited modes with depressed regions corresponding to suppressed modes. Interestingly, the striped pattern is also observed further away from the wall where the forcing is not active, in what seems to be a bottom-up effect; at the same time, modes that were previously suppressed are now free to develop in this area, contributing to the unusual secondary peak in $\langle u'u' \rangle$ seen in figure 5.11. To recover a meaningful spectrum from the observed striped pattern, the smoothing technique described in §5.1.3 is used; results are shown in panels (c, f). It is revealed that the striped pattern hides a small-scale buffer-layer peak typical of wall-bounded turbulence, which is (at least qualitatively) correctly captured. Although near-wall small scales are being targeted by the forcing, their corresponding values of the spectrum are increased with respect to the unperturbed simulations (see panels a, d). Instead, near-wall large scales of the forced simulations show unusually low energy, as will be discussed below; overall, the increase in small-scale energy dominates, so that excess energy is seen on the streamwise fluctuations in the near-wall region (as observed in the $\langle u'u' \rangle$-profiles of figure 5.11).” [MY23] Large-scale energy is observed in the outer-layer as modulation is suppressed (panels c, f), possibly suggesting once again that outer layers are to some degree autonomous from the near-wall region (Flores and Jiménez, 2006; Mizuno and Jiménez,

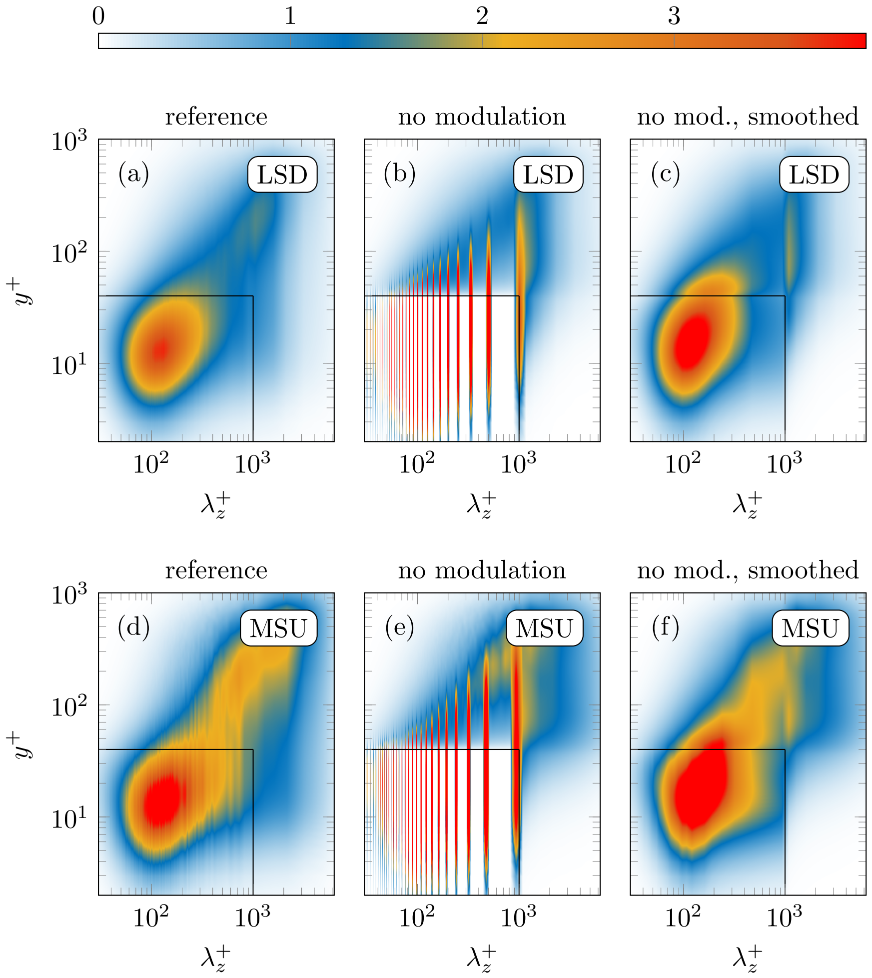

Figure 5.13: Premultiplied spanwise spectrum $\kappa_z^+ \Phi_{uu}^+$ of the streamwise fluctuation. The top row (a-c) shows LSD data, whereas the bottom one (d-f) shows MSU data. (a,d) Data from reference (unperturbed) simulations; (b,e) data from simulations with suppression of modulation; (c,f) same as (b,e), but the spectrum is smoothed using the technique presented in §5.1.3. The boundaries of the region that is targeted by the modulation-suppressing forcing are marked by a solid black line. Adapted from [MY23].

2013; Kwon and Jiménez, 2021). However, the effects of the near-wall, small-scale forcing are surely felt by outer-layer large scales too. In the LSD case, Fourier modes with a wavelength $\lambda_z = 1\,h$ appear to become dominant in the outer layer when modulation is suppressed, as can be seen by comparing panels (c) and (a). As for MSU simulations, the suppression of modulation appears to be linked to somewhat weaker outer-layer large-scale structures (see panels f and d). In brief, the present forcing does not fully remove outer-layer large scales, and yet its effect on them is not negligible. A thorough discussion of the matter is outside of the scope of this chapter.

“The reduction of the near-wall large-scale energy seen in figure 5.13 when modulation is suppressed cannot be trivially explained (panels c, f as compared to a, d); near-wall large scales are indeed not directly affected by the forcing. At $(y^+, \lambda_z^+) \approx (10.2, 1750)$ an 87% reduction of the value of Φ_{uu}^+ is observed for the MSU case (panel f as compared to d). This might be interpreted as the absence of superposition phenomena, possibly suggesting that superposition might be in fact enhanced by the large-scale modulation of the amplitude of the small scales. The above conjecture is supported by evidences of a small- to large-scale power transfer in the buffer-layer of wall-bounded flows observed, for instance, by Cho et al. (2018); Chiarini et al. (2022) and in chapter 3. Exploiting a generalised quasilinear approximation of a turbulent channel flow, Hernández et al. (2022) also support the idea that small-scale fluctuations may be involved in large-scale generation mechanisms. They found that the inhibition of particular triadic interactions involved in the inverse energy transfer in the spanwise direction within the near-wall region led to the suppression of the near-wall positive turbulent transport at large scales." [MY23] Similarly, it was discussed in §5.1.2 that modulation phenomena are intimately linked to triadic interactions; the present modulation-suppressing volume force directly blocks the large-small energy exchange, possibly explaining the observed results.

5.3 A discussion of the quasi-steady quasi-homogeneous theory

In this section, the results yielded by the suppression of superposition (§5.2.1) will be discussed, as they are relevant for the quasi-steady quasi-homogeneous (QSQH) theory of turbulence (Zhang and Chernyshenko, 2016). To help the discussion, some conditional views of the large scales found in both forced and unforced channel flows will be presented.

The conditional views are obtained as follows. As done by Hutchins and Marusic (2007b), the fluctuation field u'_i (where i indicates the i-th component) is conditionally averaged on ejection events (here simplified to $u' < 0$) in the log-layer ($y^+ = 150$) to yield the conditional average $\bar{u}_i$:

$$\bar{u}_i(y, r_z) = \left\langle u'_i(t, x, y, z + r_z) \mid u'(t, x, y^+ = 150, z) < 0 \right\rangle \tag{5.13}$$

where r_z is the conditioned spanwise coordinate, so that the condition point is found at $(y^+, r_z^+) = (150, 0)$. Choosing a condition point that lies in the log-layer helps capturing a large-scale event. Similarly, a conditional average of the wall shear stress is produced, yielding $\bar{\tau}_w$; notice that $\bar{\tau}_w$ captures not only the fluctuations of the wall shear stress, but also its mean value τ_w.

The conditional averages are shown in figure 5.14 for the reference (unforced) MSU simulation and the MSU simulation with suppression of superposition. In the reference case (panel a), the conditional average captures a large-scale ejection as intended: a large-scale region of negative streamwise fluctuation (blue colour) is flanked by two large-scale counter-rotating streamwise vortices (represented by the streamlines); both the vortices help induce an upwelling motion that coincides with the negative streamwise fluctuation. Moreover, the large-scale ejection is associated to a large-scaled region of below-average wall shear stress. As for the simulation with suppression of superposition (panel b), a similar picture is seen – except for some crucial differences in the near wall region. Away from the wall, a large-scaled region of negative streamwise fluctuation (blue colour) is still seen; such region is also flanked by the usual counter-rotating vortices. Although the vortices still extend to the near-wall region as they did in panel (a), they shrink in size in doing so, leaving space for some smaller circulatory motions that are marked in panel (b) by blue crosses. The conditional view then suggests that the superposition-suppressing volume force manages to break down large circulatory motions into smaller eddies in the near-wall region. Moreover, the pattern of streamwise fluctuation is also small-scaled in the near-wall region. Crucially for the coming discussion, the large-scale ejection seen in panel (b) is not associated to a large-scale region of below-average wall shear stress as it was in panel (a): the superposition-suppressing volume force breaks the large-scale wall shear stress pattern into a small-scale one.

To discuss how the results of §5.2.1 challenge the QSQH theory, an estimate of the value of the amplitude modulation coefficient C^*_{AM} will be now built with the help of some simplified QSQH-like assumptions. The core assumption underlying the QSQH theory is that small scales react to changes of the wall shear

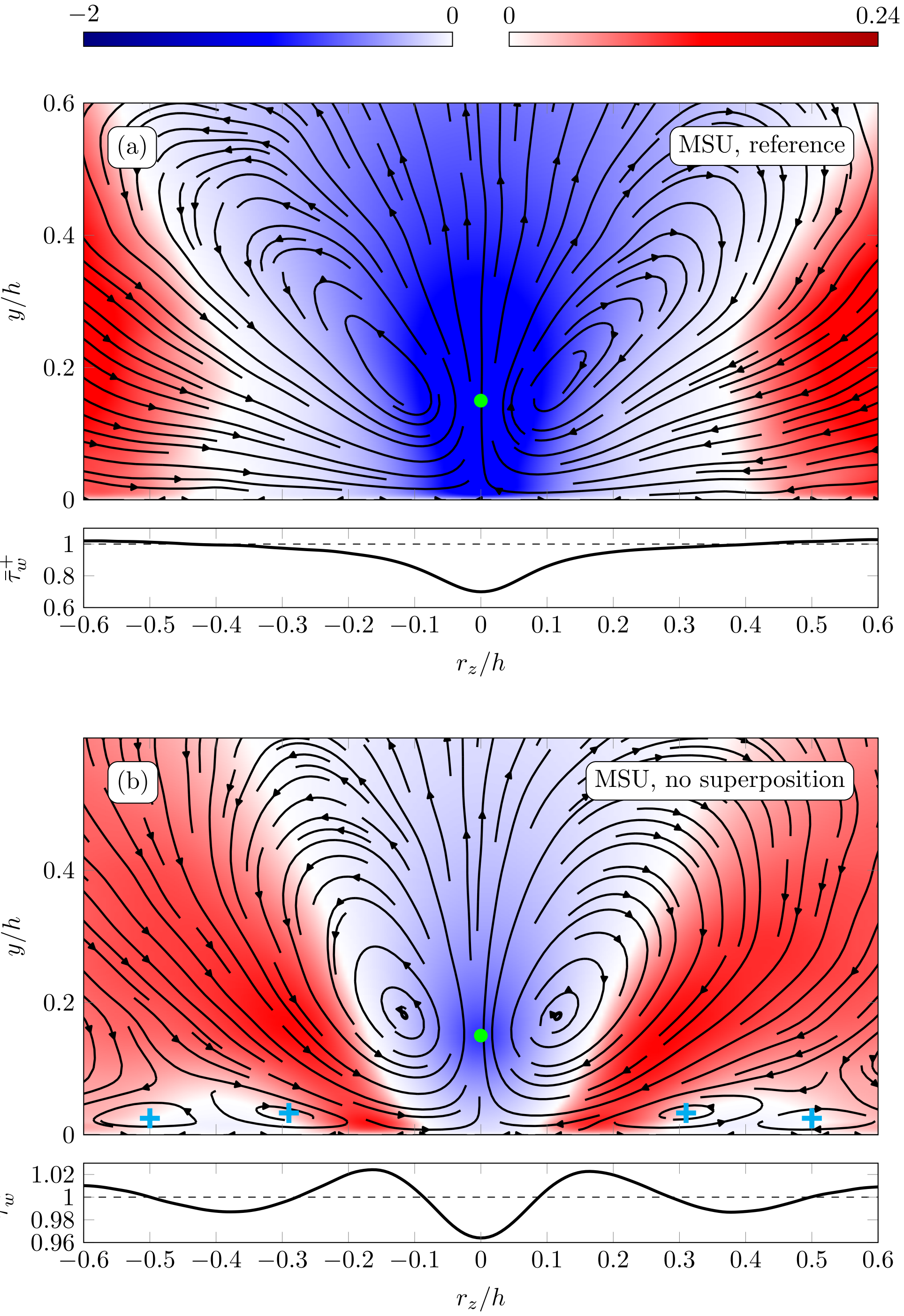

Figure 5.14: Conditional views of large-scale ejection events (see equation 5.13). Color: conditionally averaged streamwise fluctuation field $\bar{u}^+$. Streamlines: conditionally averaged cross-sectional fluctuation field $(\bar{v}, \bar{w})$. Below each main panel, a secondary panel shows the distribution of the conditionally averaged wall shear stress $\bar{\tau}_w$; a horizontal, dashed line indicates the unconditional average τ_w. (a) MSU reference (no forcing term) data; (b) data from the MSU with suppression of superposition.

stress with almost no delay in space or time[2] (Zhang and Chernyshenko, 2016). In particular, a large-scale wall shear stress $\tau_{w,L}$ is typically defined in the context of the QSQH theory; notice that $\tau_{w,L}$ captures both the average value τ_w and the large-scale fluctuations. In light of the QSQH assumption, the order of magnitude of the energy of the buffer-layer small scales can be written as:

$$u_s^2(t, x, y_{buf}, z) \approx k_1 \frac{\tau_{w,L}}{\rho} \tag{5.14}$$

where k_1 is some positive dimensionless constant and y_{buf} indicates some buffer layer wall-normal position. Notice that the above heuristic expression is a rough simplification of the theory presented by Zhang and Chernyshenko (2016); yet, it will suit the present discussion. To estimate C^*_{AM}, the order of magnitude of u_ℓ is also needed. Figure 5.14(a) suggests that, owing to the observed wall-normal coherence of large-scale fluctuations, the large-scale wall-shear stress fluctuation at the wall can be used to estimate the outer-layer large-scale velocity signal if the flow is unperturbed:

$$u_\ell(t, x, y_{ol}, z) \approx \frac{k_2}{\rho \mathcal{U}} \underbrace{(\tau_{w,L} - \tau_w)}_{\tau'_{w,L}} \qquad \text{if unperturbed} \tag{5.15}$$

where y_{ol} is some outer-layer position, k_2 some positive dimensionless constant, $\mathcal{U}$ some velocity scale and $\tau'_{w,L}$ the fluctuation of $\tau_{w,L}$. It follows:

$$C^*_{\mathrm{AM}}(y_{buf}, y_{ol}) = \frac{1}{u_\tau^3} \left\langle u_s^2(y_{buf})\, u_\ell(y_{ol}) \right\rangle \approx \frac{k_1 k_2}{\rho^2 u_\tau^3 \mathcal{U}} \left\langle \left(\tau'_{w,L}\right)^2 \right\rangle > 0 \qquad \text{if unperturbed} \tag{5.16}$$

The above estimate is coherent with the results shown in figure 5.5(d): if the flow is undisturbed, a positive value of C^*_{AM} is seen when considering buffer-layer small scales and outer-layer large ones (see the off-diagonal positive peak in figure). In other words, the amplitude of buffer-layer small scales is phase-locked to outer-layer large ones.

If superposition is suppressed, the estimate of u_ℓ given in equation 5.15 is not valid anymore. Indeed, as can be seen in figure 5.14(b), the distribution of conditioned wall shear stress (which is an approximant of $\tau_{w,L}$) becomes small-scaled, so that it cannot be used to estimate outer-layer large scales. If the QSQH assumption (as captured by equation 5.14) is valid, then a zero value of C^*_{AM} should be observed when considering buffer-layer small scales and outer-layer large ones:

$$C^*_{\mathrm{AM}}(y_{buf}, y_{ol}) \approx \frac{k_1}{\rho u_\tau^3} \left\langle \tau_{w,L}\, u_\ell(y_{ol}) \right\rangle = 0 \qquad \text{if no superposition and QSQH valid} \tag{5.17}$$

where $\langle \tau_{w,L}\, u_\ell(y_{ol}) \rangle = 0$ is identically zero owing to the orthogonality of Fourier modes (bear in mind that $\tau_{w,L}$ becomes small-scaled owing to the superposition-suppressing action). In other words, if one assumes small scales to be modulated by the distribution of wall shear stress, one would not expect to observe amplitude modulation when suppressing the superposition of large scales. Yet, the results seen in figure 5.8 contradict this expectation. Amplitude modulation is in fact observed regardless of whether the superposed large scales are removed or not; although it cannot be excluded that the wall shear stress has a modulating action on small scales as postulated by the QSQH theory, the present results suggest that at least another mechanism yielding the phase-locking of small and large scales must be at play.

As a final note, notice that the present discussion is not aimed at challenging the validity of the QSQH theory under regular circumstances. Indeed, a correlation between the amplitude of small scales and the

---

[2] If the small scales can be thought of as the fast modes of a turbulent flow, the QSQH theory is in effect equivalent to a static residualisation of the fast dynamics.

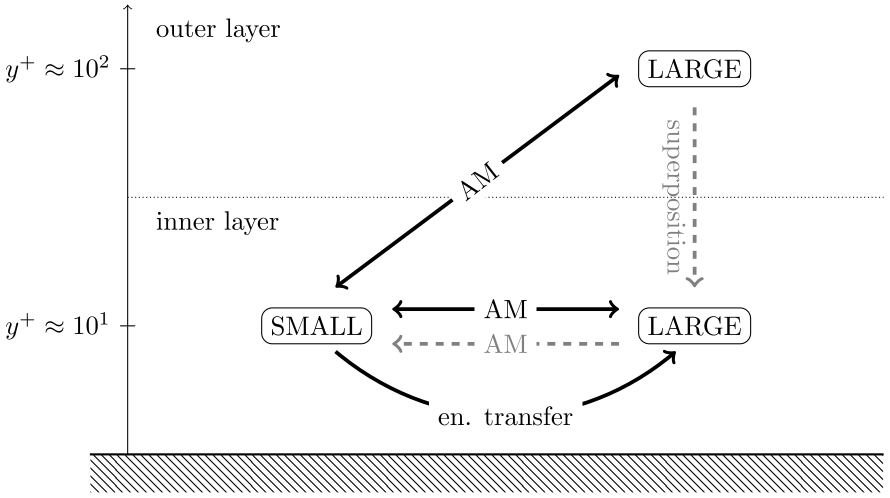

Figure 5.15: A schematic representation of the widely accepted scale interaction mechanism (grey arrows) and the present observations observations (black). Adapted from [MY23].

distribution of wall shear stress is usually observed (unless the flow is altered, as is done here), meaning that the theory can yield realistic results. Simply, the present discussion is yet another reminder that correlation does not imply causality.

5.4 Summary and conclusions

In this chapter, two numerical experiments are presented. One numerical experiment consists in preventing the superposition of the large scales at the wall, the other in preventing small scales from having a large-scaled envelope (suppression of superposition and of modulation respectively). The suppression of these two phenomena was achieved through “purposely designed body forces. Both standard, long streamwise domains (LSD) and minimal streamwise unit (MSU) domains have been used; no qualitative difference between the two has been observed in the results, although quantitative differences do arise. This suggests that MSUs can capture the fundamental mechanisms of the investigated scale interactions; a similar conclusion was drawn by Kawata and Tsukahara (2021). Streamwise-elongated structures that are longer than the computational box of the MSU are represented in such restricted domain as streamwise-invariant (Toh and Itano, 2005); the lifetime of these structures in a MSU reflects their streamwise extent in a LSD (Abe et al., 2018). Therefore, the large scales of a MSU are expected to modulate the amplitude of the small ones in the spanwise direction and in time; this is indeed what is observed.” [MY23]

The present findings concerning “scale interactions are summarised in figure 5.15. Suppression of superposition means that large scales are removed from the near-wall region. In absence of the near-wall large scales, it is revealed that the amplitude of the buffer-layer small scales still correlates well with the outer-layer large ones. According to some studies (for instance, Ganapathisubramani et al., 2012; Zhang and Chernyshenko, 2016; Agostini and Leschziner, 2019a), the removed large scales cause the amplitude modulation of the small scales; this is schematically depicted in figure 5.15 by a grey line. However, it is self-evident that the currently observed correlation cannot be explained as an effect of the superposed large scales, nor of the large-scale gradient at the wall or in its proximity, as these have been removed. Hence, amplitude modulation should not be understood as a local modulation mechanism, but rather as a correlation between the amplitude of the small scales in the buffer layer and the large scales from several wall-normal positions, represented in figure 5.15 by a black line. Other authors have linked scale interactions to the circulatory congregative and dispersive motions induced at the wall by log-layer sweeps and ejections (for instance, Toh and Itano, 2005; Hwang et al., 2016). Since the superposition removal affects all velocity components, the present results also challenge the theory of Toh and Itano (2005): in absence of near-wall large scales, there cannot be any spanwise large-scale wind transporting near-wall streaks towards large-scale ejections as proposed by the authors. Moreover, it is unclear how the large-scale circulatory structure associated to log-layer sweeps and ejections, observed for instance by Hwang et al. (2016), would penetrate to the wall as it normally does.

Suppression of modulation is performed near the wall by making modulation non-representable in the spectral simulation domain, more precisely by damping selected small-scale spanwise Fourier modes. In addition to blocking modulation, this forcing prevents the interaction between small-scale modes from resulting in a transfer of energy to large scales; moreover, triadic interactions between small and large modes are indirectly blocked. Interestingly, this forcing significantly affects the mean velocity profile, as the produced flow rate is substantially increased at constant pressure gradient. Also, near-wall large-scale modes seem to vanish, indicating that these might receive a significant amount of energy from the interaction of near-wall small scale modes, rather than from a top-down footprinting effect; this idea is schematically reported in figure 5.15 as a black line.

While the latter observation is in line with the evidence of a small-to-large energy transfer in the near-wall region found by Cho et al. (2018), Jacobi et al. (2021) and Hernández et al. (2022), the results yielded by suppression of superposition show that the current understanding of amplitude modulation is only partial. The present results do not exclude that, for instance, the large-scale velocity gradient may locally have a modulating action on small-scale activity as proposed by Agostini and Leschziner (2019a); moreover, the ansatz that near-wall small scales are locally modulated by near-wall large scales (for instance, Zhang and Chernyshenko, 2016) can still be a starting point for models that yield satisfactory results, owing to the spatial coherence of the large scales. Nevertheless, the present data indicates that a local mechanism involving near-wall large scales can – at best – only partially explain the correlation commonly known as amplitude modulation.” [MY23]

6 Temporal decay of turbulent secondary motions in channel flows

The results shown in this chapter are under consideration for publication at the time of writing – see Andreolli et al. [MY24b]. *The scientific colour maps by* Crameri *(*2023*) are used in this chapter to prevent visual distortion of the data and exclusion of readers with colour-vision deficiencies (*Crameri et al., 2020*).*

In an attempt to provide evidence in support of Townsend's hypothesis (see §1.2.6), the life time of secondary motions of different sizes is investigated in this chapter. Townsend's hypothesis is summarised by the following scientific question:

> **4. Is Townsend's hypothesis (as formulated in §1.2.6) plausible? Or, in other words: can secondary motions induced by a lateral wall shear stress pattern of a specific, large size self-sustain, so as to outlive motions of any other size?**

The investigation proceeds as follows. Instead of directly imposing a pattern of wall shear stress, a spanwise-heterogeneous roughness pattern is applied to the walls of a channel flow so as to produce a distribution of wall shear stress with the desired spanwise periodicity (size). The roguhness pattern also triggers the formation of secondary motions; once these reach a steady state, the roughness pattern is suddenly removed, so that the secondary motions decay and their life time can be measured. This is done numerically through direct numerical simulations.

A thorough description of the numerical setup used to produce the data shown in this chapter is given in §6.1. In §6.2, steady-state secondary motions over heterogeneous roughness are analysed and their main features are identified. These features are then tracked in time in §6.3 as the secondary motions decay, first using volume-averaged statistics (§6.3.1) and then using plane averages (§6.3.2) to achieve a finer level of detail. As the discussion of §6.3 is entirely based on averaged quantities, a description of how the fluctuation field evolves in time is presented in §6.4 for completeness. Finally, §6.5 contains a summarising remark.

6.1 Problem statement and numerical method

The present investigation is based on a set of "direct numerical simulations (DNS) of incompressible channel flows at constant pressure gradient (CPG). The peculiarity of the present dataset is that the simulations capture the decay of secondary motions of different sizes; this process is clearly not at a statistically steady state. Rather, the simulations describe the transition from a statistically steady state (flow with secondary motions) to a second steady state (flow in a smooth channel). To still be able to compute averages, each simulation is then run several times, each time starting from a different realisation of a given statistically steady state. Ensemble averages are then calculated." [MY24b]

The channel geometry is derived from the one described in §2.2.1 and is shown in figure 6.1. Let time be indicated by t. "At $t = 0$, the flow is at a statistically steady state in presence of secondary motions. These are sustained by a spanwise roughness pattern consisting of alternating streamwise-elongated strips of

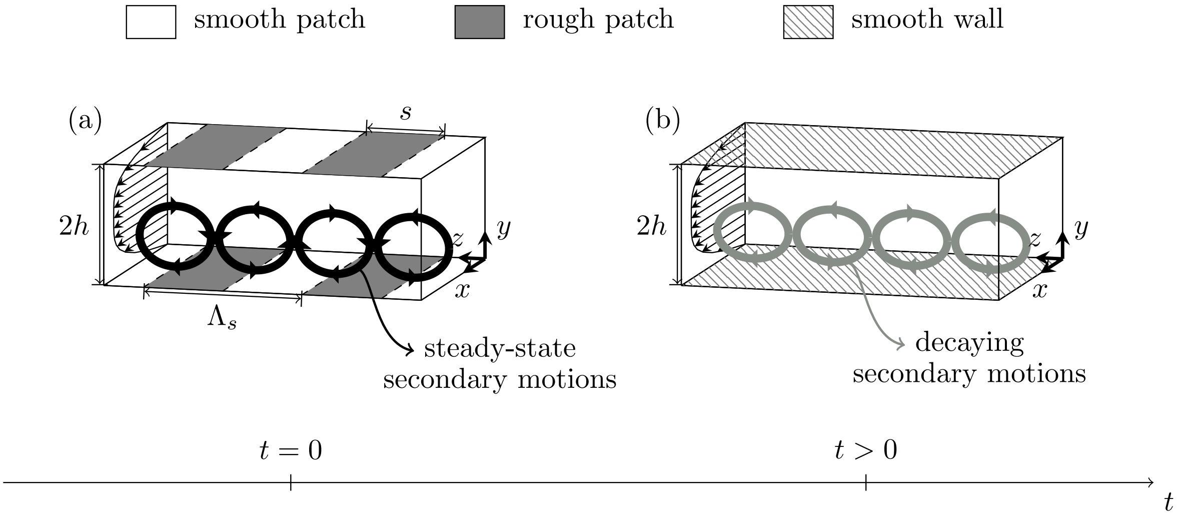

Figure 6.1: Schematic problem description with a graphical representation of secondary motions. The initial condition ($t = 0$) for the present numerical setup is shown on the left (a): steady-state secondary motions are observed over strip-type roughness. A generic point t in time (with $t > 0$) is depicted on the right (b): the secondary motions decay as they evolve over a smooth wall. Box size not to scale. Adapted from Neuhauser et al. (2022) and [MY24b].

smooth and rough wall. This setup will be referred to as *strip-type roughness*. The spanwise width of each strip is s, so that the spanwise period of the pattern is $\Lambda_s = 2s$. For $t > 0$, the spanwise roughness pattern is suddenly replaced by a smooth wall, so that the decay of the secondary motions is observed." [MY24b]

The simulations presented in this chapter differ from the ones shown so far in that they are not at a statistically steady state, nor they can be regarded as spanwise homogeneous. This leads to some differences in the way averaging is performed: although in the previous chapters the expected value $\langle ... \rangle$ of some quantity was calculated as a streamwise, spanwise and time average, the same cannot be done in the current context. Instead, the expected value "is computed as an average over multiple repetitions of the same simulation, over the streamwise direction and over multiple spanwise periods of the selected geometry (phase average, see Reynolds and Hussain, 1972); known symmetries in the wall-normal and spanwise directions are used to improve convergence wherever possible. The resulting statistics depend on the conditioned spanwise variable ζ and time, as well as on the wall-normal coordinate y. If an additional spanwise average is performed, the symbol $\langle \cdot \rangle_z$ is used.

As for inner units, the expected value $\tau_w(t, \zeta)$ of the wall shear stress is a function of time and of the spanwise coordinate" [MY24b] owing to the above discussion. "So are the friction velocity $u_\tau(t, \zeta) = \sqrt{\tau_w / \rho}$ and the viscous length scale $\delta_v(t, \zeta) = \nu / u_\tau$. For the calculation of the worst-case inner-scaled grid spacing, the maximum value $u_{\tau,m}$ of the friction velocity can be used:

$$u_{\tau,m} = \max_{t,\zeta} u_\tau(t, \zeta); \qquad \delta_{v,m} = \frac{\nu}{u_{\tau,m}}. \tag{6.1}$$

Leveraging the fact that the pressure gradient $-G,\ G > 0$ is forcedly kept constant during the simulations, a global friction velocity u_p and a length scale δ_p can also be defined:" [MY24b]

$$u_p = \sqrt{\frac{hG}{\rho}}; \qquad \delta_p = \frac{\nu}{u_p}. \tag{6.2}$$

Differently from the previous chapters, a plus superscript $(...)^+$ will be used to indicate quantities made non-dimensional with u_p and δ_p, and not with the usual viscous units. Similarly, the friction Reynolds number $Re_\tau = hu_p/\nu$ is defined by the global viscous velocity u_p. This choice is dictated by the fact that u_p has a constant value in time and in the spanwise direction, whereas the same cannot be said about u_τ. "The relation between global and local viscous units can be found by integrating the streamwise momentum balance of the Navier-Stokes equations." [MY24b] Bearing in mind that the bulk velocity U_b is the volume-average of the expected streamwise component,

$$U_b(t) = \frac{1}{2h} \int_0^{2h} \langle u \rangle_z \, \mathrm{d}y, \tag{6.3}$$

"the following relation is obtained:

$$\rho h \frac{\mathrm{d}U_b}{\mathrm{d}t} = hG - \langle \tau_w \rangle_z \, . \tag{6.4}$$

Under steady conditions ($t = 0$ and $t \to \infty$ for the problem considered here), the global u_p is the friction velocity defined by the spanwise average of τ_w." [MY24b] In other words, $u_p = u_\tau$ in the case of a statistically steady and spanwise homogeneous flow.

The lack of spanwise homogeneity also implies that a simple Reynolds decomposition is not suited to describe the present data. The mean velocity profile $U(t, y)$ can be still defined as the streamwise-, spanwise- and ensemble-averaged streamwise velocity – similarly to what was done in §2.2.1:

$$U(t, y) = \langle u \rangle_z$$

However, U does not coincide with the expected value of the velocity anymore. Indeed, the expected velocity $\langle \vec{u} \rangle$ depends on the conditioned spanwise coordinate ζ and all its components are non-zero; the deviations of the expected velocity $\langle \vec{u} \rangle$ from the mean profile U are referred to as the dispersive velocity field $\vec{u}_d = (\tilde{u}, \tilde{v}, \tilde{w})$:

$$\vec{u}_d = \langle \vec{u} \rangle - U \underline{x} = \langle \vec{u} \rangle - \langle \vec{u} \rangle_z \tag{6.5}$$

Doing so, the velocity field can be decomposed into its mean, dispersive and fluctuation components (triple decomposition):

$$\vec{u}(t, x, y, z) \; = \; U(t, y) \, \underline{x} \; + \; \vec{u}_d(t, y, \zeta(z)) \; + \; \vec{u}'(t, x, y, z) \tag{6.6}$$

6.1.1 Numerical method and details

Numerical simualations are performed using the method described in §2.4.2 and implemented in the open-source solver Xcompact3d (Laizet and Lamballais, 2009; Laizet and Li, 2011; Bartholomew et al., 2020). "Different configurations for varying Λ_s at two different friction Reynolds numbers ($Re_\tau = 180$ and $Re_\tau = 500$) are tested. While the streamwise extent L_x of the simulation domain is set to standard values, the spanwise box size L_z is set alternatively to $12h$, $8h$, or $6h$ in order to accomodate an integer, even number of strips for each of the tested values of Λ_s. The $6h$ box size is preferred at high-*Re* wherever possible to minimize the computational load of a single simulation.

The data production pipeline consists of two stages. First, initial conditions are produced by simulating a channel flow with a spanwise roughness pattern of period Λ_s (see figure 6.1a). Rough wall sections are

colour	Re_τ	Λ_s/h	N_0 or N_s	$T_f\,u_\tau/h$	$(L_x, L_z)/h$	$(\Delta x, \Delta z, \Delta y_c, \Delta y_w)/\delta_{v,m}$	CFL$_{max}$	Fo_{max}
	180	smooth	170	N.A.	(8, 12)	(8.0, 3.75, 8.48, 0.85)	0.5350	0.1246
●	180	0.5	80	5	(8, 12)	(8.54, 4.00, 9.05, 0.91)	0.7009	0.1246
●	180	1	200	5	(8, 12)	(8.86, 4.15, 9.39, 0.94)	0.6781	0.1246
●	180	2	200	5	(8, 12)	(8.69, 4.07, 9.21, 0.92)	0.6115	0.1246
●	180	4	250	8	(8, 12)	(8.75, 4.10, 9.28, 0.93)	0.7020	0.1246
●	180	6	300	10	(8, 12)	(8.73, 4.09, 9.25, 0.93)	0.6998	0.1246
	500	smooth	151	N.A.	(12, 6)	(10.00, 5.00, 9.76, 1.00)	0.7096	0.0700
●	500	0.5	108	3.1	(12, 6)	(10.81, 5.41, 10.56, 1.08)	0.6696	0.0700
●	500	1	162	3.5	(12, 6)	(10.85, 5.42, 10.59, 1.08)	0.6974	0.0700
●	500	2	162	5.1	(12, 6)	(10.89, 5.45, 10.63, 1.09)	0.6764	0.0700
●	500	4	165	8.2	(12, 8)	(10.96, 5.48, 10.70, 1.10)	0.7619	0.0700
●	500	6	180	8.2	(12, 6)	(10.87, 5.44, 10.61, 1.09)	0.7646	0.0700

Table 6.1: Numerical details for all tested combinations of Λ_s/h and Re_τ for our smooth (steady) and time-evolving simulations. The grid spacing is uniform in the streamwise and spanwise directions and is indicated by Δx, Δz respectively. The wall-normal grid spacing at the wall and centerline are instead indicated by Δy_w and Δy_c. The maximum in time, over each grid point and over the three spatial directions (or velocity components) of the Courant-Friedrichs-Lewy (CFL $= \mathcal{U}\Delta t/q$, where Δt is the simulation time step, q is the grid spacing at some generic point in a given direction and $\mathcal{U}$ is the velocity component at that point in the same direction) and Fourier ($Fo = \nu\Delta t/q^2$) numbers are also reported. The dot to the left of each row indicates the colour used in the following figures to indicate a given value of Λ_s/h. Adapted from [MY24b].

modelled by imposing a slip length ℓ for the spanwise velocity component at the wall as in Neuhauser et al. (2022). This results in the following Robin boundary condition:

$$w_w = \ell\, \underline{n}_w \cdot (\nabla w)_w \tag{6.7}$$

where the $(\cdot)_w$ subscript indicates a quantity evaluated at the wall, $\underline{n}_w$ a unit vector that is orthogonal to the wall and pointing into the fluid. The value of the slip length is set to $\ell^+ = 9$ following Neuhauser et al. (2022). After the simulation reaches a steady state, a set of N_s snapshots is stored; the sample time is set to $1h/u_p$ to ensure that snapshots are reasonably uncorrelated. Each snapshot represents an instantaneous realisation of the secondary motions triggered by the roughness pattern.

Each of these N_s snapshots is used as the initial condition for a second simulation between smooth walls (see figure 6.1b). The duration of the simulation T_f is chosen to satisfactorily capture the decay of the secondary motions. Streamwise-averaged flow fields are stored every $0.01h/u_p$, even though a laxer time resolution could have been used in retrospect. Streamwise-averaged velocity fields are preferred to three-dimensional snapshots as the present procedure is particularly data-intensive; disk space represents indeed a more severe bottleneck than, say, computational power, although this strongly depends on the available resources. Exploiting the several repetitions of the simulation, a total of N_s fields at the same time t from the initial conditions are averaged together to produce an ensemble-average of the decaying secondary motions. The whole procedure is repeated for different values of Λ_s and Re_τ.

Numerical details for the complete dataset used for this study are reported in table 6.1. The grid spacing is normalised with the worst-case value $\delta_{v,m}$ of the viscous length scale; such a value is usually observed at the initial conditions. Additionally to the decaying simulations, two reference simulations between smooth walls ($Re_\tau = 180$, $Re_\tau = 500$) have been produced using the same grid used for rough simulations. In this case, N_0 indicates the number of samples used for the calculation of steady-state statistics.” [MY24b]

6.2 Steady-state secondary motions

“In this section, the dispersive velocity field (as defined in §6.1) is analysed at the initial, steady state. It is argued that the main consequence of the presence of strip-type roughness is the existence of a non-zero dispersive velocity field. Later on, in light of this analysis, the dispersive velocity field will be tracked in time as the secondary motions decay.

The dispersive velocity field is linked to an easily identifiable and isolable feature of the velocity spectra of the investigated flows over heterogeneous roughness. As an example, the two-dimensional streamwise velocity spectra of two flows at $Re_\tau = 500$ are compared, one of which runs between smooth walls (figure 6.2a) whereas the other (b) runs over a roughness pattern ($\Lambda_s/h = 1$). This combination of parameters has been chosen to best highlight the observed behaviour and is representative of the remaining cases. The bar below each panel shows the $\kappa_x = 0$ mode (where κ_x is the Fourier wavenumber in the streamwise direction; κ_z is the one in the spanwise direction), which would otherwise not be visible owing to the logarithmic scale. The $\kappa_x = 0$ mode is premultiplied with the Fourier resolution $\Delta\kappa_x = 2\pi/L_x$ of the spatial grid. The spectrum is evaluated in proximity of the wall ($y^+ = 10$), as, according to the attached eddy model of turbulence (Marusic and Monty, 2019), most scales of motion are observable at this wall-normal location. Further away from the wall, only the largest scales would be visible. This heuristic is confirmed by the spectra of the isolated dispersive motion, later shown in figure 6.5. Notice that no decomposition is used (unless explicitly stated), so that the spectra include both features linked to velocity fluctuations and to the dispersive velocity.

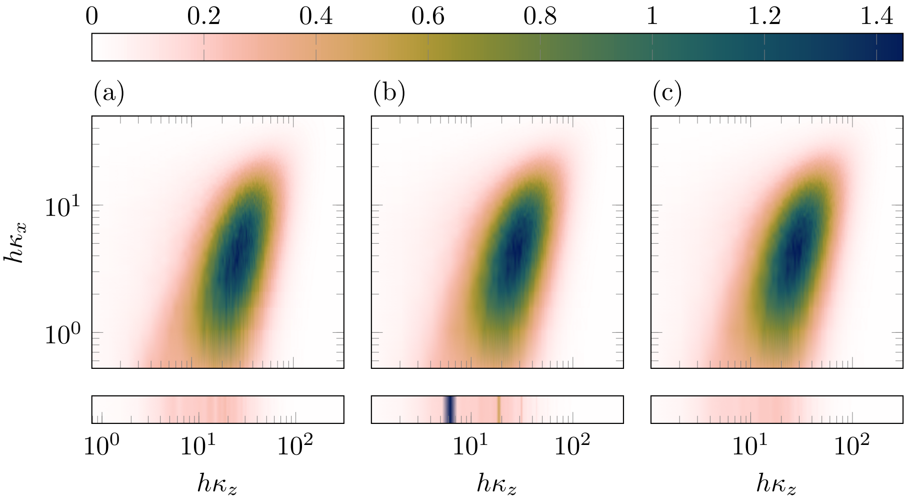

Figure 6.2: Inner-scaled premultiplied two-dimensional velocity spectra at $y^+ = 10$ for steady-state simulations. The bar below each panel represents the mode $\kappa_x = 0$, which would otherwise not be visible due to the logarithmic scale. (a) Premultiplied spectrum $\kappa_x^+ \kappa_z^+ \phi_{uu}^+$ of the streamwise fluctuations; $Re_\tau = 500$, smooth walls. (b) Premultiplied spectrum of the full streamwise velocity signal (including both the dispersive velocity and fluctuations); $Re_\tau = 500$, $\Lambda_s/h = 1$. (c) Premultiplied spectrum $\kappa_x^+ \kappa_z^+ \phi_{uu}^+$ of the streamwise fluctuations; $Re_\tau = 500$, $\Lambda_s/h = 1$ (same as b, but the contribution of the dispersive velocity is removed). Adapted from [MY24b].

All panels of figure 6.2 share the same qualitative spectral peak typical of turbulent fluctuations; in agreement with the attached-eddy hypothesis (see §2.2.4), most of the energy is seen on (κ_x, κ_z)-modes of roughly constant aspect ratio, meaning that motions that are large in the x-direction also tend to be large in z. The dominant feature that differentiates the smooth (a) and the rough (b) spectra is the occurrence of a banded energy pattern at $\kappa_x = 0$ in panel (b). This banded pattern is associated with the dispersive velocity: by removing the latter in panel (c), the energy bands are also eliminated so that the remaning spectrum can be hardly distinguished from the one of the smooth case. In other words, the dispersive average captures the main spectral feature differentiating a flow over a smooth wall from the one over strip-type roughness.

Nevertheless, further and yet less apparent differences arise between smooth and rough spectra; a separate analysis (not shown for brevity) shows for instance that the spectral peak associated to turbulent fluctuations gets closer to the wall in presence of a roughness pattern. This is expected: consistently with the protrusion height theory of Luchini et al. (1991), using a sliplength to model roughness (as is done here) aims at pulling turbulence fluctuations towards the wall to locally increase the wall shear stress (Neuhauser et al., 2022). As for the meandering of secondary motions (Wangsawijaya et al., 2020), no spectral feature that can be clearly linked to it is observed. Meandering would manifest itself as energy content for $\kappa_x \neq 0$ at the same κ_z values of the banded energy pattern associated to the dispersive velocity. The lack of such features is perhaps a consequence of the relatively low Reynolds number; most importantly, meandering is best observed at larger values of y^+ than the one used in figure 6.2 (Wangsawijaya et al., 2020).

Having found that the dispersive velocity isolates a distinct feature of the turbulent spectra, we proceed to inspect it both in real and Fourier space. Figure 6.3 shows the dispersive velocity field for all available values of Λ_s/h at $Re_\tau = 500$. The averaged flow fields at $Re_\tau = 180$ (not shown for brevity) return a similar picture. Similarly to other studies concerning secondary motions (Chung et al., 2018), VLSMs (Hutchins and Marusic, 2007b) and flow over multi-scale roughness (Barros and Christensen, 2014; Womack et al., 2022), these visualisations reveal the presence of high- and low-momentum path-

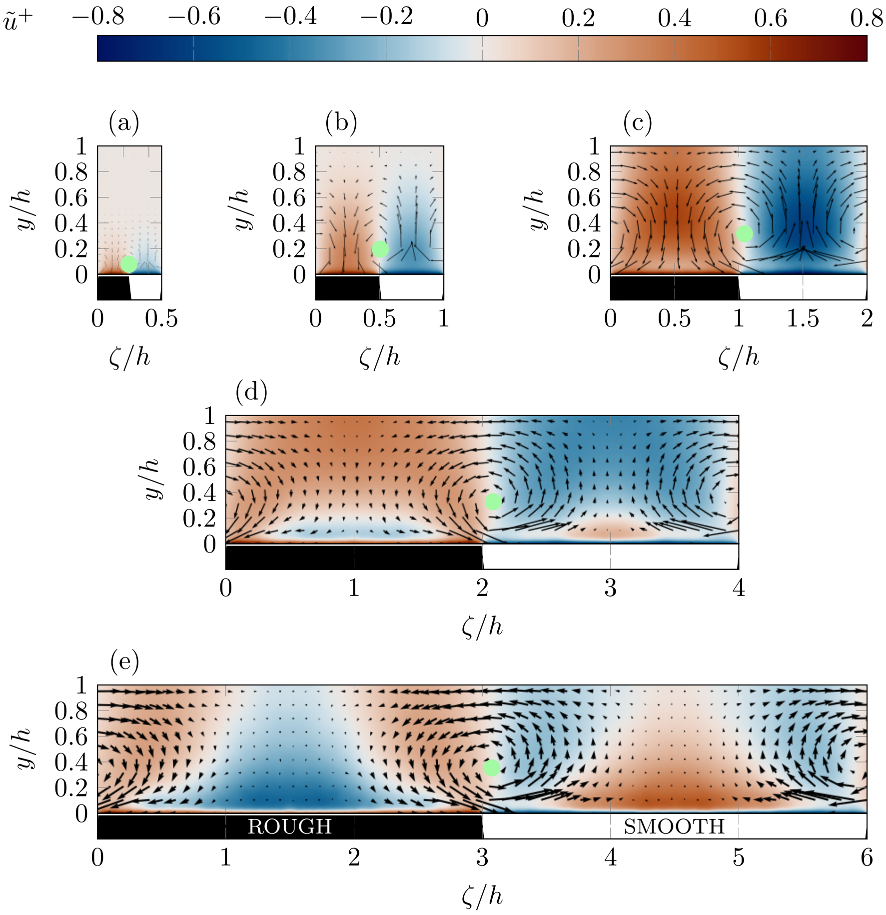

Figure 6.3: Dispersive velocity field at the initial steady state ($t = 0$) divided in its streamwise $\tilde{u}^+$ (color) and circulatory $\tilde{v}^+$-$\tilde{w}^+$ (arrows) patterns; all data at $Re_\tau = 500$. Notice that the length and thickness of arrows is proportional to the magnitude of the plotted vector; yet, arrow lengths and thicknesses are not consistent across different panels. (a) $\Lambda_s/h = 0.5$; (b) $\Lambda_s/h = 1$; (c) $\Lambda_s/h = 2$; (d) $\Lambda_s/h = 4$; (e) $\Lambda_s/h = 6$. Below each panel, it is indicated whether the wall at that spanwise position is rough (black) or smooth (white). A green dot marks the position of the vortex center as defined later in §6.3.1. Adapted from [MY24b].

ways flanked by circulatory motions. For low strip widths ($\Lambda_s/h \leq 2$ roughly), regions of downwash ($\tilde{v} < 0$, or sweep events) coincide with regions of high streamwise momentum, and vice-versa for ejection events ($\tilde{v} > 0$). Secondary motions are confined to a region close to the wall for $\Lambda_s/h = 0.5$; they grow taller as the strip width is increased (up to $\Lambda_s/h \approx 2$). For $\Lambda_s/h = 2$ (figure 6.3c), the secondary motions fill the entire channel half-height; under such conditions, high absolute values of streamwise dispersive momentum (regions of darker colour in figure 6.3) are seen at two separate wall-normal positions. One is located in the immediate proximity of the wall; here, the spanwise distribution of $\tilde{u}$ is well described by a square wave. The velocity distribution in this region is a good approximant of the distribution of wall shear stress, which is in turn affected by the imposed square-wave spanwise roughness pattern. Further away from the wall, the $\tilde{u}$-distribution becomes sinuisoidal in the spanwise direction; a second region of intense momentum appears around $y/h \approx 0.4$ ($y^+ \approx 200$).

As the strip width is further increased (roughly $\Lambda_s/h > 2$), the circulatory cross-plane motions shown by the $\tilde{v}$-$\tilde{w}$ vector field are progressively confined to the roughness transitions - that is, the interfaces between adjacent rough and smooth strips. The velocity at the center of each strip, instead, approaches local equilibrium with the wall (Chung et al., 2018; Neuhauser et al., 2022). For $\Lambda_s/h = 6$, intense cross-plane circulatory motions are only seen in a $2h$-wide region centered about transitions. As previously observed for lower strip widths, $\tilde{u}$ and $\tilde{v}$ are anti-correlated where these intense circulatory motions are present. The expected square-wave pattern of $\tilde{u}$ is seen at the wall; moving away from it, $\tilde{u}$ changes in sign at the center of each strip. For $\Lambda_s/h = 4$ (panel d of figure 6.3), this region of reversed sign is bounded in the wall-normal direction; for $\Lambda_s/h = 6$ (e), instead, it reaches the channel centerline. In this latter case, the profile of $U + \tilde{u}$ in the middle of each strip collapses on the inner-scaled velocity profile of a homogeneous flow between either rough or smooth walls, if scaled with the local value of u_τ (not shown for brevity; the reader can refer to Neuhauser et al., 2022). In light of the above, the reversal in sign of $\tilde{u}$ can be interpreted as a sign of the flow in the middle of each strip being driven towards equilibrium with the local surface condition.

Both the $\tilde{u}$-$\tilde{v}$ anti-correlation and the fact that large absolute values of the streamwise momentum are seen at a certain distance from the wall in figure 6.3(c) suggest that the streamwise pattern $\tilde{u}$ is mainly generated by transport of the mean velocity field U by wall-normal motions $\tilde{v}$. High-speed fluid from the core of the channel (where the largest values of U are found) is transported towards the wall by a coherent downwash ($\tilde{v} < 0$) to create coherent high-momentum regions ($\tilde{u} > 0$), and *vice-versa* low-speed fluid from the near-wall region is transported upwards to yield low-momentum regions. The wall-normal component $\tilde{v}$ is expected to be small in proximity of the wall, both due to the impermeability condition and to the topology of the $\tilde{v}$-$\tilde{w}$ circulatory motion. Consequently, $\tilde{v}$ can be expected to be most effective at leveraging $\tilde{u}$-production at a given distance from the wall, as is observed. To better explain and corroborate this idea, the steady-state momentum budget of $\tilde{u}$ is inspected. Such a budget is readily available from Reynolds and Hussain (1972); after suitable simplifications due to the present geometry, the budget reads:

$$\begin{aligned} \underbrace{\frac{\partial \tilde{u}}{\partial t}}_{=0} = {} & \underbrace{-\tilde{v}\frac{\partial \tilde{u}}{\partial y} - \tilde{w}\frac{\partial \tilde{u}}{\partial \zeta}}_{\text{self-advection}} + \underbrace{\frac{\mathrm{d}}{\mathrm{d}y}\left\langle \tilde{u}\tilde{v}\right\rangle_z}_{\text{correction}} \underbrace{-\tilde{v}\frac{\mathrm{d}U}{\mathrm{d}y}}_{\text{prod.}} \\ & \underbrace{-\frac{\partial}{\partial y}\Big(\langle u'v'\rangle - \langle u'v'\rangle_z\Big)}_{\text{Reynolds stress: } \langle u'v'\rangle} \underbrace{-\frac{\partial}{\partial \zeta}\langle u'w'\rangle}_{\text{R. stress: } \langle u'w'\rangle} + \underbrace{\nu\left(\frac{\partial^2 \tilde{u}}{\partial y^2} + \frac{\partial^2 \tilde{u}}{\partial \zeta^2}\right)}_{\text{viscous stress}} . \end{aligned} \tag{6.8}$$

A budget for the kinetic energy $\tilde{u}^2/2$ is trivially found by multiplication by $\tilde{u}$. The author prefers to show the momentum budget (instead of the energy one) to highlight the functional form of the production term, which exactly represents transport of the mean velocity U by the wall-normal dispersive component $\tilde{v}$. Once multiplied by $\tilde{u}$, the term is analogous to the canonical turbulence production term of the Reynolds stress tensor budget equation (see §2.2.6). As for the remaining terms, the usual self-advection and diffusion ones appear in the equation; the former has a non-zero spanwise average, so that an additional correction is needed. Just like the production term, the correction represents an exchange of momentum with the mean field U. Finally, momentum exchange with turbulent fluctuations occurs through the Reynolds stresses.

The terms of the energy budget obtained by multiplying equation 6.8 by $\tilde{u}$ are shown in figure 6.4 at the initial steady state for two selected flow cases ($Re_\tau = 500$, $\Lambda_s/h = 2$ and $\Lambda_s/h = 6$). The self-advection term and its correction are not shown: while their absolute values are not exactly negligible, they are small enough to be dominated by the remaining source (or sink) terms. Positive values of each term indicate that the term is providing energy to the $\tilde{u}$ pattern, or, in other words, that the term acts to sustain the dispersive velocity. Negative values, instead, indicate that energy is being subtracted. As previously stated, while $\tilde{u}$ and $\tilde{v}$ are everywhere anti-correlated for $\Lambda_s/h = 2$, the anti-correlation region is restricted to $2h$-wide neighbourhoods of each roughness transition for $\Lambda_s/h = 6$. The borders of this

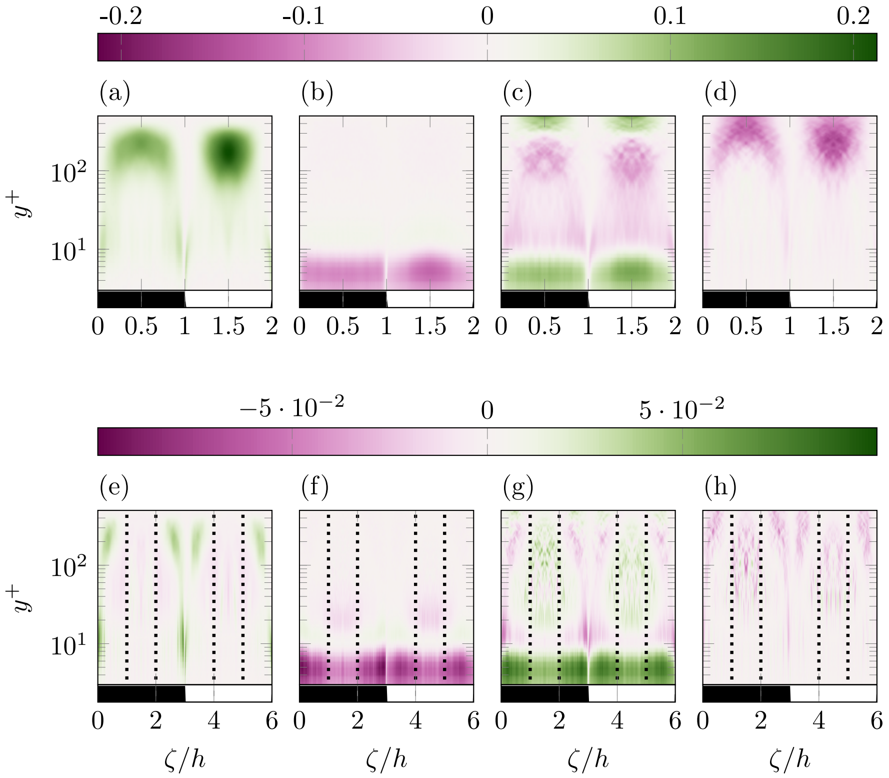

Figure 6.4: Inner-scaled premultiplied terms of the budget equation for coherent $\tilde{u}^2/2$ energy, defined by multiplying equation 6.8 by $\tilde{u}$. All data at $Re_\tau = 500$, steady state. Top row shows data for $\Lambda_s/h = 2$; (a) premultiplied production $y^+\Sigma^+_{\mathcal{P}}$, (b) viscous term $y^+\mathcal{V}^+$, (c) contribution $y^+\mathcal{T}^+_{uv}$ of the $\langle u'v' \rangle$ Reynolds stress and (d) contribution $y^+\mathcal{T}^+_{uw}$ of the $\langle u'w' \rangle$ stress. Bottom row (e-h): same as (a-d) but for $\Lambda_s/h = 6$. Please be aware of the different scale of the horizontal axis. Adapted from [MY24b].

region are marked with dotted lines in panels (e-h); the remaining portion of the channel is referred to as the equilibrium region. There, the wall-normal profile of $U + \tilde{u}$ is indeed roughly at equilibrium with the local wall shear stress (see the discussion above).

The main outer-layer ($y^+ > 10$) energy donor in the anti-correlation regions of both considered flow cases is the production term (panels a, e of figure 6.4); all remaining terms are negative, except for a minor positive contribution from $\langle u'v' \rangle$ in panel (c) towards the centerline. The production term is maximum around $y^+ \approx 200$; in this same region, intense values of $\tilde{u}$ were found in figure 6.3(c). This is further evidence in favour of the hypothesis that $\tilde{v}$-transport of U drives the formation of the $\tilde{u}$ pattern. It is also reminiscent of linear-transient growth analysis: the energy growth of optimally-amplified modes found by studying the evolution of perturbations in linearised channel flows is driven by the same mechanism (Del Álamo and Jiménez, 2006).

Both for the lower and the higher strip widths, the energy budget is dominated by the viscous (figure 6.4 b, f) and $\langle u'v' \rangle$ (c, g) terms in the near-wall region ($y^+ < 10$). The former subtracts energy from the intense near-wall $\tilde{u}$ pattern; most of this energy is dissipated, while part of it is returned to the flow just above $y^+ = 10$, where the term has a weak positive value (this is better observable in panel f). The $\langle u'v' \rangle$ stress, instead, is the main provider of energy in this region. This suggests that the formation of the near-wall $\tilde{u}$ pattern might be driven by turbulence through the Reynolds shear stress; such an interpretation is coherent with the findings of §5, that blocking the energy exchange between small turbulent fluctuations and large ones prevents the formation of large-scaled patterns of wall shear stress. Interestingly, the $\langle u'v' \rangle$ term is also the only source of energy in the equilibrium region for the higher strip

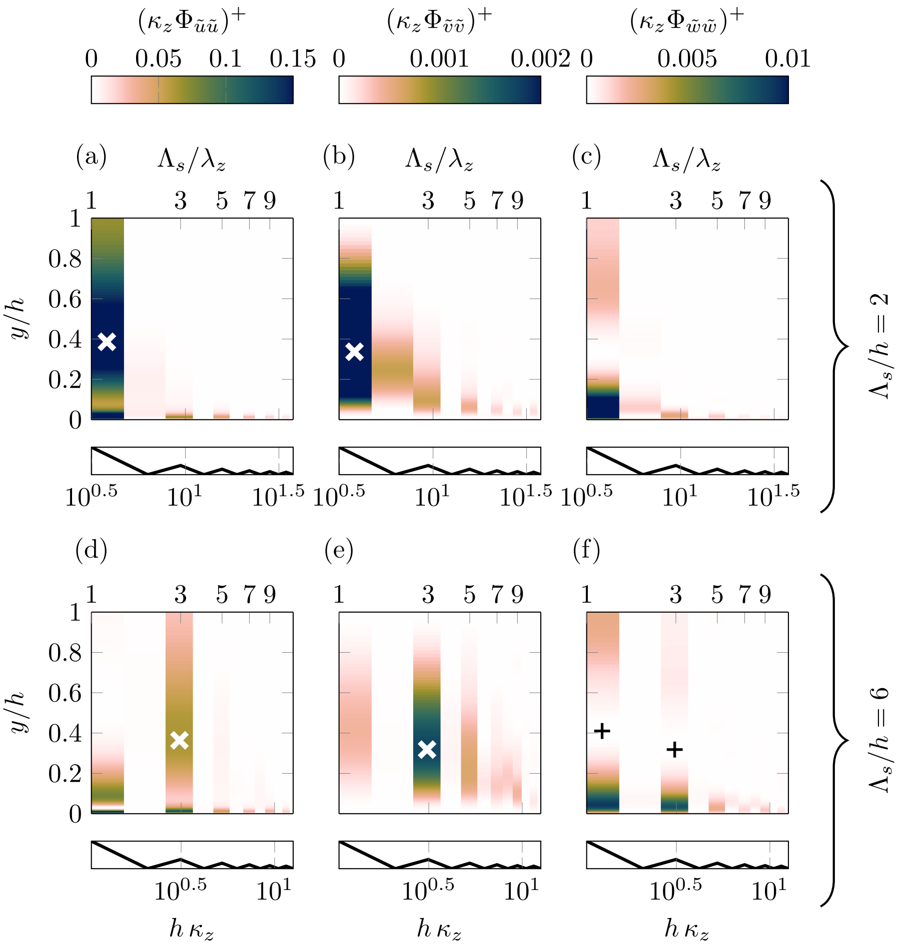

Figure 6.5: Premultiplied one-dimensional energy spectra of the streamwise (a, d, $\kappa_z^+ \Phi_{\tilde{u}\tilde{u}}^+$), wall-normal (b, e, $\kappa_z^+ \Phi_{\tilde{v}\tilde{v}}^+$) and spanwise (c, f, $\kappa_z^+ \Phi_{\tilde{w}\tilde{w}}^+$) dispersive velocity components. All data at $Re_\tau = 500$. (a,b,c) $\Lambda_s/h = 2$; (d,e,f) $\Lambda_s/h = 6$. The power spectral density of the roughness pattern applied to the wall is shown below each panel. The harmonic number Λ_s/λ_z associated to each Fourier mode is shown at the top of each panel. Selected local extrema of each spectrum are marked as × (white, maxima) and + (black, minima). Adapted from [MY24b].

width (panel g), indicating that it might be responsible for driving the flow towards equilibrium. This is reasonable, as under homogeneous conditions the mean velocity profile results from the equilibrium of viscous and $\langle u'v' \rangle$ stresses only.

Next, the dispersive velocity field is inspected in spectral space. Its spanwise spectra at the initial steady state are shown in figure 6.5 for $\Lambda_s/h = 2$, 6 and $Re_\tau = 500$. Notice that, much like the dispersive velocity, these steady-state spectra only depend on the wall-normal coordinate y and the spanwise wavenumber κ_z. The spectra better show the striped structure that was observed in figure 6.2; a similar pattern has also been found experimentally by Wangsawijaya and Hutchins (2022). Likely, the striped appearance is caused by the square-wave shape of the roughness pattern that is applied to the wall, whose power spectral density (shown below each panel) is also striped. It is indeed observed that most of the energy of the dispersive velocity field is found on the same Fourier modes that are excited by the roughness pattern. For both the roughness pattern and the velocity field, the first harmonic of the Fourier transform usually holds the most energy. The first harmonic is the Fourier mode whose spanwise wavelength λ_z matches the period of the transformed signal; higher harmonics have a wavelength that is a fraction of such period. For convenience, a harmonic number Λ_s/λ_z is defined such that the first harmonic has $\Lambda_s/\lambda_z = 1$, the second $\Lambda_s/\lambda_z = 2$, and so on. The harmonic number is shown at the top of each panel in figure 6.5.

In proximity of the wall, energy is seen on a wide range of wavelengths, reinforcing the idea that the velocity distribution there roughly takes the shape of a square wave. As a rule of thumb, energy is restricted to progressively larger Fourier modes as one moves away from the wall, this being reminiscent of the attached eddy hypothesis (see, for instance, Baars et al., 2017b, or §2.2.4), until the velocity field is dominated by a single sinusoidal wave at the centerline. There is however a notable exception to this trend of larger Fourier modes being taller in the wall-normal direction. This is seen for $\Lambda_s/h = 6$ (panel d): the amount of energy on the first harmonic at the centerline is unexpectedly negligible, whereas most of the energy is found on the third harmonic. Similarly, the third harmonic of the $\tilde{v}$ distribution (panel e) has the largest energy values throughout the channel height. This behaviour can also be observed without premultiplication of the spectrum; it is not as pronounced at the lower Reynolds number ($Re_\tau = 180$).

Although the roughness pattern significantly excites the first harmonic, then, it fails to leverage a secondary motion of matching size if its period is too large ($\Lambda_s/h = 6$); rather, the response of the flow contains a substantial amount of energy on a narrower – but still h-scaled – wavelength. The wavelength of the dominant harmonic ($\lambda_z = 2h$) of panels (d,e) suggests this might be linked to the observed confinement of secondary motions to a $2h$-wide region about the spanwise surface transitions (see figure 6.3e). As confirmed by a separate analysis of artificial signals, this is likely true for the pattern of $\tilde{v}$. The $\tilde{u}$-spectrum must be interpreted with care instead: the dominance of the $\lambda_z = 2h$ mode might be an artifact caused by the specific value ($\Lambda_s = 6h$) of the period of the roughness pattern. Roughness transitions are flanked by a high- and a low-momentum pathway, each of which has a $1h$ width. The remaining space between adjacent roughness transitions is then occupied by a local-equilibrium region where $\tilde{u}$ has opposite sign with respect to the secondary-motion-induced momentum pathways that surround it. This equilibrium region has a width of $3h - 2h = 1h$, so that effectively the spanwise $\tilde{u}$ distribution at the centerline is well described by a sinusoid of period $2h$. This is captured by the Fourier transform, whose dominant mode is not the first harmonic, but rather the one with a $2h$ wavelength. If the strip width were larger, the width of the anti-correlation region would likely remain constant, whereas the equilibrium region would get larger. In this case, the first harmonic might be dominant even at the centerline (depending on the relative intensity between the values of $\tilde{u}$ in the equilibrium and anti-correlation regions).

Several wall-normal gaps, or minima, can be observed in the vertical stripes of the spectra. Most w-modes contain one such gap: as an example, in figure 6.5(f), at $y/h = 0.4103$ (first harmonic, see the mark in figure) and $y/h = 0.3181$ (third harmonic). Analogous minima of the spectrum can be observed for the remaining energy-containing modes (as well as in panel c) by adjusting the colour scale. These minima could be thought of as the centers of rotation of the circulatory motions associated to each of these Fourier modes. Indeed, $\tilde{w}$-energy is expected at the bottom and top of these wall-attached circulatory motions as previously shown. Also coherently with the previous observations, $\tilde{v}$ energy is not seen at the wall; rather, its global maximum is seen between $y/h \approx 0.3$ and $y/h \approx 0.4$ ($y^+ \approx 150-200$) both for $\Lambda_s/h = 2$ and $\Lambda_s/h = 6$ (first harmonic in panel b and third one in panel e respectively; see the marks in figure). A local maximum of $\tilde{u}$-energy is seen on matching harmonics at matching wall-normal positions, consistently with the idea that the $\tilde{u}$ pattern is generated by $\tilde{v}$ transporting the mean velocity profile U. Finally, the short energy gap seen at the wall on the first $\tilde{u}$-harmonic for the $\Lambda_s/h = 6$ case could be linked to the change in sign seen in physical space at a matching wall-normal distance at the center of each strip.” [MY24b]

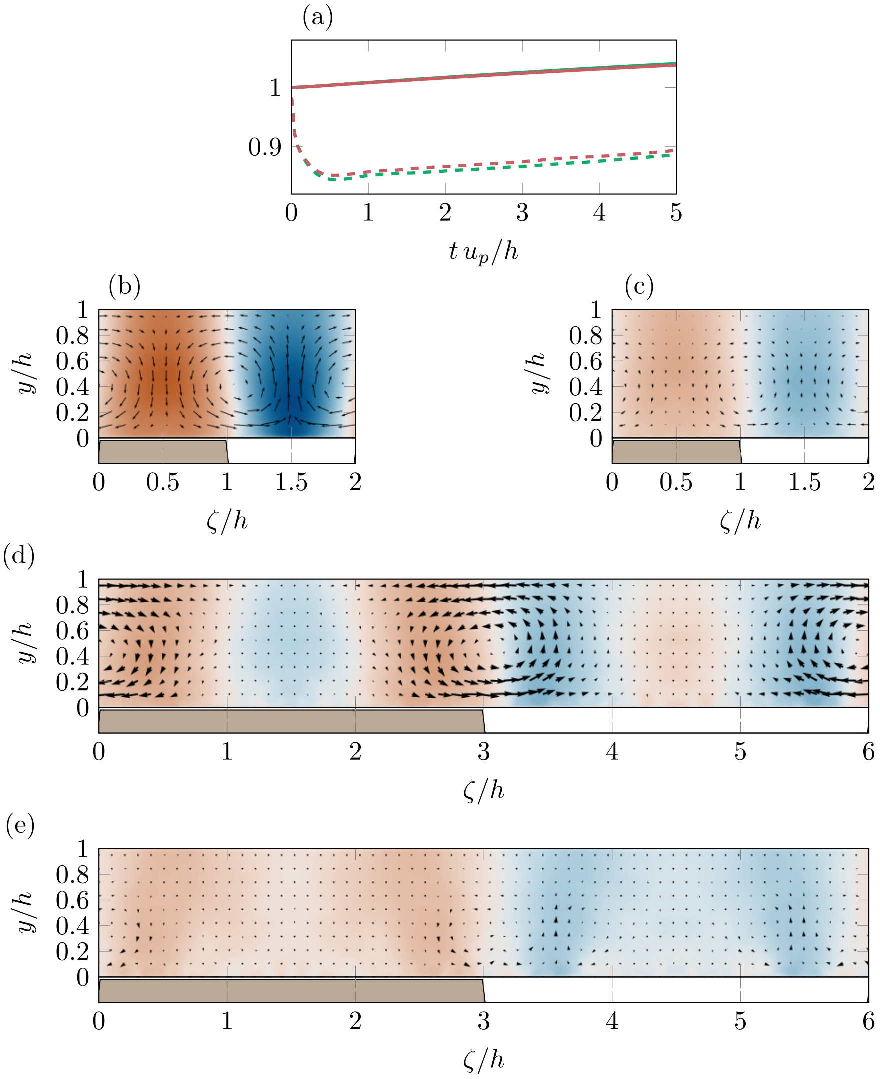

Figure 6.6: Time evolution (a) of the bulk velocity $U_b/U_b(0)$ normalised by its initial, steady-state value (solid) and of the inner-scaled wall shear stress τ_w^+ (dashed); $Re_\tau = 500$, $\Lambda_s/h = 2$ (green, as of table 6.1) and $\Lambda_s/h = 6$ (red). Decaying dispersive velocity field: $Re_\tau = 500$, $\Lambda_s/h = 2$, $t = 1h/u_p$ (b) and $t = 3.2h/u_p$ (c). Colors as of figure 6.3; arrow lengths are proportional to the magnitude of the plotted vector. Below each panel, a grey fill indicates portions of the wall that were rough at the initial condition. Panels (d,e): same as (b,c), but for $\Lambda_s/h = 6$. Adapted from [MY24b].

6.3 Decaying secondary motions

The focus is now turned "to the time evolution of the secondary motions. As explained in §6.1, their decay is triggered by suddenly removing the roughness strips from the walls. The process happens at a constant pressure gradient; the sudden removal of the roughness allows the flow rate to increase, as shown in figure 6.6(a) for two combinations of Λ_s and Re_τ chosen as an example. Coherently with equation 6.4, the increase in bulk velocity is driven by a temporary drop of the wall shear stress. As the flow approaches a new steady state for $t \to \infty$, the inner-scaled wall shear stress recovers its typical unitary value; however, this final equilibrium is reached at a point in time that exceeds the duration of the present simulations, which only capture the decay of the dispersive velocity field. In other words, the spanwise-averaged field U evolves at a different rate from that of secondary motions.

Videos of the decaying dispersive velocity field are available (`https://dx.doi.org/10.35097/farApPGYflANpeIi`); as an example, snapshots at two different instants in time are shown in figure 6.6 for $Re_\tau = 500$, $\Lambda_s/h = 2$ (b, c) and $\Lambda_s/h = 6$ (d,e). The typical qualitative picture of the decay for low values of Λ_s/h, which is well represented by panels (b, c), is rather straightforward. The secondary motions slowly fade away, while the intense $\tilde{u}$ pattern at the wall quickly diffuses. A different behaviour is seen for higher strip widths ($\Lambda_s/h = 6$, panels d, e) at both the investigated Reynolds numbers: at $t = 0$ (steady state), the equilibrium region at the centre of each strip shows opposite values of $\tilde{u}$ with respect to the flanking regions where the secondary motions appear (see figure 6.3e). This still holds true at $tu_p/h = 1$ (panel d of figure 6.6), although the regions of $\tilde{u}$ that are anti-correlated to $\tilde{v}$ lose their triangular shape (as evident in figure 6.3e at $t = 0$) and become rather invariant in the wall-normal direction. Advancing in time, the equilibrium region is progressively filled with momentum of the opposite sign; eventually ($tu_p/h = 3.2$, panel e), the sign of the dispersive velocity is roughly uniform across each strip (figure 6.6c). It is unlikely that this switch of the sign of $\tilde{u}$ in time is caused by $\tilde{v}$-transport of the U field, as $\tilde{v}$ is not particularly intense in this region.

Before measuring the time to decay of the secondary motions as per the objective of this study, such a time scale needs to be defined. Defining a time scale for the decay of turbulent eddies is an arbitrary process. For instance, Flores and Jiménez (2010) found that the log-layer of turbulent flows in a restricted simulation box bursts quasiperiodically, and linked the estimated period to the life span of log-layer eddies. LeHew et al. (2013) and Lozano-Durán and Jiménez (2014), instead, resorted to identifying turbulent coherent structures and tracking them in time; their lifespan is given by the distance in time between their first and last identification. In the present case, no sophisticated strategy is needed to track the secondary motions, as their spatial position is fixed and their features are satisfactorily captured by the dispersive average. Thus, some energy measure $e(t) \geq 0$ can be defined using the dispersive velocity and tracked in time. The energy will start from a value $e(0)$ seen at the steady state and then decline to zero for $t \to \infty$ as the secondary motions decay. The time scale T for the decay can then be defined as the time required for most of the energy to vanish; more precisely, as the minimum value of t after which the energy e never exceeds a threshold ε:

$$T \;\mid\; e(T) = \varepsilon, \;\; e(T + \Delta t) < \varepsilon \;\;\; \forall \;\;\; \Delta t > 0. \tag{6.9}$$

The threshold ε is set to 5% of the initial value $e(0)$ for multiple reasons. First, having a relatively large threshold is beneficial for the signal-to-noise ratio: the smaller the measured value of e, the greater its relative statistical uncertainty. It is moreover desirable to have the value of the threshold depend on the initial condition: secondary motions with different values of Λ_s/h hold different amounts of energy at a steady state (Wangsawijaya and Hutchins, 2022). It would not be sensible, then, to compare the time to decay of secondary motions of different sizes as measured by a fixed ε: every secondary motion starts from a different initial energy value. Instead, by letting $\varepsilon = 5\%\, e(0)$, the inverse $1/T$ of the time scale measures some sort of generalised decay rate ($1/T$ would exactly be a multiple of the decay rate in case of an exponential decay).” [MY24b]

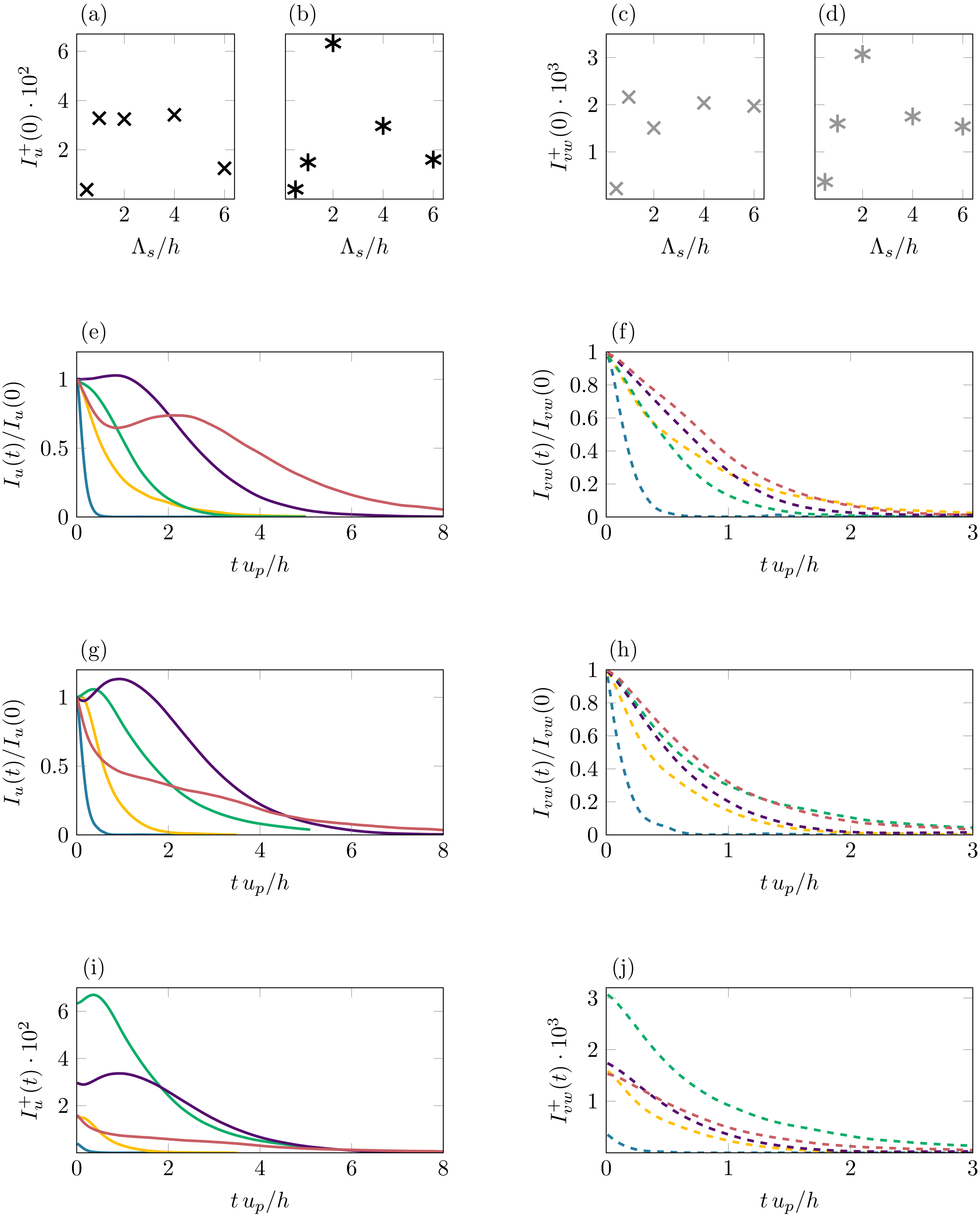

Figure 6.7: Volume-averaged coherent energy. (a,b) I_u^+ at the initial condition (steady state) for varying spanwise period Λ_s of the roughness pattern; $Re_\tau = 180$ and $Re_\tau = 500$ respectively. (c,d) same as (a,b), but for I_{vw}^+. Time evolution of the volume-averaged energy normalised by its initial value: (e) $I_u(t)/I_u(0)$, $Re_\tau = 180$; (f) $I_{vw}(t)/I_{vw}(0)$, $Re_\tau = 180$; (g-h) same as (e-f), but at $Re_\tau = 500$. As an example, panels (g-h) are reproduced again in (i-j) but without normalising the volume averages by their initial values. In panels (e-j), different colours indicate different values of Λ_s/h as of table 6.1. Adapted from [MY24b].

6.3.1 Volume-averaged coherent energy

"We start by tracking in time the total amount of energy held by the secondary motions. This is measured by the volume-averaged dispersive (also referred to as coherent) kinetic energy. The volume-averaged energy I_u and I_{vw} of the streamwise and circulatory dispersive patterns are separately defined:

$$I_u(t) = \frac{1}{2h} \int_0^{2h} \frac{1}{2} \left\langle \tilde{u}^2 \right\rangle_z \, \mathrm{d}y, \tag{6.10}$$

$$I_{vw}(t) = \frac{1}{2h} \int_0^{2h} \frac{1}{2} \left\langle \tilde{v}^2 + \tilde{w}^2 \right\rangle_z \, \mathrm{d}y. \tag{6.11}$$

Notice that the energy held by $\tilde{v}$ and $\tilde{w}$ is summed in a single quantity I_{vw}. This is justified by the incompressibility constraint, which reads $\nabla \cdot \vec{u}_d = 0$ for the dispersive field. Since $\tilde{u}$ is streamwise-invariant, the two-dimensional vector field given by $\tilde{v}$ and $\tilde{w}$ is divergence-less:

$$\frac{\partial \tilde{v}}{\partial y} + \frac{\partial \tilde{w}}{\partial \zeta} = 0. \tag{6.12}$$

That is, one can fully determine the distribution of $\tilde{v}$ if $\tilde{w}$ is known (or *vice-versa*), and the two form a single circulatory pattern. Thus, I_{vw} is used to quantify the energy held by the circulatory motions, whereas I_u quantifies the energy held by the momentum pathways.

The initial, steady-state values of these integral quantities are shown in figure 6.7(a-d) for each available flow configuration; panels (e-h) show their time evolution. At the lower Reynolds number (figure 6.7a,c), motions with $h \leq \Lambda_s \leq 4h$ hold a similar amount of energy independently of their size. This contradicts the observation (Wangsawijaya and Hutchins, 2022) that structures of period $\Lambda_s \approx 2h$ ($s \approx h$) are more energetic than the ones of any other size; this discrepancy is likely a consequence of the low Reynolds number. Indeed, low-Re data suffers from two issues. It is known, for instance, that linear transient growth analysis predicts large structures to show significant values of transient growth only for sufficiently high Reynolds numbers (Cossu et al., 2009); moreover, large-scaled outer-layer eddies only become significantly energetic in channel flows if the Reynolds number is high enough (Lee and Moser, 2015). It can be thus expected that, if the flow acts to favour structures of a specific outer-scaled size, this would only be seen at a sufficiently high Reynolds number. The data at $Re_\tau = 500$ (panels b,d) confirms this line of reasoning: the energy held by secondary motions is maximum for $\Lambda_s = 2h$ as expected. A second issue with low-Re data is given by the lack of scale separation: at the considered Reynolds number ($Re_\tau = 180$), the outer-layer length scale h is equivalent to $180\,\delta_v$. Such a value is not too far from the dominant spanwise scale of near-wall structures ($100\,\delta_v$, see Kline et al., 1967); in other words, small scales cannot be easily distinguished from the imposed outer-scaled motions that would be expected to be significantly energetic. Care must be then exerted in interpreting low-Re data.

As for the time evolution of the volume averages (6.7e-h), they typically show a monotonically decreasing trend both for the streamwise and circulatory patterns. There are, however, notable exceptions. At low Reynolds number (panel e), the energy of the streamwise pattern temporarily exceeds its initial value for $\Lambda_s/h = 4$, to then decay as expected; similarly, it temporarily increases after an initial decay for $\Lambda_s/h = 6$. Most importantly, at the higher Reynolds number (g) the volume-averaged energy monotonically decays in all cases, except for the energy of the streamwise pattern for $\Lambda_s/h = 2$ and $\Lambda_s/h = 4$.

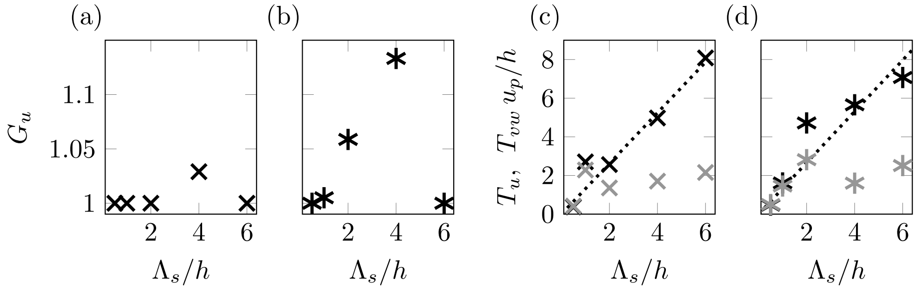

Figure 6.8: Transient growth G_u of the streamwise coherent energy $I_u(t)$; (a) $Re_\tau = 180$, (b) $Re_\tau = 500$. Time to decay (as defined per equation 6.9 applied to I_u and I_{uv}) for the streamwise (T_u, black) and circulatory (T_{vw}, gray) coherent energy; (c) $Re_\tau = 180$, (d) $Re_\tau = 500$. The dotted line represents a linear fit for T_u performed by rejecting data at $\Lambda_s/h = 1$ (c) and at $\Lambda_s/h = 2$ (d). Adapted from [MY24b].

An excess of streamwise energy with respect to the initial condition is seen for these cases. To better illustrate such a findings, a transient growth coefficient G_u is defined:

$$G_u = \max_t \frac{I_u(t)}{I_u(0)} \tag{6.13}$$

G_u is plotted against the size of the secondary motions in figure 6.8(a,b). At $Re_\tau = 180$, transient growth is only observed for $\Lambda_s/h = 4$ and is not particularly pronounced (3%). At $Re_\tau = 500$, a small (6%) - and yet measurable - transient growth of the dispersive $\tilde{u}$-energy is seen for $\Lambda_s/h = 2$; a larger growth (13%) is seen for $\Lambda_s/h = 4$. No such excess energy is seen for other values of Λ_s, except for a negligible transient growth for $\Lambda_s/h = 1$. For $2 \leq \Lambda_s/h \leq 4$, then, the generation of the high- and low-momentum pathways continues for a short time even after removing the rough strips that enable their sustainment. This might be evidence in favour of the hypothesis of Townsend (1976), who predicted that structures of this size ($\Lambda_s/h \leq 4$) would be able to self-sustain: not only do the momentum pathways maintain their energy for a short time, but they even show excess energy with respect to the initial conditions. The excess energy is also reminiscent of linear transient growth analysis and its results (Del Álamo and Jiménez, 2006), in the sense that I_u undergoes a transient growth before its decay. Moreover, the spanwise periods at which transient growth is seen in the present context ($\Lambda_s/h \approx 2 - 4$) are in good agreement with the spanwise wavelength of maximum linear transient growth ($\lambda_z/h = 3$) found by the aforementioned study. There is, however, a crucial difference between the present simulations and linear transient growth analysis, apart from the obvious non-linearity of the present system. Linear transient growth analysis studies the evolution of a perturbation of a given size, whereas here the focus lies on the evolution of a fully developed structure.

In linear transient growth analysis, the transient growth of u-energy is found to be driven by the v component through transport of the mean field (Del Álamo and Jiménez, 2006). Similarly, in §6.2, it was proposed that the formation of the $\tilde{u}$ momentum pathways might be driven by $\tilde{v}$ transport of the U-field. It could be expected, then, that this same mechanism would drive the observed initial overshoot of I_u energy. If this were the case, I_{vw} should be able to maintain its initial energy for a longer time in cases for which excess I_u is seen, or perhaps to decay slowlier than in other cases. A preliminary scrutiny of figure 6.7(f,h) suggests this is not the case: no initial plateau of I_{vw} is seen for values of Λ_s at which transient growth is observed. Moreover, no link could be found between the rate of change of I_{vw} at $t = 0$ and the occurrence of transient growth. The matter is further investigated by calculating a time scale for the decay of I_u and I_{vw} based on definition 6.9. The resulting time scales are T_u and T_{vw}

respectively. Results are shown in figure 6.8(c,d) and are scaled with h/u_p, as this time scale remains constant in physical terms across different simulations at the same Re_τ.

At the lower Reynolds number, T_{vw} generally increases with Λ_s, though the circulatory motions remain in the flow for an unexpectedly long time for $\Lambda_s/h = 1$. At the higher Reynolds number, T_{vw} increases with Λ_s until it reaches a maximum value for $\Lambda_s/h = 2$. For larger values of Λ_s, the circulatory motions remain confined in a $2h$-wide region around roughness transitions (see figure 6.3), so that effectively they stop growing in size. Similarly, their time to decay stops increasing. The maximum of T_{vw} for $\Lambda_s/h = 2$ might suggest that the longer living circulatory motion is able to leverage production of I_u for a longer time, causing the observed overshoot of I_u. However, data at $\Lambda_s/h = 4$ contradicts this idea: for this value of Λ_s, I_u undergoes an even stronger transient growth - and yet the circulatory motion decays in an unexpectedly short time. More generally, momentum pathways tend to live longer than the circulatory motions (as $T_u > T_{vw}$ in most cases), reinforcing the idea that the momentum pathways only decay when the circulatory motions that sustain them disappear. Yet, the variability in T_{vw} fails to predict the variability in T_u, indicating that production through $\tilde{v}$-transport of U alone cannot explain the dynamics of I_u.

The time to decay of I_u generally increases with the spanwise periodicity Λ_s; interestingly, the observed transient growth of I_u has no strong influence on T_u. Then, in contradiction with Townsend's hypothesis, the larger the spanwise periodicity of the pattern of high- and low-momentum pathways, the longer the pathways remain in the flow. Pathways of period $\Lambda_s = h$ at $Re_\tau = 180$ are the only exception to this rule of thumb, as they subsist in the flow longer than what could be expected by extrapolating the observed trend. Although this could be a sign of the flow favouring these specific h-scaled structures, it should be kept in mind that the structures might as well be inner-scaled owing to the lack of scale separation. As previously explained, a $1h$ period is indeed equivalent to $180\delta_v$ in wall units at $Re_\tau = 180$; such an inner-scaled value of the period is not far from the typical spanwise spacing of buffer-layer small scales ($100\delta_v$, see Kline et al., 1967).

Starting from the gathered temporal information, the streamwise distance needed for the $\tilde{u}$ pattern (that is, for the high- and low-momentum pathways) to decay is now estimated. This enables the comparison of the present results with other studies measuring the streamwise coherence of momentum pathways (e.g. Womack et al., 2022). First, a linear fit to the trend of T_u against Λ_s is found; the two datapoints at $Re_\tau = 180$, $\Lambda_s/h = 1$ and $Re_\tau = 500$, $\Lambda_s/h = 2$ are rejected to do so. While this is a rough approximation, the fit (shown by a dotted line in figure 6.8c, d) correctly captures the order of magnitude of T_u. Then, the streamwise distance L_d needed for the decay of momentum pathways is estimated as $L_d = U_{b,s}\,T_u$, where $U_{b,s}$ is the bulk velocity seen at a matching value of Re_τ between smooth walls. The underlying idea is that structures are advected downstream as they evolve and that the bulk velocity is the mean velocity at which this happens. Using the value of the bulk velocity seen between smooth walls is an arbitrary choice; again, it is only meant to roughly capture the order of magnitude of L_d. The following estimates are obtained:

$$\begin{aligned} L_d &\approx 20.6\,\Lambda_s \quad \text{at } Re_\tau = 180 \\ L_d &\approx 24.2\,\Lambda_s \quad \text{at } Re_\tau = 500 \end{aligned}$$

thus, the larger the spanwise size of the structure, the larger its streamwise coherence. The order of magnitude of the present estimate for a spanwise wavelength $\Lambda_s = h$ is in line with the experiments of (Womack et al., 2022), who reported the streamwise extent of momentum pathways to be of $18h$ at least.

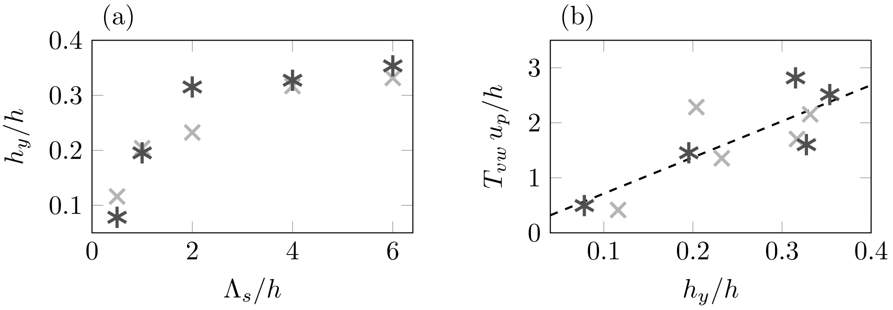

Figure 6.9: (a) Wall-normal position h_y of the vortex center of the circulatory motions against the spanwise period Λ_s. (b) Time to decay T_{vw} of the circulatory motions against the wall-normal position h_y of the vortex center. Light gray crosses indicate data at $Re_\tau = 180$; dark gray asterisks indicate data at $Re_\tau = 500$. In panel (b), a linear fit to all available data is shown as a dashed line. Adapted from [MY24b].

As already discussed, the value of the timescale T_{vw} associated to the circulatory motions saturates for high values of Λ_s (contrarily to T_u). One way of explaining the observed saturation could be given by the findings of Lozano-Durán and Jiménez (2014). The authors identified and tracked naturally occurring structures that are both wall-attached and associated to $u'v'$-anticorrelation events; they found the lifetime T_{ae} of these structures to be proportional to their height H_{ae},

$$T_{ae}^+ \approx H_{ae}^+. \tag{6.14}$$

In the case of the present study, the timescale T_u cannot be considered to be analogous to T_{ae}, as it measures the lifespan of a velocity pattern that is not necessarily wall-attached and that includes regions in which $\tilde{u}$ and $\tilde{v}$ are positively correlated. The circulatory motions, instead, satisfy these two requirements: they extend upwards from the near-wall region and they are responsible for the $\tilde{u}$-$\tilde{v}$ anticorrelation (see §6.2). Thus, T_{vw} will be considered to be equivalent to T_{ae}; by making equation 6.14 dimensional, it is expected:" [MY24b]

$$T_{vw} \approx 2\frac{h_y}{u_p} \tag{6.15}$$

where h_y measures the half-height of the circulatory motions. A suited estimate of h_y needs to be defined "to enable a comparison between the present results and the ones of Lozano-Durán and Jiménez (2014). A vortex center is defined as the point at which, simultaneously, $\tilde{v}$ changes in sign in z and $\tilde{w}$ changes in sign in y. The so-defined vortex centers are marked in figure 6.3 and satisfactorily represent the center of the cross-sectional circulatory motions. The structure half-height h_y is then simply given by the wall-normal position of the vortex center.

Figure 6.9(a) shows how the half-height h_y changes with the spanwise period Λ_s of the roughness pattern. A good collapse of low- and high-*Re* data is observed. The circulatory motions get taller for increasing Λ_s; as Λ_s approaches large values (say, $\Lambda_s/h \geq 2$), the growth of h_y slows down. This saturation effect is expected: as can be seen from figure 6.3, the circulatory motions fill the entire channel half-height for $\Lambda_s/h \approx 2$, so that their wall-normal growth is phyisically limited for larger values of Λ_s. As the structures stop getting taller, they also become confined to a region surrounding roughness transitions (see §6.2): it appears that the circulatory motions roughly maintain their y-z aspect ratio – in a way that is reminiscent of the attached eddy hypothesis (see Marusic and Monty, 2019, or §2.2.4). Finally, the present data is compared to the one of Lozano-Durán and Jiménez (2014) by plotting the timescale T_{vw} of the circulatory motions against their half-height h_y in figure 6.9(b): owing to equation

6.15, a linear trend is expected. Although the data does not appear to collapse on a single line, its dispersion appears to be directional, so that a linear fit is reasonable. By considering both low- and high-*Re* data, the following linear fit is obtained:

$$\frac{T_{vw,fit}}{h/u_p} = 6.57\frac{h_y}{h} + 0.056 \tag{6.16}$$

Although the intercept of the present fit is small (and thus in agreement with equation 6.14), the obtained slope is three times larger than expected. This quantitative difference can be explained by the fact that the structures tracked here differ from the ones of Lozano-Durán and Jiménez (2014); moreover, different definitions of the time scale and of the structure half-height – all of which are arbitrary – are used here. To conclude, the ansatz of equation 6.14 does not fully explain the variability of T_{vw}, but it correctly captures the general trend of larger values of h_y being typically associated to larger values of T_{vw}. Then, the fact that the circulatory motions stop growing in size for large values of Λ_s can help explain the observed saturation of T_{vw}.” [MY24b]

6.3.2 Plane-averaged coherent energy: the decay of the wall shear stress pattern

“Albeit easily interpretable, volume-averaged quantities hide the spatial complexity of the observed phenomena. To recover information in the wall-normal direction, the average i_u of the streamwise coherent energy on wall-parallel planes is inspected:

$$i_u(t,y) = \frac{1}{2}\left\langle \tilde{u}^2 \right\rangle_z \tag{6.17}$$

Bear in mind that the value of i_u seen at a given wall-normal position is equal to the integral contribution of all Fourier modes of the spectrum $\Phi_{\tilde{u}\tilde{u}}$ (shown in figure 6.5) at the same distance from the wall (see §2.3.2, equation 2.52):

$$i_u(t,y) = \frac{1}{2}\int_{-\infty}^{\infty} \Phi_{\tilde{u}\tilde{u}}\left(t,y,\kappa_z\right)\,\mathrm{d}\kappa_z. \tag{6.18}$$

Notice that the above expression may change depending on how the Fourier transform is normalised.

The plane-averaged energy i_u is shown in figure 6.10 for a selection of flow cases at $Re_\tau = 500$ for a short time interval after the spanwise heterogeneity has been removed. Notice that no premultiplication is performed for this figure despite the log-scaled vertical axis: this is done to better highlight its near-wall features. As a consequence, though, the total amount of energy contained in the outer layer is misrepresented by the visualisation of figure 6.10. Similarly to what has been observed in figures 6.3 and 6.5, two separate energy peaks can be identified in figure 6.10 at the initial condition ($t = 0$, steady state) for large enough values of Λ_s/h: one in the viscous sublayer ($y^+ \leq 10$), one further away from the wall. This second peak is particularly pronounced for $\Lambda_s/h = 2$ ($y^+ \approx 200$, panel b), and not particularly so for $\Lambda_s/h = 6$ ($y^+ \approx 50$, panel c); it is not observed at the lower Reynolds number, or at least it is not as pronounced. In general, the streamwise pattern for $\Lambda_s/h = 6$ is much less energetic than the one for $\Lambda_s/h = 2$, as previously observed by analysing volume averages (figure 6.7b). The common feature of all data in figure 6.10 (which is also observed for values of Λ_s and Re_τ that are not shown) is that the near-wall peak diffuses towards the core of the channel. The steady-state analysis of the streamwise momentum budget (see §6.2) suggests that viscous diffusion is responsible for this process. The near-wall peak is associated to the near-wall square-wave distribution of $\tilde{u}$ seen in figure 6.3, and hence to the spanwise distribution of wall shear stress.

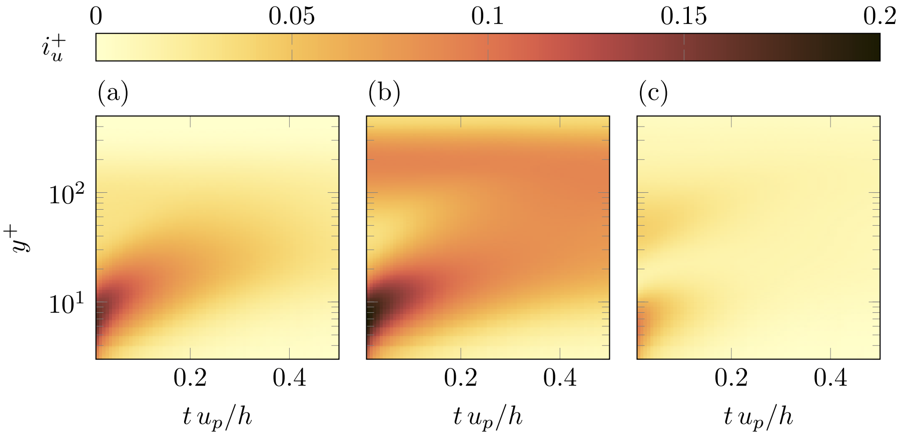

Figure 6.10: Time evolution of the plane-averaged coherent energy i_u^+ of the streamwise dispersive velocity. Please notice that, in spite of the logarithmic scale on the vertical axis, no premultiplication is used: consequently, the visual representation given by this figure is not well representative of the total (integral) amount of energy contained in different regions of the channel. All data at $Re_\tau = 500$; (a) $\Lambda_s/h = 1$, (b) $\Lambda_s/h = 2$ and (c) $\Lambda_s/h = 6$. Adapted from [MY24b].

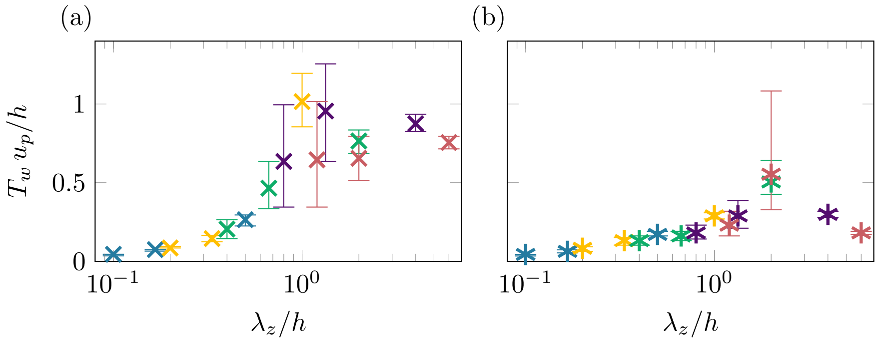

Figure 6.11: Time to decay $T_w(\lambda_z)$ of the Fourier harmonics (represented by their wavelength λ_z) that compose the dispersive wall shear stress distribution, calculated by applying the definition 6.9 to the spectrum $\Phi_{\tilde{u}\tilde{u}}$ (shown in figure 6.5) at $y^+ \approx 1$. Only the first three odd, energy-containing harmonics are shown. (a) $Re_\tau = 180$; (b) $Re_\tau = 500$. Different colours indicate different periods Λ_s/h of the roughness pattern (see table 6.1). The error bars indicate the 99% confidence interval. Adapted from [MY24b].

While the near-wall pattern of $\tilde{u}$ is particularly intense, it resides in a restricted region of the channel that shrinks in size as Re_τ increases. As a consequence, its contribution to the volume-averaged energy is marginal, so that the time scales measured in figure 6.8 are not representative of the decay of the dispersive wall shear stress distribution. A suitable time scale for this purpose could be defined, for instance, by applying the definition 6.9 to the plane-averaged energy i_u at the wall. Instead, we go one step further and analyse the individual contributions to i_u of each Fourier mode (as per equation 6.18) and measure their time to decay. In other words, the definition 6.9 of the time scale is applied to the spectrum $\Phi_{\tilde{u}\tilde{u}}$ – evaluated at the first wall-normal grid point ($y^+ \approx 1$, please refer to table 6.1) to be representative of the wall shear stress. In this way, a different time scale $T_w(\lambda_z)$ is obtained for each Fourier mode (of wavelength $\lambda_z = 2\pi/\kappa_z$) that constitues the pattern of wall shear stress.

Results are shown in figure 6.11, which collates data for all available values of Λ_s/h. Only the first three energy-containing harmonics are shown; higher harmonics hold little energy so that the signal-to-noise ratio is excessively low. The statistical uncertainty on the time to decay is measured as follows. When computing the Fourier-transformed dispersive field, the uncertainty of its real and imaginary parts is estimated by assuming the spatial and phase average of different snapshots at the same time t to be uncorrelated and to describe a Gaussian distribution. Bear in mind that the dispersive field is given by the ensemble average of these- space and phase-averaged snapshots. Then, the uncertainty is propagated to the spectra and the 99% confidence interval is computed for the energy of each Fourier mode. Doing so, three curves are available for each Fourier mode: one describing the time evolution of its energy, and two describing the confidence interval. The intersections of these three curves with the ε of definition 6.9 then define the time scale and its confidence interval. The uncertainty on ε is neglected.

Patterns of wall shear stress of different period Λ_s may contain Fourier modes with the same (or, similar) spanwise wavelength λ_z. The time needed for Fourier modes of comparable wavelengths from different simulations (different Λ_s/h) to decay is similar: data from different simulations at the same Re_τ appears to collapse on the same curve. In other words, it appears that the time evolution of the Fourier modes is influenced by their own wavelength λ_z (and, of course, by the Reynolds number), but not much by the geometry of the problem (that is, by Λ_s/h) or by the amount of energy they hold at the initial steady state. As an example, the first harmonic of figure 6.5(a) and the third one in figure 6.5(d) hold a different amount of energy at the wall at the initial steady state; yet, they share the same spanwise wavelength $\lambda_z/h = 2$ and take a comparable amount of time to decay as measured by T_w (see figure 6.11).

Figure 6.11(a) shows data at $Re_\tau = 180$: the time to decay increases with the wavelength until $\lambda_z/h = 1$. Harmonics with $\lambda_z/h = 1$ take the longest time to decay among all available data; similarly, secondary motions of a matching period ($\Lambda_s/h = 1$) also remain in the flow for an unexpectedly long time (see figure 6.8c). For larger wavelengths ($\lambda_z/h > 1$), slightly shorter times to decay are seen as the trend effectively saturates. At the higher Reynolds number (figure 6.11b), instead, the time to decay increases up until its peak value at $\lambda_z/h = 2$ to then decrease for higher values of the wavelength. That is, Fourier modes of the wall shear stress with $\lambda_z/h = 2$ are the longest-lived ones. This value of the wavelength matches the period $\Lambda_s/h = 2$ for which secondary motions are the most energetic; also, the associated circulatory pattern is the longest-lived.

The above observations are interpreted as follows. The longer time to decay might be a sign that near-wall Fourier modes of a specific wavelength ($\lambda_z/h = 2$ at $Re_\tau = 500$, for instance) are less damped (e.g., by viscous dissipation) than the remaining modes during their evolution. This does not help to explain the monotonically increasing trend of T_u against Λ_s seen in figure 6.8(d): T_u measures indeed the time to decay of a quantity that is integrated in the wall-normal direction over the channel half-height. Nevertheless, the near-wall behaviour discussed here might play a crucial role in the formation of secondary motions. Consider, for instance, a fully-developed flow suddenly hitting a patch of spanwise heterogeneous roughness. The roughness can be idealised as a disturbance applied to the near-wall region; in light of the above discussion, it can be expected that disturbances of a specific size would be less damped than others in this region, so that they grow more energetic. This mechanism might help to explain why secondary motions with a spanwise period of $\Lambda_s/h = 2$ are the most energetic at $Re_\tau = 500$ (see figure 6.7b); bear in mind that a spanwise roughness pattern of period Λ_s significantly excites the Fourier mode with wavelength $\lambda_z = \Lambda_s$ (as can be seen from the spectra of the roughness patterns in figure 6.5). Similarly, one would expect Fourier modes with wavelength $\lambda_z/h \geq 1$ to be roughly equally damped in the near-wall region at $Re_\tau = 180$ in light of figure 6.11(a); indeed, at such Reynolds number secondary motions with $\Lambda_s/h \geq 1$ hold roughly the same amount of energy (see figure 6.7a)." [MY24b]

6.4 The fluctuation field

"So far, the time evolution of the dispersive velocity field was inspected, as it is contains the information regarding the high- and low-momentum pathways which are of interest for this study. Nevertheless, the fluctuation field also contains valuable information: the secondary flows investigated here are

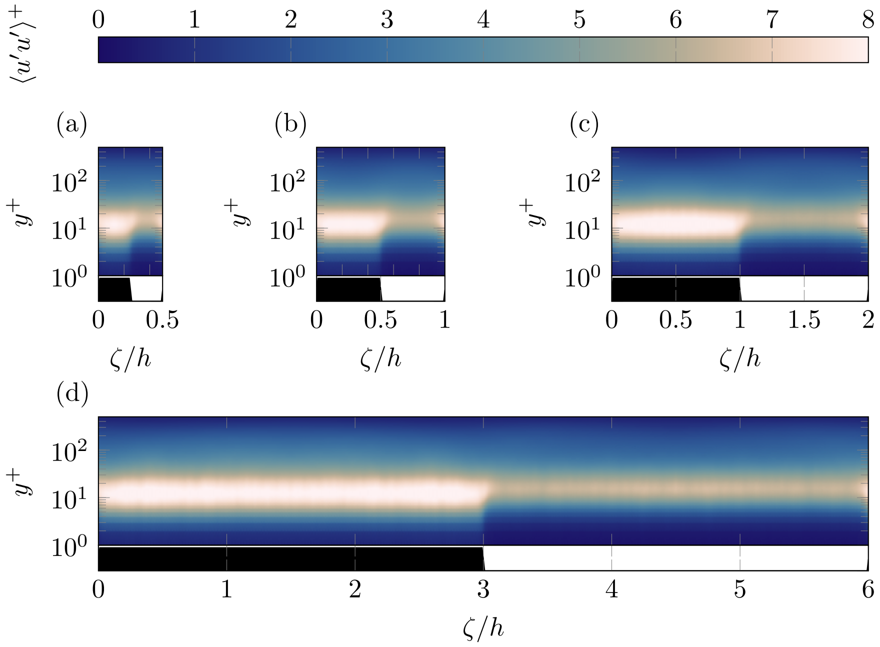

Figure 6.12: Distribution of the Reynolds stress $\langle u'u' \rangle$ over strip-type roughness at a steady state. The bar below each panel indicates regions of rough (black) or smooth (white) wall. Please notice that, in spite of the logarithmic scale on the vertical axis, no premultiplication is used. (a) $\Lambda_s/h = 0.5$; (b) $\Lambda_s/h = 1$; (c) $\Lambda_s/h = 2$; (d) $\Lambda_s/h = 6$. All data at $Re_\tau = 500$. Adapted from [MY24b].

commonly understood to be of Prandtl's second kind (Wang and Cheng, 2006; Anderson et al., 2015), meaning that they are driven by turbulence and arise owing to lateral dishomogeneities of the Reynolds stresses. For completeness then, and as an example, the normal Reynolds stress $\langle u'u' \rangle$ is analysed to recover some information about the fluctuation field, as this stress is usually the dominant term of the turbulent kinetic energy. Figure 6.12 shows its distribution at the initial steady state in the presence of strip-type roughnes for a selection of flow cases at $Re_\tau = 500$. Fluctuation intensites are roughly uniform over each smooth or rough strip; strong lateral changes of $\langle u'u' \rangle$ are only seen at roughness transitions. Typically, $\langle u'u' \rangle$ is maximum in the buffer layer ($y^+ \approx 10$); as would be expected from the viscous scaling of near-wall turbulence, this maximum is more energetic and closer to the wall over rough strips than over smooth ones for all tested values of Λ_s. Interestingly, then, the energy of u' fluctuations correlates well with the distribution of dispersive wall shear stress, although the fluctuations themselves are deprived of any coherent information owing to their definition. This could be interpreted as the random u'-fluctuations being modulated in amplitude (Mathis et al., 2009) by a coherent envelope, so that their amplitude (and thus, energy) is larger over rough strips. Notice that the position at which large spanwise gradients of the turbulent kinetic energy are found is indicative of the position of the circulatory motions.

The time evolution of this dishomogeneity in the kinetic energy is tracked in time using the following strategy. The value of $\langle u'u' \rangle$ is averaged in the buffer layer ($5 \leq y^+ \leq 30$) over rough or smooth strips alternatively; this defines the two quantities $\langle u'u' \rangle_R$ (averaged over portions of the wall that are, or were, rough) and $\langle u'u' \rangle_S$ (averaged over portions of the wall that are smooth from the initial condition). Similarly, the wall shear stress is averaged over rough or smooth strips to yield $\tau_{w,R}$ and $\tau_{w,S}$. Then, a quantitiy Δ_{uu} is defined as the difference between the two averaged values of the kinetic energy, $\Delta_{uu} = \langle u'u' \rangle_R - \langle u'u' \rangle_S$. Positive values indicate that turbulence is more energetic over portions of the wall that were rough at the initial condition, whereas the opposite holds for negative values. A zero

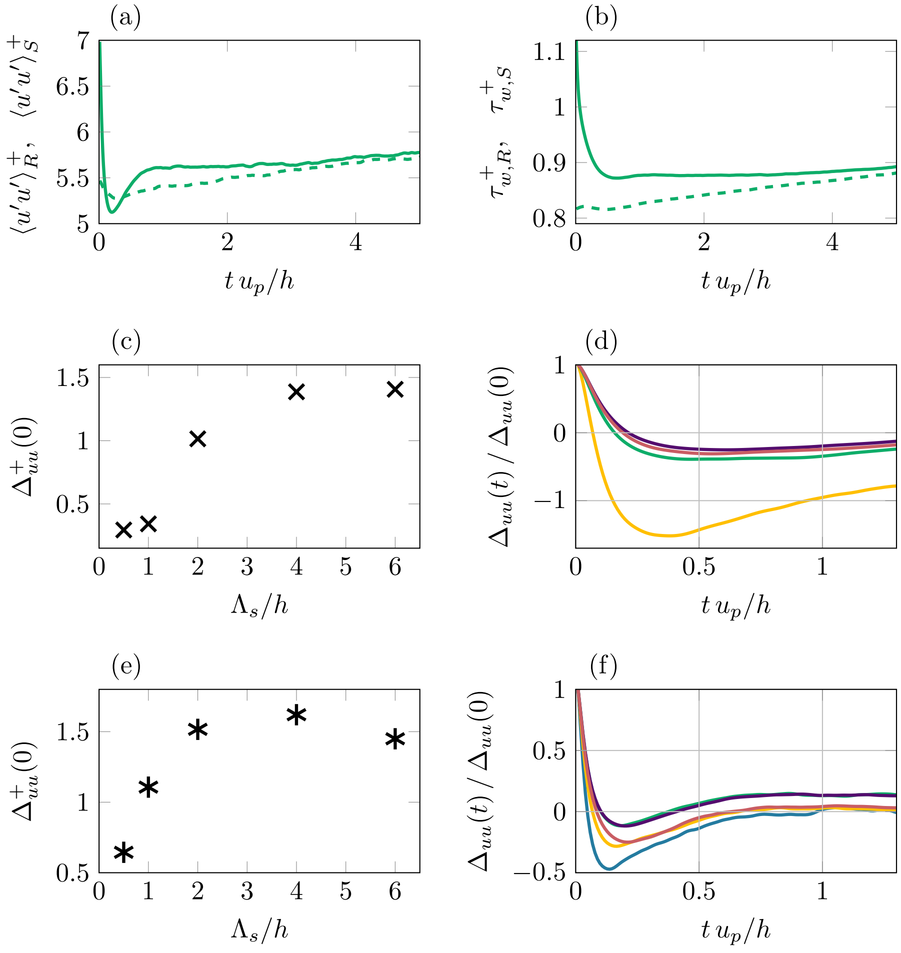

Figure 6.13: (a) Time evolution of $\langle u'u'\rangle^+_R$ (solid) and $\langle u'u'\rangle_S$ (dashed); $Re_\tau = 500$, $\Lambda_s/h = 2$. (b) Time evolution of $\tau_{w,R}$ (solid) and $\tau_{w,S}$ (dashed) for the same flow case as (a). (c) Initial values of Δ^+_{uu} as a function of Λ_s at $Re_\tau = 180$. (d) Time evolution of Δ_{uu} at $Re_\tau = 180$; different colours indicate different values of Λ_s/h as of table 6.1. (e,f) Same as (c,d), but at $Re_\tau = 500$. Adapted from [MY24b].

value of the difference indicates instead that the distribution of kinetic energy in the buffer layer has become homogeneous. Figure 6.13(a,b) shows, as an example, the evolution of $\langle u'u'\rangle_R$, $\langle u'u'\rangle_S$, $\tau_{w,R}$ and $\tau_{w,S}$ for a selected flow case ($Re_\tau = 500$, $\Lambda_s/h = 2$). As the rough strips are removed from the walls, the flow accelerates (as seen from figure 6.6a). This acceleration damps u'-fluctuations at all spanwise positions. Most of the loss in kinetic energy is seen for $\langle u'u'\rangle_R$; this loss is then quickly partially recovered before the system slowly approaches homogeneity. After an initial, not so pronounced decrease, $\langle u'u'\rangle_S$ also increases to reach roughly the same value as $\langle u'u'\rangle_R$. Notice that less kinetic energy is found over a smooth strip at a steady state in the context of strip-type roughness than over a smooth, homogeneous wall in a steady-state setting. As for the wall shear stress, a substantial decrease of $\tau_{w,R}$ is seen starting from the initial condition; $\tau_{w,R}$ then reaches a minimum - although such a minimum is not as prononuced as the minimum of $\langle u'u'\rangle_R$. Moreover, the minimum of $\langle u'u'\rangle_R$ is seen at an earlier time ($t = 0.196\,h/u_p$) than the one of $\tau_{w,R}$ (at $t = 0.65\,h/u_p$), suggesting that fluctuations evolve at a faster pace than the wall shear stress. After the minimum, the wall shear stress $\tau_{w,R}$ roughly remains constant, whereas the value of $\tau_{w,S}$ slowly increases from its initial value to reach that of $\tau_{w,R}$.

The remaining panels of figure 6.13 show instead the initial value and the evolution of Δ_{uu} for all considered flow cases at the low (c,d) and high (e,f) Reynolds number. Notice that only a limited number of repetitions is available for $\Lambda_s/h = 0.5$, $Re_\tau = 180$; this is sufficient to achieve a satisfactory accuracy of first-order velocity momenta (e.g. the dispersive velocity), but not of the second-order ones needed in this case (e.g., $\langle u'u' \rangle$). Data for this specific combination of parameters is thus not shown. At the steady state, the difference in kinetic energy between rough and smooth strips increases with Λ_s at the lower Reynolds number, until it saturates for $\Lambda_s/h \geq 4$. At the higher Reynolds number, instead, it is maximum for $\Lambda_s/h = 4$. For all considered flow cases, the initial condition (consisting in higher energy over portions of the wall that are, or were, rough) is quickly reversed as the values of Δ_{uu} turn negative. For $\Lambda_s/h = 2$ and $\Lambda_s/h = 4$ at $Re_\tau = 500$, interestingly, the initial sign of Δ_{uu} is recovered at roughly $t = 0.3h/u_p$; advancing in time, sections of the wall that were rough maintain a slightly higher fluctuation intensity $\langle u'u' \rangle$ than the remaining ones for an extended period of time. These are the only two cases for which this behaviour is observed; interestingly, these are also the only two cases for which a significant overshoot of I_u is seen at the higher Reynolds number." [MY24b]

6.5 Summary and conclusions

In this chapter, "the secondary motions found in turbulent channel flows in the presence of a spanwise-heterogeneous roughness pattern (strip-type roughness) of varying spanwise period Λ_s have been studied. The investigation is carried out both at a steady state and as the secondary motions decay towards a spanwise-homogeneous configuration. The decay is obtained by suddenly removing the strip-type roughness, so that the flow evolves between smooth walls. The temporal evolution of the secondary motions is captured by ensemble-averaging multiple realisations (simulations) of each considered flow case. To the author's best knowledge, it is the first time that time-evolving ensemble averages of secondary flows are produced from direct numerical simulations (DNSs).

Steady-state data over strip-type roughness is used to highlight the features of the secondary motions, which have been investigated both in physical and Fourier space. By comparing the spectra of smooth-wall simulations to those observed over strip-type roughness, it is found that a dispersive average correctly isolates the main differences between the two setups. The dispersive velocity field captures both the cross-sectional circulatory motions typically associated to secondary motions and the streamwise-momentum pathways observed, for instance, by Barros and Christensen (2014); Womack et al. (2022). The dispersive velocity field can be partitioned into three different regions: a near-wall velocity pattern (closely linked to the wall shear stress), an anti-correlation region and an equilibrium one. The anti-correlation region is the one where the streamwise and wall-normal components of the dispersive velocity ($\tilde{u}$ and $\tilde{v}$ respectively) are indeed anti-correlated; this is also where strong cross-sectional circulatory motions are observed. In the equilibrium region, instead, the wall-normal profile of the streamwise velocity $U + \tilde{u}$ scaled in local viscous units roughly collapses on the profile observed in spanwise-homogeneous conditions (either over a smooth or a rough wall). The three regions are only clearly distinguishable for large values of Λ_s. Indeed, the secondary motions grow taller in the wall-normal direction for increasing value of Λ_s, so that the anti-correlation region and the near-wall pattern become separated in the wall-normal direction. Moreover, while the anti-correlation region is dominant for small values of Λ_s, it remains confined at roughness transitions (regions of large spanwise gradient of roughness properties) for large values of Λ_s, so that an equilibrium region arises in the middle of each strip. By analysing the budget equation for $\tilde{u}$, it is speculated that the $\langle u'v' \rangle$ Reynolds stress is mainly responsible for the formation of the equilibrium region and of the wall shear stress pattern. The formation of the anti-correlation region, instead, appears to be driven by $\tilde{v}$-transport of the mean field U.

Then, time-coherence of the dispersive field once the strip-type roughness is suddenly replaced by smooth walls is investigated. A previous study (Kaminaris et al., 2023) had indeed highlighted that momentum pathways (here captured by $\tilde{u}$) can sustain for a long streamwise distance in the wake of the rough patch that triggers them. It is observed that the timescale T_u describing the decay of the volume-averaged $\tilde{u}$-energy (that is, the overall energy held by the momentum pathways) increases monotonically with Λ_s. By converting the present temporal information to a spatial one, crude estimates of the streamwise coherence of the momentum pathways are provided ($L_d \approx 20 - 24\,\Lambda_s$). The present estimates are in good agreement with the results of Womack et al. (2022). The time scale T_{vw} associated to the circulatory motions also generally increases for increasing Λ_s; saturation is however observed for large values of it. It is argued that the circulatory motions are wall-attached; the present results are then compared to the ones of Lozano-Durán and Jiménez (2014), who found the lifetime of attached eddies to be proportional to their wall-normal extent. In most considered cases, the momentum pathways take a significantly longer time to decay than the cross-sectional circulatory motions; similarly to the findings of Del Álamo and Jiménez (2006), this suggests that the momentum pathways are mainly, but not exclusively, produced by $\tilde{v}$-transport of U.

The time-coherence of the spanwise wall shear stress pattern is not well captured by the time scale defined with the volume-averaged energy. Such a pattern can be decomposed into the sum of many Fourier modes of spanwise period λ_z. The time to decay of each Fourier mode appears to strongly depend on the wavelength λ_z of the Fourier mode itself and on the Reynolds number, but not much on the global geometry of the flow as captured by the spanwise period Λ_s. Finally, it is shown that the energy of the fluctuation field found over strip-type roughness is spanwise-heterogeneous; though the fluctuations are random and deprived of any coherent information by definition, their amplitude is coherent with the roughness pattern at the wall. These heterogeneities are tracked in time.” [MY24b]

The aim of this chapter “is to verify the plausibility of the estimates put forward by Townsend (1976) to explain the recurrence of h-scaled flow features in turbulent flows, where h is some outer-layer length scale (here, the channel half-height). Townsend predicted that wall shear stress patterns of a specific characteristic spanwise wavelength ($\lambda_z \approx h$, $\lambda_z \leq 4h$) would be able to self-sustain through some induced secondary motion and hence dominate other flow features. It would be then expected that secondary motions of a matching period take the longest time to decay; alternatively, the time to decay could increase as Λ_s grows larger until a threshold value of Λ_s in the range proposed by Townsend is reached. For larger values of Λ_s, the time scale would saturate.

Mixed evidence was found in reviewing Townsend’s estimates. The analysis of volume-averaged quantities reveals that the temporal coherence of streamwise-momentum pathways generally increases for increasing Λ_s, clearly contradicting Townsend’s calculations. However, the present data suggests that the time to decay of the circulatory motions is maximum for some value of Λ_s in the range proposed by Townsend ($\Lambda_s/h = 1$ at $Re_\tau = 180$, $\Lambda_s/h = 2$ at $Re_\tau = 500$); it saturates for larger values. Interestingly, the volume-averaged energy I_u of the momentum pathways undergoes a transient growth with respect to its initial value for values of Λ_s in the range $2 \leq \Lambda_s/h \leq 4$. This transient growth might be evidence that motions of this specific size can self-sustain as proposed by Townsend. An analogy with linear transient growth theory suggests that the growth might be driven by $\tilde{v}$-transport of U; this does not appear to be the case in the present context, though. It was not possible to link the time evolution of the circulatory motions (which account for $\tilde{v}$) to the occurence of transient growth. Other mechanisms are likely at play.

Although some evidence appears to contradict Townsend’s speculations, the author maintains that the latter could be plausible. Indeed, the present study considers the temporal decay of fully-developed secondary motions which, for large values of Λ_s, become spatially confined to a $2h$-wide region. In these cases, then, we do not effectively study the evolution of a Λ_s-sized structure as intended, but rather of a $2h$-sized one regardless of the value of Λ_s. The confinement itself is evidence in favour of Townsend’s idea: the Λ_s-sized perturbation provided by the roughness pattern fails to leverage a secondary motion of comparable size. Instead, some $2h$-sized motions become dominant. The topic could be further investigated, for instance, by studying the evolution of artificial perturbations whose size can be exactly controlled. The perturbations could be then tracked using the methodology proposed in the present paper. If a constant perturbation is applied to different snapshots of the same steady-state flow between smooth walls and the snapshots are allowed to evolve independently, an ensemble average should be able to isolate the evolution of the coherent perturbation. Using a near-wall periodic perturbation applied to the spanwise velocity component is recommended: linear analysis suggests that wall-bounded flows are particularly sensitive to such a disturbance (Jovanović and Bamieh, 2005). Spanwise positions at which this disturbance is maximum would be equivalent to roughness transitions. Such a setup could shed light on the mechanisms driving the formation of secondary motions; moreover, it could help to explain why they remain confined at roughness transitions for large values of Λ_s." [MY24b]

7 Conclusions

As per its title, this manuscript deals with large, turbulent eddies and their interaction with the wall shear stress. In particular, two macroscopic themes are of interest. First, the wall shear stress is directly responsible for the expenses (e.g. in the form of skin friction drag, or power expenses) in a turbulent flow; assessing how much large scales contribute to these expenses and how much can be spared by controlling them is of interest for this dissertation. On the other hand, it is of interest to investigate how the wall shear stress alters the dynamics of the large scales, and vice-versa how the large scales can have an effect on the near-wall region.

These two macroscopic themes are explored in terms of four specific scientific questions, as discussed in §1.3; each question has been addressed by a numerical investigation (§3, §4, §5 and §6). The results obtained in each individual investigation are combined in this section to provide useful insights on the two macroscopic themes of this thesis. In §7.1, a final comment on flow control – and, more specifically, on the targeting of large scales to achieve drag reduction – will be presented. In §7.2, instead, the effect of the distribution of wall shear stress on the dynamics of large scales will be discussed in terms of the gathered evidence. Before doing so, the results of each chapter are briefly summarised in the next lines by directly addressing the corresponding scientific questions.

1. **How do the costs (in terms of power input or wall shear stress) associated to small and large scales differ?**
   In §3, turbulent plane Couette and Poiseuille flows were compared. Couette flows are characterised by strong large scales, whereas large structures are either absent or weak in Poieseuille flows (as far as the considered range of low to moderate Reynolds numbers is concerned). Using the Constant Power Input (CPI) framework, it was determined that, when fed with the same power input, Couette flows are less efficient, but more effective at producing flow rate than Poiseuille flows. In other words, Couette flows are able to produce a slightly larger flow rate out of a given power input (more effective). In doing so, Couette flows lose a larger share of said power input to turbulence (less efficient). The CPI framework was analyitically extended to be able to discriminate the effects of large and small scales of turbulence; doing so, it was clearly shown that the intense large scales of Couette flows induce costly deviations of the mean velocity from its ideal profile, whereas small scales are directly associated to turbulent dissipation. These two effects are captured by separate energy fluxes (namely, deviation and turbulent dissipation) defined in the CPI framework, the sum of which corresponds to the overall overhead expense caused by turbulence.
2. **How much of the cost (power input or skin friction) caused by large scales can be saved by removing them?**
   In the context of the previous scientific objective, it was shown that large scales mainly cause distortions of the mean velocity profile, which in turn induce additional expenses in the form of deviation dissipation. In §4, the large scales of Couette flows were suppressed using a weak Coriolis force. The effect of the Coriolis force on small scales was found to be marginal. It was shown that the deviation dissipation associated to large scales can be spared by suppressing them; however, the suppression of large scales is accompanied by the energisation of smaller (yet not

necessarily inner-scaled) scales. These energised scales cause additional expenses. The overall savings were nevertheless satisfactory (13% reduction of the wall shear stress at constant flow rate at the highest tested Reyonlds number), indicating that targeting large scales might be a profitable flow control strategy.

3. **Is the wall-shear stress the mediator in the scale-interaction mechanism known as amplitude modulation?**
   The numerical experiments presented in §5 have highlighted that a correlation between the amplitude of near-wall small scales and outer-layer large scale exists even if the near-wall, superimposed large scales (including large-scaled patterns of the wall shear stress) are suppressed. The present findings cannot confirm nor confute that spatial variations of the wall-shear stress have a modulating action on the small scales; however, they clearly indicate that a second modulating mechanism must exist, so that amplitude modulation is observed even in absence of the superposed large scales. An additional numerical experiment was performed, in which small scales are prevented from having a large-scale envelope. It was found that, under such circumstances, the near-wall superposed large scales are significantly weakened, suggesting that near-wall large scales might be produced by the non-linear interaction of small scales. This second result might be of interest for LES modelling: it indicates that large scales are aware of (and influenced by) instantaneous spatial variations of the small-scale energy. Such spatial variations are typically not captured in the context of LES simulations, in which the unresolved small scales typically have a passive role (see §1.2.5 or Davidson, 2015, chapter 7.1.2).
4. **Is Townsend's hypothesis (as formulated in §1.2.6) plausible? Or, in other words: can secondary motions induced by a lateral wall shear stress pattern of a specific, large size self-sustain, so as to outlive motions of any other size?**
   The lifetime of secondary motions of different sizes was investigated in §6. The secondary motions ensue from the application of a spanwise-heterogeneous roughness pattern to the walls of a channel flow; such a roughness pattern indirectly produces a lateral variation of the wall shear stress. According to Townsend's original formulation, the secondary motions are directly produced by the pattern of wall shear stress; however, the investigation presented in §6 as well as further evidence found in the literature (e.g. Anderson et al., 2015) suggest that both the lateral wall shear stress pattern and the secondary motions are generated by dishomogeneities of the Reynolds stresses. The core idea behind Townsend's hypothesis is that turbulent flows tend to favour the formation of energetic, h-scaled structures; this is indeed well verified, as the results shown in §6 indicate, for instance, that structures with a spanwise size of roughly $2h$ are the most energetic and that their presence is felt at every wall-normal distance up to the channel centerline. Nevertheless, mixed evidence is found when specifically investigating whether structures of such a size take a longer time to decay (that is, they live longer) than structures of any other size. The decay of the structures is produced by suddenly removing the roughness pattern that allows for their sustainment. It is found that the life time of structures of streamwise momentum (momentum pathways) gets longer the larger their spanwise size is. As for cross-sectional circulatory motions, instead, their lifetime is maximum when their spanwise size is roughly $2h$ – in agreement with Townsend's hypothesis. Moreover, the energy held by structures whose spanwise size falls in the range $2h - 4h$ undergoes a transient growth before decaying, possibly indicating that structures of this size might be able to self-sustain.

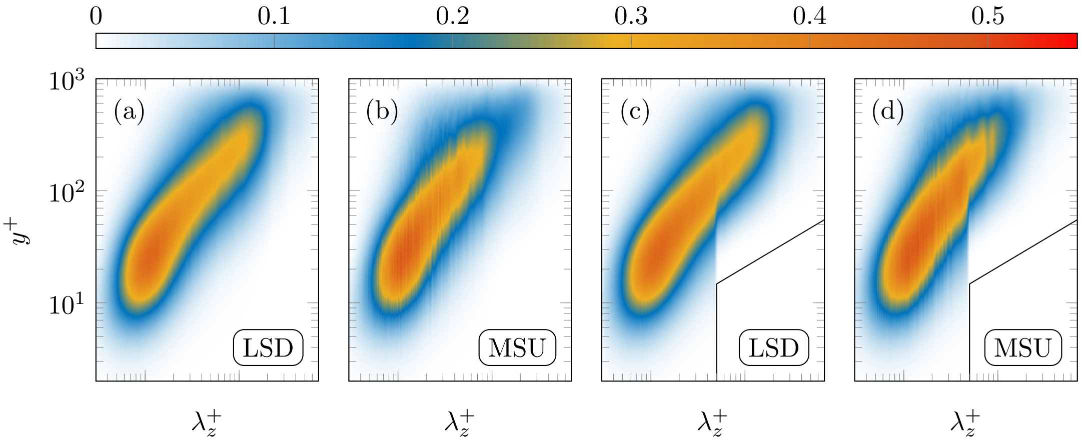

Figure 7.1: Premultiplied spanwise co-spectra $-\kappa_z^+ \mathcal{R}e\left(\Phi_{uv}\right)^+$ of the Reynolds shear stress. (a,b) Channel flow at $Re_\tau = 1000$ in a LSD or MSU domain respectively. (c,d) Same channel flow and same combination of domains, but the superposed, near-wall large scales have been removed as described in §5.1.1. A solid black line indicates the border of the space-scale region where modal damping is applied. Adapted from [MY23].

7.1 Takeaways for flow control: a discussion

The feasibility of large-scale control as a means of achieving skin-friction drag reduction was directly addressed in §4. Although they address different topics, the results of §5 and §6 also provide useful insights for flow control; their relevance will be discussed in this section.

In §4, it was shown that a weak Coriolis force is able to remove large scales from turbulent Couette flows and thereby achieve a significant skin-friction reduction. While these results are encouraging, the Coriolis force cannot practically be used to achieve drag reduction on, for example, an aircraft wing. This is because the Coriolis force is a body force that acts on every fluid element in the flow, whereas the actuators that can be practically used in flow control applications act only at discrete spatial positions, typically at the wall. It is unclear whether the results obtained by the Coriolis force can be replicated by an external force only acting on the near-wall region.

In this respect, §5 contains useful insights. In this chapter, the near-wall large-scales were removed from a turbulent channel flow by a localised, near-wall modal damping. Doing so, no significant effect was obsered on the mean velocity profile (see figure §5.7), and in particular no drag-reduction was observed. The reason why the removal of near-wall large scales produces little to no effect on the dynamics of the flow can be readily found in the co-spectra of the Reynolds shear stress. These are shown in figure 7.1 for the data of §5.2.1; a solid black line indicates the near-wall large-scales that were artificially removed from the flow. The contribution of the suppressed motions to the Reynolds shear stress is marginal before the suppression (panels a, b); it is then reasonable to expect the suppression to leave the co-spectrum practically unchanged as, simply put, the motions being suppressed play a marginal role in the flow. Figure 7.1(c,d) confirms this idea. The distribution of Reynolds shear stress is unchanged by the suppression, and the Reynolds shear stress essentially determines the velocity profile across the channel (see equation 2.9): this explains why the suppression of the superposed, near-wall large scales produces no effect on the mean flow. Moreover, the FIK identity (equation 4.8) indicates that the Reynolds shear stress is directly linked to the wall shear stress, hence explaining the lack of drag reduction. As a side note, surprising results in terms of drag reduction were observed in §5.2.2 by targeting the large-scaled envelope of near-wall small scales instead of large scales directly.

The above evidence suggests that, if an actuator located at the wall is only able to have an effect on near-wall large scales, practical implementations of large-scale actuation should have little effect on the flow. Luckily, this should not be the case: it is reasonable to believe that large-scale actuation at the wall should be able to produce effects not only on near-wall large scales, but also on outer-layer ones. Evidence in this respect can be found in §6. In this chapter, a spanwise-heterogeneous roughness pattern was applied to the walls of a channel flow. If the spanwise period (size) of the pattern is small-scaled, its effects (in the form of a secondary motion) are only perceived in the near-wall region. If, instead, the pattern is large-scaled, its effect will reach the channel centerline (see figure 6.3). In other words, some near-wall large-scale action can have an effect on the outer layer of a turbulent flow. This outer-layer effect should then be capable of delivering drag reduction, as confirmed by the experimental results of, for instance, Marusic et al. (2021) and Dacome et al. (2024).

7.2 Large scales and the wall shear stress: a chicken and egg problem

Throughout the manuscript, contrasting ideas regarding the dynamics of large scales and the way they interact with the wall shear stress have been reviewed. For instance, in §5 it was explored whether large-scaled patterns of wall shear stress are created by outer-layer large scales that superpose themselves on the near-wall region – as widely believed in the literarture (see §1.2.5). An anthitetical hypothesis was investigated in §6: the random occurrence of large-scaled patterns of the wall shear stress might trigger the formation of large-scaled motions (as proposed by Townsend, 1976, see also §1.2.6). Both the investigated ideas discuss the mutual interaction between large scales and the distribution of wall shear stress at the wall. Crucially, they differ in that one postulates that large scales generate large-scaled patterns of wall shear stress, whereas the other suggests the opposite. Simply put, this is a chicken and egg problem. Does the wall shear stress come first, or is it large scales that generate a wall shear stress pattern?

Surprisingly, the evidence gathered in reviewing such two opposing ideas points in a single direction. Both the data of §5 and of §6 clearly suggest that large-scale patterns of wall-shear stress are caused by (transient or coherent) dishomogeneities of the Reynolds stresses. Moreover, as will be discussed below, it is likely that large-scale structures (or secondary motions over strip-type roughness at least) arise as a consequence of the dishomogeneity of the Reynolds stresses. It appears, then, that neither large-scales create particular patterns of wall shear stress nor that large-scale variations of the wall shear stress cause the formation of large eddies: both appear to arise owing to the local variations of the Reynolds stresses.

In §5, it was found that near-wall large scales (including large-scale patterns of wall shear stress) disappear when near-wall small scales are prevented from having a large-scale envelope (see §5.2.2). The implications of manipulating the envelope of the small scales are non-trivial. The amplitude of naturally occurring small scales typically appears to be modulated by a large-scale signal (if the Reynolds number is sufficiently high; see, for instance, §5.2). Spatial regions where the amplitude of small scales is larger (smaller) than usual can be thought of as regions of higher (lower) small-scale kinetic energy. In other words, the istantaneous field of small-scale energy is, in a sense, heterogeneous, as one observes large-scaled region of enhanced (or reduced) energy. Manipulating the envelope of the small scales as done in §5.2.2 effectively prevents the small-scale energy field from having such heterogeneities; it is observed that such a constraint blocks the formation of near-wall large scales. Specifically, non-linear interactions yielding an inter-scale energy transfer are hindered (see §5.1.2). It appears, then, that near-wall large scales draw energy from the local small ones (as also pointed out, for instance, by Cimarelli et al., 2016; Cho et al., 2018; Kawata and Alfredsson, 2018; Chiarini et al., 2022), and that this energy transfer occurs as a consequence of istantaneous spatial heterogeneities of the small scale kinetic energy. Similar observations were put forward in §6 while studying the effects of spanwise-heterogeneous roughness patterns. An analysis of coherent energy budgets (figure 6.4 in §6.2) suggests that coherent patterns of wall shear stress are formed by the action of $\langle u'v' \rangle$ Reynolds stresses[1]. The heterogeneous distribution of roughness is linked to a heterogeneous distribution of the Reynolds stresses (see §6.4), which is then reflected in a heterogeneous distribution of wall shear stress.

As for how large scale structures originate, not much can be said judging on the present data. However, useful considerations arise by scrutinising the momentum budget of the dispersive velocity field of a flow over strip-type roughness. If the analogy between secondary motions and randomly occurring large-scale eddies (as proposed in §1.2.6) holds, similar considerations apply to large scales too. Secondary motions over strip-type roughness are commonly understood to originate from heterogeneities of the Reynolds shear stresses (Anderson et al., 2015). In §6.2 (figure 6.4), it was argued that the coherent distribution of wall shear stress is indeed formed by heterogeneities in the Reynolds shear stress by scrutinising the streamwise dispersive momentum budget. Here, instead, the spanwise momentum budget is of interest:

$$\begin{aligned}\frac{\partial \tilde{w}}{\partial t} + \tilde{v}\frac{\partial \tilde{w}}{\partial y} + \tilde{w}\frac{\partial \tilde{w}}{\partial \zeta} + \frac{1}{\rho}\frac{\partial \tilde{P}}{\partial \zeta} &= \nu \nabla^2 \tilde{w} + \frac{\partial}{\partial y}\langle \tilde{v}\tilde{w}\rangle_z + \\ &- \frac{\partial}{\partial y}\left(\langle v'w' \rangle - \langle v'w' \rangle_z\right) - \frac{\partial}{\partial \zeta}\langle w'w' \rangle\end{aligned} \tag{7.1}$$

The term involving the normal Reynolds stress $\langle w'w' \rangle$ has particular relevance for the present discussion:

$$-\frac{\partial}{\partial \zeta}\langle w'w' \rangle$$

Such a term indicates that coherent heterogeneities of the $\langle w'w' \rangle$ stress produce a mean $\tilde{w}$-momentum transfer; specifically, momentum is transferred from regions of high-energy to regions of low energy (owing to the minus sign). This is relevant for two reasons. First off, it is likely that heterogeneous roughness induces such a heterogeneity of $\langle w'w' \rangle$. One can indeed speculate that roughness elements in proximity of the wall redirect u' fluctuations in the spanwise and wall normal directions, thus locally increasing the kinetic energy $\langle w'w' \rangle$. Such $\langle w'w' \rangle$ kinetic energy is expected to be lower in regions where the wall is smooth, or somehow less rough[2]. Last but not least, this momentum flux is relevant as it may shed light on how secondary motions (and possibly large-scale turbulent eddies) originate. The position of large spanwise gradients of the $\langle w'w' \rangle$-energy is well predictive of the position of secondary motions: owing to the above discussion, large gradients of $\langle w'w' \rangle$-energy are found at roughness transitions, which is where secondary motions are centered (see §6.2). Most importantly, it is known from linear transient growth analysis (Jovanović and Bamieh, 2005) that turbulent flows are particularly sensitive to near-wall spanwise perturbances – such as the one provided by the spanwise gradient of $\langle w'w' \rangle$. Perhaps, such a disturbance gets amplified by linear mechanisms to produce the observed secondary motions (or large-scale eddies). The verification of such a hypothesis is left for future works.

---

[1] Notice that, at a first glance, it might appear that the distribution of wall shear stress is directly imposed by the slip-length boundary condition used in the simulations of §6 to mimick roughness. However, the distribution of wall shear stress is produced indirectly: the only direct effect of the boundary condition is to allow for the existence of non-zero spanwise velocity fluctuations at the wall. The mechanism through which the observed distribution of wall shear stress is produced is not trivial.

[2] Notice, moreover, that no preferential direction is given at the wall for w' fluctuations. Consider two adjacent regions of high- and low-$\langle w'w' \rangle$-energy, such that the high-energy region is located to the left. Let now the interface between these two regions be considered. Positive w' fluctuations move left to right and can be thus interpreted to originate in the high-energy region; viceversa, negative fluctuations originate in the low-energy area and have low energy. By assuming that positive and negative fluctuations are equally likely to occur, a net momentum flux from the left (high-energy) to right (low-energy) is expected – as the positive fluctuations dominate the negative ones in magnitude.

Bibliography

M. Abbassi, W. Baars, N. Hutchins, and I. Marusic. Skin-friction drag reduction in a high-Reynolds-number turbulent boundary layer via real-time control of large-scale structures. *International Journal of Heat and Fluid Flow*, 67:30–41, Oct. 2017. ISSN 0142727X.

H. Abe and R. A. Antonia. Relationship between the energy dissipation function and the skin friction law in a turbulent channel flow. *Journal of Fluid Mechanics*, 798:140–164, July 2016. ISSN 0022-1120, 1469-7645.

H. Abe, H. Kawamura, and H. Choi. Very Large-Scale Structures and Their Effects on the Wall Shear-Stress Fluctuations in a Turbulent Channel Flow up to Reτ=640. *Journal of Fluids Engineering*, 126(5): 835–843, Dec. 2004. ISSN 0098-2202.

H. Abe, R. A. Antonia, and S. Toh. Large-scale structures in a turbulent channel flow with a minimal streamwise flow unit. *Journal of Fluid Mechanics*, 850:733–768, Sept. 2018. ISSN 0022-1120, 1469-7645.

M. Abramowitz and I. A. Stegun. *Handbook of Mathematical Functions*. Number 55 in Applied Mathematics Series. National Bureau of Standards, 1964.

L. Agostini and M. Leschziner. The Impact of Footprints of Large-Scale Outer Structures on the Near-Wall Layer in the Presence of Drag-Reducing Spanwise Wall Motion. *Flow, Turbulence and Combustion*, 100(4):1037–1061, June 2018. ISSN 1386-6184, 1573-1987.

L. Agostini and M. Leschziner. The connection between the spectrum of turbulent scales and the skin-friction statistics in channel flow at Re=1000. *Journal of Fluid Mechanics*, 871:22–51, July 2019a. ISSN 0022-1120, 1469-7645.

L. Agostini and M. Leschziner. On the departure of near-wall turbulence from the quasi-steady state. *Journal of Fluid Mechanics*, 871, July 2019b. ISSN 0022-1120, 1469-7645.

L. Agostini, M. Leschziner, and D. Gaitonde. Skewness-induced asymmetric modulation of small-scale turbulence by large-scale structures. *Physics of Fluids*, 28(1):015110, Jan. 2016. ISSN 1070-6631.

F. Alizard, S. Pirozzoli, M. Bernardini, and F. Grasso. Optimal transient growth in compressible turbulent boundary layers. *Journal of Fluid Mechanics*, 770:124–155, May 2015. ISSN 0022-1120, 1469-7645.

W. Anderson, J. M. Barros, K. T. Christensen, and A. Awasthi. Numerical and experimental study of mechanisms responsible for turbulent secondary flows in boundary layer flows over spanwise heterogeneous roughness. *Journal of Fluid Mechanics*, 768:316–347, Apr. 2015. ISSN 0022-1120, 1469-7645.

F. Auteri, A. Baron, M. Belan, G. Campanardi, and M. Quadrio. Experimental assessment of drag reduction by traveling waves in a turbulent pipe flow. *Physics of Fluids*, 22(11):115103, Nov. 2010. ISSN 1070-6631, 1089-7666.

W. J. Baars, N. Hutchins, and I. Marusic. Reynolds number trend of hierarchies and scale interactions in turbulent boundary layers. *Philosophical Transactions of the Royal Society A: Mathematical, Physical and Engineering Sciences*, 375(2089):20160077, Mar. 2017a.

W. J. Baars, N. Hutchins, and I. Marusic. Self-similarity of wall-attached turbulence in boundary layers. *Journal of Fluid Mechanics*, 823:R2, July 2017b. ISSN 0022-1120, 1469-7645.

S. C. C. Bailey and A. J. Smits. Experimental investigation of the structure of large- and very-large-scale motions in turbulent pipe flow. *Journal of Fluid Mechanics*, 651:339–356, May 2010. ISSN 1469-7645, 0022-1120.

B. Balakumar and R. Adrian. Large- and very-large-scale motions in channel and boundary-layer flows. *Philosophical Transactions of the Royal Society A: Mathematical, Physical and Engineering Sciences*, 365 (1852):665–681, Mar. 2007. ISSN 1364-503X, 1471-2962.

J. R. Baltzer, R. J. Adrian, and X. Wu. Structural organization of large and very large scales in turbulent pipe flow simulation. *Journal of Fluid Mechanics*, 720:236–279, Apr. 2013. ISSN 0022-1120, 1469-7645.

J. M. Barros and K. T. Christensen. Observations of turbulent secondary flows in a rough-wall boundary layer. *Journal of Fluid Mechanics*, 748:R1, June 2014. ISSN 0022-1120, 1469-7645.

J. M. Barros and K. T. Christensen. Characteristics of large-scale and superstructure motions in a turbulent boundary layer overlying complex roughness. *Journal of Turbulence*, 20(2):147–173, Feb. 2019. ISSN 1468-5248.

P. Bartholomew, G. Deskos, R. A. Frantz, F. N. Schuch, E. Lamballais, and S. Laizet. Xcompact3D: An open-source framework for solving turbulence problems on a Cartesian mesh. *SoftwareX*, 12:100550, July 2020. ISSN 23527110.

K. H. Bech and H. I. Andersson. Secondary flow in weakly rotating turbulent plane Couette flow. *Journal of Fluid Mechanics*, 317:195–214, June 1996. ISSN 0022-1120, 1469-7645.

M. Bernardini and S. Pirozzoli. Inner/outer layer interactions in turbulent boundary layers: A refined measure for the large-scale amplitude modulation mechanism. *Physics of Fluids*, 23(6):061701, June 2011. ISSN 1070-6631.

T. R. Bewley. A fundamental limit on the balance of power in a transpiration-controlled channel flow. *Journal of Fluid Mechanics*, 632:443–446, Aug. 2009. ISSN 0022-1120, 1469-7645.

P. Bradshaw and J. B. Perot. A note on turbulent energy dissipation in the viscous wall region. *Physics of Fluids A: Fluid Dynamics*, 5(12):3305–3306, Dec. 1993. ISSN 0899-8213.

G. J. Brereton and J.-L. Hwang. The spacing of streaks in unsteady turbulent wall-bounded flow. *Physics of Fluids*, 6(7):2446–2454, July 1994. ISSN 1070-6631, 1089-7666.

E. O. Brigham. *The Fast Fourier Transform and Its Applications*. Prentice-Hall Signal Processing Series. Prentice Hall, Englewood Cliffs, N.J, 1988. ISBN 978-0-13-307505-2.

M. H. Buschmann and M. Gad-El-Hak. Debate Concerning the Mean-Velocity Profile of a Turbulent Boundary Layer. *AIAA Journal*, 41(4):565–572, Apr. 2003. ISSN 0001-1452, 1533-385X.

J. Canton, R. Örlü, C. Chin, N. Hutchins, J. Monty, and P. Schlatter. On Large-Scale Friction Control in Turbulent Wall Flow in Low Reynolds Number Channels. *Flow, Turbulence and Combustion*, 97(3): 811–827, Oct. 2016a. ISSN 1386-6184, 1573-1987.

J. Canton, R. Örlü, C. Chin, and P. Schlatter. Reynolds number dependence of large-scale friction control in turbulent channel flow. *Physical Review Fluids*, 1(8):081501, Dec. 2016b. ISSN 2469-990X.

Y. Chang, S. S. Collis, and S. Ramakrishnan. Viscous effects in control of near-wall turbulence. *Physics of Fluids*, 14(11):4069–4080, Nov. 2002. ISSN 1070-6631, 1089-7666.

C. Chen and L. He. On locally embedded two-scale solution for wall-bounded turbulent flows. *Journal of Fluid Mechanics*, 933:A47, Feb. 2022. ISSN 0022-1120, 1469-7645.

A. Chiarini, M. Mauriello, D. Gatti, and M. Quadrio. Ascending–descending and direct–inverse cascades of Reynolds stresses in turbulent Couette flow. *Journal of Fluid Mechanics*, 930:A9, Jan. 2022. ISSN 0022-1120, 1469-7645.

M. Cho, Y. Hwang, and H. Choi. Scale interactions and spectral energy transfer in turbulent channel flow. *Journal of Fluid Mechanics*, 854:474–504, Nov. 2018. ISSN 0022-1120, 1469-7645.

H. Choi, P. Moin, and J. Kim. Active turbulence control for drag reduction in wall-bounded flows. *Journal of Fluid Mechanics*, 262:75–110, Oct. 1994.

D. Chung and B. J. McKeon. Large-eddy simulation of large-scale structures in long channel flow. *Journal of Fluid Mechanics*, 661:341–364, Oct. 2010. ISSN 0022-1120, 1469-7645.

D. Chung, J. P. Monty, and N. Hutchins. Similarity and structure of wall turbulence with lateral wall shear stress variations. *Journal of Fluid Mechanics*, 847:591–613, July 2018. ISSN 0022-1120, 1469-7645.

D. Chung, N. Hutchins, M. P. Schultz, and K. A. Flack. Predicting the Drag of Rough Surfaces. *Annual Review of Fluid Mechanics*, 53(1):439–471, Jan. 2021. ISSN 0066-4189, 1545-4479.

A. Cimarelli, E. De Angelis, J. Jiménez, and C. M. Casciola. Cascades and wall-normal fluxes in turbulent channel flows. *Journal of Fluid Mechanics*, 796:417–436, June 2016. ISSN 0022-1120, 1469-7645.

C. Cossu, G. Pujals, and S. Depardon. Optimal transient growth and very large–scale structures in turbulent boundary layers. *Journal of Fluid Mechanics*, 619:79–94, Jan. 2009. ISSN 0022-1120, 1469-7645.

F. Crameri. Scientific colour maps. Zenodo, Oct. 2023.

F. Crameri, G. E. Shephard, and P. J. Heron. The misuse of colour in science communication. *Nature Communications*, 11(1):5444, Oct. 2020. ISSN 2041-1723.

G. Dacome, R. Mörsch, M. Kotsonis, and W. J. Baars. Opposition flow control for reducing skin-friction drag of a turbulent boundary layer. *Physical Review Fluids*, 9(6):064602, June 2024. ISSN 2469-990X.

P. Davidson. *Turbulence: An Introduction for Scientists and Engineers*. Oxford University Press, 2nd edition, June 2015. ISBN 978-0-19-872258-8.

M. de Giovanetti, Y. Hwang, and H. Choi. Skin-friction generation by attached eddies in turbulent channel flow. *Journal of Fluid Mechanics*, 808:511–538, Dec. 2016. ISSN 0022-1120, 1469-7645.

M. de Giovanetti, H. J. Sung, and Y. Hwang. Streak instability in turbulent channel flow: The seeding mechanism of large-scale motions. *Journal of Fluid Mechanics*, 832:483–513, Dec. 2017. ISSN 0022-1120, 1469-7645.

S. Deck, N. Renard, R. Laraufie, and P.-É. Weiss. Large-scale contribution to mean wall shear stress in high-Reynolds-number flat-plate boundary layers up to re=13650. *Journal of Fluid Mechanics*, 743: 202–248, Mar. 2014. ISSN 0022-1120, 1469-7645.

J. C. Del Álamo and J. Jiménez. Linear energy amplification in turbulent channels. *Journal of Fluid Mechanics*, 559:205, July 2006. ISSN 0022-1120, 1469-7645.

R. Deshpande, C. M. De Silva, and I. Marusic. Evidence that superstructures comprise self-similar coherent motions in high Reynolds number boundary layers. *Journal of Fluid Mechanics*, 969:A10, Aug. 2023. ISSN 0022-1120, 1469-7645.

E. Dogan, R. Örlü, D. Gatti, R. Vinuesa, and P. Schlatter. Quantification of amplitude modulation in wall-bounded turbulence. *Fluid Dynamics Research*, 51(1):011408, Jan. 2019. ISSN 1873-7005.

S. Duvvuri and B. J. McKeon. Triadic scale interactions in a turbulent boundary layer. *Journal of Fluid Mechanics*, 767:R4, Mar. 2015. ISSN 0022-1120, 1469-7645.

G. Eitel-Amor, R. Örlü, and P. Schlatter. Simulation and validation of a spatially evolving turbulent boundary layer up to re=8300. *International Journal of Heat and Fluid Flow*, 47:57–69, June 2014. ISSN 0142-727X.

O. Flores and J. Jiménez. Effect of wall-boundary disturbances on turbulent channel flows. *Journal of Fluid Mechanics*, 566:357, Nov. 2006. ISSN 0022-1120, 1469-7645.

O. Flores and J. Jiménez. Hierarchy of minimal flow units in the logarithmic layer. *Physics of Fluids*, 22 (7):071704, July 2010. ISSN 1070-6631.

P. Forooghi, A. Stroh, P. Schlatter, and B. Frohnapfel. Direct numerical simulation of flow over dissimilar, randomly distributed roughness elements: A systematic study on the effect of surface morphology on turbulence. *Physical Review Fluids*, 3(4):044605, Apr. 2018.

B. Frohnapfel, Y. Hasegawa, and M. Quadrio. Money versus time: Evaluation of flow control in terms of energy consumption and convenience. *Journal of Fluid Mechanics*, 700:406–418, June 2012. ISSN 0022-1120, 1469-7645.

B. Frohnapfel, L. Von Deyn, J. Yang, J. Neuhauser, A. Stroh, R. Örlü, and D. Gatti. Flow resistance over heterogeneous roughness made of spanwise-alternating sandpaper strips. *Journal of Fluid Mechanics*, 980:A31, Feb. 2024. ISSN 0022-1120, 1469-7645.

K. Fukagata, K. Iwamoto, and N. Kasagi. Contribution of Reynolds stress distribution to the skin friction in wall-bounded flows. *Physics of Fluids*, 14(11):L73–L76, Nov. 2002. ISSN 1070-6631, 1089-7666.

K. Fukagata, N. Kasagi, and K. Sugiyama. Feedback control achieving sublaminar friction drag. In *Proceedings of the 6th Symposium on the Smart Control of Turbulence*, pages 143–148, 2005.

K. Fukagata, K. Sugiyama, and N. Kasagi. On the lower bound of net driving power in controlled duct flows. *Physica D: Nonlinear Phenomena*, 238(13):1082–1086, June 2009. ISSN 01672789.

K. Fukagata, M. Kobayashi, and N. Kasagi. On the Friction Drag Reduction Effect by a Control of Large-Scale Turbulent Structures. *Journal of Fluid Science and Technology*, 5(3):574–584, 2010. ISSN 1880-5558.

B. Ganapathisubramani, N. Hutchins, J. P. Monty, D. Chung, and I. Marusic. Amplitude and frequency modulation in wall turbulence. *Journal of Fluid Mechanics*, 712:61–91, Dec. 2012. ISSN 0022-1120, 1469-7645.

S. Gandía-Barberá, S. Hoyas, M. Oberlack, and S. Kraheberger. Letter: The link between the Reynolds shear stress and the large structures of turbulent Couette-Poiseuille flow. *Physics of Fluids*, 30(4): 041702, Apr. 2018. ISSN 1070-6631, 1089-7666.

D. Gatti and M. Quadrio. Reynolds-number dependence of turbulent skin-friction drag reduction induced by spanwise forcing. *Journal of Fluid Mechanics*, 802:553–582, Sept. 2016. ISSN 0022-1120, 1469-7645.

D. Gatti, A. Cimarelli, Y. Hasegawa, B. Frohnapfel, and M. Quadrio. Global energy fluxes in turbulent channels with flow control. *Journal of Fluid Mechanics*, 857:345–373, Dec. 2018. ISSN 0022-1120, 1469-7645.

D. Gatti, A. Chiarini, A. Cimarelli, and M. Quadrio. Structure function tensor equations in inhomogeneous turbulence. *Journal of Fluid Mechanics*, 898:A5, Sept. 2020. ISSN 0022-1120, 1469-7645.

J. M. Hamilton, J. Kim, and F. Waleffe. Regeneration mechanisms of near-wall turbulence structures. *Journal of Fluid Mechanics*, 287:317–348, Mar. 1995. ISSN 0022-1120, 1469-7645.

Y. Hasegawa, M. Quadrio, and B. Frohnapfel. Numerical simulation of turbulent duct flows with constant power input. *Journal of Fluid Mechanics*, 750:191–209, July 2014. ISSN 0022-1120, 1469-7645.

C. G. Hernández, Q. Yang, and Y. Hwang. Generalised quasilinear approximations of turbulent channel flow. Part 2. Spanwise triadic scale interactions. *Journal of Fluid Mechanics*, 944:A34, Aug. 2022. ISSN 0022-1120, 1469-7645.

R. Hide. Experiments With Rotating Fluids. *Quarterly Journal of the Royal Meteorological Society*, 103(435): 1–28, Jan. 1977. ISSN 0035-9009, 1477-870X.

J. O. Hinze. Secondary Currents in Wall Turbulence. *Physics of Fluids*, 10(9):S122, 1967. ISSN 00319171.

S. Hoyas and J. Jiménez. Scaling of the velocity fluctuations in turbulent channels up to Reτ=2003. *Physics of Fluids*, 18(1):011702, Jan. 2006. ISSN 1070-6631.

E. Hurst, Q. Yang, and Y. M. Chung. The effect of Reynolds number on turbulent drag reduction by streamwise travelling waves. *Journal of Fluid Mechanics*, 759:28–55, Nov. 2014. ISSN 0022-1120, 1469-7645.

N. Hutchins. Large-scale structures in high Reynolds number wall-bounded turbulence. In A. Talamelli, M. Oberlack, and J. Peinke, editors, *Progress in Turbulence V*, volume 149 of *Springer Proceedings in Physics*, pages 75–83, Cham, 2014. Springer International Publishing. ISBN 978-3-319-01860-7.

N. Hutchins and I. Marusic. Evidence of very long meandering features in the logarithmic region of turbulent boundary layers. *Journal of Fluid Mechanics*, 579:1–28, May 2007a. ISSN 1469-7645, 0022-1120.

N. Hutchins and I. Marusic. Large-scale influences in near-wall turbulence. *Philosophical Transactions of the Royal Society A: Mathematical, Physical and Engineering Sciences*, 365(1852):647–664, Mar. 2007b.

J. Hwang, J. Lee, H. J. Sung, and T. A. Zaki. Inner–outer interactions of large-scale structures in turbulent channel flow. *Journal of Fluid Mechanics*, 790:128–157, Mar. 2016. ISSN 0022-1120, 1469-7645.

Y. Hwang. Near-wall turbulent fluctuations in the absence of wide outer motions. *Journal of Fluid Mechanics*, 723:264–288, May 2013. ISSN 0022-1120, 1469-7645.

Y. Hwang. Statistical structure of self-sustaining attached eddies in turbulent channel flow. *Journal of Fluid Mechanics*, 767:254–289, Mar. 2015. ISSN 0022-1120, 1469-7645.

Y. Hwang and C. Cossu. Self-Sustained Process at Large Scales in Turbulent Channel Flow. *Physical Review Letters*, 105(4):044505, July 2010a. ISSN 0031-9007, 1079-7114.

Y. Hwang and C. Cossu. Linear non-normal energy amplification of harmonic and stochastic forcing in the turbulent channel flow. *Journal of Fluid Mechanics*, 664:51–73, Dec. 2010b. ISSN 0022-1120, 1469-7645.

G. Iacobello, L. Ridolfi, and S. Scarsoglio. Large-to-small scale frequency modulation analysis in wall-bounded turbulence via visibility networks. *Journal of Fluid Mechanics*, 918, July 2021. ISSN 0022-1120, 1469-7645.

J. I. Ibrahim, A. Guseva, and R. Garcia-Mayoral. Selective opposition-like control of large-scale structures in wall-bounded turbulence. *Journal of Physics: Conference Series*, 1522(1):012015, Apr. 2020. ISSN 1742-6588, 1742-6596.

S. J. Illingworth. Streamwise-constant large-scale structures in Couette and Poiseuille flows. *Journal of Fluid Mechanics*, 889:A13, Apr. 2020. ISSN 0022-1120, 1469-7645.

K. Iwamoto, N. Kasagi, and Y. Suzuki. Dynamical Roles of Large-Scale Structures in Turbulent Channel Flow. *Computational Mechanics, WCCM VI in conjunction with APCOM '04*, Sept. 5-10, 2004, Beijing, China, 2004.

K. Iwamoto, K. Fukagata, N. Kasagi, and Y. Suzuki. Friction drag reduction achievable by near-wall turbulence manipulation at high Reynolds numbers. *Physics of Fluids*, 17(1):011702–011702–4, Jan. 2005. ISSN 1070-6631, 1089-7666.

I. Jacobi, D. Chung, S. Duvvuri, and B. J. McKeon. Interactions between scales in wall turbulence: Phase relationships, amplitude modulation and the importance of critical layers. *Journal of Fluid Mechanics*, 914:A7, May 2021. ISSN 0022-1120, 1469-7645.

J. Jeong, F. Hussain, W. Schoppa, and J. Kim. Coherent structures near the wall in a turbulent channel flow. *Journal of Fluid Mechanics*, 332:185–214, Feb. 1997. ISSN 0022-1120, 1469-7645.

J. Jiménez. Cascades in Wall-Bounded Turbulence. *Annual Review of Fluid Mechanics*, 44(1):27–45, Jan. 2012. ISSN 0066-4189, 1545-4479.

J. Jiménez. Coherent structures in wall-bounded turbulence. *Journal of Fluid Mechanics*, 842, May 2018. ISSN 0022-1120, 1469-7645.

J. Jiménez and P. Moin. The minimal flow unit in near-wall turbulence. *Journal of Fluid Mechanics*, 225: 213–240, Apr. 1991. ISSN 0022-1120, 1469-7645.

J. Jiménez and A. Pinelli. The autonomous cycle of near-wall turbulence. *Journal of Fluid Mechanics*, 389: 335–359, June 1999. ISSN 0022-1120, 1469-7645.

J. P. Johnston, R. M. Halleent, and D. K. Lezius. Effects of spanwise rotation on the structure of two-dimensional fully developed turbulent channel flow. *Journal of Fluid Mechanics*, 56(03):533, Dec. 1972. ISSN 0022-1120, 1469-7645.

M. R. Jovanović and B. Bamieh. Componentwise energy amplification in channel flows. *Journal of Fluid Mechanics*, 534:145–183, June 2005. ISSN 0022-1120, 1469-7645.

I. K. Kaminaris, E. Balaras, M. P. Schultz, and R. J. Volino. Secondary flows in turbulent boundary layers developing over truncated cone surfaces. *Journal of Fluid Mechanics*, 961:A23, Apr. 2023. ISSN 0022-1120, 1469-7645.

G. Karniadakis and K.-S. Choi. Mechanisms on Transverse Motions in Turbulent Wall Flows. *Annual Review of Fluid Mechanics*, 35(1):45–62, Jan. 2003. ISSN 0066-4189, 1545-4479.

N. Kasagi, Y. Suzuki, and K. Fukagata. Microelectromechanical Systems–Based Feedback Control of Turbulence for Skin Friction Reduction. *Annual Review of Fluid Mechanics*, 41(1):231–251, Jan. 2009. ISSN 0066-4189, 1545-4479.

T. Kawata and P. H. Alfredsson. Experiments in rotating plane Couette flow – momentum transport by coherent roll-cell structure and zero-absolute-vorticity state. *Journal of Fluid Mechanics*, 791:191–213, Mar. 2016a. ISSN 0022-1120, 1469-7645.

T. Kawata and P. H. Alfredsson. Turbulent rotating plane Couette flow: Reynolds and rotation number dependency of flow structure and momentum transport. *Physical Review Fluids*, 1(3):034402, July 2016b. ISSN 2469-990X.

T. Kawata and P. H. Alfredsson. Inverse Interscale Transport of the Reynolds Shear Stress in Plane Couette Turbulence. *Physical Review Letters*, 120(24):244501, June 2018. ISSN 0031-9007, 1079-7114.

T. Kawata and P. H. Alfredsson. Scale interactions in turbulent rotating planar Couette flow: Insight through the Reynolds stress transport. *Journal of Fluid Mechanics*, 879:255–295, Nov. 2019. ISSN 0022-1120, 1469-7645.

T. Kawata and T. Tsukahara. Scale interactions in turbulent plane Couette flows in minimal domains. *Journal of Fluid Mechanics*, 911:A55, Mar. 2021. ISSN 0022-1120, 1469-7645.

K. Kevin, J. P. Monty, H. L. Bai, G. Pathikonda, B. Nugroho, J. M. Barros, K. T. Christensen, and N. Hutchins. Cross-stream stereoscopic particle image velocimetry of a modified turbulent boundary layer over directional surface pattern. *Journal of Fluid Mechanics*, 813:412–435, Feb. 2017. ISSN 0022-1120, 1469-7645.

K. Kevin, J. Monty, and N. Hutchins. The meandering behaviour of large-scale structures in turbulent boundary layers. *Journal of Fluid Mechanics*, 865:R1, Apr. 2019. ISSN 0022-1120, 1469-7645.

J. Kim, P. Moin, and R. Moser. Turbulence statistics in fully developed channel flow at low Reynolds number. *Journal of Fluid Mechanics*, 177:133–166, Apr. 1987. ISSN 0022-1120, 1469-7645.

K. C. Kim and R. J. Adrian. Very large-scale motion in the outer layer. *Physics of Fluids*, 11(2):417–422, Feb. 1999. ISSN 1070-6631.

O. Kitoh and M. Umeki. Experimental study on large-scale streak structure in the core region of turbulent plane Couette flow. *Physics of Fluids*, 20(2):025107, Feb. 2008. ISSN 1070-6631, 1089-7666.

S. J. Kline, W. C. Reynolds, F. A. Schraub, and P. W. Runstadler. The structure of turbulent boundary layers. *Journal of Fluid Mechanics*, 30(4):741–773, Dec. 1967. ISSN 1469-7645, 0022-1120.

L. Klotz, A. Pavlenko, and J. Wesfreid. Experimental measurements in plane Couette–Poiseuille flow: Dynamics of the large- and small-scale flow. *Journal of Fluid Mechanics*, 912:A24, Apr. 2021. ISSN 0022-1120, 1469-7645.

A. N. Kolmogorov. The local structure of turbulence in incompressible viscous fluid for very large Reynolds numbers. *Proceedings of the Royal Society of London. Series A: Mathematical and Physical Sciences*, 434(1890):9–13, July 1991. ISSN 0962-8444, 2053-9177.

J. Komminaho, A. Lundbladh, and A. V. Johansson. Very large structures in plane turbulent Couette flow. *Journal of Fluid Mechanics*, 320(-1):259, Aug. 1996. ISSN 0022-1120, 1469-7645.

R. Kristoffersen and H. I. Andersson. Direct simulations of low-Reynolds-number turbulent flow in a rotating channel. *Journal of Fluid Mechanics*, 256:163–197, Nov. 1993. ISSN 0022-1120, 1469-7645.

Y. Kwon and J. Jiménez. An isolated logarithmic layer. *Journal of Fluid Mechanics*, 916:A35, June 2021. ISSN 0022-1120, 1469-7645.

S. Laizet and E. Lamballais. High-order compact schemes for incompressible flows: A simple and efficient method with quasi-spectral accuracy. *Journal of Computational Physics*, 228(16):5989–6015, Sept. 2009. ISSN 00219991.

S. Laizet and N. Li. Incompact3d: A powerful tool to tackle turbulence problems with up to $O(10^5)$ computational cores. *International Journal for Numerical Methods in Fluids*, 67(11):1735–1757, Dec. 2011. ISSN 0271-2091, 1097-0363.

M. Lee and R. D. Moser. Direct numerical simulation of turbulent channel flow up to re=5200. *Journal of Fluid Mechanics*, 774:395–415, July 2015. ISSN 0022-1120, 1469-7645.

M. Lee and R. D. Moser. Extreme-scale motions in turbulent plane Couette flows. *Journal of Fluid Mechanics*, 842:128–145, May 2018. ISSN 0022-1120, 1469-7645.

M. Lee and R. D. Moser. Spectral analysis of the budget equation in turbulent channel flows at high Reynolds number. *Journal of Fluid Mechanics*, 860:886–938, Feb. 2019. ISSN 0022-1120, 1469-7645.

J. A. LeHew, M. Guala, and B. J. McKeon. Time-resolved measurements of coherent structures in the turbulent boundary layer. *Experiments in Fluids*, 54(4):1508, Apr. 2013. ISSN 0723-4864, 1432-1114.

S. K. Lele. Compact finite difference schemes with spectral-like resolution. *Journal of Computational Physics*, 103(1):16–42, Nov. 1992. ISSN 00219991.

D. K. Lezius and J. P. Johnston. Roll-cell instabilities in rotating laminar and trubulent channel flows. *Journal of Fluid Mechanics*, 77(1):153–174, Sept. 1976. ISSN 0022-1120, 1469-7645.

A. Lozano-Durán and J. Jiménez. Time-resolved evolution of coherent structures in turbulent channels: Characterization of eddies and cascades. *Journal of Fluid Mechanics*, 759:432–471, Nov. 2014. ISSN 0022-1120, 1469-7645.

A. Lozano-Durán, N. C. Constantinou, M.-A. Nikolaidis, and M. Karp. Cause-and-effect of linear mechanisms sustaining wall turbulence. *Journal of Fluid Mechanics*, 914:A8, May 2021. ISSN 0022-1120, 1469-7645.

P. Luchini. Linearized no-slip boundary conditions at a rough surface. *Journal of Fluid Mechanics*, 737: 349–367, Dec. 2013. ISSN 0022-1120, 1469-7645.

P. Luchini. Structure and interpolation of the turbulent velocity profile in parallel flow. *European Journal of Mechanics - B/Fluids*, 71:15–34, Sept. 2018. ISSN 09977546.

P. Luchini and M. Quadrio. A low-cost parallel implementation of direct numerical simulation of wall turbulence. *Journal of Computational Physics*, 211(2):551–571, Jan. 2006. ISSN 0021-9991.

P. Luchini, F. Manzo, and A. Pozzi. Resistance of a grooved surface to parallel flow and cross-flow. *Journal of Fluid Mechanics Digital Archive*, 228:87, July 1991. ISSN 1750-6859, 1750-6859.

I. Marusic and J. P. Monty. Attached Eddy Model of Wall Turbulence. *Annual Review of Fluid Mechanics*, 51(1):49–74, 2019.

I. Marusic and A. E. Perry. A wall-wake model for the turbulence structure of boundary layers. Part 2. Further experimental support. *Journal of Fluid Mechanics*, 298:389–407, Sept. 1995. ISSN 0022-1120, 1469-7645.

I. Marusic, D. D. Joseph, and K. Mahesh. Laminar and turbulent comparisons for channel flow and flow control. *Journal of Fluid Mechanics*, 570:467–477, Jan. 2007. ISSN 0022-1120, 1469-7645.

I. Marusic, R. Mathis, and N. Hutchins. High Reynolds number effects in wall turbulence. *International Journal of Heat and Fluid Flow*, 31(3):418–428, June 2010a. ISSN 0142-727X.

I. Marusic, R. Mathis, and N. Hutchins. Predictive Model for Wall-Bounded Turbulent Flow. *Science*, 329(5988):193–196, July 2010b.

I. Marusic, D. Chandran, A. Rouhi, M. K. Fu, D. Wine, B. Holloway, D. Chung, and A. J. Smits. An energy-efficient pathway to turbulent drag reduction. *Nature Communications*, 12(1):5805, Oct. 2021. ISSN 2041-1723.

R. Mathis, N. Hutchins, and I. Marusic. Large-scale amplitude modulation of the small-scale structures in turbulent boundary layers. *Journal of Fluid Mechanics*, 628:311–337, June 2009. ISSN 1469-7645, 0022-1120.

R. Mathis, N. Hutchins, and I. Marusic. A predictive inner–outer model for streamwise turbulence statistics in wall-bounded flows. *Journal of Fluid Mechanics*, 681:537–566, Aug. 2011a. ISSN 1469-7645, 0022-1120.

R. Mathis, I. Marusic, N. Hutchins, and K. R. Sreenivasan. The relationship between the velocity skewness and the amplitude modulation of the small scale by the large scale in turbulent boundary layers. *Physics of Fluids*, 23(12):121702, Dec. 2011b. ISSN 1070-6631.

R. Mathis, I. Marusic, S. I. Chernyshenko, and N. Hutchins. Estimating wall-shear-stress fluctuations given an outer region input. *Journal of Fluid Mechanics*, 715:163–180, Jan. 2013. ISSN 0022-1120, 1469-7645.

B. J. McKeon and A. S. Sharma. A critical-layer framework for turbulent pipe flow. *Journal of Fluid Mechanics*, 658:336–382, Sept. 2010. ISSN 0022-1120, 1469-7645.

T. Medjnoun, C. Vanderwel, and B. Ganapathisubramani. Characteristics of turbulent boundary layers over smooth surfaces with spanwise heterogeneities. *Journal of Fluid Mechanics*, 838:516–543, Mar. 2018. ISSN 0022-1120, 1469-7645.

R. Mejia-Alvarez and K. T. Christensen. Wall-parallel stereo particle-image velocimetry measurements in the roughness sublayer of turbulent flow overlying highly irregular roughness. *Physics of Fluids*, 25 (11):115109, Nov. 2013. ISSN 1070-6631, 1089-7666.

R. Mejia-Alvarez, J. M. Barros, and K. T. Christensen. Structural Attributes of Turbulent Flow Over a Complex Topography. In J. G. Venditti, J. L. Best, M. Church, and R. J. Hardy, editors, *Coherent Flow Structures at Earth's Surface*, pages 25–41. Wiley, 1 edition, Oct. 2013. ISBN 978-1-119-96277-9 978-1-118-52722-1.

Y. Mizuno and J. Jiménez. Wall turbulence without walls. *Journal of Fluid Mechanics*, 723:429–455, May 2013. ISSN 0022-1120, 1469-7645.

J. Moehlis, H. Faisst, and B. Eckhardt. A low-dimensional model for turbulent shear flows. *New Journal of Physics*, 6:56–56, May 2004. ISSN 1367-2630.

J. P. Monty, N. Hutchins, H. C. H. Ng, I. Marusic, and M. S. Chong. A comparison of turbulent pipe, channel and boundary layer flows. *Journal of Fluid Mechanics*, 632:431–442, Aug. 2009. ISSN 0022-1120, 1469-7645.

K. Nakabayashi, O. Kitoh, and Y. Katoh. Similarity laws of velocity profiles and turbulence characteristics of CouettePoiseuille turbulent flows. *Journal of Fluid Mechanics*, 507:43–69, May 2004. ISSN 0022-1120, 1469-7645.

J. Neuhauser, K. Schäfer, D. Gatti, and B. Frohnapfel. Simulation of turbulent flow over roughness strips. *Journal of Fluid Mechanics*, 945:A14, Aug. 2022. ISSN 0022-1120, 1469-7645.

V. I. Nikora, T. Stoesser, S. M. Cameron, M. Stewart, K. Papadopoulos, P. Ouro, R. McSherry, A. Zampiron, I. Marusic, and R. A. Falconer. Friction factor decomposition for rough-wall flows: Theoretical background and application to open-channel flows. *Journal of Fluid Mechanics*, 872:626–664, Aug. 2019. ISSN 0022-1120, 1469-7645.

B. Nugroho, N. Hutchins, and J. Monty. Large-scale spanwise periodicity in a turbulent boundary layer induced by highly ordered and directional surface roughness. *International Journal of Heat and Fluid Flow*, 41:90–102, June 2013. ISSN 0142727X.

P. Orlandi, M. Bernardini, and S. Pirozzoli. Poiseuille and Couette flows in the transitional and fully turbulent regime. *Journal of Fluid Mechanics*, 770:424–441, May 2015. ISSN 0022-1120, 1469-7645.

R. L. Panton. Overview of the self-sustaining mechanisms of wall turbulence. *Progress in Aerospace Sciences*, 37(4):341–383, May 2001. ISSN 03760421.

D. V. Papavassiliou and T. J. Hanratty. Interpretation of large-scale structures observed in a turbulent plane Couette flow. *International Journal of Heat and Fluid Flow*, 18(1):55–69, Feb. 1997. ISSN 0142727X.

A. Pascarelli, U. Piomelli, and G. V. Candler. Multi-Block Large-Eddy Simulations of Turbulent Boundary Layers. *Journal of Computational Physics*, 157(1):256–279, Jan. 2000. ISSN 00219991.

U. Piomelli, T. A. Zang, C. G. Speziale, and M. Y. Hussaini. On the large-eddy simulation of transitional wall-bounded flows. *Physics of Fluids A: Fluid Dynamics*, 2(2):257–265, Feb. 1990. ISSN 0899-8213.

U. Piomelli, W. H. Cabot, P. Moin, and S. Lee. Subgrid-scale backscatter in turbulent and transitional flows. *Physics of Fluids A: Fluid Dynamics*, 3(7):1766–1771, July 1991. ISSN 0899-8213.

S. Pirozzoli, M. Bernardini, and P. Orlandi. Large-scale motions and inner/outer layer interactions in turbulent Couette–Poiseuille flows. *Journal of Fluid Mechanics*, 680:534–563, Aug. 2011. ISSN 1469-7645, 0022-1120.

S. Pirozzoli, M. Bernardini, and P. Orlandi. Turbulence statistics in Couette flow at high Reynolds number. *Journal of Fluid Mechanics*, 758:327–343, Nov. 2014. ISSN 0022-1120, 1469-7645.

S. B. Pope. *Turbulent Flows*. Cambridge University Press, 1 edition, Aug. 2000. ISBN 978-0-521-59125-6 978-0-521-59886-6 978-0-511-84053-1.

M. Puccioni, M. Calaf, E. R. Pardyjak, S. Hoch, T. J. Morrison, A. Perelet, and G. V. Iungo. Identification of the energy contributions associated with wall-attached eddies and very-large-scale motions in the near-neutral atmospheric surface layer through wind LiDAR measurements. *Journal of Fluid Mechanics*, 955:A39, Jan. 2023. ISSN 0022-1120, 1469-7645.

M. Quadrio. Drag reduction in turbulent boundary layers by in-plane wall motion. *Philosophical Transactions of the Royal Society A: Mathematical, Physical and Engineering Sciences*, 369(1940):1428–1442, Apr. 2011. ISSN 1364-503X, 1471-2962.

M. Quadrio, P. Ricco, and C. Viotti. Streamwise-travelling waves of spanwise wall velocity for turbulent drag reduction. *Journal of Fluid Mechanics*, 627:161–178, May 2009. ISSN 0022-1120, 1469-7645.

A. Quarteroni. *Numerical Models for Differential Problems*. Number v. 2 in MS & A. Springer, Milan New York, 2009. ISBN 978-88-470-1071-0.

H. Rebbeck and K.-S. Choi. A wind-tunnel experiment on real-time opposition control of turbulence. *Physics of Fluids*, 18(3):035103, Mar. 2006. ISSN 1070-6631, 1089-7666.

N. Renard and S. Deck. A theoretical decomposition of mean skin friction generation into physical phenomena across the boundary layer. *Journal of Fluid Mechanics*, 790:339–367, Mar. 2016. ISSN 0022-1120, 1469-7645.

R. T. Reynolds, P. Hayden, I. P. Castro, and A. G. Robins. Spanwise variations in nominally two-dimensional rough-wall boundary layers. *Experiments in Fluids*, 42(2):311–320, Jan. 2007. ISSN 0723-4864, 1432-1114.

W. C. Reynolds and A. K. M. F. Hussain. The mechanics of an organized wave in turbulent shear flow. Part 3. Theoretical models and comparisons with experiments. *Journal of Fluid Mechanics*, 54(2):263–288, July 1972. ISSN 0022-1120, 1469-7645.

P. Ricco, C. Ottonelli, Y. Hasegawa, and M. Quadrio. Changes in turbulent dissipation in a channel flow with oscillating walls. *Journal of Fluid Mechanics*, 700:77–104, June 2012. ISSN 0022-1120, 1469-7645.

L. F. Richardson and P. Lynch. *Weather Prediction by Numerical Process*. Cambridge University Press, 2 edition, Aug. 2007. ISBN 978-0-521-68044-8 978-0-511-61829-1.

A. Roccon, F. Zonta, and A. Soldati. Energy balance in lubricated drag-reduced turbulent channel flow. *Journal of Fluid Mechanics*, 911:A37, Mar. 2021. ISSN 0022-1120, 1469-7645.

S. Russo and P. Luchini. A fast algorithm for the estimation of statistical error in DNS (or experimental) time averages. *Journal of Computational Physics*, 347:328–340, Oct. 2017. ISSN 0021-9991.

N. D. Sandham, R. Johnstone, and C. T. Jacobs. Surface-sampled simulations of turbulent flow at high Reynolds number: Surface-sampled simulations of turbulent flow. *International Journal for Numerical Methods in Fluids*, 85(9):525–537, Nov. 2017. ISSN 02712091.

K. Schäfer. *Turbulent Large-Scale Structures over Heterogeneous Surfaces*. PhD thesis, Karlsruhe Institute for Technology (KIT), 2023.

P. Schlatter and R. Örlü. Quantifying the interaction between large and small scales in wall-bounded turbulent flows: A note of caution. *Physics of Fluids*, 22(5):051704, May 2010. ISSN 1070-6631.

P. Schlatter, R. Örlü, Q. Li, G. Brethouwer, J. H. M. Fransson, A. V. Johansson, P. H. Alfredsson, and D. S. Henningson. Turbulent boundary layers up to Re=2500 studied through simulation and experiment. *Physics of Fluids*, 21(5):051702, May 2009. ISSN 1070-6631, 1089-7666.

W. Schoppa and F. Hussain. A large-scale control strategy for drag reduction in turbulent boundary layers. *Physics of Fluids*, 10(5):1049–1051, May 1998. ISSN 1070-6631, 1089-7666.

F. S. Sherman. *Viscous Flow*. McGraw-Hill Series in Mechanical Engineering. McGraw-Hill, New York, 1990. ISBN 978-0-07-056579-1.

J. A. Sillero, J. Jiménez, and R. D. Moser. One-point statistics for turbulent wall-bounded flows at Reynolds numbers up to $\delta+ \approx 2000$. *Physics of Fluids*, 25(10):105102, Oct. 2013. ISSN 1070-6631, 1089-7666.

A. J. Smits, B. J. McKeon, and I. Marusic. High–Reynolds Number Wall Turbulence. *Annual Review of Fluid Mechanics*, 43(1):353–375, 2011.

A. Stroh, Y. Hasegawa, J. Kriegseis, and B. Frohnapfel. Secondary vortices over surfaces with spanwise varying drag. *Journal of Turbulence*, 17(12):1142–1158, Dec. 2016a. ISSN 1468-5248.

A. Stroh, Y. Hasegawa, P. Schlatter, and B. Frohnapfel. Global effect of local skin friction drag reduction in spatially developing turbulent boundary layer. *Journal of Fluid Mechanics*, 805:303–321, Oct. 2016b. ISSN 0022-1120, 1469-7645.

A. Stroh, K. Schäfer, B. Frohnapfel, and P. Forooghi. Rearrangement of secondary flow over spanwise heterogeneous roughness. *Journal of Fluid Mechanics*, 885:R5, Feb. 2020. ISSN 0022-1120, 1469-7645.

H. Taha, C. Gonzalez, and M. Shorbagy. A minimization principle for incompressible fluid mechanics. *Physics of Fluids*, 35(12):127110, Dec. 2023. ISSN 1070-6631, 1089-7666.

Y. Tang and R. Akhavan. Computations of equilibrium and non-equilibrium turbulent channel flows using a nested-LES approach. *Journal of Fluid Mechanics*, 793:709–748, Apr. 2016. ISSN 0022-1120, 1469-7645.

M. M. M. E. Telbany and A. J. Reynolds. Velocity distributions in plane turbulent channel flows. *Journal of Fluid Mechanics*, 100(01):1, Sept. 1980. ISSN 0022-1120, 1469-7645.

M. M. M. E. Telbany and A. J. Reynolds. Turbulence in plane channel flows. *Journal of Fluid Mechanics*, 111(-1):283, Oct. 1981. ISSN 0022-1120, 1469-7645.

N. Tillmark and P. H. Alfredsson. Experiments On Rotating Plane Couette Flow. In R. Moreau, S. Gavrilakis, L. Machiels, and P. A. Monkewitz, editors, *Advances in Turbulence VI*, volume 36, pages 391–394. Springer Netherlands, Dordrecht, 1996. ISBN 978-94-010-6618-1 978-94-009-0297-8.

S. S. Toedtli, M. Luhar, and B. J. McKeon. Predicting the response of turbulent channel flow to varying-phase opposition control: Resolvent analysis as a tool for flow control design. *Physical Review Fluids*, 4(7):073905, July 2019. ISSN 2469-990X.

S. Toh and T. Itano. Interaction between a large-scale structure and near-wall structures in channel flow. *Journal of Fluid Mechanics*, 524:249–262, Feb. 2005. ISSN 0022-1120, 1469-7645.

C. D. Tomkins and R. J. Adrian. Spanwise structure and scale growth in turbulent boundary layers. *Journal of Fluid Mechanics*, 490:37–74, Sept. 2003. ISSN 00221120, 14697645.

A. A. Townsend. *The Structure of Turbulent Shear Flow*. 2nd edition, Jan. 1976.

D. J. Tritton. Stabilization and destabilization of turbulent shear flow in a rotating fluid. *Journal of Fluid Mechanics*, 241:503–523, Aug. 1992. ISSN 0022-1120, 1469-7645.

T. Tsukahara, N. Tillmark, and P. H. Alfredsson. Flow regimes in a plane Couette flow with system rotation. *Journal of Fluid Mechanics*, 648:5–33, Apr. 2010. ISSN 0022-1120, 1469-7645.

L. S. Tuckerman, T. Kreilos, H. Schrobsdorff, T. M. Schneider, and J. F. Gibson. Turbulent-laminar patterns in plane Poiseuille flow. *Physics of Fluids*, 26(11):114103, Nov. 2014. ISSN 1070-6631, 1089-7666.

S. Türk, G. Daschiel, A. Stroh, Y. Hasegawa, and B. Frohnapfel. Turbulent flow over superhydrophobic surfaces with streamwise grooves. *Journal of Fluid Mechanics*, 747:186–217, May 2014. ISSN 0022-1120, 1469-7645.

M. van Dyke. *An Album of Fluid Motion*. Parabolic Press, Stanford, California, 14. print edition, 2012. ISBN 978-0-915760-02-2.

C. Vanderwel and B. Ganapathisubramani. Effects of spanwise spacing on large-scale secondary flows in rough-wall turbulent boundary layers. *Journal of Fluid Mechanics*, 774:R2, July 2015. ISSN 0022-1120, 1469-7645.

C. Vanderwel, A. Stroh, J. Kriegseis, B. Frohnapfel, and B. Ganapathisubramani. The instantaneous structure of secondary flows in turbulent boundary layers. *Journal of Fluid Mechanics*, 862:845–870, Mar. 2019. ISSN 0022-1120, 1469-7645.

R. Vinuesa, M. H. Hites, C. E. Wark, and H. M. Nagib. Documentation of the role of large-scale structures in the bursting process in turbulent boundary layers. *Physics of Fluids*, 27(10):105107, Oct. 2015. ISSN 1070-6631.

Z.-Q. Wang and N.-S. Cheng. Time-mean structure of secondary flows in open channel with longitudinal bedforms. *Advances in Water Resources*, 29(11):1634–1649, Nov. 2006. ISSN 03091708.

D. Wangsawijaya and N. Hutchins. Investigation of unsteady secondary flows and large-scale turbulence in heterogeneous turbulent boundary layers. *Journal of Fluid Mechanics*, 934:A40, Mar. 2022. ISSN 0022-1120, 1469-7645.

D. D. Wangsawijaya, R. Baidya, D. Chung, I. Marusic, and N. Hutchins. The effect of spanwise wavelength of surface heterogeneity on turbulent secondary flows. *Journal of Fluid Mechanics*, 894:A7, July 2020. ISSN 0022-1120, 1469-7645.

J. Williamson. Low-storage Runge-Kutta schemes. *Journal of Computational Physics*, 35(1):48–56, Mar. 1980. ISSN 00219991.

D. Willingham, W. Anderson, K. T. Christensen, and J. M. Barros. Turbulent boundary layer flow over transverse aerodynamic roughness transitions: Induced mixing and flow characterization. *Physics of Fluids*, 26(2):025111, Feb. 2014. ISSN 1070-6631, 1089-7666.

K. M. Womack, R. J. Volino, C. Meneveau, and M. P. Schultz. Turbulent boundary layer flow over regularly and irregularly arranged truncated cone surfaces. *Journal of Fluid Mechanics*, 933:A38, Feb. 2022. ISSN 0022-1120, 1469-7645.

J. Yao, X. Chen, F. Thomas, and F. Hussain. Large-scale control strategy for drag reduction in turbulent channel flows. *Physical Review Fluids*, 2(6):062601, June 2017. ISSN 2469-990X.

A. Zampiron, S. Cameron, and V. Nikora. Secondary currents and very-large-scale motions in open-channel flow over streamwise ridges. *Journal of Fluid Mechanics*, 887:A17, Mar. 2020. ISSN 0022-1120, 1469-7645.

A. Zampiron, S. Cameron, and V. Nikora. Momentum and energy transfer in open-channel flow over streamwise ridges. *Journal of Fluid Mechanics*, 915:A42, May 2021. ISSN 0022-1120, 1469-7645.

C. Zhang and S. I. Chernyshenko. Quasisteady quasihomogeneous description of the scale interactions in near-wall turbulence. *Physical Review Fluids*, 1(1):014401, May 2016.

Z. Zhou, C.-X. Xu, and J. Jiménez. Interaction between near-wall streaks and large-scale motions in turbulent channel flows. *Journal of Fluid Mechanics*, 940:A23, June 2022. ISSN 0022-1120, 1469-7645.

Journal Publications

[MY21] A. Andreolli, M. Quadrio, and D. Gatti, “Global energy budgets in turbulent Couette and Poiseuille flows". *Journal of Fluid Mechanics*, vol. 924, p. A25, 2021.

[MY23] A. Andreolli, D. Gatti, R. Vinuesa, R. Örlü, and P. Schlatter, “Separating large-scale superposition and modulation in turbulent channels". *Journal of Fluid Mechanics*, vol. 958, p. A37, 2023.

[MY24a] A. Andreolli, M.K. Singh, and D. Gatti, “Skin friction reduction via suppression of large scales in turbulent Couette flows". *International Journal of Heat and Fluid Flow*, vol. 108, 109444, 2024.

[MY24b] A. Andreolli, N. Hutchins, B. Frohnapfel, and D. Gatti, “Temporal decay of secondary motions in turbulent channel flows". *Under consideration for publication in the Journal of Fluid Mechanics*

Conference Contributions

A. Andreolli, D. Gatti, R. Vinuesa, R. Örlü, and P. Schlatter. Suppression of either large-scale modulation or superposition in wall turbulence (Presentation). In 13^{th} *International ERCOFTAC symposium on engineering, turbulence, modelling and measurements (ETMM)*, Rhodes, Greece, 2021a.

A. Andreolli, M. Quadrio, and D. Gatti. Global turbulent efficiency in plane Couette and Poiseuille flows (Presentation). In *IX. iTi Conference on Turbulence*, Online, 2021b.

A. Andreolli, M. K. Singh, and D. Gatti. Suppressing very-large-scale motions in turbulent Couette flows (Presentation). In 23^{rd} *Australasian Fluid Mechanics Conference (AFMC)*, Sydney, Australia, 2022.

A. Andreolli, N. Hutchins, B. Frohnapfel, and D. Gatti. Decay and formation of secondary motions in a turbulent channel flow (Presentation). In *X. iTi Conference on Turbulence*, Bertinoro, Italy, 2023.

Code and Data Repositories

A. Andreolli. Python tools for *channel*. https://github.com/andyandreolli/channel_pytools.

A. Andreolli, D. Gatti, R. Vinuesa, R. Örlü, and P. Schlatter. Data for the publication: Separating large-scale superposition and modulation in turbulent channels. https://dx.doi.org/10.35097/EEXRgyvGozfhsyqo, 2024a.

A. Andreolli, N. Hutchins, B. Frohnapfel, and D. Gatti. Videos of decaying turbulent secondary motions. https://dx.doi.org/10.35097/farApPGYflANpeIi, 2024b.

A. Andreolli, M. K. Singh, and D. Gatti. Data for the publication: Skin friction reduction via suppression of large scales in turbulent Couette flows. https://dx.doi.org/10.35097/EhgiloDgsqkMSqTn, 2024c.

D. Gatti. Channel. A program for the direct numerical simulation of channel flows. Contains contributions by A. Andreolli. https://github.com/davecats/channel.

Co-supervised Theses

O. Oyedele. Amplitude modulation in wall-bounded turbulent flows: the role of small-scale energy production. Master's thesis, 2022.

M. K. Singh. Suppression of superstructures with Coriolis force in Couette flows. Bachelor's thesis, 2022.

List of Figures

List of Tables

A DNS simulation of the flow around a car: an order-of-magnitude estimate of the costs

Consider a car travelling down a road. The relative speed of the car with respect to the wind is U_∞ and the kinematic viscosity of the air ν_{air}; it is assumed that sidewinds are absent. The width of the car and its length are indicated by W and L respectively. Realistic values for all of the above parameters are given in table A.1; these values will be used to carry out an order-of-magnitude estimate of the cost of simulating the air flow around the car through a direct numerical simulation (DNS).

Quantity	Value for cost estimate
U_∞	20 m/s ($\approx$ 72 km/h)
L	4.5 m
W	1.8 m
ν_{air}	$1.48 \cdot 10^{-5}$ m^2/s

Table A.1: Values used for the present cost estimate. The kinematic viscosity ν_{air} refers to values seen at a temperature of 15°C.

The mesh used for simulating the air flow around the car needs to be refined in proximity of the car itself: this is indeed the region where turbulence is found, and turbulence requires a fine resolution to be captured. To simplify the discussion, it will be assumed that only this turbulence-affected volume is simulated. Although this is not possible, most of the grid points of the simulation are found in this region; that is, this portion of fluid is the one that contributes the most to the computational expenses.

The cost estimate will proceed as follows. First, the volume occupied by the turbulence-affected fluid region will be estimated. Then, the necessary grid spacing will be determined and used to estimate the total number of grid points. The grid spacing also determines the size of the time step through the CFL condition; this informaion will be used to estimate the total number of time steps needed to complete the simulation. Finally, by extrapolating the cost of the set of simulations performed in §6, an estimate of the computational cost of performing the DNS of a car will be provided.

A crude estimate of the volume of fluid affected by turbulence is provided as follows. It is assumed that turbulence is only found in the boundary layer that builds around the car; the boundary layer is considered to be two-dimensional, as if the car were a flat plate of size $W \times L$. This is a rough approximation. First off, the three-dimensionality of the car is neglected; most importantly, the car is a bluff body, meaning that flow separations are more than likely to occur. Furthermore, corner effects and the existence of a wake will be completely ignored. In reality, then, the volume of fluid affected by turbulence will be larger than the value estimated here; this will lead to an optimistic estimate of costs.

Let δ be the boundary layer thickness; the value of δ will be approximated by Blausius' laminar solution,

$$\delta \approx 5 \sqrt{\frac{\nu_{air}\, x}{U_\infty}}, \tag{A.1}$$

where x is the streamwise coordinate, $x = 0$ indicates the front of the car and $x = L$ its back. The volume V_{BL} of the boundary layer is approximated as follows:

$$V_{BL} \approx W \int_0^L \delta \, \mathrm{d}x = \frac{10W}{3} \sqrt{\frac{\nu_{air} L^3}{U_\infty}} \tag{A.2}$$

As for the resolution of the simulation, it is assumed that the grid spacing is equal to δ_v (the viscous length scale) in all spatial directions. An estimate of δ_v is thus required. The value of δ_v is readily available if the one of τ_w is known; the latter can be estimated as follows:

$$\tau_w = \mu \frac{\partial \langle u \rangle}{\partial x} \approx \rho_{air} \, \nu_{air} \, \frac{U_\infty}{\delta} \tag{A.3}$$

By combining equations A.1, A.3 and 1.2, one gets:

$$\delta_v \approx \frac{\sqrt{5} \, \nu_{air}^{3/4} \, x^{1/4}}{U_\infty^{3/4}} \tag{A.4}$$

As highlighted by the above equations, both the wall shear stress and the viscous length scale change with streamwise fetch (as they depend on the boundary layer thickness); it is thus necessary to select a reasonable value for the present estimates. Close to the leading edge of the boundary layer ($x = 0$), unphysically large values of the wall shear stress are predicted by the present estimates (as they indeed diverge); the wall shear stress then reaches lower values with streamwise fetch. The intermediate values of τ_w and δ_v seen at $x = L/4$ will be used for the present estimates, leading to:

$$\delta_v \approx 5.8 \cdot 10^{-5} \, \mathrm{m} \tag{A.5}$$

Then, the order of magnitude of the number N of grid points required by the present simulation can be estimated as:

$$N \approx \frac{V_{BL}}{\delta_v^3} \approx 2.5 \cdot 10^{11} \tag{A.6}$$

It is now necessary to estimate how many simulation time steps are needed. DNS data needs to be averaged for a long enough period of time to obtain well-converged statistics. Judging on the simulation datasets included in this thesis (§3 to §6), averaging data collected over a time window $T_{avg} = 150 \, h/u_\tau$ should be sufficent to do so. An estimate of the timestep Δt is readily obtained from the CFL condition (see §2.4.3):

$$CFL \approx \frac{U_\infty \Delta t}{\delta_v} \approx 1 \tag{A.7}$$

Bearing in mind that the order of magnitude of the CFL number has to be $\mathcal{O}(1)$ to guarantee numerical stability, an estimate of Δt can be found:

$$\Delta t \approx \frac{\delta_v}{U_\infty} = \frac{\nu_{air}}{u_\tau U_\infty} \tag{A.8}$$

so that the total number N_t of required time steps is:

$$N_t = \frac{T_{avg}}{\Delta t} \approx 150 \frac{\delta U_\infty}{\nu_{air}} \approx 10^6 \tag{A.9}$$

Notice, once again, that the boundary layer thickness has been evaluated at $x = L/4$.

To produce the simulation campaign presented in §6, it was observed that the computational cost of a timestep for a simulation with 10^8 grid points is rougly $0.3\,\mathrm{CPU\,h}$. This cost estimate was obtained by using Xcompact3d (Laizet and Li, 2011) on the Apollo (HAWK) cluster at HLRS Stuttgart. Assuming linear scaling (which is a very optimistic assumption), the cost of a timestep for the present simulation can be extrapolated to be:

$$\text{comp. cost of a timestep} \approx 750\,\mathrm{CPU\,h} \tag{A.10}$$

And thus the cost of simulating the flow around the car is:

$$\text{comp. cost of the simulation} \approx 750 \cdot 10^6\,\mathrm{CPU\,h} \tag{A.11}$$

which, assuming the cost of a CPU hour to be 0.03 €, is equivalent to roughly 23 million euros. Notice, once again, that the present estimate is only meant to capture the order of magnitude of the costs; since only a portion of the fluid domain was considered, this estimate is likely optimistic (meaning that actual costs will be higher).

Acknowledgements

This work was supported by the Priority Programme SPP 1881 Turbulent Superstructures of the Deutsche Forschungsgemeinschaft (grant no. GA 2533/1-1).

The author acknowledges the Karlsruhe House of Young Scientists (KHYS) for sponsoring a research stay abroad at the University of Melbourne. Results produced during this research stay are presented in §6 and published in [MY24b].

I'd like to thank Bettina, Davide and Maurizio, for the all the opportunities and the support I've been given. A sincere thank you to Nick, a true gentleman. To all of my great colleagues at ISTM (thanks for the memes, Alex!). A special thank to Carola and Daniele, for helping me with the German *Kurzfassung* of this thesis.

To my parents – thanks for always being there. To my friends in Milan, the craziest bunch of people I've ever met.

To all of the awesome people I've met during this journey - Jacopo, Ramis, Jelle, Pece, Aditya, Mery, Magid, Laura, Daniele, Gabriele, Gianluca, Jo, Vitoria... and I'm sure I'm forgetting someone!